DISSERTATION

Early-stage nucleation in metallic materials: A computational study using Monte Carlo and rare event sampling methods

Submitted for the degree “Doktor der technischen Wissenschaften”, under supervision of

Univ.Prof. Dipl.-Ing. Dr.techn. E. Kozeschnik

Institute for Materials Science and Technology

Submitted at TU Wien

Faculty for Mechanical and Industrial Engineering

by

MSc. Lin Qin

Matr.Nr.

Vienna, 2019

Personal Signature

This dissertation has been assessed by

Declaration

I declare in lieu of oath, that I wrote this thesis and performed the associated research myself, using only literature cited in this volume.

Vienna, December 2019

List of Publications

Journal articles

[1] L.Qin, C.Dellago, and E. Kozeschnik, "An efficient method to reconstruct free energy profiles for diffusive processes in transition interface sampling and forward flux sampling simulations," **The Journal of Chemical Physics**, vol. 150, no. 9, p. 094 114, 2019. DOI: 10.1063/1.5080933.

[2] L. Qin, A. Redermeier, C. Dellago, E. Kozeschnik, and C. Karner, "Rigid-lattice monte carlo study of nucleation kinetics in dilute bcc fe-cu alloys using statistical sampling techniques," **Acta Materialia**, vol. 159, pp. 429–438, 2018. DOI: 10.1016/j.actamat.2018.08.035

[3] L. Qin and E. Kozeschnik, "Morphological analysis of nano-sized Cu particles during nucleation in tempered Fe-Cu alloys", in preparation.

Conference Proceedings

[4] L. Qin, A. Redermeier, E. Kozeschnik, C. Karner, and C. Dellago, "A statistical methodology to reconstruct nucleation pathways in the fe-cu system," in THERMEC 2016, ser. Materials Science Forum, vol. 879, Trans Tech Publications Ltd, Feb. 2017, pp. 1529–1534. DOI: 10.4028/www.scientific.net/MSF.879.1529.

Acknowledgement

In last five years, I have received plentiful kindness and support from many individuals in the process of earning a doctorate. I want to take this opportunity to give my gratitude to all of them.

First, I would like to thank my mentor, Prof. Ernst Kozeschnik, who is inspiring and guiding me through the whole journey. Without his advice, expertise and encouragement, this thesis would have never come into reality. I also want to thank my dear friend and colleague, Alice Redermeier, for the insights and feedbacks she shared with me in my research. Working with her is an interesting and rewarding experience. I would like to give my thanks to Erwin Povoden-Karadeniz, who give me the opportunity to join the group, to Piotr Warczok and Yao Shan, who are always helping, to Matthias Wagner, who not only helps me with programming but also teaches me smoking. It is a pleasure and honor to work in the Institute of WWWT in TU Wien in the last five years. I would like to thank everyone of my colleagues for the wonderful time I spent in TU Wien. Last, I give the gratitude to my family for their love, support and understanding, specially to my boyfriend, Ran Baobao, for his love and company in these years.

Abstract

Nucleation is the initial stage of a first-order phase transition, such as vapor-liquid condensation, crystallization and precipitation, when the system evolves from the thermodynamic metastable state into a stable state. In metallic systems, the nucleation process determines the kinetics of new phase formation, and strongly influences the evolution of intermediate products during phase transition. The nucleation mechanism has drawn the academic attention for years, but there are still many questions remaining unsolved. The well-known Classical Nucleation Theory (CNT) captures the essence of nucleation, but the macroscopic description of the very small critical nucleus also calls into question in real applications.

In this work, the atomistic Monte Carlo simulation technique combined with enhanced sampling methods is used to investigate the nucleation mechanism in binary metallic systems. Profound insights into microscopic aspects of the nucleation mechanism are provided and compared with the concepts from CNT, such as the cluster description, interfacial energy, nucleation energy barrier and driving force. The enhanced sampling methods provide a plausible way to bridge the gap between continuum modelling and atomic simulations, which enables the validation of classical theories or other non-classical continuum modelling by computational experiments in atomic dimension.

Additionally, a novel and efficient way, the Reweighted Partial Path (RPP) method, is developed and proposed to compute free energy profiles for diffusive processes in single Transition Interface Sampling (TIS) or Forward Flux Sampling (FFS) simulations. The method employs a partial path reweighting strategy, based on the memory loss assumption for diffusive systems, to derive the equilibrium distribution of states along a chosen order parameter from TIS or FFS trajectories. No additional calculations, such as, reverse TIS or Umbrella Sampling are required.

Abbreviations

BC	Bennett-Chandler (method)
bcc	body-centered cubic
CNT	Classical Nucleation Theory
FFS	Forward Flux Sampling
fcc	face-centered cubic
LCE	Local Chemical Environment (potential)
MC	Monte Carlo
PPTIS	Partial Path Transition Interface Sampling
RPP	Reweighted Partial Path
TST	Transition State Theory
TPS	Transition Path Sampling
TIS	Transition Interface Sampling
US	Umbrella Sampling
VC-SGC	Variance-Constrained Semi-Grand-Canonical
WHAM	Weighted Histogram Analysis Method

Contents

1 Introduction

Nucleation is an important process in science and technology, which represents the initial stage of first-order phase transitions, such as crystallization in a liquid, vapor condensation and precipitation in supersaturated solid solution, as the system is evolving from a metastable state into a stable state. This transition often occurs as the intensive condition, like temperature or pressure, is changed such that the system is brought out of equilibrium. When the perturbation is not strong enough to trigger the spinodal decomposition, the system stays in a metastable state, and the transition proceeds involving of the system to overcome an energy barrier, as illustrated in Figure 1.1, to form the stable new phase. The nanoscopic nuclei of a new phase are firstly formed from random density fluctuations in the metastable state. Due to the energy barrier, most of the nuclei will disappear again in a short time and only a rare amount of them reach the critical size and further grow into the thermodynamic favorable state.

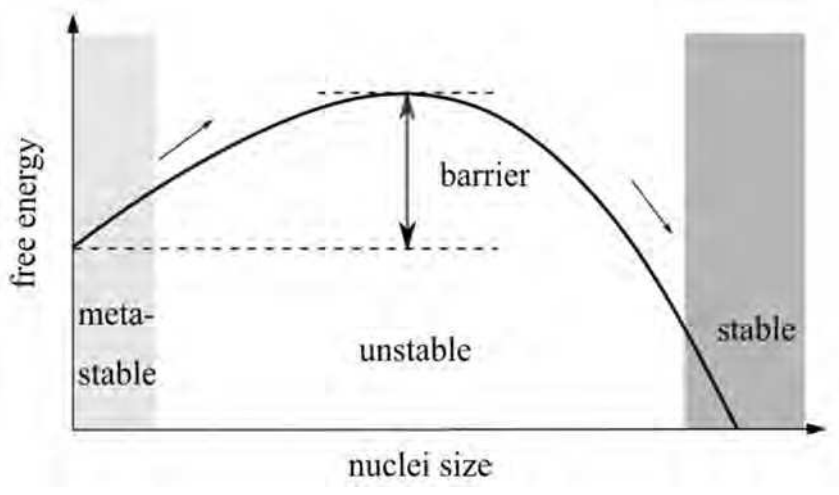

Figure 1.1 Illustration of the nucleation free energy as a function of the nucleus size.

The essence of the nucleation mechanism is well described in the framework known as the Classical Nucleation Theory (CNT), which was developed more than a

century ago and has been successfully applied in various different systems with proper modifications. Despite the huge success of CNT, a major problem remains insofar that CNT is based on the continuum thermodynamic treatment, where the critical clusters of a new phase are assumed to have the same properties as the corresponding bulk material, while, in practice, the critical clusters often only contain tens of atoms or molecules and, hence, do not fulfill the macroscopic description in continuum modelling. Since nucleation is a non-equilibrium process, the validation of classical theories and other non-classical continuum-based methods are extremely difficult in both experimental and theoretical aspects.

In recent years, atomic simulations are frequently used in the studies of various nucleation scenarios with the huge potential for providing unique insight into microscopic aspects of nucleation. However, since nucleation is a rare event, i.e., the waiting time before a transition occurring can be many orders of magnitude longer than the time required for the transition event itself. This separation of time scale makes it impractical to study nucleation processes with sufficient statistics using conventional brute-force simulations on current computers.

Rare event problems can be tackled with trajectory-based sampling techniques that focus on the segments of time evolution where the reaction of interest happens. In the last decade, a series of trajectory-based sampling techniques, also known as Rare Event Sampling methods, have been designed for the investigation of non-equilibrium transitions with stochastic nature. These methods provide efficient means to grasp large information about transition pathways, which enables more sophisticated analysis of complex nucleation transitions compared with conventional simulations.

The main purpose of Rare Event Sampling methods is to reveal the transition mechanism and determine rate constants for the process. To analyze equilibrium properties, such as, the reaction free energy, usually, additional calculations are necessary. This can be done by either employing a biased sampling technique, such as, Umbrella Sampling (US) or performing an additional path simulation for the reverse transition. Both choices require additional, usually significant, amount of computation time to obtain an accurate estimation of the transition free energy. Under certain

circumstances, e.g., in diffusive processes, free energies can also be extracted directly from path sampling simulations. In these cases, the rate constant as well as the free energy profile can be simultaneously calculated in one simulation.

So far, the main applications of Rare Event Sampling methods are to investigate the activated transitions in soft matters, e.g., biochemical switches, protein unfolding, and liquid-solid transition in water. However, these methods are barely used in the study of solid-solid transitions in metallic systems. Setting up a framework to implement Rare Event Sampling methods in such scenarios will be informative and inspiring for future researches in this area. It is performed in the present work.

2 Objectives

This thesis comprises of a comprehensive study of nucleation transitions in a binary metallic system through atomic simulations combined with enhanced sampling methods. The main tasks are:

(i) Setting up a framework for atomistic simulation of the nucleation process using the lattice Monte Carlo method and advanced Rare Event Sampling techniques;

(ii) Providing thorough understanding of the nucleation process from a microscopic point of view, including the quantitative analysis of the nuclei evolution in size, chemical composition and geometrical shape;

(iii) Evaluating important features of nucleation, such as, nucleation rates, critical cluster size and energy barriers, using the enhanced sampling methods;

(iv) Validating some basic concepts in classical theories;

(v) Proposing an efficient strategy to calculate the free energy profile directly from the nucleation trajectories in sampling simulations.

3 State of the art

This section gives a brief introduction to the methodologies used in this work, including the Classical Nucleation Theory, Monte Carlo approaches, Rare Event Sampling methods, Umbrella Sampling technique and Variance-Constrained Semi-Grand-Canonical (VC-SGC) ensemble.

3.1 Classical nucleation theory

In classical nucleation theory [1–8], the microscopic nucleus of a new phase is assumed to have the same properties as the new phase in bulk state. The important properties, such as, the chemical potential and composition are evaluated using a thermodynamic continuum treatment, so that one only needs the extensive parameters of the new-phase nuclei, such as volume and mass, as the order parameters to quantitatively describe the progress of nucleation. Generally, the work of formation of a secondary-phase nucleus is expressed as a volume free energy contribution combined with the interfacial free energy:

$$\Delta G = \Delta G_{\text{vol}} + \Delta G_{\text{surf}} \tag{3-1}$$

where ΔG_{vol} is the free energy contribution from the volume of the new phase, and ΔG_{vol} is the surface energy from the interface formed between the old and new phases as illustrated in Figure 3.1.

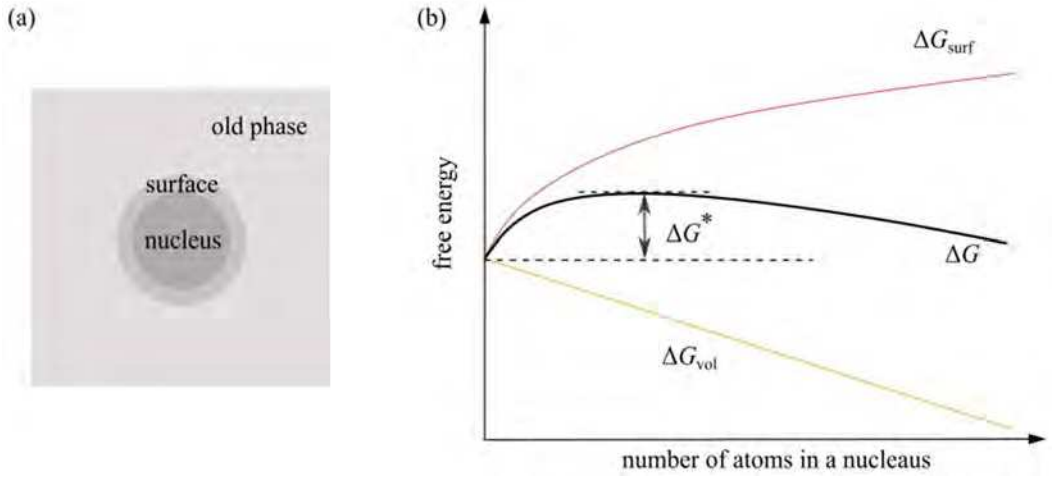

Figure 3.1 (a) The graph displaying a nucleus of new phase formed in the old phase, where a surface is

formed between the old and new phases; (b) The free energy of nucleation as a function of the number of atoms in a nucleus, along with the energy terms from nucleus volume and surface.

Classical theory uses a capillarity approximation to describe the particle of new phase, which is assumed to be a sphere with radius r, and the surface between two phases is a sharp interface with thickness approximately equaling to 0. Defining $\Delta G_{\mathrm{vol}}^{\mathrm{m}}$ as the volume free energy—the energy change by forming an unit volume of new phase from the old phase without considering the interface between two phases, and γ as the interfacial energy per unit area of nuclei/parent interface, one can rewrite the equation (3-1) as

$$\Delta G = \frac{4\pi r^3}{3}\Delta G_{\mathrm{vol}}^{\mathrm{m}} + 4\pi r^2 \gamma \qquad (3\text{-}2).$$

For a nucleus to arrive at a stable overcritical size, an energy barrier with the height ΔG^* must be overcome, typically by thermal activation. In CNT, the critical quantities for the energy barrier, ΔG^*, and the radius, r^*, are straightforwardly obtained from the extremum values calculus as

$$\Delta G^* = \frac{16\pi}{3}\frac{r^3}{\left(\Delta G_{\mathrm{vol}}^{\mathrm{m}}\right)^2} \qquad (3\text{-}3)$$

and

$$r^* = -\frac{2\gamma}{\Delta G_{\mathrm{vol}}^{\mathrm{m}}} \qquad (3\text{-}4).$$

Both quantities, volume free energy change and interfacial energy, can straightforwardly be evaluated from computational thermodynamics as, for instance, described in the CALPHAD method [9].

In the capillarity approximation, γ takes the value from interfacial energy of a planar interface between the bulk of a nucleus and parent phase, which is independent of the nucleus size. This approximation is strongly disputed since the interfacial energy between nuclei and parent phase is a size-dependent value. Tolman et.al. [10] have proposed that the interfacial energy between a droplet with radius r and supersaturated

vapor follows the form as $\gamma = \gamma_{\text{plan}} / (1 + r/\delta)$, where γ_{plan} is the planar interfacial energy of a flat droplet/vapor interface and δ is called the Tolman length. Although there are still arguments on the form of Tolman length, it is acknowledged that the interfacial energy for small particle formed during nucleation is size-dependent. Apart from Tolman's equation, there are also other forms available on the size-dependent interfacial energy, which consider the correction for the high-order expansion component in the Tolman theory. For nucleation in solid solutions, a size dependent GBB model [11,12] has been proposed to evaluate the interfacial energy for small particles by including a correction for missing broken bond due to the curvature of particle compared with a flat interface. In the mentioned models, the definition of precipitate/matrix (or droplet/vapor) interface is based on an equimolar rule for homogeneous nucleation to conserve the thermodynamic consistency. However, this macroscopic assumption is not always plausible to the nano-sized critical clusters observed in a nucleation process in solid solution.

The review articles of McDonald [5,6] and Feder et al. [7] provide a general picture of the classical nucleation theories from a series of works by Volmer-Weber [1], Becker-Döring [2], Zeldovich [4] and Frenkel [3]. In classical theories, the nucleation kinetics is driven by the change of nucleus size due to attaching or releasing monomeric molecular or atom, whereas the size change contributed from clusters, such as dimers and triples, is negligible. Therefore, the master equation of nucleation can be written as

$$\frac{\partial N_{n,t}}{\partial t} = (N_{n-1,t} k_{n-1}^{+} + N_{n+1,t} k_{n+1}^{-}) - (N_{n,t} k_{n}^{+} + N_{n,t} k_{n}^{-}) \tag{3-5}$$

where $N_{n,t}$ is the number density of nuclei consisting of n molecules. $k_n^{+(-)}$ is the corresponding frequency of attaching (detaching) a nearby monomer to these nuclei. When the system reaches equilibrium, the transition rate from n-atom (or molecule) clusters to n+1-atom clusters equals to the reverse rate, i.e.

$$N_n^0 k_n^{+} = N_{n+1}^0 k_{n+1}^{-} \tag{3-6}$$

where N_n^0 is the number density of n-atom clusters at equilibrium.

Accordingly, N_n^0 is related to the nucleation free energy $\Delta G(n)$ as $N_n^0 = N_{\text{norm}} \exp\left(-\Delta G(n)/k_{\text{B}}T\right)$, where N_{norm} is the normalization factor as $N_{\text{norm}} = \int_1^\infty N_n^0 dn$. Considering equation (3-6), one can rearrange equation (3-5) as

$$\begin{aligned}\frac{\partial N_{n,t}}{\partial t} &= N_n^0 k_n^+ \left(\frac{N_{n+1,t}}{N_{n+1}^0} - \frac{N_{n,t}}{N_n^0}\right) - N_{n-1}^0 k_{n-1}^+ \left(\frac{N_{n,t}}{N_n^0} - \frac{N_{n-1,t}}{N_{n-1}^0}\right) \\ &= \frac{\partial}{\partial n}\left(N_n^0 k_n^+ \frac{\partial}{\partial n}\left(\frac{N_{n,t}}{N_n^0}\right)\right)\end{aligned} \tag{3-7}.$$

According to equation (3-7), the flux of clusters on the *n*-size coordinate, i.e. the change of total number of clusters per unit time in unit volume, also known as the nucleation rate, is written as

$$J = -N_n^0 k_n^+ \frac{\partial}{\partial n}\left(\frac{N_{n,t}}{N_n^0}\right) \tag{3-8}.$$

In steady-state condition, $J_{\text{s}} = -N_n^0 k_n^+ \frac{\partial}{\partial n}\left(\frac{N_{n,t}}{N_n^0}\right) = \text{const}$. Accordingly, the nucleation rate is obtained as [6,7]

$$J_{\text{s}} = NZ\upsilon^* \exp\left[-\frac{\Delta G^*}{k_{\text{B}}T}\right] \tag{3-9}$$

where N is the number of potential nucleation sites, Z is the Zeldovich factor, υ^* is the atomic attachment rate, n is the number of atoms in the cluster and ΔG^* is the free energy barrier at the critical cluster size n^*. The Zeldovich factor Z is related to the curvature of the free energy barrier at the critical size, $Z = \sqrt{-\frac{\Delta G''(n^*)}{2\pi k_{\text{B}}T}}$.

In classical theories, a continuums-mechanical expression for the atomic attachment rate has been suggested by Svoboda et al. [13] for spherical precipitates in multi-component system as

$$\upsilon^* = \frac{4\pi(\rho^*)^2}{a^4\Omega}\left[\sum_{i=1}^{n}\frac{(c_{ki}-c_{0i})^2}{c_{0i}D_{0i}}\right]^{-1} \tag{3-10}$$

where ρ^* is the radius of the critical cluster, a is the nearest-neighbor atomic distance, Ω is the molar volume, c_{ki} are the concentrations of element i in the precipitate with

index k, c_{0i} are the concentrations in the matrix, and D_{0i} is the tracer diffusivity of element i in the matrix.

3.2 Monte Carlo simulation

The modern Monte Carlo method [14] can be dated back to the 1940s, when people started to use random numbers to examine physical problems in a stochastic manner. Simple strategies in early Monte Carlo methods are derived to provide means to estimate answers to analytically intractable problems. In old times, a main difficulty of implication of the Monte Carlo method is the limitation of computing efficiency. With modern computation power dramatically increasing, simple Monte Carlo strategies are more frequently used to investigate complex problems in physics, such as the ferro-magnetic transition, radiative decay and precipitation. The basic algorithm of Monte Carlo is very simple. The master equation in Monte Carlo method to simulate the canonical system evolution is

$$\frac{\partial P_n(t)}{\partial t} = -\sum_{n \neq m} \left[P_n(t) W_{n \to m} - P_m(t) W_{m \to n} \right] \tag{3-11}$$

where $P_n(t)$ is the probability of the system in state n at time t, and $W_{n \to m}$ is the transition rate of the system from state n to state m. According to statistical physics, the probability $P_n(t)$, following the Boltzmann distribution, can be expressed as

$$P_n(t) = \frac{\exp(-E_n / k_B T)}{\mathbf{Z}} \tag{3-12}$$

where E_n is the energy of the system at state n and $\mathbf{Z}$ is the partition function. The dominator in equation (3-12) is difficult to determine, but one can calculate the probability $P_n(t)$ based on the probability of previous states as a Markovian chain. Therefore, the dominator $\mathbf{Z}$ is automatically cancelled, and only the energy difference between states, i.e. $\Delta E = E_n - E_m$, is needed in the calculation of a state probability.

In equilibrium, $\partial P_n(t)/\partial t = 0$, hence the right side of equation (3-11) also equals 0, i.e. $P_n(t) W_{n \to m} - P_m(t) W_{m \to n} = 0$. The transition rates satisfying this equilibrium balance are acceptable in simulations.

Accordingly, a Metropolis form of the transition rate from state $m \to n$ is defined as

$$W_{m\to n} = \begin{cases} \tau_o^{-1} \exp(-\Delta E / k_B T) & \text{when } \Delta E > 0 \\ \tau_o^{-1} & \text{when } \Delta E \le 0 \end{cases} \tag{3-13}$$

where τ_o is the time required for an MC trial attempt. Usually, τ_o is referred as time unit of MC steps. The Metropolis Monte Carlo algorithm for equilibration in a typical flipping Ising system can be described as follows:

(1) Choose an initial state;

(2) Choose a site i;

(3) Calculate the energy difference if the sign at site i is turned over;

(4) The acceptance probability of this flip-over attempt is $P = \min\{\exp(-\Delta E / k_B T), 1\}$;

(5) Generate a random number a in [0, 1]. If $a<P$, this trial step is accepted and the sign at site i is turned over. Otherwise, this trial is rejected;

(6) Go to (3) until equilibration.

3.3 Rare event sampling methods

Activated processes dominated by rare events, including chemical reactions, crystal nucleation and biochemical switching, play important roles in many areas of science and technology. In principle, atomistic simulation techniques, such as, Monte Carlo and molecular dynamics simulations can be used to study the kinetics and mechanism of these processes. Due to the presence of high activation barriers, however, the waiting times for activated events can be many orders of magnitude longer than the time required for the transition event itself. This separation of time scale makes it impractical to study activated processes with sufficient statistics using conventional brute-force simulation on current computers. Rare event problems can be tackled with trajectory-based sampling techniques that focus on the segments of the time evolution where the reaction of interest happens. For instance, in the Transition Path Sampling (TPS) method [15][16][17][18][19], rare transition pathways are generated by carrying

out a Monte Carlo simulation in trajectory space while maintaining reactivity at each instant of the simulation. Based on the TPS framework, van Erp *et al.* [20] introduced the Transition Interface Sampling (TIS) method for the efficient calculation of reaction rate constants, in which one considers ensembles of trajectories crossing a series of interfaces between reactants and products. Following similar ideas, Allen *et al.* [21,22] proposed the Forward Flux Sampling (FFS) algorithm, which is also applicable to non-equilibrium systems where detailed balance is violated. In contrast to TIS, in FFS, pathways are generated in a ratchet-like manner only in forward direction, which can slow down the sampling of trajectory space.

In this chapter, a brief review of rare event methods is given, including the Bennet-Chandler method (TST-BC), Transition Path Sampling (TIS), Transition Interface Sampling (TIS) and Forward Flux Sampling (FFS). Even though only FFS is used in the Monte Carlo simulations for solid-solid nucleation (see section 4), reviewing the other methods can help the readers to comprehend the theoretical basis of the FFS method and provide necessary background information for the subsequent discussion of the RPP-FFS method in section 6.

3.3.1 Bennett-Chandler method (TST-BC)

The Bennett-Chandler method [23,24], also known as the reactive flux method, is proposed to calculate the reaction rate constant based on the Transition State Theory (TST) [23]. Consider a reversible transition between two stable phases, A and B, in a high dimensional system specified by the vector **x** in phase space, as shown in Figure 3.2(a). The transition is characterized by an order parameter $\lambda(\mathbf{x})$. In TST, the phase space is partitioned by a surface with $\lambda(\mathbf{x})= \lambda^*$ into two adjacent regions, i.e. A' and B' in Figure 3.2(a), which contain the actual stable states A and B, respectively. As shown in Figure 3.2(b), λ^* is the critical point where the maximum of transition energy barrier lies on λ-coordinate. In Transition State Theory, the actual stable A and B states are replaced with the two adjacent phase regions A' and B', so that the system can only be in two states – either A' or B'. Once the system leaves A', it enters B', and vice versa.

Based on this assumption, the rate constant for reaction A→B can be calculated from the mean residue time of the system in state A' as:

$$k_{AB}^{TST} = \frac{1}{t_{AB}^{mr}} = \frac{\left\langle \left| \dot{\lambda} \right| \right\rangle_{\lambda=\lambda^*}}{2} \frac{\exp\left(-W(\lambda^*)/k_B T\right)}{\int_{-\infty}^{\lambda^*} d\lambda' \exp\left(-W(\lambda')/k_B T\right)} \tag{3-14}$$

where $\left\langle \left| \dot{\lambda} \right| \right\rangle_{\lambda=\lambda^*}$ is the average velocity to cross the diving surface λ^* and $W(\lambda)$ is the reversible work needed to move the system from state A to λ. The TST rate constant is derived from the mean residue time, t_{AB}^{mr}, which measures the average time the system spends in A' state in equilibrium.

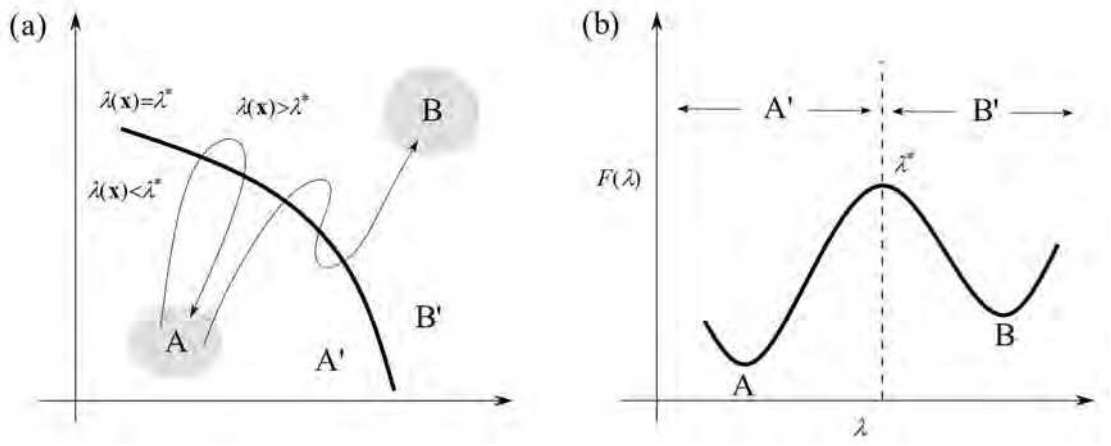

Figure 3.2 (a) In the phase space of a bi-stable system, the regions of two stable states A and B are marked by the grey areas. In TST, the surface with $\lambda(\mathbf{x})= \lambda^*$ (displayed as the thick black curve) separates the phase space into two adjacent regions A′ ($\lambda(\mathbf{x})< \lambda^*$) and B′ ($\lambda(\mathbf{x})> \lambda^*$), which contain the actual stable states A and B, respectively. The thin arrow lines indicate the trajectories in transitions between A and B. (b) The projection of phase space in (a) on the coordinate of order parameter λ. $F(\lambda)$ is the free energy, where λ^* is the critical point and the diving surface in (a) is at $\lambda= \lambda^*$(the dashed line).

However, for non-equilibrium reactions, equation (3-14) overestimates the rate constant by assuming that the trajectories will only cross the surface $\lambda(\mathbf{x})= \lambda^*$ once and there is no recursive behavior of the system to re-cross the dividing surface from B'. For example, under TST assumptions, the upper trajectory in Figure 3.2(a), which crosses the dividing surface but do not reach B, is falsely considered as a transition.

While the other trajectory being considered to have positively crossed the surface twice, it only positively crosses the dividing surface once starting from state A. In order to avoid these problems, Bennett and Chandler[23,24] provide a correction to the rate constant expression in TST (equation (3-14)).

In Bennett and Chandler (BC) method [23,24], a correlation function $C(t)$ is defined as

$$C(t) = \frac{\langle h_A(\mathbf{x}_0) h_B(\mathbf{x}_t) \rangle}{\langle h_A(\mathbf{x}_0) \rangle} \tag{3-15}$$

where $\mathbf{x}_t$ is the configuration of the system at time t. $h_{A(B)}(\mathbf{x}_t)$ is a characteristic function, which equals 1 for $\mathbf{x}_t$ in region A' (B') and 0 elsewhere (Figure 3.3 (a)).

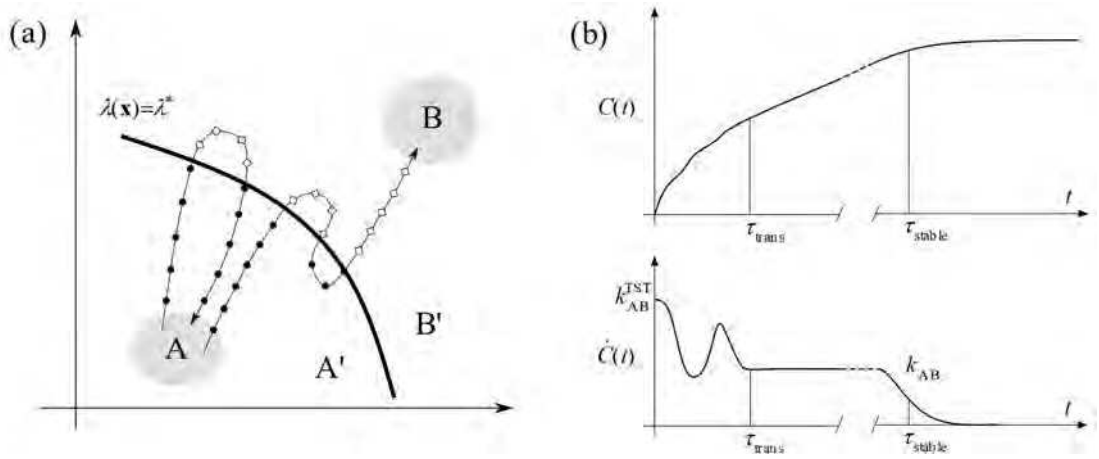

Figure 3.3 (a) In the TST-BC methods, the characteristic function of phase point $\mathbf{x}$, $h_A(\mathbf{x})$, equals to 1 when $\mathbf{x}$ is in the region A' (lines with solid dots), and $h_A(\mathbf{x})=0$ otherwise (lines with empty squares). (b) Illustration of the correlation function $C(t)$ and its derivative $\dot{C}(t)$.

The BC method keeps the TST treatment of dividing the phase space into two adjacent regions to replace the actual stable states, hence, the system is either in state A or B, and there is no middle ground. In this case, the characteristic functions $h_A(\mathbf{x}_t)$ and $h_B(\mathbf{x}_t)$ are related as $h_A(\mathbf{x}_t)=1-h_{A(B)}(\mathbf{x}_t)$. The rate constant is calculated as the derivative of $C(t)$:

$$k_{AB}(t) = \dot{C}(t) = \kappa(t) k_{AB}^{TST} \tag{3-16}$$

where $\kappa(t)$ is called reactive flux or positive flux with value less than unity and k_{AB}^{TST}

is the rate constant defined by Transition State Theory, i.e. equation (3-14). $k_{AB}(t)$ in equation (3-16), also known as TST-BC rate constant, is based on the mean first passage time of crossing the surface $\lambda(\mathbf{x})=\lambda^*$ from A. As shown in Figure 3.3(b), k_{AB} equals to k_{AB}^{TST} at t=0, and then k_{AB} varies with time until the system reaches the steady-state region. The plateau with $t\in[\tau_{trans}, \tau_{stable}]$ in the lower picture in Figure 3.3(b) corresponds to the steady-state rate constant, which is commonly referred as "reaction rate constant". In the present work, the rate constant k_{AB} refers to the value of $k_{AB}(t)$ at the plateau.

When computing the reaction rate constant with TST-BC method (equation (3-16)), one needs to firstly evaluate the critical value λ^* from the free energy profile $F(\lambda)$, since the definition of characteristic functions, $h_A(\mathbf{x})$ and $h_B(\mathbf{x})$, are dependent on λ^*. Usually, $F(\lambda)$ is calculated with the Umbrella Sampling technique. Then, a massive number of trajectories are starting from λ^*, and the reactive flux $\kappa(t)$ is determined as the fraction of trajectories ending in the product states. Since the expression of k_{AB}^{TST} uses the Boltzmann distribution as equilibrium, the TST-BC rate expression is not suitable for non-equilibrium cases. Meanwhile, the TST-BC method assumes that the critical point λ^* must exist on the chosen order parameter, therefore this method is very sensitive to the choice of order parameter. A poor λ can lead to significant error in the estimation of k_{AB}.

3.3.2 Transition Path Sampling (TPS)

TPS [15,17–19] is a sampling method to investigate the non-equilibrium transitions by exploring the transition trajectory space with a Monte Carlo strategy. Unlike TST and TST-BC methods, TPS does not require the pre-knowledge of a free energy profile and the precise location of λ^*. TPS is also insensitive to the choice of order parameter, and a λ which properly distinguishes the reactant and product states is adequate in the application of TPS.

A trajectory or path, $\mathbf{x}^{\tau} = \{\mathbf{x}_0, \cdots, \mathbf{x}_t, \cdots, \mathbf{x}_{\tau}\}$, consists of a discrete sequence of phase points or snapshots $\mathbf{x}_t$ indexed by time t, where τ is the total duration or length of the path. The probability of observing a particular trajectory $\mathbf{x}^{\tau}$ is given by

$$\mathcal{P}(\mathbf{x}^{\tau}) = \rho(\mathbf{x}_0) \prod_{t=0}^{\tau-\Delta t} p(\mathbf{x}_t \to \mathbf{x}_{t+\Delta t}) \tag{3-17}$$

where $\rho(\mathbf{x}_0)$ is the equilibrium probability density of $\mathbf{x}_0$, for instance, in the canonical ensemble, and $p(\mathbf{x}_t \to \mathbf{x}_{t+\Delta t})$ is the Markovian probability of transitioning from $\mathbf{x}_t$ to $\mathbf{x}_{t+\Delta t}$ in the time interval Δt. To study the reaction from state A to B, TPS directly samples the Transition Path Ensemble (TPE) using a Monte Carlo scheme. The details of sampling strategy in TPS can be found in Ref. [18,19]. Once the TPE is obtained, based on the correlation function in equation (3-16), the rate constant is calculated as

$$k_{\mathrm{AB}} = \dot{C}(t) = \frac{\left\langle \dot{h}_{\mathrm{B}}(\mathbf{x}_t) \right\rangle_{\mathrm{AB}}}{\left\langle h_{\mathrm{B}}(\mathbf{x}_{t'}) \right\rangle_{\mathrm{AB}}} C(t') \tag{3-18}$$

where the subscript AB indicates the average over trajectories starting from A and ending in B. Equation (3-18) enables the calculation of $C(t')$ from an arbitrary time with $t' \in [0, t]$ in the plateau of $C(t)$ as

$$C(t') = \int_{\lambda_{\min}^{\mathrm{B}}}^{\lambda_{\max}^{\mathrm{B}}} d\lambda P_{\mathrm{A}}(\lambda, t') \tag{3-19}$$

where $\lambda_{\max}^{\mathrm{B}}$ and $\lambda_{\min}^{\mathrm{B}}$ define the region of B as $\left\{\mathbf{x} \in \mathbf{B} : \lambda_{\max}^{\mathrm{B}} \geq \lambda(\mathbf{x}) \geq \lambda_{\min}^{\mathrm{B}}\right\}$. The calculation of $C(t')$ involves the integration over states with small probabilities, so normally one needs to combine the path sampling with a biased sampling method, such as, Umbrella Sampling, to get an accurate estimation of $C(t')$.

In TPS, one does not need to divide the phase space like in TST and TST-BC methods. The characteristic functions $h_{\mathrm{A(B)}}(\mathbf{x}_t)$ use the definitions of the actual stable state A and B as shown in Figure 3.4. Also, one does not need to have an accurate λ^*, and the pre-evaluation of free energy profile is omittable.

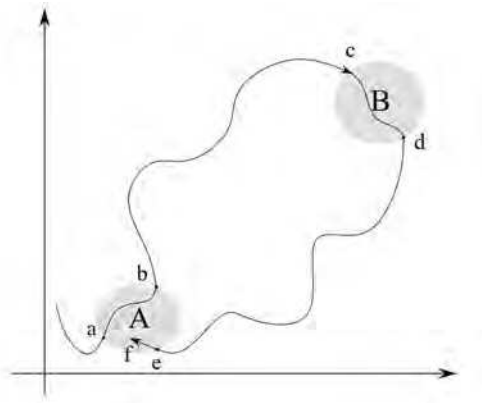

Figure 3.4 In TPS, there is no need to partition the phase space like in TST-BC methods. The stable A and B states keep their original definition and represent the reactant and product states, respectively. A phase point **x** can be categorized to A or B state, or neither of them. Accordingly, the characteristic functions $h_{A(B)}(\mathbf{x})$ are different from the ones in TST-BC methods. For example, the trajectory visits A from a→b and e→f, where the phase points give $h_A(\mathbf{x})=1$ and $h_B(\mathbf{x})=0$. To the phase points from c→d, $h_A(\mathbf{x})=0$ and $h_B(\mathbf{x})=1$. As to the remaining phase points on the trajectory, $h_A(\mathbf{x})=0$ and $h_B(\mathbf{x})=0$.

3.3.3 Transition Interface Sampling (TIS)

The TIS method [25] is a modification of TPS to improve the computation efficiency by constraining the searching of trajectories in adjacently separated transition phase regions. In TIS [20], the region between states A and B is partitioned by a series of M+1 non-overlapping interfaces defined by corresponding values $\{\lambda_i\}_{i=0\ldots M}$ of the order parameter as shown in Figure 3.5 (a). The interfaces are selected such that the first and the last interface coincide with the boundaries of regions A and B, respectively, $\lambda_0=\lambda_A$ and $\lambda_M=\lambda_B$. Trajectories are categorized into ensembles based on the interfaces they cross. To describe the crossing order of a trajectory through two interfaces i and j ($i \neq j$), the two-fold characteristic functions are introduced as:

$$\bar{h}^b_{i,j}(\mathbf{x})=\begin{cases}1 & \text{if } t^b_i(\mathbf{x})<t^b_j(\mathbf{x})\\ 0 & \text{otherwise}\end{cases}$$
$$\bar{h}^f_{i,j}(\mathbf{x})=\begin{cases}1 & \text{if } t^f_i(\mathbf{x})<t^f_j(\mathbf{x})\\ 0 & \text{otherwise}\end{cases} \qquad (3\text{-}20)$$

where $t^b_i(\mathbf{x})$ and $t^f_i(\mathbf{x})$ are the time durations tracing backward and forward,

respectively, from phase point **x** until the trajectory crosses interface *i* for the first time. Hence, $\overline{h}_{i,j}^{b}(\mathbf{x})=1$ means that, before visiting **x**, the trajectory first crossed *j* and then *i* without having revisited *j*. On the other hand, $\overline{h}_{i,j}^{f}(\mathbf{x})=1$ indicates that the trajectory presently visits **x** and will continue to reach *i* before *j*. Note that these characteristic functions depend both on the phase space point **x** as well as on the particular trajectory going through **x**. When the system is ergodic, both interfaces *i* and *j* will be crossed in finite time, hence $\overline{h}_{i,j}^{b}(\mathbf{x})+\overline{h}_{j,i}^{b}(\mathbf{x})=\overline{h}_{i,j}^{f}(\mathbf{x})+\overline{h}_{j,i}^{f}(\mathbf{x})=1$.

Next, one can use $h_{\mathcal{A}}(\mathbf{x})=\overline{h}_{0,M}^{b}(\mathbf{x})$ and $h_{\mathcal{B}}(\mathbf{x})=\overline{h}_{M,0}^{b}(\mathbf{x})$ to define the TIS overall states $\mathcal{A}$ and $\mathcal{B}$. According to this definition, a point **x** is assigned to overall state $\mathcal{A}$ if region A is reached before B when the trajectory through **x** is followed backwards in time (see Figure 3.5(a)). Hence, overall states $\mathcal{A}$ and $\mathcal{B}$ consist of points **x** located on trajectories coming from A and B, respectively.

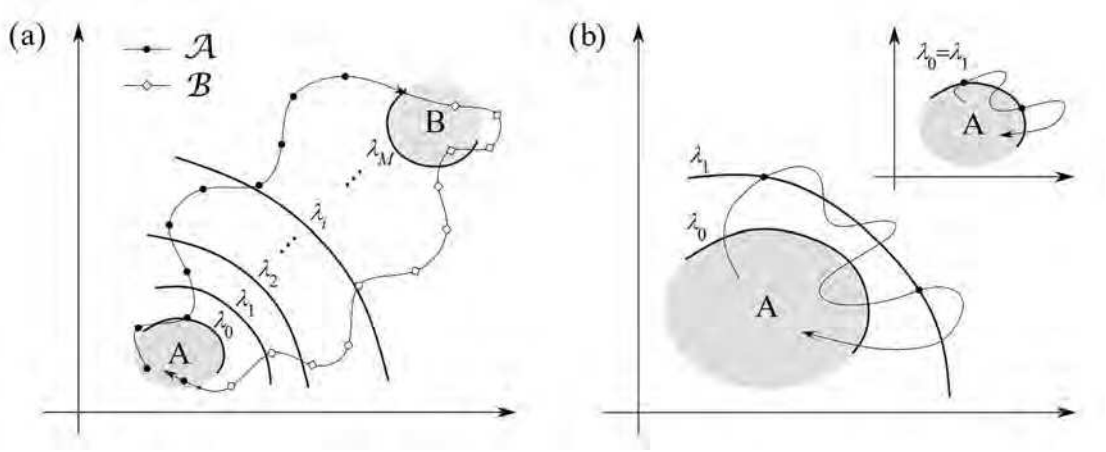

Figure 3.5 (a) In TIS, a set of interfaces with $\lambda(\mathbf{x})=\{\lambda_0, \lambda_1, \ldots, \lambda_M\}$ are defined in phase space and the boundary of A(B) is set to overlapped with $\lambda_{0(M)}$. The overall TIS state $\mathcal{A}$ and $\mathcal{B}$ are history-dependent overall states for trajectories. After a trajectory reaches state A, the trajectory is in state $\mathcal{A}$ until it hits state B. Then, the trajectory is in state $\mathcal{B}$ until it reaches state A again. (b) When calculating the initial flux using brute-force simulations, one needs to count the number of effective positive crossings of the first interface. The black dots indicate the points of effective crossing of a trajectory in the cases $\lambda_0 \neq \lambda_1$ (the main diagram) and $\lambda_0=\lambda_1$ (the inset diagram).

Similarly, one can write the correlation function in equation (3-15) using the TIS overall stable states as

$$C(t) = \frac{\langle h_{\mathcal{A}}(\mathbf{x}_0) h_{\mathcal{B}}(\mathbf{x}_t) \rangle}{\langle h_{\mathcal{A}}(\mathbf{x}_0) \rangle} \qquad (3\text{-}21),$$

and the reaction rate k_{AB} also satisfies $k_{AB} \equiv \dot{C}(t)$. The reaction rate in TST-BC theory, as shown in Figure 3.3(b), displayed a plateau in $t \in [\tau_{trans}, \tau_{stable}]$, while the one calculated from equation (3-21) remain constant from 0 to τ_{stable} with the same value as the rate constant at the plateau given by TST-BC and TPS methods.

Based on the characteristic function, the general crossing function is defined as

$$\psi_{i,j}(\mathbf{x}_t) = \bar{h}^{b}_{j,i}(\mathbf{x}_t)\theta(\lambda_i - \lambda(\mathbf{x}_t))\theta(\lambda(\mathbf{x}_{t+\Delta t}) - \lambda_i) \qquad (3\text{-}22)$$

where θ is the Heaviside step-function and Δt is the time step. For the phase point $\mathbf{x}_t$ visited by a trajectory at time t, $\psi_{i,j}(\mathbf{x}_t)$ will equal 1 only if the trajectory comes directly from j and immediately crosses i in the next time step of length Δt. For convenience, an effective crossing function is defined as

$$\begin{aligned} \Psi^{l,m}_{i,j}(\mathbf{x}_t) &= \bar{h}^{b}_{j,i}(\mathbf{x}_t)\theta(\lambda_i - \lambda(\mathbf{x}_t))\theta(\lambda(\mathbf{x}_{t+\Delta t}) - \lambda_i)\bar{h}^{f}_{l,m}(\mathbf{x}_t) \\ &= \psi_{i,j}(\mathbf{x}_t)\bar{h}^{f}_{l,m}(\mathbf{x}_t) \end{aligned} \qquad (3\text{-}23).$$

When $\Psi^{l,m}_{i,j}(\mathbf{x}_t)=1$, the trajectory, which crosses i at $\mathbf{x}_t$ directly from j, will visit l earlier than m, otherwise $\Psi^{m,l}_{i,j}(\mathbf{x}_t)=0$. Clearly, $\Psi^{m,l}_{i,j}(\mathbf{x}_t) + \Psi^{l,m}_{i,j}(\mathbf{x}_t) = \psi_{i,j}(\mathbf{x}_t)$. The crossing functions defined in equations (3-22) and (3-23) are to characterize the trajectories according to the interfaces they cross in a time sequence. When taking equation (3-22) to the extreme, $\Delta t \to 0$, one can get the velocity of crossing interface i at time t in a trajectory coming directly from j before recrossing i,

$$\phi_{i,j}(\mathbf{x}_t) = \lim_{\Delta t \to 0} \frac{1}{\Delta t} \psi_{i,j}(\mathbf{x}_t) \qquad (3\text{-}24)$$

where $\phi_{i,j}$ is also called the effective flux from j to i. Accordingly, the reaction rate of transition A→B can be written as the effective flux from interface 0 to M, i.e.

$$k_{\mathrm{AB}} = \langle \phi_{M,0} \rangle / \langle h_{\mathrm{A}} \rangle \qquad (3\text{-}25),$$

and the reverse reaction rate as $k_{\mathrm{BA}} = \langle \phi_{0,M} \rangle / \langle h_{\mathrm{B}} \rangle$.

The flux $\langle \phi_{j,0} \rangle$ can be considered as the effective flux on a given interface i ($0<i<j$) continuing to cross j before coming back to 0, i.e.

$$\langle \phi_{j,0} \rangle = \langle \phi_{i,0} \bar{h}^{f}_{j,0} \rangle \qquad (3\text{-}26).$$

Therefore, $\langle \phi_{M,0} \rangle$ can be rewritten as the product of fraction like the Markovian chain:

$$\begin{aligned} \langle \phi_{M,0} \rangle &= \langle \phi_{1,0} \bar{h}^{f}_{M,0} \rangle = \langle \phi_{1,0} \rangle \frac{\langle \phi_{1,0} \bar{h}^{f}_{M,0} \rangle}{\langle \phi_{1,0} \rangle} \\ &= \langle \phi_{1,0} \rangle \frac{\langle \phi_{1,0} \bar{h}^{f}_{2,0} \rangle}{\langle \phi_{1,0} \rangle} \frac{\langle \phi_{2,0} \bar{h}^{f}_{3,0} \rangle}{\langle \phi_{2,0} \rangle} \cdots \frac{\langle \phi_{M-1,0} \bar{h}^{f}_{M,0} \rangle}{\langle \phi_{M-1,0} \rangle} \\ &= \langle \phi_{1,0} \rangle \prod_{i=1}^{M-1} \langle \bar{h}^{f}_{i+1,0} \rangle_{\phi_{i,0}} \end{aligned} \qquad (3\text{-}27)$$

where $\langle g(\mathbf{x}) \rangle_{w}$ is the weighted average for an observable $g(\mathbf{x})$ and a weight function $w(\mathbf{x})$, defined as $\langle g(\mathbf{x}) \rangle_{w} = \frac{\langle g(\mathbf{x}) w(\mathbf{x}) \rangle}{\langle w(\mathbf{x}) \rangle}$. For convenience, one can define a conditional crossing probability $P(^{m}_{l} \big|^{i}_{j})$ as

$$P(^{m}_{l} \big|^{i}_{j}) = \frac{\langle \phi_{i,j} \bar{h}^{f}_{l,m} \rangle}{\langle \phi_{i,j} \rangle} = \langle \bar{h}^{f}_{m,l} \rangle_{\phi_{i,j}} \qquad (3\text{-}28).$$

$P(^{m}_{l} \big|^{i}_{j})$ describes the probability that a path having crossed interface i from j will continue to reach interface m before l. Combining equations (3-25) to (3-28) , the rate constant can be written as

$$k_{\mathrm{AB}} = \langle \phi_{1,0} \rangle / \langle h_{\mathrm{A}} \rangle \prod_{i=1}^{M-1} P(^{i+1}_{0} \big|^{i}_{0}) \qquad (3\text{-}29).$$

Here, $\langle \phi_{1,0} \rangle / \langle h_{\mathrm{A}} \rangle = \Phi_{\mathrm{A},0}$ is the initial flux coming from A state to enter the buffer region. In TIS, the initial flux can be calculated from a brute-force simulation starting from A state as $\Phi_{\mathrm{A},0} = N_0 / \Delta t_{tot}$, where N_0 is the positive crossing number as illustrated

in Figure 3.5(b), and Δt_{tot} is the total time the system remains in state A during the simulation.

3.3.4 Forward Flux Sampling (FFS)

The Forward Flux Sampling method [21] is built on the same theoretical basis as TIS, but it employs a different sampling strategy designed to obtain the transition paths in a highly activated process. In the FFS method, one considers a typically high-dimensional phase space. Each point in this space represents a microscopic state of the system specified by the multi-dimensional coordinate $\boldsymbol{X}$. Regions A and B are two stable (metastable) states defined in terms of an order parameter $\lambda(\boldsymbol{X})$, such that the system is in state A if $\lambda(\boldsymbol{X}) < \lambda_0$, and in state B if $\lambda(\boldsymbol{X}) > \lambda_m$. A series of non-overlapping interfaces $\{\lambda_i\}_{i=1\ldots m-1}$ is defined between states A and B as illustrated in Figure 3.6.

In FFS, one first performs brute-force simulations starting in state A. Every time a trajectory forward-crosses λ_0, the respective system configuration is stored and the simulation is restarted until N_0 configurations are collected. The average number of crossings through interface λ_0 out of state A per unit time is denoted as initial flux $\Phi_{\mathrm{A},0} = N_0 / \Delta t_{tot}$, where Δt_{tot} is the total time the system remains in state A during the simulation.

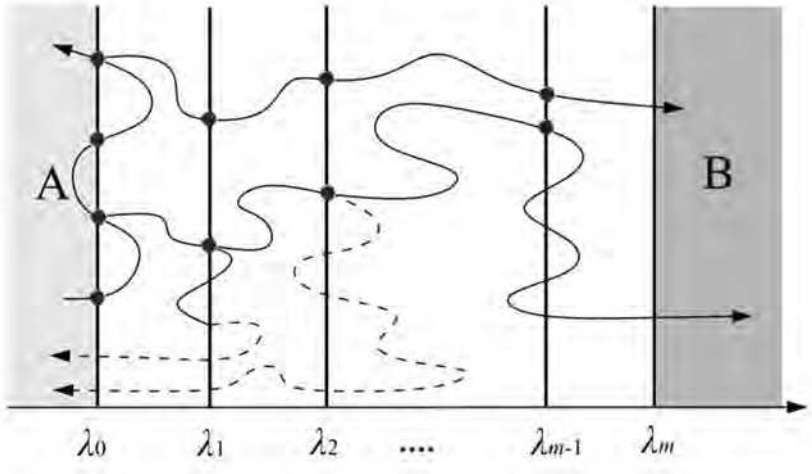

Figure 3.6 Schematic of a phase region between stable states A and B, which is sectioned into a series of non-overlapping interfaces $\{\lambda_i\}_{i=0,\,1,\cdots,\,m}$.

In the next step, the collected configurations on λ_0 serve as starting points of trajectories, which are followed until the trajectory either crosses λ_1 or returns back to state A. A total of M_0 trajectories are "fired" from λ_0 to generate a set of configurations on λ_1, which are used to start new trajectories and to repeat the process for the next interface. From each interface λ_i, M_i trajectories are fired and harvested that either reach the next interface λ_{i+1} or return to state A. The probability that a trajectory, which has crossed λ_i coming from state A, continues to cross λ_{i+1} before returning to state A is defined as the crossing probability $P(\lambda_{i+1} \mid \lambda_i) = N_i^s / M_i$. Here, N_i^s is the number of trajectories that successfully cross λ_{i+1} from λ_i. The whole procedure is terminated when at least one trajectory reaches state B, and the transition rate constant k_{AB} can be obtained from

$$k_{AB} = \Phi_{A,0} \prod_{i=0}^{m-1} P(\lambda_{i+1} \mid \lambda_i) \qquad (3\text{-}30).$$

3.4 Other enhanced sampling methods

3.4.1 Umbrella Sampling

Umbrella Sampling [26][27] is a commonly used strategy to obtain the free energy profile along a chosen physical coordinate by performing a series of simulations under a biased potential to constrain the system inside local regions in configuration space.

For example, when exploring the equilibrium distribution of a bi-stable system on a given order parameter λ using the brute-force simulation, one can find the simulation being trapped in the two stable states and the high energy region exhibits very poor statistics, i.e. little information is displayed on the histogram of λ around this region as shown in Figure 3.7(a). To investigate the properties around the poor statistics region, e.g. around $\bar{\lambda}$ in Figure 3.7(b), one can pose an umbrella potential $U(\lambda) = \frac{\kappa}{2}\left(\lambda - \bar{\lambda}\right)^2$ in simulations such that the area around $\bar{\lambda}$ is frequently visited and a histogram with enhanced distribution around this area can be obtained.

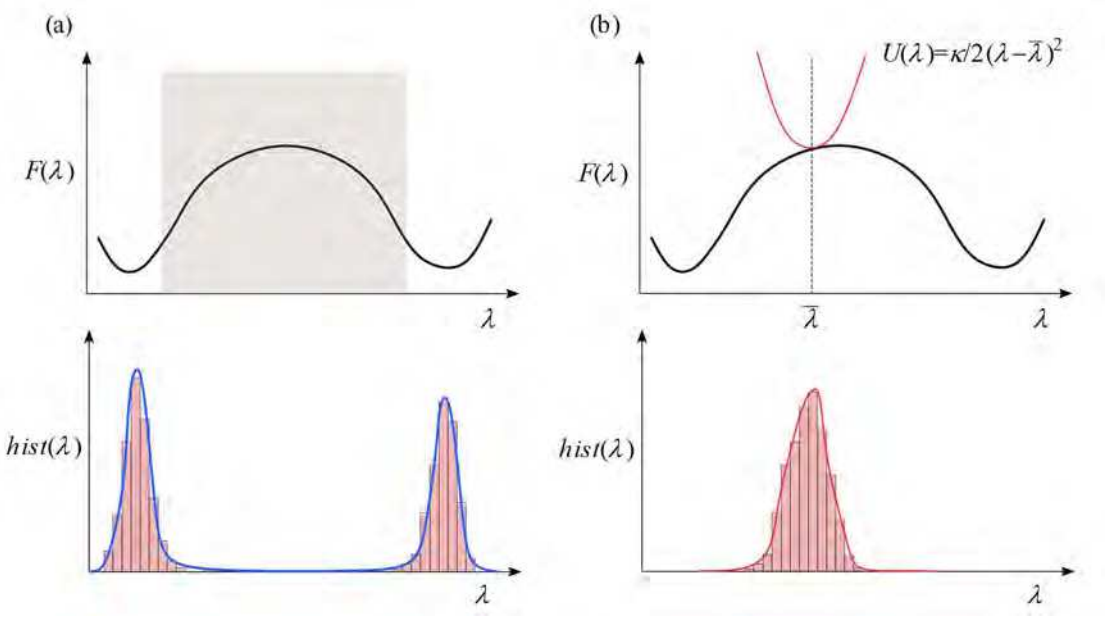

Figure 3.7 (a) The upper diagram is the free energy of a bi-stable system on λ-coordinate. The lower picture shows the equilibrium histogram of λ of the system, where the high energy region, marked by the grey area, shows very poor statistics according to the histogram. (b) Posing a biased potential $U(\lambda)=\frac{\kappa}{2}\left(\lambda-\bar{\lambda}\right)^2$ (the red curve) in Umbrella Sampling, one can obtain better statistics in the histogram around $\bar{\lambda}$.

In order to reveal the distribution of λ in region $[\lambda_0, \lambda_M]$, one needs to choose a set of biased potentials $U_i(\lambda)=\frac{\kappa}{2}\left(\lambda-\bar{\lambda}_i\right)^2$ with different $\bar{\lambda}_i$, i=1, 2, …, S, in the region of interest, as shown in Figure 3.8. With each U_i, an independent simulation is performed to obtain the enhanced histogram around $\bar{\lambda}_i$, which is denoted as $hist_i(\lambda)$. After all the histograms from S simulations are obtained, one can derive the unbiased distribution of λ with the Weighted Histogram Analysis Method (WHAM).

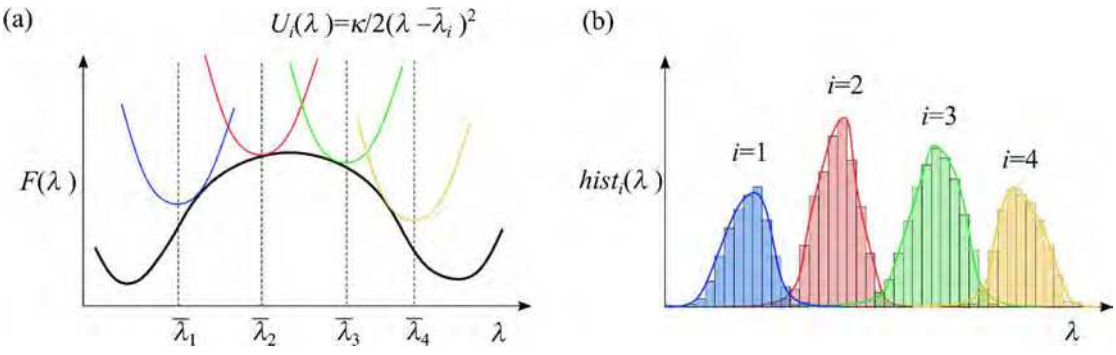

Figure 3.8 (a) The biased potentials U_i are displayed as colored curves in four independent simulations

with different $\overline{\lambda}_i$. (b) The histogram of λ obtained in each i-th simulation is displayed in the bar chart with the same color of the respective biased potential.

According to probability theory, the expected probability of observing λ in the i-th simulation, $\rho_i(\lambda)$, fulfills the following equation,

$$\rho_i(\lambda) = f_i c_i(\lambda)\rho(\lambda) \tag{3-31}$$

where $\rho(\lambda)$ is the unbiased probability of λ, which is connected to the free energy by $F(\lambda) = -k_B T \ln \rho(\lambda)$. The factor $c_i(\lambda)$ is related to the bias potential by $c_i(\lambda) = \exp\left[-U_i(\lambda)/k_B T\right]$, and f_i is a normalized factor defined as $f_i = 1\Big/\sum_{\lambda=\lambda_0}^{\lambda_M} c_i(\lambda)\rho(\lambda)$.

The probability of observing a given histogram $hist_i(\lambda)$ can be derived from the multinomial distribution as

$$P_i\left(hist_i(\lambda);\rho_i(\lambda)\right) = \frac{(N_i)!}{\prod_{\lambda=\lambda_0}^{\lambda_M}\left(hist_i(\lambda)\right)!}\prod_{\lambda=\lambda_0}^{\lambda_M}\left(\rho_i(\lambda)\right)^{hist_i(\lambda)} \tag{3-32}$$

where N_i is the total observation made in i-th simulation, i.e. $N_i = \sum_{\lambda=\lambda_0}^{\lambda_M} hist_i(\lambda)$.

Accordingly, the overall likelihood to observe the set of histograms $\{ hist_i(\lambda) \}_{i=1\ldots S}$ in S independent simulations is given as

$$P\left(\{hist_i(\lambda)\};\rho(\lambda)\right) = \prod_{i=1}^{S} P_i\left(hist_i(\lambda);\rho_i(\lambda)\right) \tag{3-33}.$$

Taking the logarithm of both sides of equation (3-35) leads to

$$\ln P\left(\{hist_i(\lambda)\};\rho(\lambda)\right) = -A\left(\rho(\lambda)\right) + \text{const} \tag{3-34}$$

where $A\left(\rho(\lambda)\right) = -\sum_{i=1}^{S} N_i f_i - \sum_{\lambda=\lambda_0}^{\lambda_M} M(\lambda)\ln\rho(\lambda)$ with $M(\lambda) = \sum_{i=1}^{S} hist_i(\lambda)$. Now, the maximum likelihood observation of $\{hist_i(\lambda)\}_{i=1\ldots S}$ corresponds to the minimum of $A\left(\rho(\lambda)\right)$. At the minimum of $A\left(\rho(\lambda)\right)$, the derivative of $A\left(\rho(\lambda)\right)$ on each individual $\rho(\lambda)$ should be zero, i.e. $\partial A\left(\rho(\lambda)\right)/\partial\rho(\lambda) = 0$. Considering that f_i is dependent on $\rho(\lambda)$, the equilibrium probability of λ can be written as

$$\rho(\lambda) = \frac{M(\lambda)}{\sum_i N_i f_i c_i(\lambda)} \qquad (3\text{-}35).$$

Equations (3-31) and (3-35) are known as the coupled nonlinear WHAM (Weighted Histogram Analysis Method) [26][28] equations, which can be solved iteratively for f_i and $\rho(n)$ until self-consistency is achieved.

3.4.2 Variance-Constrained Semi-Grand-Canonical (VC-SGC) ensemble

The variance-constrained ensembles [29,30] are proposed to study the multiphase regions of phase diagrams by enabling thermodynamic integration across phase boundaries and computation of the free energy on composition inside the miscibility gap. In the VC-SGC ensemble, the canonical free energy as a function of concentration can be calculated by integrating the energy derivatives over the whole concentration range, from which one can extract the interphase surface energy as a function of temperature and orientation.

The VC-SGC ensemble method [29,30] is analogous to Umbrella Sampling, where a harmonic external potential $\Delta U_{\mathrm{V}}^{\mathrm{b}} = \kappa/2\left(N_{\mathrm{A}} - \bar{N}_{\mathrm{A}}\right)^2$ is applied to control the fluctuation of total concentration in a semi-grand canonical ensemble of a binary AB system. Here, κ is a force constant to restrain the total number of element A, i.e. N_{A}, around a given $\bar{N}_{\mathrm{A}}$. Denoting the total number of atoms in the system as N, the constrained concentration $\bar{c}$ is defined as $\bar{c} = \bar{N}_{\mathrm{A}}/N$. Additionally, a thermodynamic variable ϕ is defined as $\phi = -2\kappa\bar{N}_{\mathrm{A}} = -2\kappa N\bar{c}$. The external potential $\Delta U_{\mathrm{V}}^{\mathrm{b}}$ is then rewritten as the function of concentration,

$$\Delta U_{\mathrm{V}}^{\mathrm{b}} = \kappa(Nc + \phi/2\kappa)^2 \qquad (3\text{-}36)$$

where c is the instant concentration of A observed in the simulation, i.e. c=N_{A}/N. Accordingly, the partition function of a VC-SGC ensemble can be expressed as

$$Z_{\mathrm{V}}(\phi,\kappa,N)=\int_0^1 \exp\{-\beta[F_{\mathrm{C}}(c,N)+\Delta U_{\mathrm{V}}^{\mathrm{b}}]\}dc \qquad (3\text{-}37)$$

where $F_{\mathrm{C}}(c,N)$ is the free energy in the canonical ensemble with total number of N atoms and concentration c. The integrand in equation (3-37) describes the probability distribution of concentration c in the entire VC-SGC ensemble, which peaks at the average concentration $\langle c\rangle_{\mathrm{V}}$. Therefore, the derivative of this integrand on concentration at $c=\langle c\rangle_{\mathrm{V}}$ equals zero, giving the relation between ϕ and $F_{\mathrm{C}}(c,N)$ as

$$\phi+2N\kappa\langle c\rangle_{\mathrm{V}}=-N^{-1}\partial F_{\mathrm{C}}/\partial c(\langle c\rangle_{\mathrm{V}},N) \qquad (3\text{-}38).$$

In the right side of equation (3-38), the derivative of canonical free energy, $\partial F_{\mathrm{C}}/\partial c(\langle c\rangle_{\mathrm{V}},N)$, is an unbiased observable, which can be used to reconstruct the free energy as $F_{\mathrm{C}}(c,N)=\int_0^c \partial F_{\mathrm{C}}/\partial c(\langle c\rangle_{\mathrm{V}},N)dc$.

For an immiscible binary A-B system with two stable phases α and β, as illustrated in Figure 3.9, the curve of free energy derivative reveals several different stages of equilibrium as the total concentration c varies from 0 to 1. Apart from the two single-phase stages with homogeneous α or β phases, there are five co-existing patterns of α and β in equilibrium at different c: (I) the sphere-like precipitate of β phase in α phase; (II) the cylindrical precipitates of β phase in α phase; (III) slabs of α and β phases contacting by planar interfaces; (IV) the cylindrical precipitates of α phase in β phase; (V) the sphere-like precipitates of α phase in β phase. Without considering other effects, such as, the elastic or magnetic fields, the excess free energy, $\Delta F_{\mathrm{xc}}(c)$, at a given concentration c can be calculated as, $\Delta F_{\mathrm{xc}}(c)=F_{\mathrm{C}}(c)-c\mu_{\mathrm{A}}N-(1-c)\mu_{\mathrm{B}}N$, where μ_{A} and μ_{B} are the chemical potentials of elements A and B in equilibrated α and β phases in the thermodynamic limit.

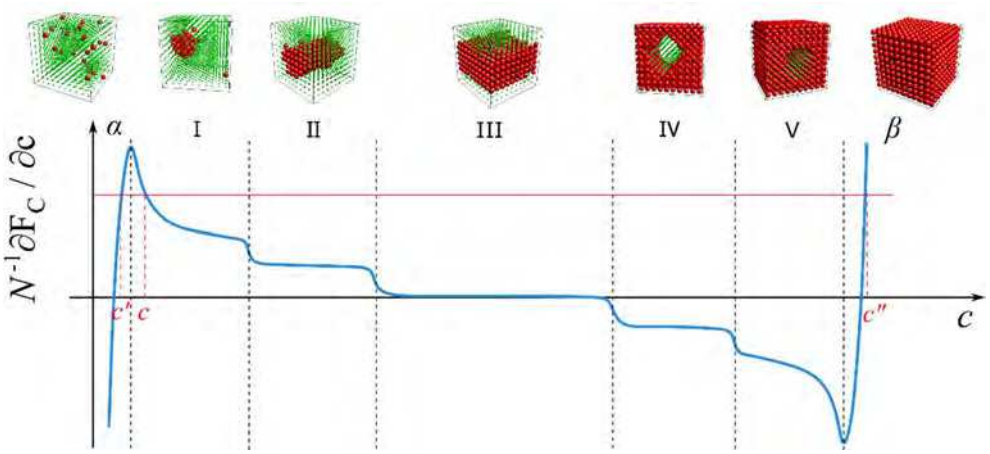

Figure 3.9 The free energy derivative as a function of concentration c in a phase-separating A-B system. The snapshots are taken from the equilibrated configurations at different regions of concentration, where the red and green spheres represent elements A and B, respectively. α and β are the single-phase regions. I to V are five different stages of co-existing α and β phases as c is increasing: (I) the sphere-like nucleus of β phase in α phase; (II) the cylindric precipitate of β phase in α phase; (III) slabs of α and β phases separated by planar interfaces; (IV) the cylindrical precipitate of α phase in β phase; (V) the sphere-like nucleus of α phase in β phase. In stage I, the system at concentration c decomposes into the β-phase precipitate with concentration c' and α phase with concentration c".

The planar α/β interfacial energy can be directly calculated from $\Delta F_{\mathrm{xc}}(c)$ in the slab region of α and β phases, i.e. region III, as,

$$\gamma_{\mathrm{plan}} = \Delta F_{\mathrm{xc}}(c) / S \tag{3-39}$$

where c is a concentration in region III, and S denotes the surface area of planar interfaces between the slabs of α and β phases. To the curved interface between sphere-like β precipitates and the α parent phase, i.e. stage I in Figure 3.9, the interfacial energy γ_{sph} is calculated as

$$\gamma_{\mathrm{sph}} = \Delta F_{\mathrm{s}}(c) / S_{\mathrm{sph}}(N'') \tag{3-40}$$

where $\Delta F_{\mathrm{s}}(c)$ is the excess free energy from the curved interface in the sphere-like precipitate region and $S_{\mathrm{sph}}(N'')$ is the surface area of β precipitate with N" atoms. At a given concentration c in stage I, the system decomposes into α and β phases with the same chemical potentials (free energy derivatives), as illustrated in Figure 3.9, therefore the corresponding α and β phases have concentrations c' and c", respectively.

Considering mass conservation, the number of atoms in β precipitates N" is calculated as

$$N'' = \frac{c' - c}{c' - c''} N \tag{3-41}$$

where $N = N' + N''$ and N' is the number of atoms in the α phase.

Therefore, the excess free energy from the curved interface at c, $\Delta F_s(c)$, can be expressed as

$$\Delta F_s(c) = \Delta F_{xc}(c) - \Delta F_{xc}(c') \frac{N'}{N} - \Delta F_{xc}(c'') \frac{N''}{N} \tag{3-42}.$$

In practice, the Monte Carlo simulation in the VC-SGC ensemble follows the standard metropolis algorithm to evaluate the average concentration $\langle c \rangle_V$ under the constrained potential ΔU_V^b. The MC trial step is performed as

(1) Select a random particle;

(2) Flip the type of the particle: A→B or B→A;

(3) Calculate the concentration change after the flipping Δc, and the energy difference as $\Delta E + \kappa[N\Delta c + \phi / 2\kappa]^2$;

(4) The acceptance probability of this trial is

$$P = \min\left\{1, \exp\left(-\frac{\Delta E + \kappa[N\Delta c + \phi / 2\kappa]^2}{k_B T}\right)\right\} \tag{3-43}.$$

Generate a random number a between 0 and 1. Accept the trial if $a<P$, otherwise reject it.

4 Simulation

This section introduces the details of implementing the Monte Carlo approach and Forward Flux Sampling method in the study of nucleation kinetics in dilute Fe-Cu alloys. In the evaluation of the nucleation free energy, the procedures of Umbrella Sampling are listed, along with the details of the newly proposed Reweighted Partial Path method. This section also illustrates the computation of the coherent α-Fe/Cu interfacial energy using the VC-SGC ensemble method.

4.1 Monte Carlo simulations in dilute Fe-Cu alloys

The nucleation dynamics simulation for Cu precipitation in dilute bcc Fe alloys is performed with the Rigid Lattice Monte Carlo (LMC) scheme implemented in the software MatCalc [31]. A bcc lattice of 30×30×30 unit cells is used with periodic boundary condition in Forward Flux Sampling to calculate nucleation rates. The system energy E is described using a Local Chemical Environment (LCE) potential and the atomic diffusion is simulated through the vacancy exchange mechanism.

In the LMC framework, the acceptance probability for a vacancy exchange with a nearest neighbor atom is given by

$$P = \exp\left(-\frac{\Delta E}{k_B T}\right) \tag{4-1}$$

where ΔE represents the total energy difference between the initial state and the state after the exchange event. If $\Delta E < 0$, $P = 1$.

In this work, the LMC simulations are used to study the nucleation process in Fe-1%Cu and Fe-1.5%Cu alloys at temperatures from 450~600 °C.

4.1.1 Atomic diffusion

Atomic diffusivity of Fe and Cu atoms in the rigid lattice is described by the vacancy exchange mechanism, where atoms can only exchange their site with a vacancy

in the nearest neighbor position. The real time is coupled to a Monte Carlo step (MCS) by defining the average time increment corresponding to one vacancy jump [32] as

$$\Delta t = \frac{a^2 x_{\mathrm{Va,MC}}}{6 D_{\mathrm{A}}} \cdot k \qquad (4\text{-}2)$$

where a is the nearest neighbor distance in bcc-Fe (2.468 Å), D_{A} is the macroscopic diffusion coefficient of the jumping atom A in bcc-Fe, $x_{\mathrm{Va,MC}}$ is the vacancy site fraction in the simulation box and k is a correction for the diffusion correlation effect in the vacancy exchange mechanism (0.727 for bcc lattice [33]). In the present MC simulations, exactly one vacancy is placed in the 30×30×30 bcc lattice, hence the vacancy site fraction $x_{\mathrm{Va,MC}}$=1/54000. Here, the tracer diffusion coefficient (e.g. D_{Cu}, is 1.5 $\mathrm{m^2 \cdot s^{-1}}$ [34], and D_{Fe} is 7.4 $\mathrm{m^2 \cdot s^{-1}}$ [35] in bcc_Fe at 500 °C) is used to couple the MC step with real time.

4.1.2 Local Chemical Environment potential (LCE)

The LMC steps are governed by an atomic interaction energy formulated in the Local Chemical Environment (LCE) framework expressed in reference to a particular center atom [32]. The energy of the system is calculated as the sum of all pair-wise bond energies extending from each atom up to the second nearest neighbors,

$$E = \frac{1}{2} \sum \sum_{i=1}^{2} n_{\mathrm{AB}}^{(i)} \varepsilon_{\mathrm{AB}}^{(i)} \qquad (4\text{-}3)$$

where $n_{\mathrm{AB}}^{(i)}$ and $\varepsilon_{\mathrm{AB}}^{(i)}$ are the number of AB bonds and the corresponding bond energy in the i-th nearest neighbor shell. $\varepsilon_{\mathrm{AB}}^{(i)} = \chi_{\mathrm{A}} \varepsilon_{\mathrm{AB}}^{\mathrm{A}(i)} + \chi_{\mathrm{A}} \varepsilon_{\mathrm{AB}}^{\mathrm{B}(i)}$, where χ_{A} and χ_{B} are the atomic fractions of A and B in the local environment and $\varepsilon_{\mathrm{AB}}^{\mathrm{A}(i)}$ ($\varepsilon_{\mathrm{AB}}^{\mathrm{B}(i)}$) is the AB bond energy in a pure A and B environment, respectively. The bond energy of the i-th nearest neighbor shell, $\varepsilon_{\mathrm{CuFe}}^{(i)}$, is approximately dependent on $\varepsilon_{\mathrm{CuFe}}^{(1)}$ as $\varepsilon_{\mathrm{CuFe}}^{(i)} = (r_i / r_1)^{-6} \varepsilon_{\mathrm{CuFe}}^{(1)}$, where r_1 and r_i are the first and i-th nearest neighbor distances, respectively. The summation includes all the possible combinations of bonds for A and B, representing

the atomic species Cu and Fe, as well as Va, representing the substitutional vacancy. The LCE potential is a very flexible and robust energy model, whose parameters can be calibrated with various methodologies, such as experimental measurements, first principle calculations, or thermodynamic assessment. The details of this potential can be found in Ref. [32].

Using this setting of LCE potential, the solubility limits of Cu in bcc-Fe ($x_{\mathrm{Cu}}^{\mathrm{bcc\_Fe}}$) and Fe in bcc-Cu ($x_{\mathrm{Fe}}^{\mathrm{bcc\_Cu}}$) are calculated from slab-diffusion LMC simulations[36]. As demonstrated in Figure 4.1, the blocks of pure Cu (red) and pure Fe (green) are initially placed adjacent to each other. Then, the LMC simulation starts to run until equilibration. In the slab-diffusion simulations, a 20×20×200 bcc lattice is used in LMC and initially each pure block takes up 20×20×100 unit cells in the manner illustrated in Figure 4.1.

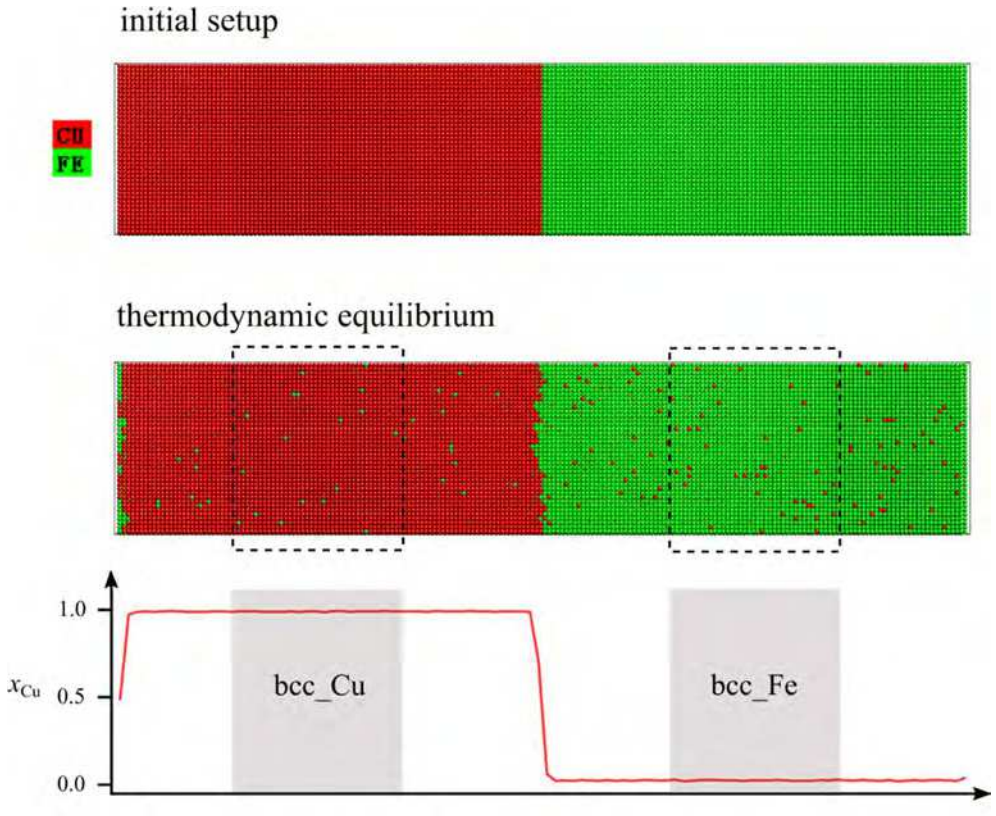

Figure 4.1 Illustration of procedures in slab-diffusion LMC simulations [36]. Initially, the blocks of pure Cu (red) and pure Fe (green) are placed adjacent to each other, then the LMC simulation starts to run until equilibration. The concentration of Cu (x_{Cu}) at each layer is measured at equilibrium, and the grey areas in the middle of each block are used to determine the solubility limit of Cu in bcc_Fe and Fe in

bcc_Cu, respectively.

Firstly, 5000 MC sweeps are carried out to equilibrate the system, and then another 5000 MC sweeps for the computation of the solubility limits. One MC sweep equals to N Monte Carlo steps, with N denoting the total number of atoms in simulations. The concentration of Cu (x_{Cu}) at each layer is measured at each equilibrium sweep, and the average of x_{Cu} in the middle of each block over all the equilibrium sweeps is used to determine the solubility limits of Fe in bcc_Cu and Cu in bcc_Fe, respectively.

Since the tracer diffusion coefficient is used to couple the MC step with real time, there is no need to additionally define interactions for atom and vacancy, i.e. $\varepsilon^{(i)}_{\mathrm{CuVa}}$ and $\varepsilon^{(i)}_{\mathrm{FeVa}}$ are set to zero. The vacancy-vacancy interaction is also neglected, because only one vacancy is placed in the simulation sample.

4.2 Forward Flux Sampling (FFS) for Cu nucleation pathways

4.2.1 Order parameter

A cluster formed during simulation is recognized as a group of solute atoms connected with each other within the nearest neighbor distance. The size of a cluster is defined as the total number of solute atoms on this network, as shown in Figure 4.2 (a). Clearly, the smallest cluster is a dimer (two Cu atoms next to each other within the nearest neighbor distance), and a Cu atom without any other Cu atom in its nearest neighbor shell is regarded as a solute atom in the matrix. This cluster detection recognizes all the clusters formed during nucleation including both, unstable pre-critical as well as stable post-critical ones, to provide a sound evaluation of the cluster size distribution.

In the present work, the order parameter describing the nucleation process is taken as the size of the largest cluster/precipitate in the simulation box. In classical theories, since nucleation is assumed to happen independently among clusters, the dynamic

description of a single-cluster nucleation is used to represent the nucleation process of the whole system on an average basis [37]. Therefore, the cluster size in CNT only refers to individual precipitates, which are not necessarily the "largest" ones. However, in the Monte Carlo simulations, one can observe several of precipitates with different sizes simultaneously forming and dissolving in the matrix. Using the size of the largest clusters as order parameter represents a simple but efficient way to characterize the nucleation stage in atomic simulations.

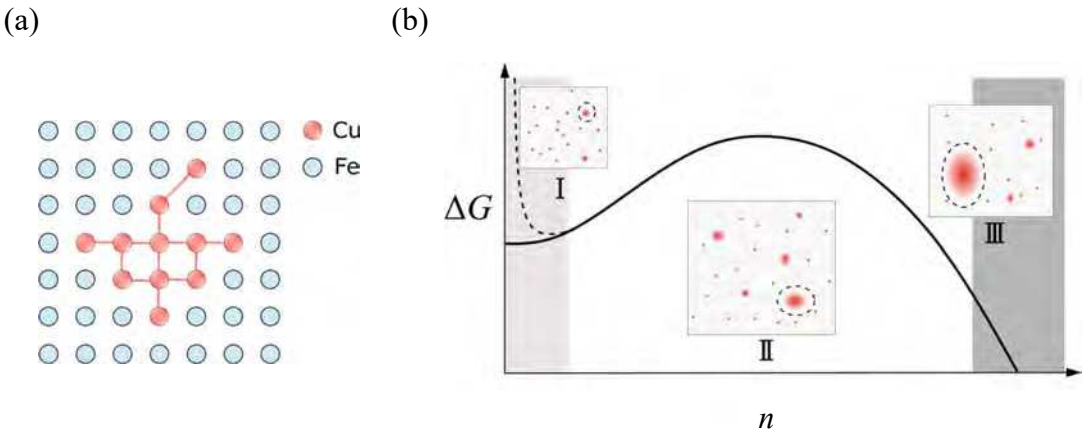

Figure 4.2 (a) A 2-D illustration for cluster detection — a cluster is recognized as a group of Cu atoms (red spheres) connected within the nearest neighbor distance. (b) The nucleation free energy as a function of the size of the largest cluster in the system coincides with the CNT free energy (solid curve) except from the random distribution region (dashed curve).

The setting of interfaces for FFS is also important to the evaluation of nucleation rates. As illustrated in Figure 4.2(b), the formation of the largest cluster (dashed circle) is accompanied by the clustering of many other smaller nuclei. Before reaching supercritical size, all these clusters are highly unstable. For each supersaturated case, FFS trajectories start from a randomly distributed state and end when the system has either formed a large and stable cluster or returns back to random state. A sound sampling of possible transition states relies on the set of properly defined interfaces, especially the first and last ones, which denote the boundaries of the random state and post-critical state, respectively. Due to natural statistical fluctuations of the system in the random state, the free energy as a function of the size of the largest cluster has a

local minimum in the region of small clusters, as illustrated by the dashed curve in Figure 4.2(b). Therefore, it is important to choose the value of λ_0 to be slightly larger than the local minimum to ensure that all transitions are starting from a stable or, at least, metastable phase. The last interface should be set at a size, which is large enough to make sure that the stable cluster will not return to the initial state once the nucleation event is completed. The details of interface setting, $\{\lambda_i\}$, in FFS are listed in Table 4-1.

Table 4-1 The setting of FFS interface $\{\lambda_i\}$ for Fe-1%Cu and Fe-1.5%Cu alloys. For all the samplings, λ_0 is set to be $\lambda_0=\lambda_1$.

Fe-1%Cu				**Fe-1.5%Cu**			
***T*/°C**	λ_1	λ_2	λ_i	***T*/°C**	λ_1	λ_2	λ_i
450	5	10	$\{15+5\times(i-3)\}_{i=3,4}$	**500**	7	10	$\{15+5\times(i-3)\}_{i=3,4}$
500	5	7	$\{10+5\times(i-3)\}_{i=3,4,\ldots,7}$	**550**	7	10	$\{15+5\times(i-3)\}_{i=3,4,5}$
550	5	7	$\{10+5\times(i-3)\}_{i=3,4,\ldots,9}$	**600**	7	10	$\{10+5\times(i-3)\}_{i=3,4,\ldots,8}$
600	5	7	$\{10+5\times(i-3)\}_{i=3,4,\ldots,14}$	**650**	7	10	$\{10+5\times(i-3)\}_{i=3,4,\ldots,12}$

4.2.2 FFS procedures

For a single nucleation event, the random (initial) state without large clusters is treated as reactant (state A) and the post-critical state, where sufficiently large and stable clusters have formed, is treated as product (state B). Generally, when using the largest cluster size n as order parameter, $\lambda(\mathbf{x})=n$, the nucleation trajectory is a time-dependent function of cluster size as $n(t)$. In simulations, a trajectory is stored by recording the size of largest cluster after every MC sweep. The forward crossing of a given interface λ_i at time t is identified when $n(t) > \lambda_i$ and $n(t-\Delta t) \leq \lambda_i$. Here, Δt is the time durance of an MC sweep, while the backward crossing is defined as $n(t) \leq \lambda_i$ and $n(t-\Delta t) > \lambda_i$.

The interfaces $\{\lambda_i\}_{i=0\ldots m}$ are a group of increasing values acting as milestones to determine the time to store the configurations in which the largest cluster first-time reaches or exceeds a given size λ_i . The reaction rate coefficient for a nucleation event expressed by equation (3-30) can be considered as the frequency of forming one stable

large cluster from the random solution, which is treated as a product of the frequency with which the largest cluster in the system attempts to grow over the small size of λ_0, i.e. the initial flux $\Phi_{A,0}$, and the conditional probability of a cluster in size λ_0 to grow to a large post-critical cluster ($n>\lambda_m$) before dissolving, i.e. the crossing probability $P(\lambda_m \mid \lambda_0) = \prod_{i=0}^{m-1} P(\lambda_{i+1} \mid \lambda_i)$. Therefore, $1/k_{AB}$ is equivalent to the average time that the system needs to form one stable post-critical precipitate from the random state. Accordingly, denoting the volume of the MC simulation box by V, the nucleation rate is calculated as [20]

$$J = k_{AB} / V \qquad (4\text{-}4).$$

In this work, the direct FFS algorithm is implemented to investigate the nucleation trajectories in the Fe-Cu system, which proceeds as follows:

(1) Calculation of the initial flux $\Phi_{A,0}$.

The MC simulation starts from the metastable state with randomly mixed Fe and Cu atoms. The trajectory of this simulation is recorded at every MC sweep. Once the trajectory forwardly crosses the first interface λ_0 ($\lambda_0=\lambda_1$), the configuration is stored and the simulation continues. When $N_{A,0}=1000$ configurations are obtained, the simulation stops and the initial flux is calculated as $\Phi_{A,0} = N_{A,0} / \Delta t_{A,0}^{MC}$, where $\Delta t_{A,0}^{MC}$ is the total time the trajectory spends in [0, λ_0]. In some cases, when the simulation has gone to the final stable state before $N_{A,0}$ configurations are accumulated, one can restart the simulation from the metastable random state and continue counting the forward crossing until obtaining $N_{A,0}$ configurations.

(2) Evaluation of $P(\lambda_{i+1} \mid \lambda_i)$.

(i) Randomly pick up a configuration from the set of $N_{A,0}$ configurations gathered in step (1) and run MC simulation from this configuration. The simulation stops when it forwardly crosses the next interface λ_2 or when it backward crosses interface λ_1. In the former case, the configuration as the simulation hits λ_2 is stored and counted as a successful trail from λ_1 to λ_2.

(ii) Repeat the step (i), until N_1=640 successful trajectories from λ_1 to λ_2 are obtained. The conditional crossing probability $P(\lambda_2 \mid \lambda_1)$ is computed as $P(\lambda_2 \mid \lambda_1) = N_1/M_1$, where M_1 is the total number of trails running from λ_1.

(iii) Following the manner of steps (i) and (ii), it is continued to sample the successful trails from λ_i to λ_{i+1} with the starting configurations obtained in the successful trails from λ_{i-1} to λ_i. The conditional crossing probability $P(\lambda_{i+1} \mid \lambda_i)$ is computed as $P(\lambda_{i+1} \mid \lambda_i) = N_i/M_i$, where M_i is the total number of trails starting from λ_i.

(iv) Repeat step (iii) until finishing the sampling from λ_{m-1} to λ_m. Then the reaction constant is calculated as $k_{AB} = \Phi_{A,0} \prod_{i=1}^{m-1} P(\lambda_{i+1} \mid \lambda_i)$.

4.3 Nucleation free energy evaluation

4.3.1 Umbrella Sampling

In the Umbrella Sampling simulations, the size of largest cluster n is chosen as simulation coordinate, or order parameter, and a set of windows is defined for the sampling with the bias energy given by $U_i = \frac{\kappa}{2}(n - \bar{n}_i)^2$, where $\bar{n}_i$ is the restrained value of the i-th simulation and κ is a spring constant. In the present Umbrella Sampling, a set of windows is defined with restrained values of $\{\bar{n}_i\}$ ={3, 5, 7, … , 65} and a spring constant of κ = 37.5meV/atom^2 for all the samplings.

Therefore, there are 32 simulations to perform in an Umbrella Sampling run. In each i-th simulation, the standard MC procedure is employed as described in section 4.1, except that the size of the largest cluster n is tracked for every MC step. The energy difference for each MC step is calculated as $\Delta E = \Delta E_{LCE} + \Delta U_i$, where ΔE_{LCE} is the energy difference stemming from the LCE potential only and ΔU_i is the difference in umbrella potential after the trial steps. In every simulation, 10000 MC sweeps are firstly

run for equilibration, and then the value of n is recorded every iteration for 50000 MC sweeps to compute the histogram $hist_i(n)$. For the purpose of demonstration, the histograms obtained in window simulations with $\bar{n}_i$=5, 11, 15 and 21 are displayed in Figure 4.3.

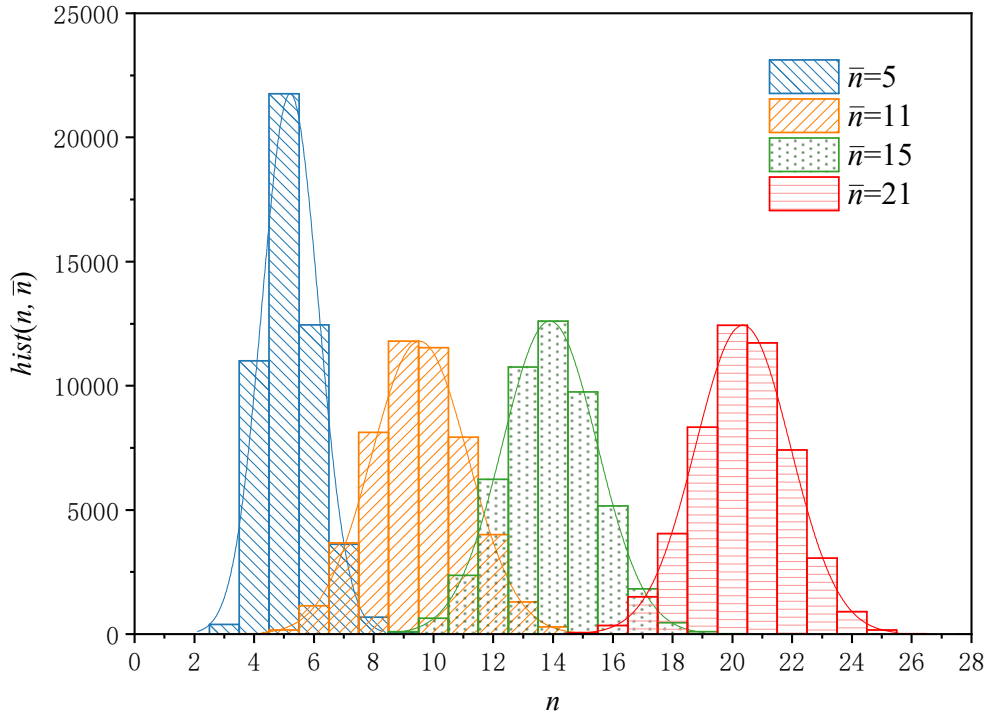

Figure 4.3 The histograms of n in the Umbrella Sampling with a biased potential $U = \frac{\kappa}{2}(n-\bar{n})^2$ with κ=37.5 meV/atom^2 and $\bar{n}$=5, 11, 15, 21, respectively. The curves are the trendlines of histograms.

After finishing all the 32 simulations and obtaining all the histograms $\{hist_i(n)\}_{i=1...32}$, one can use the WHAM (Weighted Histogram Analysis Method) algorithm [27,38] to evaluate the unbiased probability distribution $\rho(n)$ as

$$\rho(n) = \frac{M(n)}{\sum_i N_i f_i c_i(n)} \tag{4-5}$$

where $M(n)$ is the accumulated number of n-sized particles combining all the histograms, and N_i is the total number of samples in the i-th window simulation. In this work, N_i = 50000. In WHAM, $\rho(n)$ and f_i, where $f_i = 1 \Big/ \sum_{n=3}^{65} c_i(n)\rho(n)$, are iteratively

solved. First, one needs to make a rough guess for $\{\rho(n)\}_{n=3\ldots65}$, which is denoted as $\rho^{\text{old}}(n)$. Then, f_i for i=1…32 are calculated as $f_i = 1 \Big/ \sum_{n=3}^{65} c_i(n)\rho^{\text{old}}(n)$, which are put in equation (4-5) to compute a new set of $\rho(n)$, denoted as $\rho^{\text{new}}(n)$. Assign $\rho^{\text{new}}(n)$ to $\rho^{\text{old}}(n)$ and repeat the procedure until errors between $\rho^{\text{new}}(n)$ and $\rho^{\text{old}}(n)$ are acceptable, then the self-consistent solution to equation (4-5) is achieved.

It is emphasized that $\rho(n)$, solved by WHAM, denotes the equilibrium probability of finding the system in a state with size of the largest cluster equal to n, which is clearly different from the equilibrium probability, $f(n)$, defined on a single cluster model in classical theories. Nevertheless, $\rho(n)$ and $f(n)$ will overlap for large n, when only one cluster of that size is observed in the Umbrella Sampling simulations [39]. Accordingly, the CNT-type/single-cluster free energy, $\Delta G(n)$, can be calculated as

$$\Delta G(n)/k_{\text{B}}T = \begin{cases} -\ln f(n) & n \le n_{\text{patch}} \\ -\ln \rho(n) + C & n > n_{\text{patch}} \end{cases} \qquad (4\text{-}6).$$

n_{patch} is the point where the two free energy curves are patched up and C is an adjustable coefficient to make the free energy continuous at the patching point. For small values of n, $n \le n_{\text{patch}}$, the probability $f(n)$ approximately equals to the stationary size distribution established when nucleation takes place [40], which is calculated directly in a conventional, or brute-force, MC simulation without bias potential.

4.3.2 Reweighted Partial Path (RPP) method

In the present thesis, a novel Reweighted Partial Path (RPP) method to compute free energy profiles directly using the trajectories obtained in FFS simulations is developed and implemented. This method is very efficient, and no additional calculations, such as, reverse FFS or Umbrella Sampling are required. This new RPP method is inspired by the Partial-Path Transition Interface Sampling (PPTIS) method introduced by Moroni *et al.* [41,42]. For diffusive processes, free energy profiles can be easily determined in PPTIS together with the rate constant without the requirement

of additional calculations. The basic concept of PPTIS is very similar to other TIS methods, except that PPTIS utilizes a *memory-loss* assumption to extrapolate the long-range effective crossing flux from local partial path ensembles. The *memory-loss* assumption acts as a medium to connect the properties of long-range transition paths with the partial paths on every interface. Bearing this idea in mind, once a system obeys the *memory-loss* assumption, it is theoretically possible to use transition paths, sampled by a standard TIS algorithm (without sampling the reverse transition), to reconstruct the partial path ensembles and hence to evaluate free energy profiles. However, due to the unique sampling strategy of PPTIS, its free energy evaluation algorithm, called the *loop-boundary* method, cannot be directly implemented within other TIS approaches. Therefore, a novel approach -- Reweighted Partial Path (RPP) method is proposed in this work so that one can determine free energy profiles using the trajectory information from a single TIS/FFS calculation.

For an ergodic system, the equilibrium distribution is also preserved in trajectory space such that the equilibrium average of an observable $g(\mathbf{x})$ can be calculated as an average over trajectories,

$$\langle g(\mathbf{x})\rangle = \int \mathcal{D}\mathbf{x}^{\tau}\mathcal{P}(\mathbf{x}^{\tau})\int_0^{\tau} dt\; g(\mathbf{x}_t) \qquad (4\text{-}7).$$

In the derivations that follow, the weighted average for an observable $g(\mathbf{x})$ is used, and a weight function $w(\mathbf{x})$ is defined as $\langle g(\mathbf{x})\rangle_w = \dfrac{\langle g(\mathbf{x})w(\mathbf{x})\rangle}{\langle w(\mathbf{x})\rangle}$.

For a system evolving diffusively with high-friction character, it is reasonable to assume that the memory of trajectories is lost over some time and distance in phase space along the λ-axis. If the transition interfaces, $\{\lambda_i\}_{i=1\ldots M\text{-}1}$, between states A and B are properly set such that the memory of trajectories only persists between adjacent interfaces, the average of an observable $g(\mathbf{x}_t)$, when the trajectories cross interface i coming from a faraway interface, approximately equals the average over the trajectories coming from the adjacent interface [41],

$$\langle g(\mathbf{x}_t)\rangle_{\psi_{i,i\pm q}} \approx \langle g(\mathbf{x}_t)\rangle_{\psi_{i,i\pm 1}} \qquad (4\text{-}8)$$

where q is a given integer. As a matter of fact, the exact expression of memory loss

defined in PPTIS[41] is $\langle g(\mathbf{x}_t)\rangle_{\phi_{i,i\pm q}} \approx \langle g(\mathbf{x}_t)\rangle_{\phi_{i,i\pm 1}}$, where $\phi_{i,j}(\mathbf{x}_t) = \lim_{\Delta t\to 0}\frac{1}{\Delta t}\psi_{i,j}(\mathbf{x}_t)$ equals the velocity of crossing interface i at time t in a trajectory coming directly from j before recrossing i. In practice, Δt is given as a small but fixed time step in simulation instead of carrying out the limit $\Delta t \to 0$, and hence the definition of memory loss in PPTIS is equivalent to that expressed by equation (4-8).

Since the memory loss should be also obeyed for paths coming from the same stable state, equation (4-8) can be extended as

$$\begin{cases} \langle g(\mathbf{x}_t)\rangle_{\psi_{i,\mathrm{A}}} \approx \langle g(\mathbf{x}_t)\rangle_{\psi_{i,i-1|\mathrm{A}}} \\ \langle g(\mathbf{x}_t)\rangle_{\psi_{i,\mathrm{B}}} \approx \langle g(\mathbf{x}_t)\rangle_{\psi_{i,i+1|\mathrm{B}}} \end{cases} \tag{4-9}$$

where $\langle g(\mathbf{x}_t)\rangle_{\psi_{i,i\pm q|\mathrm{A(B)}}} = \frac{\langle \hbar_{\mathcal{A}(\mathcal{B})}(\mathbf{x}) g(\mathbf{x}_t)\psi_{i,i\pm q}\rangle / \langle \hbar_{\mathcal{A}(\mathcal{B})}(\mathbf{x})\rangle}{\langle \hbar_{\mathcal{A}(\mathcal{B})}(\mathbf{x})\psi_{i,i\pm q}\rangle / \langle \hbar_{\mathcal{A}(\mathcal{B})}(\mathbf{x})\rangle} = \frac{\langle g(\mathbf{x}_t)\psi_{i,i\pm q}\rangle_{\mathrm{A(B)}}}{\langle \psi_{i,i\pm q}\rangle_{\mathrm{A(B)}}}$. Here, $\langle ... \rangle_{\mathrm{A(B)}}$ is an averaging over the paths coming from one of the stable regions A(B) and ending in either A or B. Since $\langle g(\mathbf{x}_t)\rangle_{\psi_{i,i\pm 1}} = \omega_{\mathrm{A}}^{i,i\pm 1}\langle g(\mathbf{x}_t)\rangle_{\psi_{i,i\pm 1|\mathrm{A}}} + \omega_{\mathrm{B}}^{i,i\pm 1}\langle g(\mathbf{x}_t)\rangle_{\psi_{i,i\pm 1|\mathrm{B}}}$, where $\omega_{\mathrm{A(B)}}^{i,i\pm 1} = \langle \hbar_{\mathcal{A}(\mathcal{B})}(\mathbf{x})\psi_{i,i\pm q}\rangle / \langle \psi_{i,i\pm q}\rangle$ and $\omega_{\mathrm{A}}^{i,i\pm 1} + \omega_{\mathrm{B}}^{i,i\pm 1} = 1$, combined with equation (4-8) and (4-9), one can easily get the relation

$$\langle g(\mathbf{x}_t)\rangle_{\psi_{i,i\pm 1}} \approx \langle g(\mathbf{x}_t)\rangle_{\psi_{i,i\pm 1|\mathrm{A}}} \approx \langle g(\mathbf{x}_t)\rangle_{\psi_{i,i\pm 1|\mathrm{B}}} \tag{4-10}.$$

Equation (4-10) indicates that average properties observed in trajectories, which cross i from $i\pm 1$ in paths coming from A, are approximately equal to the averages observed in paths coming from B. The crossing probability $P(\begin{smallmatrix} m \\ l \end{smallmatrix}\big|\begin{smallmatrix} i \\ j \end{smallmatrix})$, which describes a path having crossed interface i from j and which will continue to reach interface m before l, is expressed using the crossing functions as

$$P(\begin{smallmatrix} m \\ l \end{smallmatrix}\big|\begin{smallmatrix} i \\ j \end{smallmatrix}) = \frac{\langle \Psi_{i,j}^{m,l}\rangle}{\langle \psi_{i,j}\rangle} = \frac{\langle \psi_{i,j}\bar{h}_{l,m}^{f}\rangle}{\langle \psi_{i,j}\rangle} = \langle \bar{h}_{m,l}^{f}\rangle_{\psi_{i,j}} \tag{4-11}.$$

In PPTIS [41], the one-interface crossing probabilities are defined as $p_i^{\pm} \equiv P(\begin{smallmatrix} i+1 \\ i-1 \end{smallmatrix}\big|\begin{smallmatrix} i \\ i-1 \end{smallmatrix})$,

$p_i^{=} \equiv P(^{i-1}_{i+1}\big|^{i}_{i-1})$, $p_i^{\mp} \equiv P(^{i-1}_{i+1}\big|^{i}_{i+1})$ and $p_i^{\pm}_{\mp} \equiv P(^{i+1}_{i-1}\big|^{i}_{i+1})$. According to the memory loss assumption, $\left\langle \bar{h}^{f}_{m,l}(\mathbf{x}_t)\right\rangle_{\psi_{i,i\pm1}} \approx \left\langle \bar{h}^{f}_{m,l}(\mathbf{x}_t)\right\rangle_{\psi_{i,i\pm1}|\mathrm{A}} \approx \left\langle \bar{h}^{f}_{m,l}(\mathbf{x}_t)\right\rangle_{\psi_{i,i\pm1}|\mathrm{B}}$. Hence, the one-interface crossing probability can be rewritten as

$$
\begin{aligned}
p_i^{\pm} &\equiv \frac{\left\langle \Psi_i^{\pm}\right\rangle}{\left\langle \psi_{i,i-1}\right\rangle} \approx \frac{\left\langle \Psi_i^{\pm}\right\rangle_{\mathrm{A(B)}}}{\left\langle \psi_{i,i-1}\right\rangle_{\mathrm{A(B)}}} \qquad
p_i^{=} \equiv \frac{\left\langle \Psi_i^{=}\right\rangle}{\left\langle \psi_{i,i-1}\right\rangle} \approx \frac{\left\langle \Psi_i^{=}\right\rangle_{\mathrm{A(B)}}}{\left\langle \psi_{i,i-1}\right\rangle_{\mathrm{A(B)}}} \\
p_i^{\mp} &\equiv \frac{\left\langle \Psi_i^{\mp}\right\rangle}{\left\langle \psi_{i,i+1}\right\rangle} \approx \frac{\left\langle \Psi_i^{\mp}\right\rangle_{\mathrm{A(B)}}}{\left\langle \psi_{i,i+1}\right\rangle_{\mathrm{A(B)}}} \qquad
p_i^{\pm}_{\mp} \equiv \frac{\left\langle \Psi_i^{\pm}_{\mp}\right\rangle}{\left\langle \psi_{i,i+1}\right\rangle} \approx \frac{\left\langle \Psi_i^{\pm}_{\mp}\right\rangle_{\mathrm{A(B)}}}{\left\langle \psi_{i,i+1}\right\rangle_{\mathrm{A(B)}}}
\end{aligned}
\tag{4-12}
$$

where $\left\langle \Psi_i^{\Theta}\right\rangle$ with $\Theta = \pm, \mp, =, \pm_{\mp}$ is a short notation for $\left\langle \Psi_i^{\pm}\right\rangle = \left\langle \Psi_{i,i-1}^{i+1,i-1}\right\rangle$, $\left\langle \Psi_i^{=}\right\rangle = \left\langle \Psi_{i,i-1}^{i-1,i+1}\right\rangle$, $\left\langle \Psi_i^{\pm}_{\mp}\right\rangle = \left\langle \Psi_{i,i+1}^{i+1,i-1}\right\rangle$ and $\left\langle \Psi_i^{\mp}\right\rangle = \left\langle \Psi_{i,i+1}^{i-1,i+1}\right\rangle$. In unbiased ensembles, the transition paths originate from basin A or B, and end in A or B after visiting the transition region. If a trajectory reaches interface i from i-1, it will continue to cross the adjacent interfaces (i+1 or i-1) until it leaves the transition region and reaches A or B. Considering the continuity of trajectories, the average crossing of i from i-1, $\left\langle \psi_{i,i-1}\right\rangle$ (see Figure 4.4(a)) equals the average effective crossing of i-1 from both i and i-2, e.g. $\left\langle \psi_{i,i-1}\right\rangle = \left\langle \Psi_{i-1}^{\pm}\right\rangle + \left\langle \Psi_{i-1}^{\pm}_{\mp}\right\rangle$. Similarly, the effective crossing of interface i-1 from i also obeys the continuity relation as illustrated in Figure 4.4(b), so that $\left\langle \psi_{i-1,i}\right\rangle = \left\langle \Psi_i^{\mp}\right\rangle + \left\langle \Psi_i^{=}\right\rangle$.

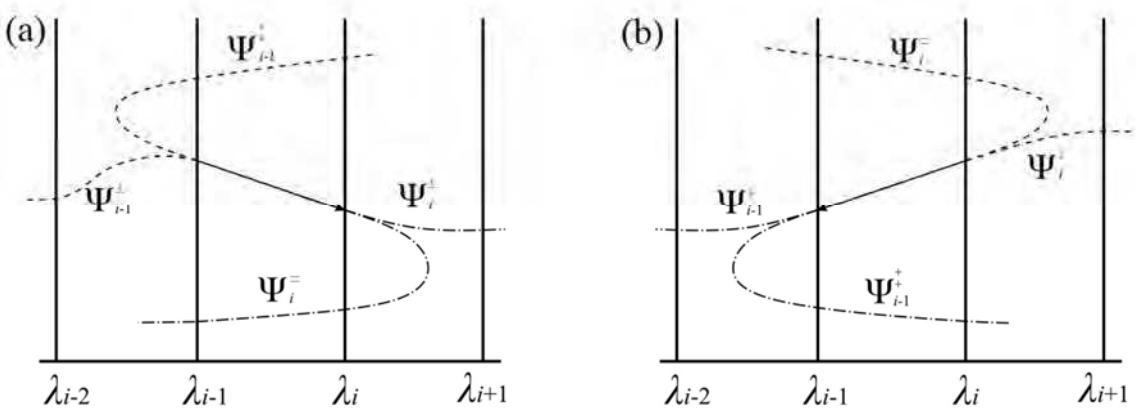

Figure 4.4 Illustration of the continuity relation for (a) the effective crossing of interface i from i-1, and (b) the effective crossing of interface i-1 from i.

Bearing in mind that $\langle \psi_{i-1,i} \rangle = \langle \Psi_{i-1}^{\mp} \rangle + \langle \Psi_{\pm i-1}^{+} \rangle$ and $\langle \psi_{i,i-1} \rangle = \langle \Psi_{i}^{\pm} \rangle + \langle \Psi_{i}^{=} \rangle$, the continuity relation can be written as

$$\begin{cases} \langle \Psi_{i-1}^{\pm} \rangle - \langle \Psi_{i-1}^{\mp} \rangle = \langle \Psi_{i}^{\pm} \rangle - \langle \Psi_{i}^{\mp} \rangle \\ \langle \Psi_{i-1}^{\mp} \rangle + \langle \Psi_{\pm i-1}^{+} \rangle = \langle \Psi_{i}^{\mp} \rangle + \langle \Psi_{i}^{=} \rangle \end{cases} \quad (4\text{-}13).$$

When denoting $J = \langle \Psi_{i-1}^{\pm} \rangle - \langle \Psi_{i-1}^{\mp} \rangle = \langle \Psi_{i}^{\pm} \rangle - \langle \Psi_{i}^{\mp} \rangle$, according to equation (4-12), equation (4-13) can be rewritten as

$$\frac{1}{p_i^{=}} \langle \Psi_{i}^{\mp} \rangle - \frac{p_i^{\pm}}{p_i^{=} p_{i-1}^{\mp}} \langle \Psi_{i-1}^{\mp} \rangle + J = 0 \quad (4\text{-}14).$$

The continuity relation should also be obeyed by the trajectories exclusively coming from state A(B) and ending in either A or B, as $\frac{1}{p_i^{=}} \langle \Psi_{i}^{\mp} \rangle_{\mathrm{A(B)}} - \frac{p_i^{\pm}}{p_i^{=} p_{i-1}^{\mp}} \langle \Psi_{i-1}^{\mp} \rangle_{\mathrm{A(B)}} + J_{\mathrm{A(B)}} = 0$, with $J_{\mathrm{A(B)}} = \langle \Psi_{i}^{\pm} \rangle_{\mathrm{A(B)}} - \langle \Psi_{i}^{\mp} \rangle_{\mathrm{A(B)}}$. Now, let's only consider the trajectories coming from state A and ending in either A or B. According to the boundary conditions, $\langle \Psi_{M-1}^{\mp} \rangle_{\mathrm{A}} = 0$, the relation between the effective crossing $\langle \Psi_{i}^{\Theta} \rangle_{\mathrm{A}}$ and $\langle \Psi_{i}^{\Theta} \rangle$ is derived by solving equation(4-14) for every interface (see Appendix B),

$$\begin{cases} \langle \Psi_{i}^{\mp} \rangle_{\mathrm{A}} = \frac{U_{i+1}}{\langle \hbar_{\mathcal{A}} \rangle} \cdot \langle \Psi_{i}^{\mp} \rangle \\ \langle \Psi_{\pm i}^{+} \rangle_{\mathrm{A}} = \frac{U_{i+1}}{\langle \hbar_{\mathcal{A}} \rangle} \cdot \langle \Psi_{\pm i}^{+} \rangle \end{cases} \text{ and } \begin{cases} \langle \Psi_{i}^{\pm} \rangle_{\mathrm{A}} = \frac{U_{i+1}}{\langle \hbar_{\mathcal{A}} \rangle} \cdot \langle \Psi_{i}^{\pm} \rangle + J_{\mathrm{A}} \\ \langle \Psi_{i}^{=} \rangle_{\mathrm{A}} = \frac{U_{i+1}}{\langle \hbar_{\mathcal{A}} \rangle} \cdot \langle \Psi_{i}^{=} \rangle + \frac{p_i^{=}}{p_i^{\pm}} J_{\mathrm{A}} \end{cases} \quad (4\text{-}15)$$

where $U_i = P(\begin{smallmatrix} 0 \\ M \end{smallmatrix} \big| \begin{smallmatrix} i \\ 0 \end{smallmatrix}) = 1 - P(\begin{smallmatrix} M \\ 0 \end{smallmatrix} \big| \begin{smallmatrix} i \\ 0 \end{smallmatrix})$ and $J_{\mathrm{A}} = \langle \Psi_{0}^{\pm} \rangle_{\mathrm{A}} (1 - U_1)$. U_i denotes the decaying probability from interface i in the transition from A to B, which corresponds to the probability that a trajectory, coming from A, returns to A before reaching B after it crossed interface i. Equation (4-15) indicates that, under the memory loss assumption, the average effective crossing of interface i from adjacent interfaces, $\langle \Psi_{i}^{\Theta} \rangle$, is connected with weighted average in the paths coming from A, $\langle \Psi_{i}^{\Theta} \rangle_{\mathrm{A}}$, by the decaying probability in transition A to B. Similar relations between $\langle \Psi_{i}^{\Theta} \rangle_{\mathrm{B}}$ and $\langle \Psi_{i}^{\Theta} \rangle$ can also

be derived with boundary conditions $\left\langle \Psi_1^{\pm} \right\rangle_B = 0$, by solving the equation (4-14) for every interface.

When a trajectory effectively crosses the interface i from i-1 or i+1, a partial path is recognized as the continuous path segment remaining between i-1 and i+1. For example, in Figure 4.5(b), when the trajectory crosses i-1 at point b coming from i-2 and leaves the interface region by crossing i at point e, it is considered as an effective crossing of i-1 represented as $\Psi_{i-1}^{\pm}(b) = 1$. The path segment from $a \rightarrow e$ is recognized as a partial path on i-1 with the crossing type denoted by $\pm$. As illustrated in Figure 4.5(a), there are four types of partial paths on interface i, denoted by $\Theta = \pm, \mp, =, \overset{+}{+}$, with each one corresponding to an effective crossing of interface i.

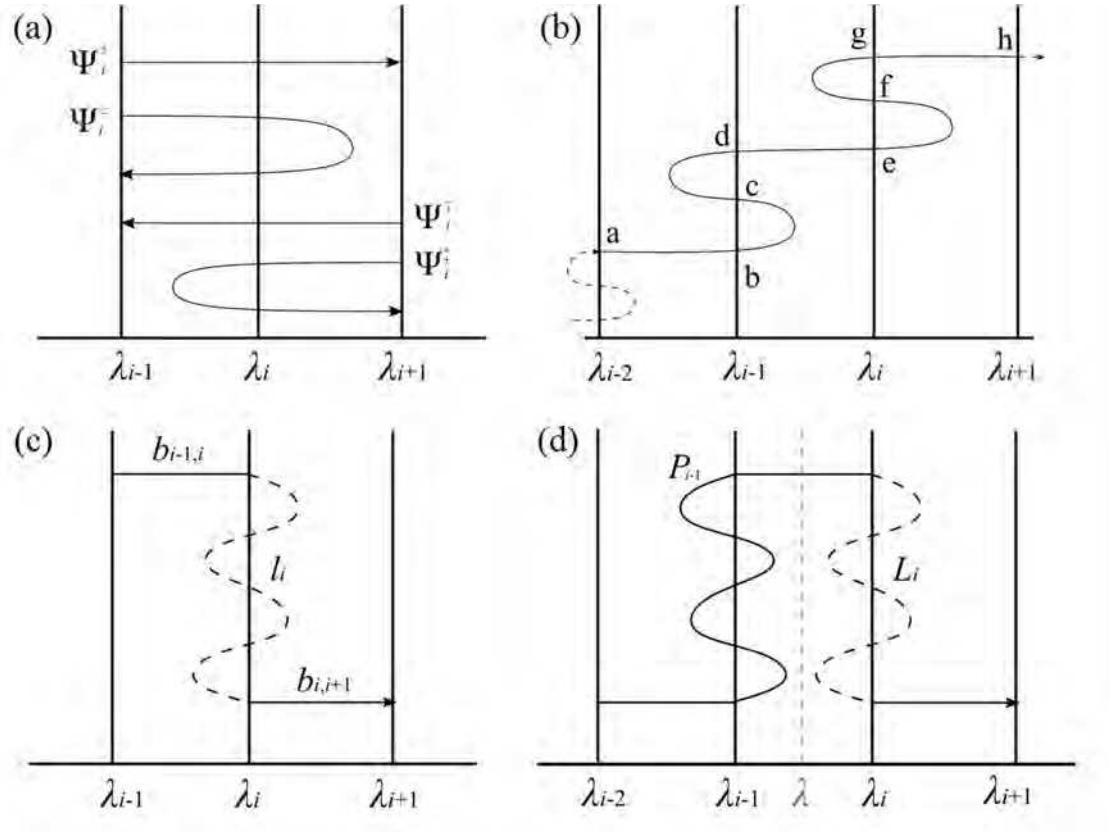

Figure 4.5 (a) Four types of partial paths corresponding to four effective crossings at interface i; (b) A trajectory effectively crosses interface i-1 and then i at points b and e, respectively. According to the definition, the partial path generated on i-1 is the segment a→e and the partial path generated on i is d→h; (c) A partial path on interface i is divided into three parts: two boundary segments (solid lines) and a loop segment (dashed line). (d) The boundary path segment between λ_{i-1} and λ_i is shared by partial paths on

interfaces i-1 and i. To avoid double counting, in the histogram of λ, where $\lambda \in (\lambda_{i-1}, \lambda_i)$, the phase points falling on λ are treated as being visited by the partial paths on interface i-1 and the loop of partial paths on i. This is equivalent to using the loop of partial paths in i-1 and the partial paths on i to calculate the histogram of λ.

In unbiased ensembles, partial paths can be generated by breaking up the trajectories into path segments based on the effective crossing of every interface. Accordingly, one partial path is coupled with one effective crossing, hence the unbiased number density of partial paths on interface i with type Θ is equal to the average effective crossing $\left\langle \Psi_i^{\Theta} \right\rangle$ in trajectory space. For the partial paths generated from trajectories exclusively coming from A (B), the number density of partial paths on i equals $\left\langle \Psi_i^{\Theta} \right\rangle_{\mathrm{A(B)}}$.

Similar to the *loop-boundary* method [42] in PPTIS, the partial paths on i are divided into three parts: two boundary segments and a loop part (illustrated in Figure 4.5(c)). The loop part is defined as the segment between the first crossing point and the last crossing point of the middle interface marked by the dashed line in Figure 4.5(c). The boundary parts are defined as the segments from the path boundary point to the last and first crossing point of interface i, marked by the solid lines in Figure 4.5(c). When a trajectory consecutively crosses two adjacent interfaces, there is an overlapping part between the partial paths generated by the trajectory on the two interfaces. For instance, the path segment $d \rightarrow e$ is shared by partial paths $a \rightarrow e$ and $d \rightarrow h$, when the trajectory crosses interface i-1 and i in a row. In the meantime, $d \rightarrow e$ is a boundary segment between interface i-1 and i for partial paths $a \rightarrow e$ and $d \rightarrow h$. Therefore, to avoid double counting, the histogram of phase points from a trajectory in a small bin $[\lambda-\delta\lambda, \lambda+\delta\lambda]$ with $\lambda \in (\lambda_{i-1}, \lambda_i)$ (see Figure 4.5(d)) can be calculated by the histogram from partial paths on interface i-1 combined with the histogram of λ in the loop part of partial paths on interface i as

$$\left\langle \delta\left(\lambda(\mathbf{x}_t)-\lambda\right)\right\rangle = \sum_{\Theta=\pm,\mp,=,\substack{+\\+}} \left\langle \Psi_{i-1}^{\Theta}\right\rangle P_{i-1}^{\Theta}(\lambda)+\left\langle \Psi_{i}^{\Theta}\right\rangle L_{i}^{\Theta}(\lambda) \qquad (4\text{-}16)$$

where $P_{i-1}^{\Theta}(\lambda)$ is the average histogram of λ in the partial path of type Θ on interface i-1, and $L_{i}^{\Theta}(\lambda)$ is the average histogram of λ from the loop on the partial path of type Θ on interface i. This is equivalent to calculating the histogram of λ from the partial paths on i and the loop of partial paths on i-1, as $\left\langle \delta\left(\lambda(\mathbf{x}_t)-\lambda\right)\right\rangle = \sum_{\Theta=\pm,\mp,=,\substack{+\\+}} \left\langle \Psi_{i-1}^{\Theta}\right\rangle L_{i-1}^{\Theta}(\lambda)+\left\langle \Psi_{i}^{\Theta}\right\rangle P_{i}^{\Theta}(\lambda)$.

When a trajectory effectively crosses interface i at phase point $\mathbf{x}_t$, the histogram of λ in the partial path is calculated as $\rho_i^{\Theta}(\lambda)=\int_{t-\Delta t_{\Theta}^{b}}^{t+\Delta t_{\Theta}^{f}} dt'\,\delta\left(\lambda(\mathbf{x}_{t'})-\lambda\right)$, where Δt_{Θ}^{f} and Δt_{Θ}^{b} are the times when the trajectory first crosses interface i+1 (i-1) forward and backward from $\mathbf{x}_t$, respectively. For Θ in $\pm,\mp,=$ and $\substack{+\\+}$, $\left(\Delta t_{\Theta}^{f},\Delta t_{\Theta}^{b}\right)$ is taken as $\left(\Delta t_{i+1}^{f},\Delta t_{i-1}^{b}\right),\left(\Delta t_{i-1}^{f},\Delta t_{i+1}^{b}\right),\left(\Delta t_{i-1}^{f},\Delta t_{i-1}^{b}\right)$ and $\left(\Delta t_{i+1}^{f},\Delta t_{i+1}^{b}\right)$, respectively. Accordingly, the average density of λ in the partial path Θ having crossed i is defined as $P_i^{\Theta}(\lambda)=\left\langle \rho_i^{\Theta}(\lambda)\right\rangle_{\Psi_i^{\Theta}}$. Similarly, the density of λ in the loop part (illustrated as dashed line in Figure 4.5 (c)) of partial paths having crossed i can also be calculated as $L_i^{\Theta}(\lambda)=\left\langle l_i^{\Theta}(\lambda)\right\rangle_{\Psi_i^{\Theta}}$, with $l_i^{\Theta}(\lambda)=\int_{t-\Delta t_{\Theta}^{b}}^{t+\Delta t_{\Theta}^{f}} dt'\,\delta\left(\lambda(\mathbf{x}_{t'})-\lambda\right)l_i(\mathbf{x}_{t'})$. Here, $l_i(\mathbf{x}_{t'})$ is a characteristic function [42], where $l_i(\mathbf{x}_{t'})$=1 if $\mathbf{x}_{t'}$ is on the loop of the partial path, otherwise $l_i(\mathbf{x}_{t'})$=0. According to the memory loss assumption, $\left\langle \rho_i^{\Theta}\right\rangle_{\Psi_i^{\Theta}} \approx \left\langle \rho_i^{\Theta}\right\rangle_{\Psi_i^{\Theta}|\mathrm{A(B)}}$ and $\left\langle l_i^{\Theta}\right\rangle_{\Psi_i^{\Theta}} \approx \left\langle l_i^{\Theta}\right\rangle_{\Psi_i^{\Theta}|\mathrm{A(B)}}$, therefore

$$\begin{aligned}\left\langle \delta\left(\lambda(\mathbf{x}_t)-\lambda\right)\right\rangle_{\mathrm{A}} &= \sum_{\Theta=\pm,\mp,=,\substack{+\\+}} \left\langle \Psi_{i-1}^{\Theta}\right\rangle_{\mathrm{A}} \left\langle \rho_i^{\Theta}\right\rangle_{\Psi_i^{\Theta}|\mathrm{A}} + \left\langle \Psi_{i}^{\Theta}\right\rangle_{\mathcal{A}} \left\langle l_i^{\Theta}\right\rangle_{\Psi_i^{\Theta}|\mathrm{A}} \\ &\approx \sum_{\Theta=\pm,\mp,=,\substack{+\\+}} \left\langle \Psi_{i-1}^{\Theta}\right\rangle_{\mathrm{A}} P_{i-1}^{\Theta}(\lambda)+\left\langle \Psi_{i}^{\Theta}\right\rangle_{\mathrm{A}} L_i^{\Theta}(\lambda)\end{aligned} \qquad (4\text{-}17).$$

Combining eqs. (12), (13) and (14), the equilibrium histogram of λ is written as

$$\left\langle \delta\left(\lambda(\mathbf{x}_t)-\lambda\right)\right\rangle = \frac{\left\langle \delta\left(\lambda(\mathbf{x}_t)-\lambda\right)\right\rangle_{\mathrm{A}} - C_i(\lambda)J_{\mathrm{A}}}{U_i} \cdot \left\langle \mathcal{H}_{\mathcal{A}} \right\rangle \qquad (4\text{-}18)$$

where $C_i(\lambda) = P_{i-1}^{\pm}(\lambda) + \frac{p_{i-1}^{=}}{p_{i-1}^{\pm}} P_{i-1}^{=}(\lambda) + p_i^{\pm} L_i^{\pm}(\lambda) + p_i^{=} L_i^{=}(\lambda) - p_i^{=} L_i^{\mp}(\lambda) - \frac{p_i^{+} p_i^{=}}{p_i^{\mp}} L_i^{\pm}(\lambda)$. In equation (4-18), $\left\langle \delta\left(\lambda(\mathbf{x}_t)-\lambda\right)\right\rangle_{\mathrm{A}}$ is the unbiased histogram of λ in the ensemble with paths coming from A and ending either in A or B. This path ensemble can be obtained in a single TIS calculation for the transition A→B by assigning an unbiased path weight $\mathcal{P}_{\mathrm{A}}(\mathbf{x}^{\tau})$ to each TIS trajectory, $\mathbf{x}^{\tau}$, using a reweighting strategy, e.g. the reweighted path ensemble method [43]. The partial paths on each interface can be generated by breaking up TIS trajectories based on the type of effective crossing. The average of effective crossings is determined as $\left\langle \Psi_i^{\Theta} \right\rangle_{\mathrm{A}} = \sum \mathcal{P}_{\mathrm{A}}(\mathbf{x}^{\tau}) n_i^{\Theta}(\mathbf{x}^{\tau})$, where $n_i^{\Theta}(\mathbf{x}^{\tau})$ describes how many times the trajectory $\mathbf{x}^{\tau}$ effectively crosses interface i with type Θ. With the memory loss assumption, p_i^{Θ}, P_i^{Θ} and L_i^{Θ} can also be evaluated in a single TIS calculation for transition A→B, and, hence, one can obtain the equilibrium histogram of λ, i.e. $\left\langle \delta\left(\lambda(\mathbf{x}_t)-\lambda\right)\right\rangle$, by equation (4-18).

In PPTIS, the partial paths are sampled from every transition interface in an unbiased manner — the trajectories are shot from the phase points on interface i forward and backward until they hit the adjacent interface i-1 or i+1. The averaged histogram P_i^{Θ} and L_i^{Θ} can be directly measured from the partial path gathered on interface i. When calculating the equilibrium histogram of λ, $\left\langle \delta\left(\lambda(\mathbf{x}_t)-\lambda\right)\right\rangle$, using the *loop-boundary* method, the average weights of partial paths on adjacent interfaces, e.g. $\left\langle \Psi_{i-1}^{\Theta} \right\rangle$ and $\left\langle \Psi_i^{\Theta} \right\rangle$ in equation (4-16), are reweighted according to the histogram of the commonly shared boundary path segment between interfaces. Therefore, in PPTIS, there is no need to derive the relation of $\left\langle \Psi_i^{\Theta} \right\rangle$ and $\left\langle \Psi_i^{\Theta} \right\rangle_{\mathrm{A(B)}}$ in the calculation of the equilibrium histogram of λ. However, due to the unique sampling strategy in PPTIS, this *loop-boundary* method cannot be directly used in a general TIS calculation. For

a TIS single transition, i.e. A→B or B→A, one can evaluate the average histogram P_i^{Θ} and L_i^{Θ} from partial paths generated by breaking up TIS trajectories, but the weights (or the effective crossing) of partial paths on each interface are $\left\langle \Psi_i^{\Theta} \right\rangle_{\mathrm{A(B)}}$ instead of $\left\langle \Psi_i^{\Theta} \right\rangle$. To evaluate the equilibrium histogram of λ, in the RPP method, the relation of $\left\langle \Psi_i^{\Theta} \right\rangle$ and $\left\langle \Psi_i^{\Theta} \right\rangle_{\mathrm{A(B)}}$ (see equation(4-15)) is derived to implement the *loop-boundary* method in the general TIS calculation for a single transition (see equation(4-18)).

To the transitions known to be diffusive, both PPTIS and TIS+RPP can be used to simultaneously evaluate the transition rate constant and energy profile. As to a transition, which is not certain to be diffusive, one can first do TIS to calculate the reaction rate constant, and then use RPP to reconstruct the energy profile and validate the memory loss assumption afterwards. If the validation is failed, i.e. RPP result is not reliable, one can still do a reverse TIS or Umbrella Sampling simulation to re-evaluate the energy profile. Since RPP does not require additional sampling, the computational cost for the energy profile is negligible.

Now let us consider an extreme case where the phase space is projected on a discrete order parameter λ_i, each i representing a state. The transition consists of the systems consecutive jumps from one state to another adjacent state. If complete memory loss is assumed, i.e. the frequency of jumping from state i to $i\pm1$ only depends on state i, then $p_i^{\mp} = p_i^{=}$ and $p_i^{+} = p_i^{\pm}$. Still considering $\{\lambda_i\}$ as transition interfaces, there is only one phase point $\mathbf{x}_t$, as $\lambda(\mathbf{x}_t)= \lambda_i$, on each partial path on interface i, i.e. $P_i^{\Theta}(\lambda_i) = \delta(\lambda(\mathbf{x}_t), \lambda_i)$. This phase point can be categorized to either boundary segment or loop segment of the partial path, while, in both cases, $C_i(\lambda_i)$ equals to 0. Therefore, in the complete memory loss assumption, equation(4-18) can be rewritten as $\left\langle \delta\left(\lambda(\mathbf{x}_t) - \lambda_i\right) \right\rangle = \left\langle \delta\left(\lambda(\mathbf{x}_t) - \lambda_i\right) \right\rangle_{\mathrm{A}} / U_i$. A similar model for the complete memory loss assumption can be found in the works of White [44] and Kashchiev [40] for homogeneous nucleation through random attachment and detachment of monomers. Here, the same conclusion is reached, namely that the equilibrium number density of

clusters of size i equals its stationary number density in a nucleation reaction divided by the decaying probability of clusters of size i dissolving to monomers instead of growing into a post-critical cluster.

4.4 Interfacial energy calculation in the VC-SGC ensemble

In the Variance-Constrained Semi-Grand-Canonical (VC-SGC) ensemble, a simulation box with 10×10×10 bcc unit cells, i.e. N=2000 atoms, is used. The free energy derivative $\partial F_C / \partial c$ is evaluated according to equation (3-38) with κN = 10eV per atom , and $\bar{c}$ from -0.1 to 1.1 by interval $\Delta\bar{c}$ =0.005. Here, c refers to the total concentration of Cu atoms in the system. At each $\bar{c}$, the mean concentration of Cu, $\langle c \rangle_V$, is computed by averaging the total concentration of Cu over 20,000 MC sweeps. For illustration, the free energy evaluated by VC-SGC in the bcc Fe-Cu system at 600°C is displayed in Figure 4.6.

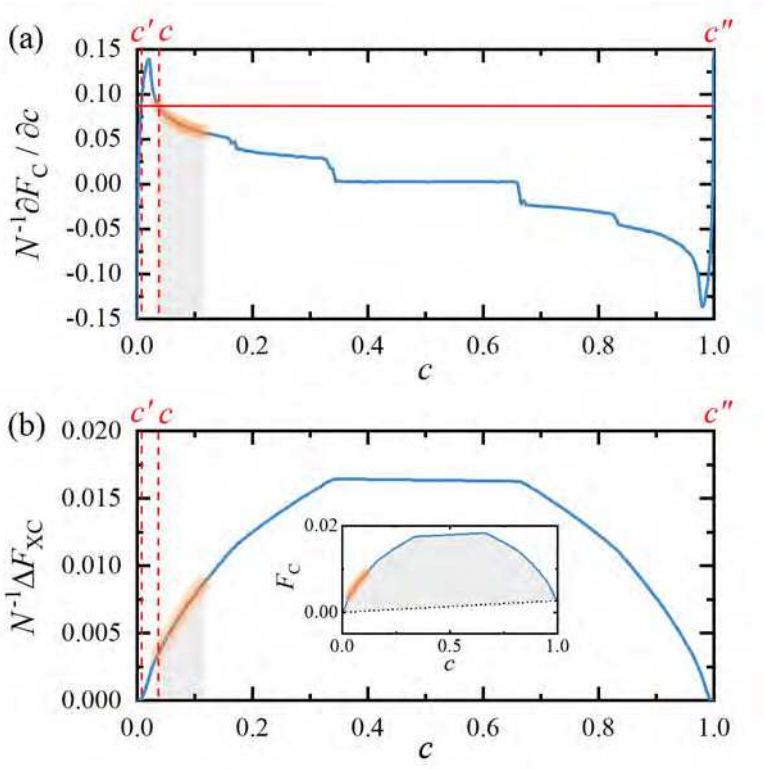

Figure 4.6 The VC-SGC calculated (a) free energy derivative and (b) excess free energy as a function of Cu content in the alloy. The small frame in (b) is the free energy evaluated by integrating the energy derivative plotted in (a) along the c-axis. The yellow shade in every picture indicates the spherical

precipitate region. In (a) and (b), $N^{-1}\partial F_C / \partial c$ and $N^{-1}\Delta F_{XC}$ are measured in eV/atom.

The free energy derivative, $N^{-1}\partial F_C / \partial c$, in the bcc Fe-Cu system at 600°C is plotted in Figure 4.6(a). The curve of $N^{-1}\partial F_C / \partial c$ reveals 5 forms of configurations with co-existing bcc Cu and bcc Fe phases, where the sphere-like Cu precipitation stage is marked by the yellow shadow in Figure 4.6 from around c = 0.03 to 0.13. The other 4 forms of phase separation are Cu cylindered pillar in Fe matrix (c = 0.2 to 0.3), Cu/Fe slabs (c = 0.36 to 0.64), Fe cylindered pillar in Cu matrix (c = 0.7 to 0.8) and sphere-like Fe precipitate in Cu matrix (c = 0.84 to 0.95). The single-phase regions with Cu solution in Fe and Fe solution in Cu appear at c = 0 to 0.02 and c = 0.98 to 1, respectively.

By integrating the energy derivative $\partial F_C / \partial c$ along the concentration variable, one can obtain the canonical free energy F_C as displayed in the small frame of Figure 4.6(b). The bcc Cu-Fe system is slightly asymmetrical, and the solubility limit of Cu in bcc_Fe is around 0.2% at 600°C. The common tangent line for the free energy, F_C, is marked by the dashed line in Figure 4.6(b) The chemical potentials, μ_{Cu} and μ_{Fe}, in the thermodynamic limit can be measured accordingly. As mentioned, the yellow shadow marked area is the Cu precipitation region, where only one spherical Cu precipitate is formed and immersed in the dilute bcc Fe matrix. At a given concentration, c, as shown in Figure 4.6(a), the system decomposes into a Cu precipitate with concentration c" and bcc Fe parent phase with concentration c'. At both, 500 and 600°C, the concentration of Cu precipitate formed in the shadowed area is almost 1, i.e. pure Cu precipitate with c"≈1, and the corresponding excess free energy at c"≈1 is close to 0. In the meantime, the concentration of bcc Fe phase in the sphere-like precipitate region, c', is descending from 0.33% to 0.16% at 500°C and from 0.78% to 0.44% at 600°C (see Figure 4.7), with the total concentration, c , increasing. Since c"≈1 and c">>c', the number of atoms in the Cu precipitate, N", can be approximately calculated as $N'' = (c - c')N$, where N is the total number of atoms in the system. Therefore, the excess free energy from the

curved interface, ΔF_s, can also be expressed as $\Delta F_s(c) = \Delta F_{xc}(c) - (1-c+c')\Delta F_{xc}(c')$, based on equation (3-42).

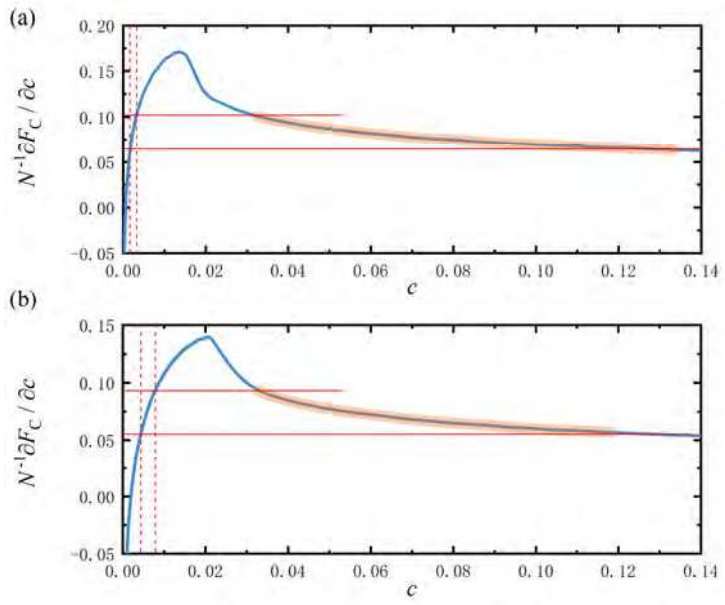

Figure 4.7 The free energy derivative on the Fe-rich side in bcc Fe-Cu system at (a) 500°C and (b) 600°C. The shadow marks the sphere-like precipitate region in each picture, where bcc-Cu nuclei with about 60 to 300 atoms are in equilibrium with α-Fe containing (a) 0.33~0.16%Cu and (b) 0.78~0.44%Cu at 500 and 600°C, respectively. In (a) and (b), $N^{-1}\partial F_C / \partial c$ is measured in eV/atom.

Using the spherical assumption, the surface area in the precipitation stage can be approximately expressed as $S = An^{2/3} = A\left(N(c-c')\right)^{2/3}$. Here, n is the number of atoms in the Cu precipitate, i.e. n=N''. A is the geometry factor of a sphere, $A = (36\pi V_0^2)^{1/3}$, where V_0 as the unit volume of an atom in dilute α-Fe. Therefore, the curved interfacial energy at the sphere-like precipitate region is calculated as $\gamma_{sph} = \dfrac{\Delta F_s(c)}{A\left(N(c-c')\right)^{2/3}}$. γ_{sph} is measured in the shadowed precipitation regions at 500 and 600°C, as shown in Figure 4.7, where Cu precipitates contain about 60 to 300 atoms at both temperatures.

5 Results

In this section, the nucleation kinetics of coherent Cu particles in dilute Fe-Cu alloys is analyzed based on the results from Monte Carlo simulations and enhanced samplings. Firstly, the Local Chemical Environment (LCE) potential is assessed and validated with the thermodynamic database. Then, the nucleation free energy for a single cluster as a function of its size is reconstructed from Umbrella Sampling (US). A fast evaluation of the energy profile by the Reweighted Partial Path (RPP) method with the trajectories from Forward Flux Sampling (FFS) is also demonstrated and compared with the results from US. The nucleation rate of Cu precipitates in the primary stage is calculated from FFS simulations at various temperatures. Additional nucleation quantities, such as the atomic attachment frequency and the Zeldovich factor, are also evaluated and compared with predictions of Classical Nucleation Theory (CNT). The configurations with the largest clusters in critical size are collected from FFS and US to perform the analysis of size, shape and concentration profiles as the major properties of critical clusters. Finally, the α-Fe/Cu interfacial energy in nucleation is evaluated from the nucleation free energy and the Variance-Constrained Semi-Grand-Canonical (VC-SGC) ensemble method.

5.1 Assessment of LCE potential

For a binary system, i.e., the Fe-Cu system in this work, the two independent parameters in the Local Chemical Environment (LCE) potentials are the first neighbor bond energies $\varepsilon_{\mathrm{CuFe}}^{\mathrm{Cu(1)}}$ and $\varepsilon_{\mathrm{CuFe}}^{\mathrm{Fe(1)}}$, which indicate the energy of the Cu-Fe bond in the pure Cu and pure Fe environment, respectively. Considering the dilute solubility limits of Cu in bcc_Fe ($x_{\mathrm{Cu}}^{\mathrm{bcc\_Fe}}$)and Fe in bcc_Cu ($x_{\mathrm{Fe}}^{\mathrm{bcc\_Cu}}$), one can assume that

$$\begin{cases} x_{\mathrm{Cu}}^{\mathrm{bcc\_Fe}} \approx \exp\left(-\Delta E_{\mathrm{Fe}\to\mathrm{Cu}}/k_{\mathrm{B}}T\right) \\ x_{\mathrm{Fe}}^{\mathrm{bcc\_Cu}} \approx \exp\left(-\Delta E_{\mathrm{Cu}\to\mathrm{Fe}}/k_{\mathrm{B}}T\right) \end{cases} \tag{5-1}$$

where $\Delta E_{\mathrm{Fe}\to\mathrm{Cu}}$ ($\Delta E_{\mathrm{Cu}\to\mathrm{Fe}}$) is the energy difference to flip the type of atom to Cu (Fe) in pure bcc iron (cooper). Analogically to the definition of local bond energy in the LCE potential, the two energy differences can be written as

$$\begin{cases} \Delta E_{\mathrm{Fe}\to\mathrm{Cu}} = w_{\mathrm{Cu}}^{\mathrm{bcc\_Fe}}\varepsilon_{\mathrm{CuFe}}^{\mathrm{Cu(1)}} + w_{\mathrm{Fe}}^{\mathrm{bcc\_Fe}}\varepsilon_{\mathrm{CuFe}}^{\mathrm{Fe(1)}} \\ \Delta E_{\mathrm{Cu}\to\mathrm{Fe}} = w_{\mathrm{Cu}}^{\mathrm{bcc\_Cu}}\varepsilon_{\mathrm{CuFe}}^{\mathrm{Cu(1)}} + w_{\mathrm{Fe}}^{\mathrm{bcc\_Cu}}\varepsilon_{\mathrm{CuFe}}^{\mathrm{Fe(1)}} \end{cases} \quad (5\text{-}2)$$

where $w_{\mathrm{Cu(Fe)}}^{\mathrm{bcc\_Fe(bcc\_Cu)}}$ is the average weight of local composition around the Cu(Fe) atom in bcc_Fe(bcc_Cu). In dilute cases, the local chemical environment of Cu in bcc_Fe is reciprocally similar to that of Fe in bcc_Cu. Therefore, it is reasonable to assume that

$$w_{\mathrm{Fe}}^{\mathrm{bcc\_Fe}} \approx w_{\mathrm{Cu}}^{\mathrm{bcc\_Cu}} \text{ and } w_{\mathrm{Cu}}^{\mathrm{bcc\_Fe}} \approx w_{\mathrm{Fe}}^{\mathrm{bcc\_Cu}} \quad (5\text{-}3).$$

Combining equations (5-1), (5-2) and (5-3), one can achieve simple linear dependencies between $\{x_{\mathrm{Cu}}^{\mathrm{bcc\_Fe}}, x_{\mathrm{Fe}}^{\mathrm{bcc\_Cu}}\}$ and $\{\varepsilon_{\mathrm{CuFe}}^{\mathrm{Cu(1)}}, \varepsilon_{\mathrm{CuFe}}^{\mathrm{Fe(1)}}\}$ as

$$\begin{cases} k_{\mathrm{B}}T\left(\ln x_{\mathrm{Cu}}^{\mathrm{bcc\_Fe}} - \ln x_{\mathrm{Fe}}^{\mathrm{bcc\_Cu}}\right) = w'\left(\varepsilon_{\mathrm{CuFe}}^{\mathrm{Cu(1)}} - \varepsilon_{\mathrm{CuFe}}^{\mathrm{Fe(1)}}\right) + O' \\ k_{\mathrm{B}}T\left(\ln x_{\mathrm{Cu}}^{\mathrm{bcc\_Fe}} + \ln x_{\mathrm{Fe}}^{\mathrm{bcc\_Cu}}\right) = w''\left(\varepsilon_{\mathrm{CuFe}}^{\mathrm{Cu(1)}} + \varepsilon_{\mathrm{CuFe}}^{\mathrm{Fe(1)}}\right) + O'' \end{cases} \quad (5\text{-}4)$$

where $w' = w_{\mathrm{Fe}}^{\mathrm{bcc\_Cu}} - w_{\mathrm{Cu}}^{\mathrm{bcc\_Cu}}$ and $w'' = 2\left(w_{\mathrm{Fe}}^{\mathrm{bcc\_Cu}} + w_{\mathrm{Cu}}^{\mathrm{bcc\_Cu}}\right)$. O' and O'' account for the small errors from the dilute assumptions. Different pairs of $\{\varepsilon_{\mathrm{CuFe}}^{\mathrm{Cu(1)}}, \varepsilon_{\mathrm{CuFe}}^{\mathrm{Fe(1)}}\}$ are tried in the slab-diffusion LMC simulations to evaluate the corresponding solubilities $\{x_{\mathrm{Cu}}^{\mathrm{bcc\_Fe}}, x_{\mathrm{Fe}}^{\mathrm{bcc\_Cu}}\}$, and the results are plotted in Figure 5.1. At each temperature, evident linear dependencies are exhibited between $\ln x_{\mathrm{Cu}}^{\mathrm{bcc\_Fe}} - \ln x_{\mathrm{Fe}}^{\mathrm{bcc\_Cu}}$ and $\varepsilon_{\mathrm{CuFe}}^{\mathrm{Cu(1)}} - \varepsilon_{\mathrm{CuFe}}^{\mathrm{Fe(1)}}$, $\ln x_{\mathrm{Cu}}^{\mathrm{bcc\_Fe}} + \ln x_{\mathrm{Fe}}^{\mathrm{bcc\_Cu}}$ and $\varepsilon_{\mathrm{CuFe}}^{\mathrm{Cu(1)}} + \varepsilon_{\mathrm{CuFe}}^{\mathrm{Fe(1)}}$, from which one can achieve good fittings for w', w'', O' and O'' (see Table 5-1).

Based on the fitted parameters in equation (5-4), the values of $\varepsilon_{\mathrm{CuFe}}^{\mathrm{Cu(1)}}$ and $\varepsilon_{\mathrm{CuFe}}^{\mathrm{Fe(1)}}$ are calculated using the real solubility limits $x_{\mathrm{Cu}}^{\mathrm{bcc\_Fe}}$ and $x_{\mathrm{Fe}}^{\mathrm{bcc\_Cu}}$ from CALPHAD assessments. Table 5-2 lists interaction energy of Fe-Cu on the first neighbor shell, $\varepsilon_{\mathrm{CuFe}}^{\mathrm{Cu(1)}}$ and $\varepsilon_{\mathrm{CuFe}}^{\mathrm{Fe(1)}}$, at different temperatures from 450 ~ 700 °C. For validation, these

values are used to evaluate the solubility limits in the slab-diffusion simulations, which give good agreement with the CALPHAD assessments [28,31,32].

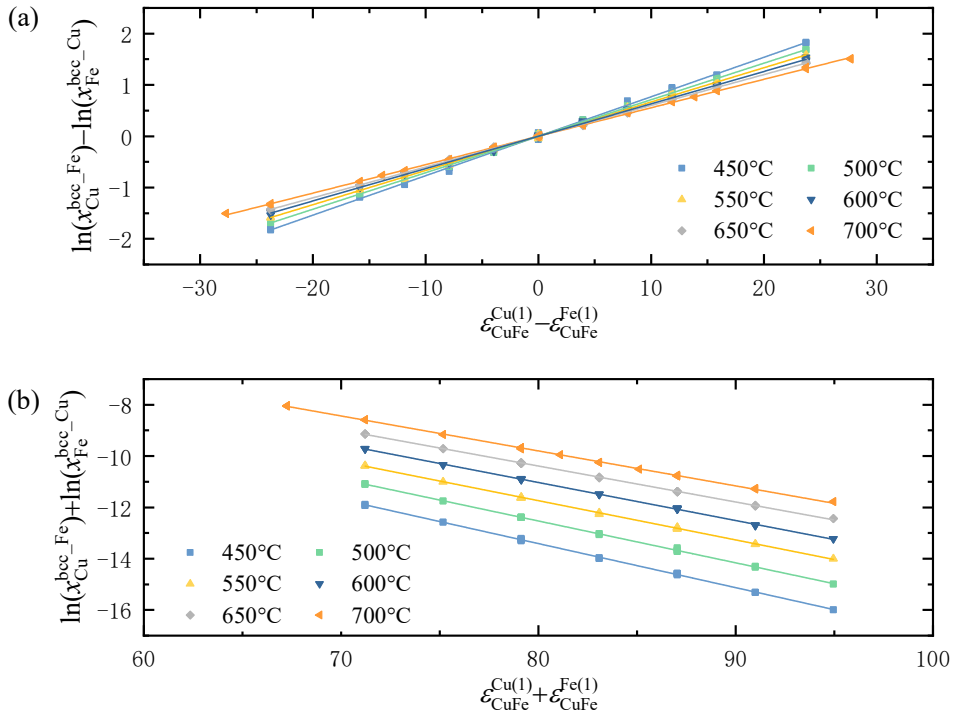

Figure 5.1 In the slab-diffusion test for solubility of Cu in bcc_Fe, linear dependencies are found between (a) $\ln x_{Cu}^{bcc\_Fe} - \ln x_{Fe}^{bcc\_Cu}$ and $\varepsilon_{CuFe}^{Cu(1)} - \varepsilon_{CuFe}^{Fe(1)}$, (b) $\ln x_{Cu}^{bcc\_Fe} + \ln x_{Fe}^{bcc\_Cu}$ and $\varepsilon_{CuFe}^{Cu(1)} + \varepsilon_{CuFe}^{Fe(1)}$. Both $\varepsilon_{CuFe}^{Cu(1)}$ and $\varepsilon_{CuFe}^{Fe(1)}$ are measured in meV.

Table 5-1 The fitted values of w', w'', O' and O'' from the results of slab-diffusion simulations plotted in Figure 5.1.

T/°C	450	500	550	600	650	700
w'/k_BT	0.0769	0.0712	0.0667	0.0631	0.06	0.0554
O'/k_BT	0	0.0002	0	0	0	0
w''/k_BT	-0.1718	-0.1631	-0.153	-0.1482	-0.1403	-0.1363
O''/k_BT	0.3304	0.5181	0.5047	0.8288	0.8321	1.1037

Table 5-2 Values of $\varepsilon_{CuFe}^{Cu(1)}$ and $\varepsilon_{CuFe}^{Fe(1)}$ used in this work and the corresponding solubility limits of Cu in bcc-Fe ($x_{Cu}^{bcc\_Fe}$) and Fe in bcc-Cu ($x_{Fe}^{bcc\_Cu}$) reproduced by the LCE potential in the slab-diffusion LMC simulations [30]. Values of solubility limits from thermodynamic (TD) assessment [28,31,32] are listed for comparison.

T /°C	$\varepsilon_{CuFe}^{Cu(1)}$ /meV	$\varepsilon_{CuFe}^{Fe(1)}$ /meV	LMC		TD-assessment	
			$x_{Cu}^{bcc\_Fe}$ at.%	$x_{Fe}^{bcc\_Cu}$ at.%	$x_{Cu}^{bcc\_Fe}$ at.%	$x_{Fe}^{bcc\_Cu}$ at.%
450	48.8	45.2	0.039	0.033	0.042	0.032
500	47.5	44.8	0.080	0.062	0.077	0.063
550	46.3	44.5	0.126	0.115	0.131	0.116
600	45.1	44.0	0.210	0.198	0.212	0.199
650	44.1	43.6	0.333	0.322	0.329	0.320
700	43.1	43.0	0.494	0.497	0.494	0.490

5.2 Nucleation free energy in Fe-Cu alloys

5.2.1 Evaluations by Umbrella Sampling

The free energy $F(n)$ for cluster formation in an Fe-1%Cu alloy at 600°C (solid curve in Figure 5.2) is calculated by $F(n) = -k_B T \ln \rho(n)$, with $\rho(n)$ obtained using equation (4-5) applied to the Umbrella Sampling results. One can clearly observe a wide and comparably flat free energy barrier with the critical size, corresponding to the top of the barrier at around n=38. The local minimum at n=5 comes from the fact that the free energy $F(n)$ is a function of the *largest cluster* size, and due to the thermal fluctuations in random state, $F(n)$ sharply increases as n approaches 0. The position of the local minimum depends on the degree of supersaturation and the size of the MC simulation box [39]. The brute-force simulation is performed to evaluate the equilibrium number density, $f(n)$, for small clusters. $-\ln f(n)$ is depicted by the dashed curve in Figure 5.2. According to equation (4-6), the CNT-type/single-cluster free energy $\Delta G(n)$ is reconstructed by merging the two curves at the patching point n=10

with the same gradient (illustrated by the dotted line in Figure 5.2). To avoid ambiguity, the term *nucleation free energy* refers to $\Delta G(n)$ in this work.

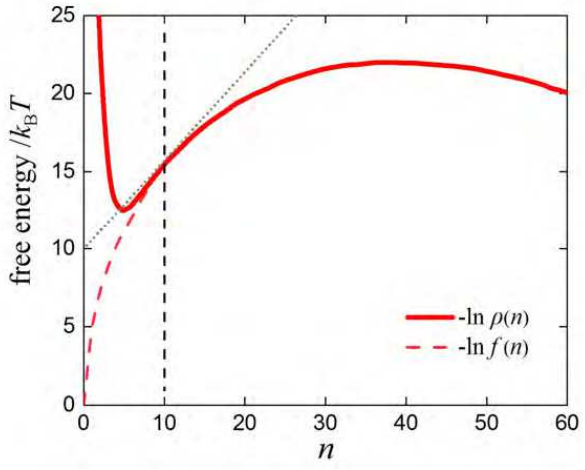

Figure 5.2 Free energy of cluster formation in an Fe-1%Cu alloy at 600°C obtained from Umbrella Sampling (solid curve) and from brute-force simulation (dashed curve). The single-cluster free energy, ΔG, is obtained by patching up the two curves at the point n=10 (indicated by the dashed line) in this case. The dotted line represents the gradient of the free energy at the patching point.

The nucleation free energy is systematically calculated for Fe_1%Cu and Fe_1.5%Cu alloys in the temperature range from 450 to 650 °C. For Fe_1%Cu (Figure 5.3(a)), the critical cluster size n^* increases from around 10 to 38 atoms when the temperature rises from 450 to 600 °C, with the free energy barrier height gradually climbing from 12 to 22 k_BT. In the case of Fe_1.5%Cu (in Figure 5.3(b)) aging in a higher temperature range from 500 to 650 °C, the critical cluster size increases from 10 to 30 atoms with the barrier height rising from 10 to 18 k_BT. A similar prediction follows from first-principles calculation [46], where the critical cluster size is calculated to be 12 with an activation barrier of 0.63 eV (9.5 k_BT) for nucleation in Fe_1.4%Cu alloy at 500°C. In both alloys, the free energy barrier becomes lower, but sharper, when the annealing temperature decreases. The free energy curves are also found to be well fitted in the classical form as $\Delta G(n) = an + bn^{2/3} + c$, where a is the volume contribution, b is the interfacial energy term and c is a normalization constant. Assuming that the clusters are spheres, the precipitate/matrix interfacial energy is evaluated to be approximately 0.28~0.30 J·m^{-2} for dilute Fe-Cu alloys, in accordance with values of 0.27~0.34 J·m^{-2}

obtained from the generalized nearest neighbor broken bond (GBB) model [11] with size correction for small clusters [12].

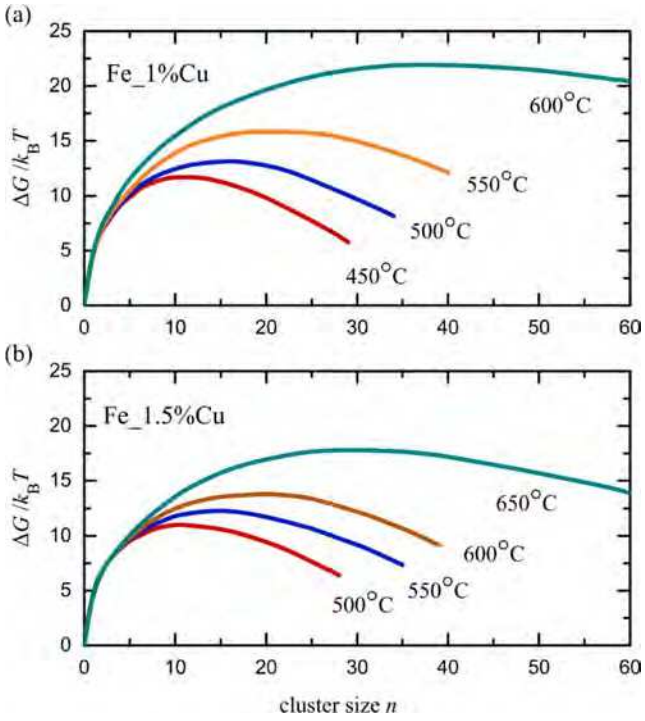

Figure 5.3 Nucleation free energies of Fe-1%Cu (a) and Fe-1.5%Cu (b) alloys between 450 °C and 650 °C obtained with the Umbrella Sampling technique.

5.2.2 Evaluations by the RPP method

For comparison, the nucleation free energy at 600 °C in an Fe-1%Cu alloy is calculated directly from FFS trajectories using the Reweighted Partial Path (RPP) method as developed in the present thesis. The details of the RPP simulation procedure and results are presented in this chapter, the theoretical basis has been described in chapter 4.3.2.

To use the RPP method, one first needs to restore the TIS-style trajectories from the ones obtained by FFS. In the transition of A→B, FFS generates trajectories starting from the boundary of basin A in a ratchet-like manner through interfaces. When a trajectory first reaches interface i at phase point $\mathbf{x}_t$ before returning to A, $\mathbf{x}_t$ is stored as the starting points in the search of trajectories crossing the next interface i+1. It is noted that the trajectory, which successfully reaches the next interface instead of returning to

region A, is not a complete path but will be continued by firing off trajectories at the next interface until finally region A or B is reached. Patching up the fired-off trajectories on every interface from FFS, one can obtain the ensemble with paths exclusively coming from A and ending in A or B, i.e. $\{\mathbf{x}^\tau\}_\mathrm{A}$. The unbiased probability of a path $\mathbf{x}^\tau$ in $\{\mathbf{x}^\tau\}_\mathrm{A}$ can be estimated as [22][47]

$$\mathcal{P}_\mathrm{A}(\mathbf{x}^\tau)=\begin{cases} P\left(\begin{smallmatrix} i \\ 0 \end{smallmatrix}\middle|\begin{smallmatrix} 1 \\ 0 \end{smallmatrix}\right)\Big/N_i & \text{if } \max\left(\lambda(\mathbf{x}^\tau)\right)\in(\lambda_i,\lambda_{i+1}) \\ P\left(\begin{smallmatrix} M \\ 0 \end{smallmatrix}\middle|\begin{smallmatrix} 1 \\ 0 \end{smallmatrix}\right) & \text{if } \max\left(\lambda(\mathbf{x}^\tau)\right)\geq\lambda_M \end{cases} \qquad (5\text{-}5).$$

As to other TIS methods, Rogal *et al.* [43] proposed a reweighting strategy to calculate the path probability in unbiased ensembles, based on the weighting factors from the Weighted Histogram Analysis Method (WHAM) [27] in the procedure of patching up the crossing probabilities of trajectories in every interface ensemble.

After the weighting procedure, the average of effective crossings on each interface can be calculated as $\left\langle \Psi_i^\Theta \right\rangle_\mathrm{A}=\sum \mathcal{P}_\mathrm{A}(\mathbf{x}^\tau)n_i^\Theta(\mathbf{x}^\tau)$, where $n_i^\Theta(\mathbf{x}^\tau)$ describes how many times the trajectory $\mathbf{x}^\tau$ effectively crosses interface *i* with crossing type Θ. According to the memory loss assumption, the one-interface crossing probability is estimated by equation (4-12) from the effective crossing in ensemble $\{\mathbf{x}^\tau\}_\mathrm{A}$. The result is plotted in Figure 5.4. In this work, λ_0 and λ_1 are set to be overlapping. Once a trajectory reaches λ_1 from λ_2, it will end in state A. In this case, $\left\langle \psi_{1,2} \right\rangle_\mathrm{A}=\left\langle \Psi_1^\mp \right\rangle_\mathrm{A}$, therefore $p_1^\mp=1$ and $p_1^\pm=0$ according to equation (4-12). In the meantime, since all the trajectories in $\{\mathbf{x}^\tau\}_\mathrm{A}$ will end when they reach state B, there is no effective crossing of *M*-1 from *M*, i.e. $\left\langle \psi_{M-1,M} \right\rangle_\mathrm{A}=0$. Therefore, the value of one-interface crossing probabilities at *M*-1=13, $p_{13}^\mp$ and p_{13}^+, cannot be evaluated in the FFS calculation for the forward transition.

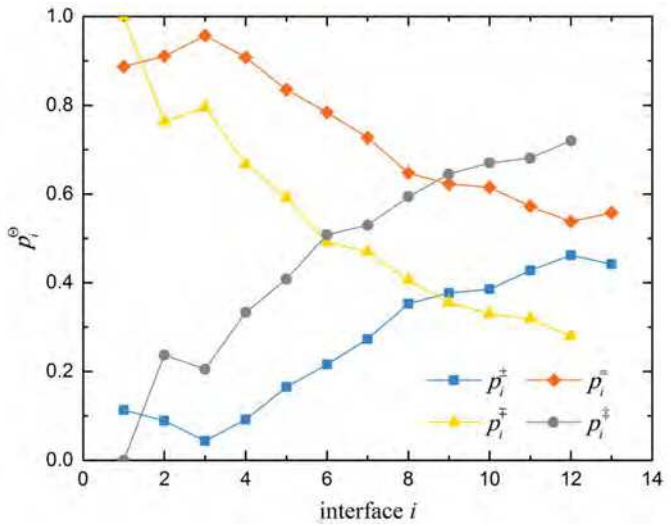

Figure 5.4 One-interface crossing probabilities calculated from the reweighted FFS trajectories for every interface.

The one-interface crossing probability, $p_i^{\ominus}$, is an average probability of the first-time crossing and re-crossing interface i from the adjacent interface. The implicit message of the memory loss assumption is that, when the trajectories presently crossing i do not have the memory in the phase region beyond the adjacent interface, there is no difference between the first crossing and re-crossing probabilities. Based on the memory loss assumption, Moroni et al. [41] derived the connection between the crossing probabilities P_i^+ (P_i^-), where $\mathrm{P}_i^+ = P\binom{i}{0}\middle|\binom{1}{0}$ and $\mathrm{P}_i^- = P\binom{0}{i}\middle|\binom{i-1}{i}$, and one-interface crossing probability $p_i^{\ominus}$ as

$$\mathrm{P}_i^+ \approx \frac{p_{i-1}^{\pm}\mathrm{P}_{i-1}^+}{p_{i-1}^{\pm} + p_{i-1}^{=}\mathrm{P}_{i-1}^-} \quad , \quad \mathrm{P}_i^- \approx \frac{p_{i-1}^{\mp}\mathrm{P}_{i-1}^-}{p_{i-1}^{\pm} + p_{i-1}^{=}\mathrm{P}_{i-1}^-} \qquad (5\text{-}6).$$

Equation (5-6) is an implicit expression of P_i^+ (P_i^-), which requires the information of $p_i^{\ominus}$ and $\mathrm{P}_{i-1}^+(\mathrm{P}_{i-1}^-)$ for every interface and then iteratively solves for the value of the crossing probability from P_1^+ (P_1^-) to P_M^+ (P_M^-). For convenience, equation (5-6) can be rewritten in a separate form for P_i^+ and P_i^- simply as the function of one-interface crossing probability (see Appendix A) as

$$P_i^+ \approx \left(\sum_{m=1}^{i-1} \frac{p_1^{\mp} p_2^{\mp} \cdots p_{m-1}^{\mp} p_m^{=}}{p_1^{\pm} p_2^{\pm} \cdots p_m^{\pm}} \right)^{-1}, \qquad P_i^- \approx \left(\sum_{m=1}^{i-1} \frac{p_1^{\mp} p_2^{\mp} \cdots p_{m-1}^{\mp} p_m^{=}}{p_1^{\pm} p_2^{\pm} \cdots p_m^{\pm}} \right)^{-1} \prod_{j=1}^{i-1} \frac{p_j^{\mp}}{p_j^{\pm}} \qquad (5\text{-}7).$$

Equations (5-6) and (5-7) are the expressions for the crossing probability under the condition that the memory-loss assumption is valid in the system. Therefore, one can do a quick check for the memory loss assumption in the target system by comparing the result of crossing probability, P_i^+, from the FFS calculation and equations (5-6) and (5-7). Figure 5.5 plots the crossing probabilities, P_i^+ and P_i^-, evaluated from the one-interface crossing probability by equation (5-7), compared with the crossing probability, P_i^+, measured in the FFS calculation (red squares in Figure 5.5). The good agreement indicates that the one-interface crossing probability is approximately the same in the first crossing and re-crossing of each interface, which is an evidence for long-range memory loss. If a large discrepancy were observed in the predictions for P_i^+ by FFS and equation (5-7), the system would apparently not be memoryless and the RPP method would produce an incorrect equilibrium distribution of states on the chosen order parameter.

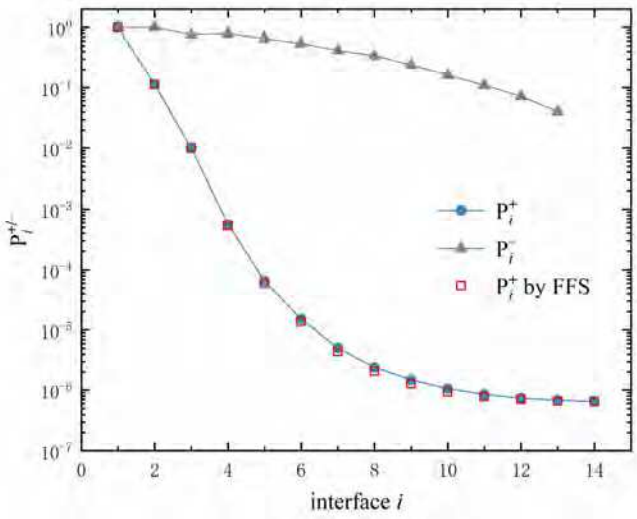

Figure 5.5 Crossing probability calculated from one-interface crossing probabilities by equation (5-7), compared with the crossing probability from the FFS algorithm

The average distribution of λ in the partial path, $P_i^{\Theta}(\lambda)$, and the loop of the partial path, $L_i^{\Theta}(\lambda)$, is calculated at the same time with the effective crossing. Once the

phase point $\mathbf{x}_t$ of an effective crossing is located on a trajectory, the histograms of λ, $\rho_i^{\Theta}(\mathbf{x}_t,\lambda)$ and $l_i^{\Theta}(\mathbf{x}_t,\lambda)$, can be determined by tracing along the trajectory from $\mathbf{x}_t$ forwardly and backwardly until the trajectory reaches the adjacent interface. The average density of λ in the partial path and the loop is calculated by $P_i^{\Theta}(\lambda)=\frac{\sum \boldsymbol{\mathcal{P}}_{\mathrm{A}}(\mathbf{x}^{\tau})\rho_i^{\Theta}(\mathbf{x}_t,\lambda)}{\left\langle \Psi_i^{\Theta}\right\rangle_{\mathrm{A}}}$ and $L_i^{\Theta}(\lambda)=\frac{\sum \boldsymbol{\mathcal{P}}_{\mathrm{A}}(\mathbf{x}^{\tau})l_i^{\Theta}(\mathbf{x}_t,\lambda)}{\left\langle \Psi_i^{\Theta}\right\rangle_{\mathrm{A}}}$. Since no trajectories cross λ_{M-1} from λ_M in $\{\mathbf{x}^{\tau}\}_{\mathrm{A}}$, $P_{M-1}^{\mp}(\lambda)$ and $L_{M-1}^{\mp}(\lambda)$ are unknown for $\lambda\in[\lambda_{M-2},\lambda_M]$. Therefore, according to equation (4-18), the equilibrium distribution of the order parameter, $\left\langle \delta(\mathbf{x})-\lambda\right\rangle$, is only derived for $\lambda\in[\lambda_0,\lambda_{M-2}]$ in the RPP method. The free energy, $F(\lambda)$, is evaluated from the equilibrium distribution by $F(\lambda)=-k_BT\ln\left\langle \delta(\mathbf{x})-\lambda\right\rangle+c$, where c is a constant from normalization.

The free energy calculated by RPP from FFS trajectories is plotted on Figure 5.6 by the red circles, compared with the results of standard Umbrella Sampling (US) [27] shown as blue solid line.

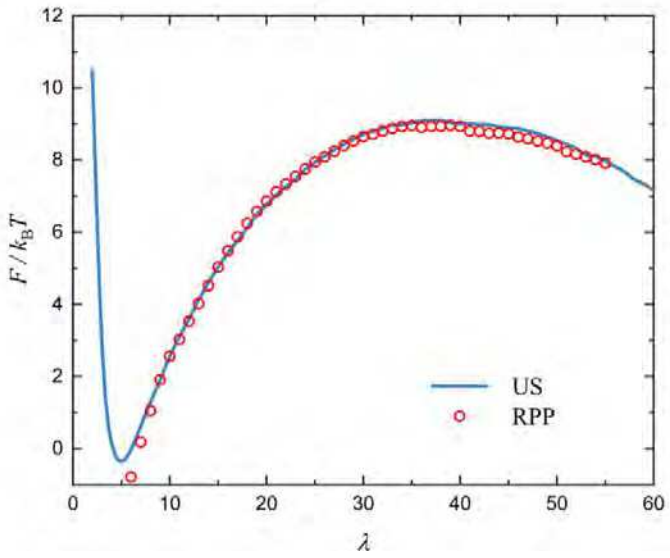

Figure 5.6 Free energy of nucleation as a function of largest cluster size calculated by the Reweighted Partial Path (RPP) method (red circles) compared with the one from Umbrella Sampling (US).

In the transition phase region, $\lambda\in[8, 55]$, the RPP method gives a very close prediction of free energy compared with US. A broad and high activation barrier is

provided by both methods with the highest point showing around $\lambda = 35$. Since the FFS algorithm only collects those trajectories visiting the transition region, the trajectories that linger in the stable region are not included for the estimation of the equilibrium distribution in the RPP method. This is the reason for the discrepancy between the RRP and US results in the area close to region A. To correct the discrepancy, one can evaluate the distribution of λ from brute-force simulations around region A, and then patch up the free energy with the predictions from the RPP method.

5.3 FFS trajectories and nucleation rates

5.3.1 Nucleation rates from FFS calculations

The nucleation trajectories in Fe_1%Cu and Fe_1.5%Cu alloys at 450 to 650 °C are generated using MC dynamics and harvested by Forward Flux Sampling (FFS) [21]. The conditional crossing probability $P(\lambda_i|\lambda_0)$ on every interface λ_i is plotted in Figure 5.7 (Fe_1%Cu) and Figure 5.8 (Fe_1.5%Cu). In all FFS simulations, the boundary of the metastable state λ_0, i.e., the largest cluster size appearing in the random metastable state, is set to be equal to λ_1, therefore, $P(\lambda_1|\lambda_0)=1$. According to the definition, $P(\lambda_i|\lambda_0)$ represents the conditional probability of the largest cluster to grow from size λ_0 into a cluster with size over λ_i before dissolving to $n<\lambda_0$. This probability is always decreasing as λ_i approaches the boundary of stable state, λ_m, but finally converges to $P(\lambda_m|\lambda_0)$. The convergence is a natural result from the fact that larger clusters are more likely to grow instead of shrinking. As a cluster reaches size λ_m, the chance for the cluster to dissolve is nearly 0, therefore, one can consider the cluster as stabilized. Taking the example of nucleation in Fe-1%Cu at 600 °C, as illustrated in Figure 5.9, the conditional crossing probability $P(\lambda|\lambda_i)$ for $\lambda\in[\lambda_{i+1}, \lambda_i]$ indicates the probability of a cluster with size λ_i to grow to λ before decaying to λ_0. As λ_i getting close to λ_m, $P(\lambda|\lambda_i)$ is approaching to 1. At $i=13$, $P(\lambda_{i+1}|\lambda_i)\approx1$, indicating that the largest cluster is stabilized as its size reaches size $\lambda_{14}=65$.

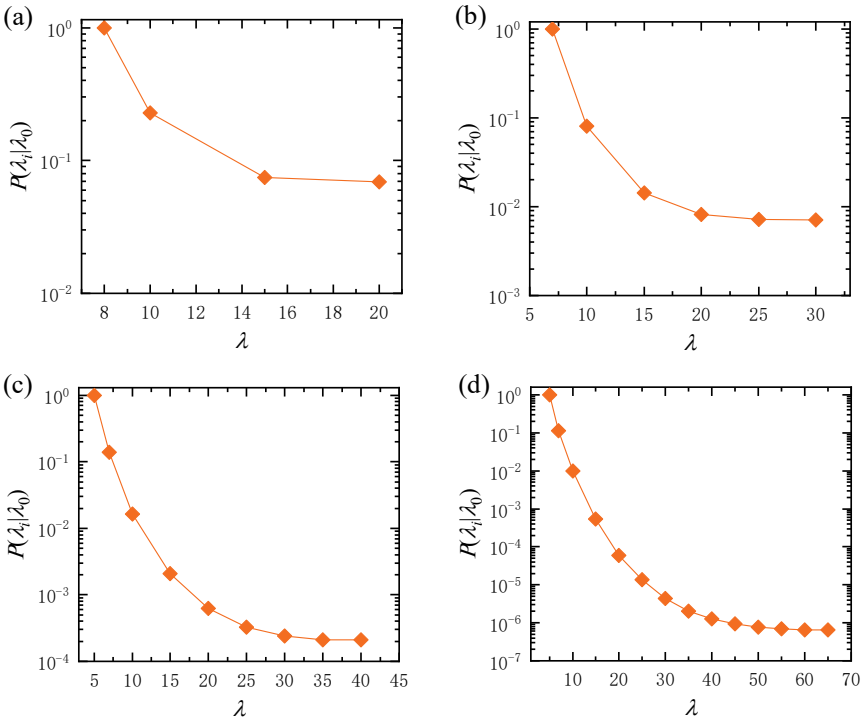

Figure 5.7 The conditional crossing probability $P(\lambda_i|\lambda_0)$ observed in FFS for Fe-1%Cu alloy at (a) 450 °C, (b) 500 °C, (c) 550 °C and (d) 600 °C.

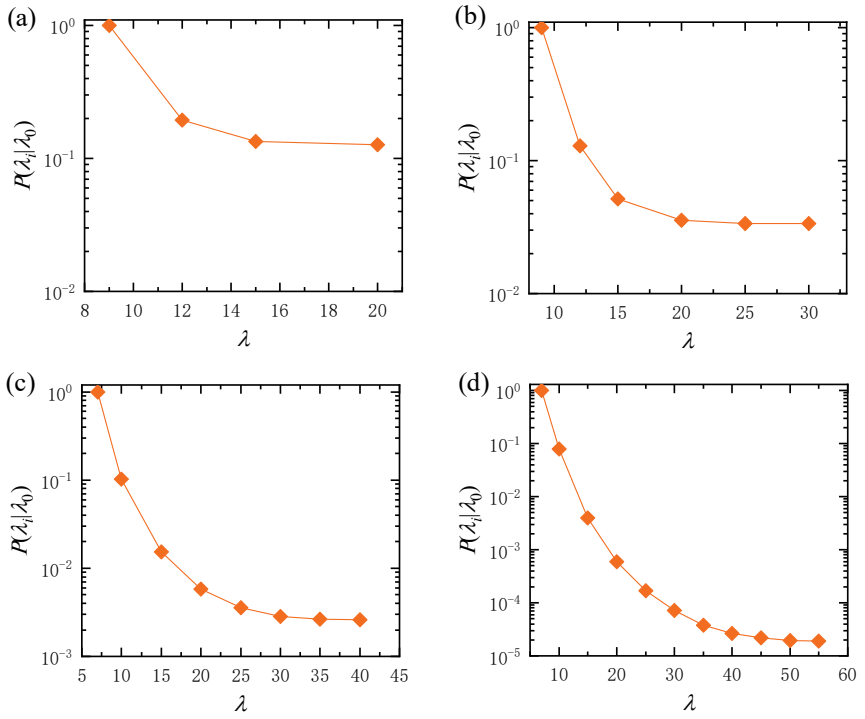

Figure 5.8 The conditional crossing probability $P(\lambda_i|\lambda_0)$ observed in FFS for Fe-1.5%Cu alloy at (a) 500 °C, (b) 550 °C, (c) 600 °C and (d) 650 °C.

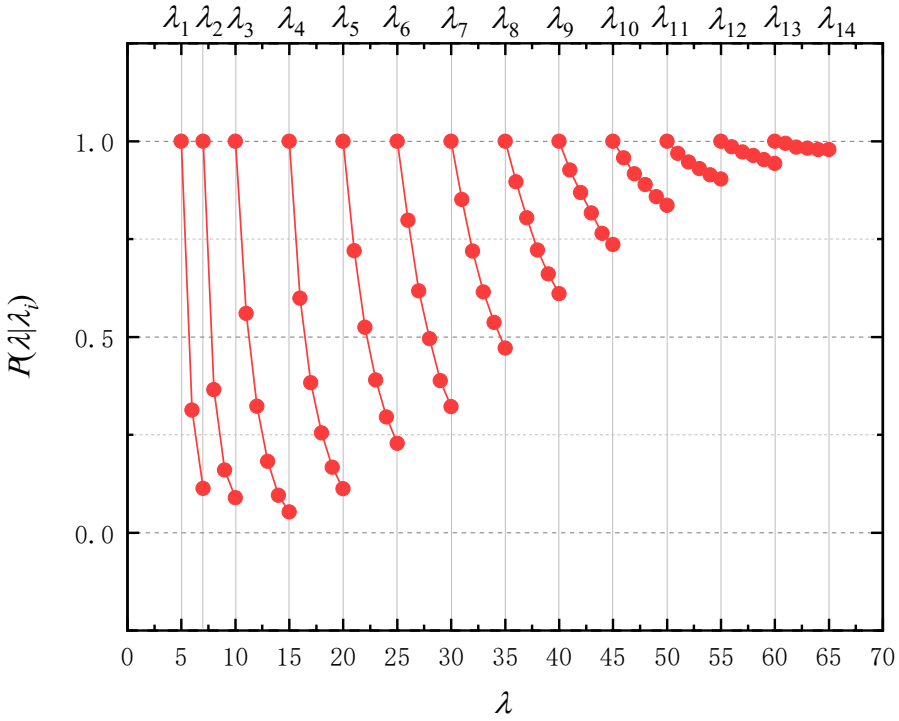

Figure 5.9 The crossing probability of $P(\lambda|\lambda_i)$ for $\lambda \in [\lambda_i, \lambda_{i+1}]$ from FFS sampling of nucleation in Fe_1%Cu alloy at 600 °C. The interfaces λ_i with i=1~14 are marked by the vertical grey lines.

Here, λ_m and $P(\lambda_m|\lambda_0)$ are closely connected to the supersaturated state. At high supersaturation, λ_m is comparably smaller and $P(\lambda_m|\lambda_0)$ is significantly higher than in under low supersaturation circumstances (see Table 5-3). For example, a cluster with size over 20 atoms can be considered as stable in Fe-1%Cu alloy at 450 °C, whereas the cluster with 40 atoms still has significant probability for dissolving in the same alloy at 600 °C. The initial flux $\Phi_{A,0}$ is mainly dependent on the atomic diffusivity, which is dramatically boosted as temperature increases (see Table 5-3).

Table 5-3 The settings of the first interface λ_0 and the last interface λ_m in FFS samplings, along with the values of initial flux $\Phi_{A,0}$, conditional crossing probability $P(\lambda_m|\lambda_0)$ and the reaction rate constant k_{AB}.

	T / °C	λ_0	λ_m	$\Phi_{A,0}$ / s^{-1}	$P(\lambda_m\|\lambda_0)$	k_{AB} / s^{-1}
X_{Cu}=1.0%	450	8	20	$3.02\cdot10^{-5}$	$6.93\cdot10^{-2}$	$2.10\cdot10^{-6}$
	500	7	30	$1.21\cdot10^{-3}$	$7.08\cdot10^{-3}$	$8.56\cdot10^{-6}$
	550	5	40	$5.07\cdot10^{-2}$	$2.09\cdot10^{-4}$	$1.06\cdot10^{-5}$
	600	5	65	0.53	$6.44\cdot10^{-7}$	$3.42\cdot10^{-7}$
X_{Cu}=1.5%	500	9	20	$1.32\cdot10^{-3}$	0.13	$1.68\cdot10^{-4}$

550	9	30	$2.80 \cdot 10^{-2}$	$3.35 \cdot 10^{-2}$	$9.40 \cdot 10^{-4}$
600	7	40	0.85	$2.60 \cdot 10^{-3}$	$2.20 \cdot 10^{-3}$
650	7	55	7.84	$1.88 \cdot 10^{-5}$	$1.48 \cdot 10^{-4}$

Nucleation rates calculated from equations (3-30) and (4-4) are plotted in Figure 5.10 as solid lines. The nucleation rates of Cu precipitates between 450°C to 650°C are in the range of 10^{17}~ 10^{20} $m^{-3}s^{-1}$ in the Fe-1%Cu alloy and 10^{20}~ 10^{22} $m^{-3}s^{-1}$ in the Fe-1.5%Cu alloy. For both alloys, nucleation rates do not significantly increase at higher supersaturation and decreasing temperature, but rather decline by one order of magnitude due to the increasingly sluggish diffusion of substitutional elements. The maximum nucleation rates are observed at around 550°C in Fe-1%Cu and around 600°C in Fe-1.5%Cu, in good agreement with the isothermal time-temperature-precipitation (TTP) diagram reported by Perez et.al [48], where the fastest nucleation is observed at 600 ~ 650°C in Fe_1.2%Cu. It is worth noting that the nucleation rate obtained from FFS corresponds to the steady state nucleation rate defined in CNT, thus, transient nucleation effects, which are manifested in the incubation time [49], are not taken into account in this work.

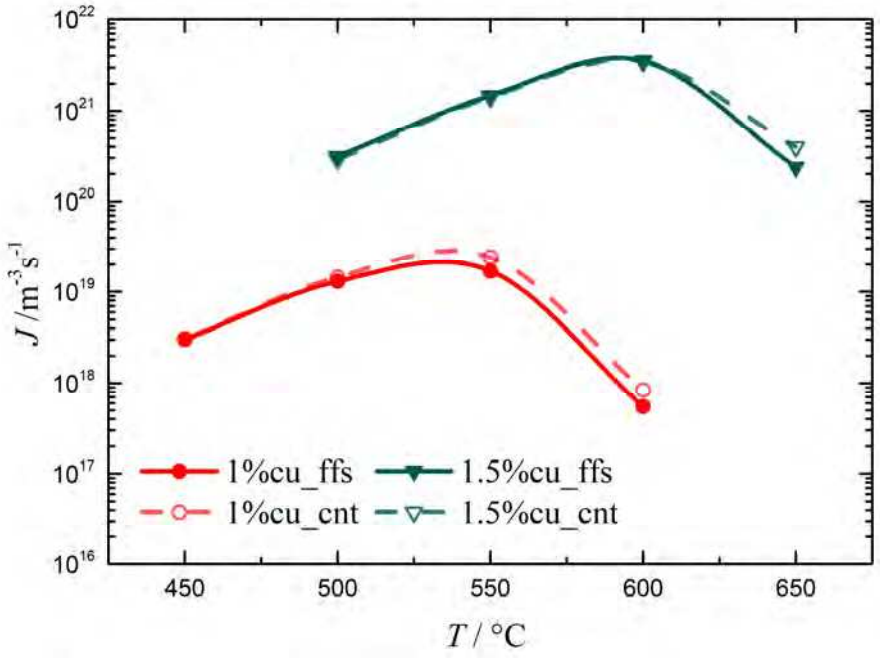

Figure 5.10 Nucleation rates obtained by FFS (full markers) and CNT (open markers) for Fe-1%Cu and Fe-1.5%Cu at temperatures between 450°C and 650°C. The trend lines are the Bézier curves generated

from each group of data points.

Unfortunately, there is not much quantitative information on nucleation rates available for the present Fe-Cu system, neither from atomistic simulations nor from experimental work. On one hand, experimental measurements for nucleation rates require accurate detection of the Cu particles (radius smaller than 0.5 nm) formed in the earliest stages of precipitation, which is almost impossible with present experimental techniques. On the other hand, the steady-state nucleation stage is inherently difficult to be observed in conventional atomistic simulations, especially under high-supersaturated conditions. In the work carried out by Soisson and Martin [50], with an estimated critical cluster size derived from the steady-state cluster distribution, the nucleation rates for Fe-Cu alloys are only reported for rather high temperatures (1000K~1500K) calculated from brute-force Monte Carlo simulations.

In continuum precipitation models, the nucleation rate is a pre-determined parameter controlling the evolution of the number density of precipitates during the process until coarsening of clusters begins. In the work of Stechauner and Kozeschnik [51], simulations of Cu-precipitation in ferrite are carried out using the KWN model [52,53] (implemented in the software package MatCalc [31]), with the nucleation rates of Cu precipitates calculated in a CNT framework at every time interval during the simulation. In their work, the steady nucleation rates at the primary stage are found to be in the order of 10^{20}~ 10^{23} $m^{-3}s^{-1}$ in the Fe-1.4%Cu alloy [**]at 450 to 650°C, with the highest value, around 8×10^{22} $m^{-3}s^{-1}$, occurring between 600 ~ 650°C. Guo *et.al.* [54], using a similar model in the study of precipitation kinetics in an Fe-Cu-X ternary alloys, report values of 1.1×10^{21} $m^{-3}s^{-1}$ for the nucleation rate of Cu-rich particles at 800K [54].

[**] the data was not published, but reproduced with the same MatCalc script from ref. [51]

5.3.2 Comparison with brute-force MC simulations

The evaluation of nucleation rates from brute-force MC simulations is based on the connection between the time-dependent nucleation rate $J_{n,t}$ and the number density of clusters as [49,55]

$$J_{n,t} = N_{n,t}k_n^+ - N_{n+1,t}k_{n+1}^- = \frac{\partial N_t(>n)}{\partial t} \qquad (5\text{-}8).$$

At a given time t, $N_{n,t}$ denotes the number density of clusters containing n atoms, and $N_t(>n)$ denotes the number density of clusters with more than n atoms. $k_n^{+/-}$ is the transition frequency for clusters with n atoms to attach (+) / detach (-) a monomer, which is assumed to be a time-independent value during nucleation. $J_{n,t}$ is variant with time in the beginning of nucleation. After a short period (incubation time), the steady size distribution will be established, i.e. $\partial N_{n,t}/\partial t = 0$, such that $J_{n,t}$ becomes a constant value and $N_t(>n)$ starts to linearly increase in time with a rate of $J_{n,t}$. The constant $J_{n,t}$, known as the steady-state nucleation rate, is the nucleation rate evaluated in FFS by equation (4-4). Here, the steady-state nucleation rate is denoted as J_s.

To validate the FFS methods, brute-force Monte Carlo simulations are performed to analyze the steady-state nucleation rate of Cu clusters in Fe-1%Cu alloy at 500°C. The same LCE potential and diffusion coefficients are used as that in FFS calculation, but the size of the MC sample is increased to 100×100×100 unit cells (28.5×28.5×28.5 nm^3) to ensure sufficient statistics to evaluate the time derivative of $N_t(>n)$. The system is first equilibrated at 1200°C and then quenched to 500°C. The measurement of $N_t(>n)$ begins right after the quenching. The threshold value n in the number density of clusters $N_t(>n)$ is set as the critical clusters size with n=15. In fact, the choice of threshold value n does not affect the value of the nucleation rate when steady-state condition is established [49]. The values of n in a range of 10~50 atoms give similar estimations for J_s in this case.

The brute-force simulation is repeated for 100 times to gain an accurate estimation of $N_t(>15)$ in Fe-1%Cu alloy at 500°C. The averaged $N_t(>15)$ at each time t is displayed in Figure 5.11 along with its Mean Square Root Deviation (MSRD) illustrated as error

bars. According to Figure 5.11(a), the linearly increasing region of N_t(>15) starts within a short period of time after quenching. The averaged steady-state nucleation rate is around 1.68×10^{19} $m^{-3}\cdot s^{-1}$ with a deviation of $\pm0.30\times10^{19}$ $m^{-3}\cdot s^{-1}$ indicated by the dotted lines. Compared with the nucleation rate from FFS, 1.41×10^{19} $m^{-3}\cdot s^{-1}$, the evaluation from brute-force MC is slightly higher. This is because brute-force simulations utilize a larger MC sample, which could have more concentration fluctuations in local area and result in a slightly higher J_s compared to the one evaluated in a smaller sample in FFS.

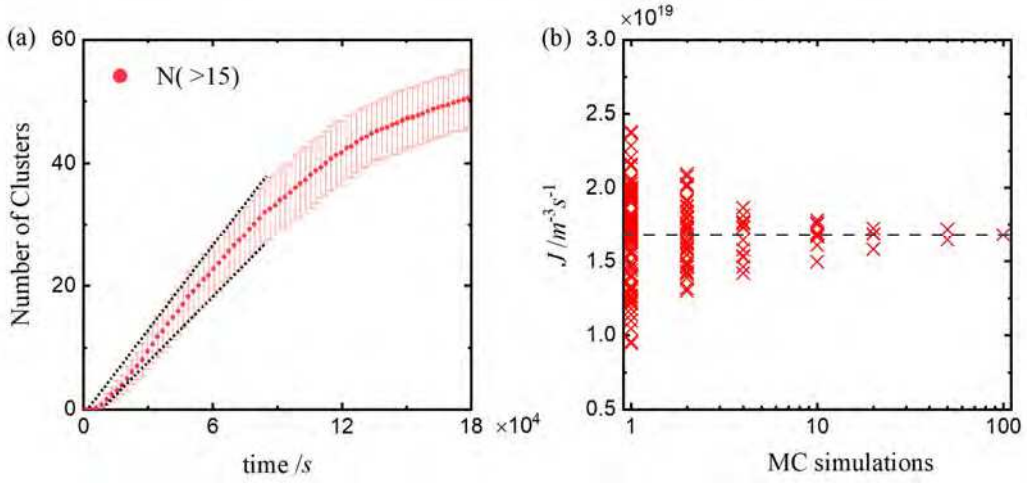

Figure 5.11 (a) The number of clusters with size larger than 15, N_t(>15) , as a function of time evaluated by averaging over 100 brute-force simulations in Fe-1%Cu alloy at 500°C. The error bars illustrate the root mean square error. The steady-state nucleation rate evaluated from the linearly increasing region is around 1.68×10^{19} $m^{-3}\cdot s^{-1}$ with a deviation of $\pm0.3\times10^{19}$ $m^{-3}\cdot s^{-1}$ indicated by the dotted lines. (b) The steady-state nucleation rate in Fe-1%Cu alloy at 500°C evaluated by N_t(>15) averaging over 1 to 100 brute-force simulations.

To test the sensitivity of estimations of J_s on the number of repeated simulations, J_s from N_t(>15) in each individual brute-force simulation is calculated as well as the average over multiple simulations (see Figure 5.11(b)). The steady-state nucleation rate evaluated by one simulation diverges from 0.9×10^{19} $m^{-3}\cdot s^{-1}$ to 2.4×10^{19} $m^{-3}\cdot s^{-1}$, and as averaging over more repeated simulations, the deviation of J becomes smaller and converges around 1.68×10^{19} $m^{-3}\cdot s^{-1}$ with 100 repeated simulation. According to Figure 5.11(b), an averaged N_t(>15) from over 20 repeated simulations in an MC sample of

100×100×100 unit bcc cell gives a reasonable estimation of the nucleation rate in the Fe-1%Cu alloy at 500°C.

Generally, to reduce the stochastic error in evaluation of nucleation rates, the brute-force method needs to either enlarge the MC sampling size or increase the repeated times of simulations. Compared with the brute-force method, FFS has much higher efficiency for the computation of reaction rate coefficient, especially in the cases with high transition barriers [56]. In this work, FFS harvests about 600 successful nucleation trajectories for calculation of J_s in Fe-1%Cu alloy at 500°C, and the total CPU time is about 50 hours on a single core. Supposing that one stable post-critical cluster formed in brute-force simulation stands for one successful nucleation trajectory, one needs to repeat the simulation for 20 times to harvest 600 trajectories, and the corresponding CPU time is about 80 hours on a single core. For a low supersaturated case, such as in Fe-1%Cu alloy at 600°C, FFS spends 680 hours on a single core to harvest 600 successful trajectories, while using the brute-force method, one may not be able to observe nucleation in a feasible CPU time at all. Theoretically, the CPU time for brute-force simulation exponentially increases with the height of the transition barrier [56], based on the CPU time for Fe-1%Cu alloy at 500°C, the brute-force method is estimated to spend 650000 hours on a single core to harvest 600 successful nucleation trajectories.

5.4 Comparison with CNT

In Classical Nucleation Theory (CNT), the nucleation rate is expressed as [57][58] $J = NZ\upsilon^* \exp\left[-\frac{\Delta G(n^*)}{k_B T}\right]$, where N is the number of potential nucleation sites, Z is the Zeldovich factor, υ^* is the atomic attachment rate, n is the number of atoms in the cluster and $\Delta G(n^*)$ is the free energy barrier at the critical cluster size n^*. The Zeldovich factor, Z, is related to the curvature of the free energy barrier at the critical size,

$Z = \sqrt{-\frac{\Delta G^{''}(n^*)}{2\pi k_B T}}$. Here, $\Delta G^{''}(n^*)$, n^* and Z can be directly evaluated from the free energy curve $\Delta G(n)$ as obtained in the previous sections.

In classical theory, the nucleation free energy $\Delta G(n)$ is expressed as

$$\Delta G(n) = \Delta G_{\text{nucl}}\, n + \sigma n^{2/3} \tag{5-9}$$

where ΔG_{nucl} is the volume energy contribution, also known as the chemical driving force. σ is the interfacial energy term, given by the product of a geometry factor A and the specific interfacial energy γ, i.e. $\sigma = A\gamma$. The nucleation free energy evaluated in US fits very well in this classical form, and the corresponding values of ΔG_{nucl} and σ obtained from the fitting are listed in Table 5-4.

Based on the regular solution model for binary systems, the nucleation driving force in a supersaturated solid solution can be expressed as[57]

$$\Delta G_{\text{nucl}} = (1-y^{\text{e}})k_B T \ln\left(\frac{1-x^{\text{e}}}{1-x^0}\right) + y^{\text{e}} k_B T \ln\left(\frac{x^{\text{e}}}{x^0}\right) + \omega(x^0 - x^{\text{e}}) \tag{5-10}$$

where x^{e} and y^{e} is the equilibrated concentration of solute element in matrix phase and precipitation phase at temperature T, respectively. ω is the interaction parameter for a binary A-B system given by $\omega = z_{\text{L}}(\varepsilon_{\text{AA}} + \varepsilon_{\text{BB}} - 2\varepsilon_{\text{AB}})/2$, where ε_{ij} is the bond energy and z_{L} is the number of nearest neighbors (coordination number). x^0 is the concentration of solute element in the matrix during nucleation, where a maximum value of ΔG_{nucl} is provided. In a dilute solution, the concentration of solute solution $x^{\text{s}} << 1$, $x^0 \approx x^{\text{s}}$. When $x^{\text{e}} << 1$, equation (5-10) can be approximately rewritten as

$$\Delta G_{\text{nucl}} = -y^{\text{e}} k_B T \ln S \tag{5-11}$$

where S is the degree of supersaturation given as $S = x^{\text{s}}/x^{\text{e}}$. Here, x^{s} is the initial Cu concentration in the alloy and x^{e} is the equilibrium Cu solubility at temperature T.

Fig.6 displays the relation of driving force, ΔG_{nucl}, and supersaturation, S, for nucleation in Fe-1%Cu and Fe-1.5%Cu alloys at 450 to 650 °C. According to Table 5-2, the equilibrium bcc_Cu phase is almost pure Cu at temperature from 450 to 650 °C, i.e. $y^{\text{e}}=1$, therefore, the relation of ΔG_{nucl} and S suggested by eq.(11) is $\Delta G_{\text{nucl}} = -k_B T \ln S$ (illustrated by the solid line in Figure 5.12). However, this tendency is not obeyed and

a non-linear relation is displayed between ΔG_{nucl} and ln$S$. At high supersaturation, the nucleation driving force is much weaker than the one predicted by equation (5-11). With ln$S$ decreasing, the discrepancy is getting smaller and ΔG_{nucl} starts approaching to the value of $-k_B T \ln S$. Equation (5-11) is derived with the assumption that the clusters formed during nucleation inherit the properties of the equilibrium precipitation phase. The trend line of ΔG_{nucl} in Figure 5.12 indicates that the Cu clusters formed during nucleation are all in metastable state and energetically unfavorable compared to the equilibrium precipitation phase.

Table 5-4 The driving force ΔG_{nucl} and interfacial energy term σ evaluated by fitting the nucleation free energy from US to classical form. S is the supersaturated degree.

	T / °C	ln$S$	$\Delta G_{nucl}/k_B T$ per Atom	$\sigma/k_B T$ per Atom$^{2/3}$
X_{Cu}=1.0	450	3.23	-2.05	6.91
	500	2.52	-1.75	6.45
	550	2.07	-1.49	6.19
	600	1.56	-1.13	5.74
X_{Cu}=1.5	500	2.93	-1.91	6.48
	550	2.48	-1.68	6.16
	600	1.96	-1.48	5.89
	650	1.51	-1.15	5.42

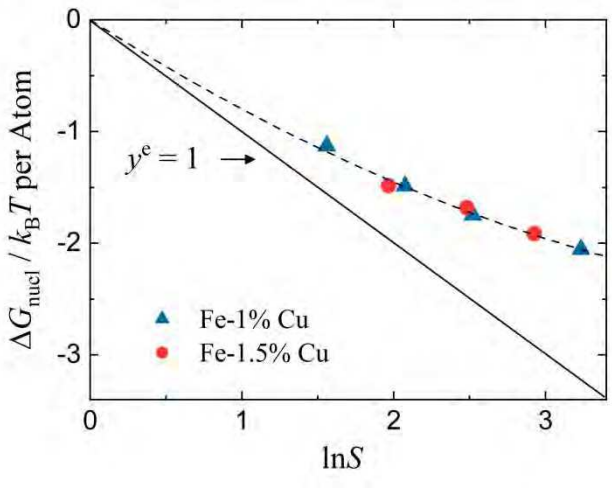

Figure 5.12 The nucleation driving force, ΔG_{nucl}, as a function of ln$S$. The solid line illustrates the

equation $\Delta G_{nucl} = -y^e k_B T \ln S$, with the Cu concentration in precipitates y^e =1. The dashed line marks the trend of ΔG_{nucl} considering that ΔG_{nucl} will vanish in the case without supersaturation.

The interfacial energy, σ, does not show evident connection with the degree of supersaturation (see Table 5-4) At different temperatures, the value of σ slightly changes in a range between 4.9~5.2×10^{-4} J·mol$^{-2/3}$. The geometry factor, A, is a unit transfer as $A=a/n^{2/3}$, where a is the matrix/precipitate interfacial area and n is the number of atoms in the precipitate. Supposing the precipitates are spheres and V_m is the effective volume of an atom, the geometry factor is calculated as $A=(4\pi)^{1/3}(3V_m)^{2/3}$. When using this spherical approximation, the specific interfacial energy, γ, is estimated to be in a range of 0.28~0.30 J·m^{-2} during Cu nucleation in dilute Fe-Cu alloys at 450~600°C. However, this is only a rough estimation, since the shape of Cu clusters during nucleation is much more complex than simple spheres and the geometry factor needs to be carefully evaluated in this case.

The atomic attachment rate, υ^*, describing the frequency at which monomers are attaching to a critical cluster during nucleation [8], is evaluated from FFS trajectories by

$$\upsilon^* = \frac{P\left\{n(t+\Delta t) > n(t) \middle| n(t) = n^*\right\}}{\Delta t} \tag{5-12}$$

where $P\left\{n(t+\Delta t) > n(t) \middle| n(t) = n^*\right\}$ is the mean probability for a cluster at n^* to absorb one atom at the next time slice in each trajectory and Δt is the average time interval that the system resides between adjacent slices. Since the attachment and detachment frequencies approximately have the same value on the top of the energy barrier, the critical attachment rate can be also determined from the mean square displacement of cluster size [59] in a short time Δt, as $\upsilon^* = \frac{1}{2\Delta t}\left\langle \left(n(t+\Delta t) - n(t)\right)^2 \right\rangle_{n(t)=n^*}$.

In Figure 5.13, the values of υ^* from FFS trajectories (equation (5-12)) are compared to the values obtained from CNT (equation (3-10)). Evidently, good agreement is achieved. In FFS, Cu nuclei are observed to change their size mainly by attachment or detachment of monomers in dilute alloys, while the contribution from

small clusters (e.g. dimers or triplets) is rarely detected during nucleation. This phenomenon is in agreement with the classical description for atomic attachment expressed by equation (3-10). However, small systematic deviations are observed particularly at lower temperatures. This effect can probably be attributed to the non-spherical shape of very small critical clusters, which one can observe in the analysis of the critical nucleus shape. Figure 5.17 shows some snapshots of small clusters with less than 30 atoms observed in FFS. In order to characterize the geometry of nuclei, the clusters are fitted to ideal ellipsoids and an anisotropy factor, ξ, is defined as the ratio between the longest and shortest radius of the ellipsoid (ξ =1 for a sphere). In this work, the critical clusters in the size between 10 ~ 30 atoms are commonly observed in a non-spherical shape with average anisotropy factors ranging from 2.0 to 3.5.

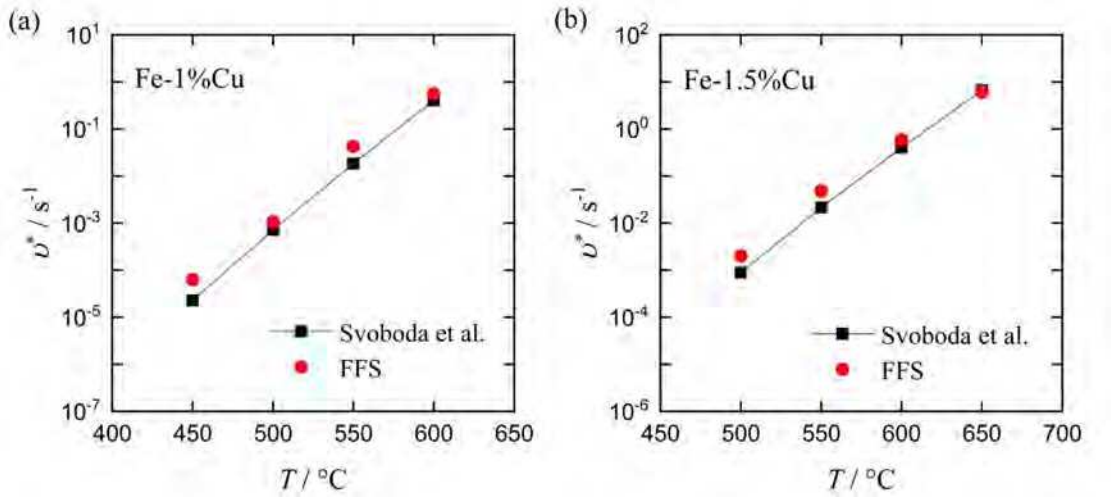

Figure 5.13 Atomic attachment rate, υ*, evaluated according to Svoboda et al. [13] compared with the prediction of equation (5-12).

Table 5-5 summarizes the values of CNT-type parameters as evaluated from the free energy profiles and the FFS nucleation trajectories. The CNT nucleation rate calculated using equation (3-9) is plotted on Figure 5.10 to compare with FFS predictions. It is not surprising that the two methods give almost the same prediction on nucleation rates in this work, since the free energy used in equation (3-9) is a direct reflection of the equilibrium properties of the atomic system, and the kinetics of cluster growth is also quite "classical" in dilute Fe-Cu alloys based on the above discussion.

Table 5-5 Number n^* of atoms in the critical cluster, Zeldovich factor Z, nucleation barrier $\Delta G(n^*)/k_BT$ and atomic attachment rate, υ^*, as evaluated from FFS trajectories for alloys with Cu contents of 1 at-% and 1.5 at-%. The nucleation rates, J, are calculated according to CNT (equation (3-9)).

	T / °C	n^*	Z	$\Delta G(n^*)/k_BT$	υ^* /s^{-1}	J /m^{-3}s^{-1}
X_{Cu}=1.0%	450	12	0.10	12.07	$6.32\cdot10^{-5}$	$3.06\cdot10^{18}$
	500	15	0.08	13.13	$1.07\cdot10^{-3}$	$1.44\cdot10^{19}$
	550	22	0.06	16.04	$4.24\cdot10^{-2}$	$2.40\cdot10^{19}$
	600	38	0.06	21.91	0.56	$8.39\cdot10^{17}$
X_{Cu}=1.5%	500	11	0.09	10.94	$2.01\cdot10^{-3}$	$2.87\cdot10^{20}$
	550	15	0.08	12.33	$4.81\cdot10^{-2}$	$1.42\cdot10^{21}$
	600	20	0.07	13.78	0.59	$3.49\cdot10^{21}$
	650	30	0.05	17.90	6.07	$3.95\cdot10^{20}$

5.5 Chemical composition and shape of critical Cu-clusters

5.5.1 Concentration profiles across the precipitate/matrix interface

The concentration profiles across the precipitate/matrix interfaces are analyzed for clusters of critical size at different temperatures. In the evaluation, the center atom is defined as the one atom residing closest to the geometric center of the cluster, i.e. the center of a fitted ellipsoid. The concentration profile is then calculated from the center up to the 20th neighbor shell as illustrated in Figure 5.14(a). The Cu concentration in the i^{th} shell is determined as $c^{(i)} = n_{Cu}^{(i)} / n_{tot}^{(i)}$, where $n_{Cu}^{(i)}$ and $n_{tot}^{(i)}$ are the number of Cu atoms and total number of atoms in the i^{th} shell, respectively.

The concentration profiles, averaged over 500 configurations of critical clusters with the same size, are shown in Figure 5.14 (b). In the Fe-1%Cu alloy, the critical nucleus at 500°C contains approximately 10% Fe in the center, with the Fe amount significantly increasing to approximately 50% in the first neighbor shell. At a temperature of 600°C, the Cu concentration increases to almost 100% in the center of the critical clusters. A similar observation of for the concentration profile of critical clusters is reported by Nagano and Enomoto [60] based on a study of cluster growth

with the Cahn-Hilliard theory for dilute Fe-Cu alloys. According to their calculations, the Cu content at the center of critical clusters is around 85% at 400°C in the Fe_1.5%Cu alloy and almost 100% when the temperature is increased to 550°C. The average concentration of Cu clusters was evaluated by Kozeschnik and Stechauner [51] based on the minimum $\Delta G(n^*)$ concept [61]. In their work, the critical clusters in Fe-1%Cu is estimated to contain 70% Cu at 500°C and gradually increase to almost 100% at 650°C.

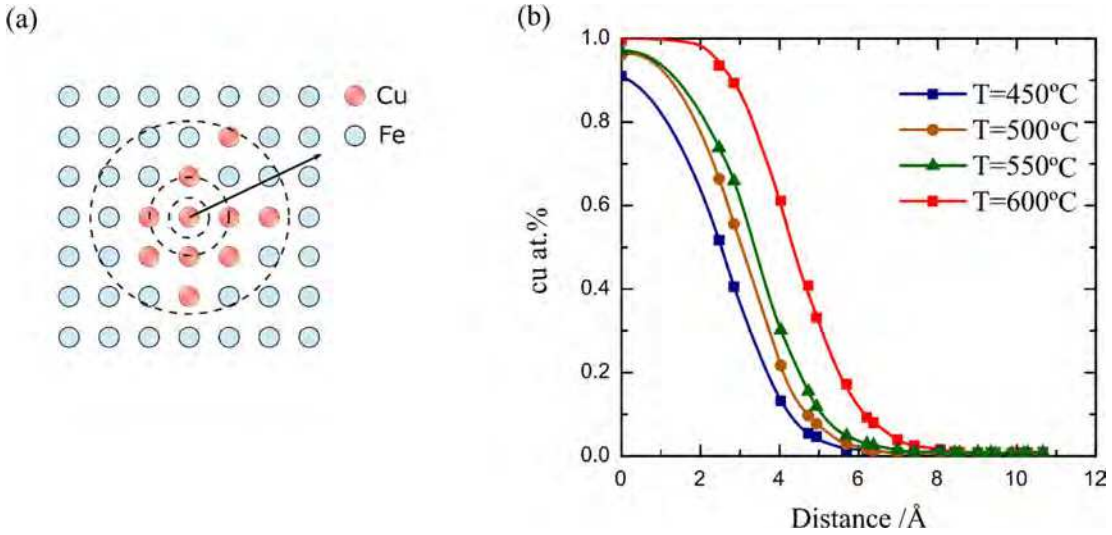

Figure 5.14 (a) Illustration of the procedure for finding the geometric center of an irregular cluster and of the evaluation of the composition profile from the center atom to neighbor shells; (b) Concentration profile of critical clusters in Fe-1%Cu alloy at 450°C, 500°C, 550°C and 600 °C, where the corresponding critical sizes are 12, 15, 22 and 38 atoms, respectively.

In the present analysis, there is no meaning to do further speculation on absolute numbers of the chemical composition of critical clusters because the actual value of this quantity is very sensitive to the choice of criterion defining the matrix/precipitate interface. Still, the concentration profiles of critical clusters indicate that the clusters formed first in dilute alloys are not always pure Cu clusters, and a substantial amount of Fe atoms can reside within Cu clusters at low temperature. At 600°C, the critical clusters maintain a high Cu content above 90% from the center up to the 2nd neighbor shell. At a temperature of 450°C, a large amount of Fe infiltrates into the core of the clusters and significantly reduces the Cu content around the center of the clusters. For

small clusters with less than 20 atoms, no strict "core" region can be defined any more, since these small clusters are composed of only 2~3 layers of solute atoms, and almost every atom in the clusters is partially "exposed" to the matrix.

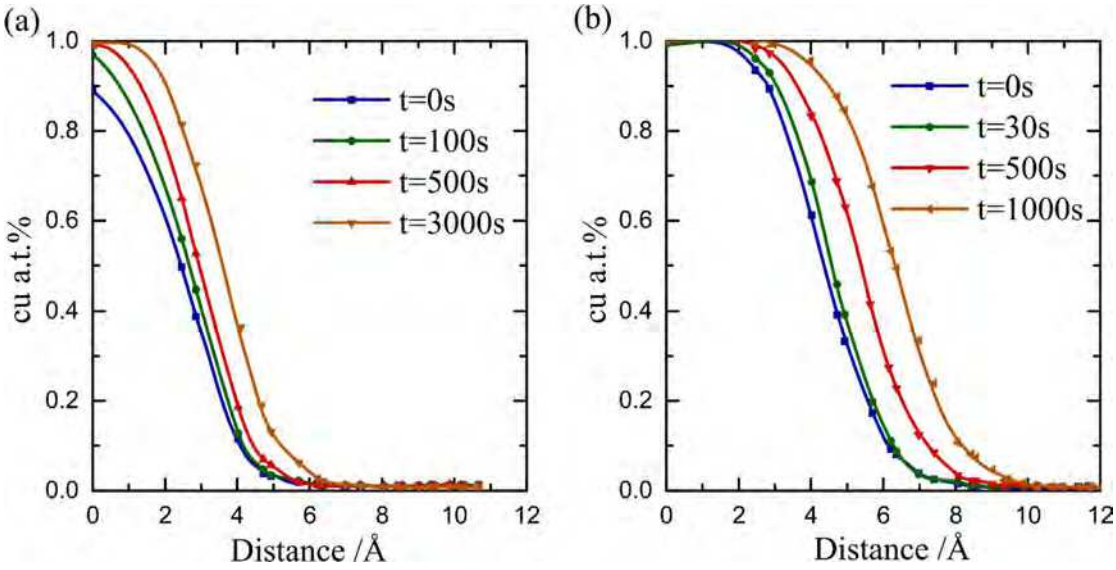

Figure 5.15 Concentration profiles of clusters in a 1.5%Cu alloy at 500°C (a) and in an 1%Cu alloy at 600°C (b) when aging from the critical state for different times.

To analyze the concentration profiles of clusters during super-critical growth, for each temperature and chemical composition of the alloys, a group of configurations at "critical states", i.e. the states with the largest cluster of critical size, are taken from the nucleation trajectories in FFS and a brute-force simulation is performed for these configurations until the system forms a large stable cluster or decays back to the random state. Those simulations, which successfully form a stable supercritical cluster are stored and used to calculate the concentration profile of the largest clusters at different times. Figure 5.15 summarizes the evolution of concentration profiles in the clusters in a weakly supersaturated case (in Fe-1%Cu at 600°C) and strongly supersaturated case (in Fe-1.5%Cu at 500°C). At high temperature, the size of Cu clusters steadily increases without significant change in the chemical environment around it (Figure 5.15(b)). At low temperature, the clusters first tend to increase the Cu content to almost 100% until they finally start growing (Figure 5.15(a)). This Cu-enrichment of clusters during nucleation at lower temperatures was recently confirmed by the Differential Scanning

Calorimetry (DSC) experiment of 15-5 PH steel in continuous aging at 300 to 500°C [62][63]. However, according to Figure 5.15(a), the enrichment of Cu content in clusters happens very fast. The clusters with over 20% Fe are mainly found to be in small size with radius less than 0.5 nm, and when growing over more than 0.8nm, they are almost pure Cu clusters. This observation is inconsistent with the recent APT results [64][65][66], where 50%~70% Fe are found in large precipitates with radius 1~1.5nm.

5.5.2 Shape analysis of early-stage Cu-clusters

The geometry factor, *A*, determines the *interface area/volume* ratio of clusters during nucleation. This factor is often derived from basic geometrical bodies such as sphere and rod-like shapes in numerical models [67–71]. In the Fe-Cu system, the spherical (or near-spherical) assumption for large coherent and semi-coherent clusters with radius 1~2nm during coarsening and before transforming into the rod-like fcc precipitate [72][73], is justified by the experimental observations [66,69,74]. But for small Cu nuclei, both, the exact chemical composition and the geometrical properties, are still uncertain. Figure 5.16 illustrates the shape analysis of a nano-sized Cu cluster (about 100 atoms) discovered in simulation, whose shape is clearly not a sphere.

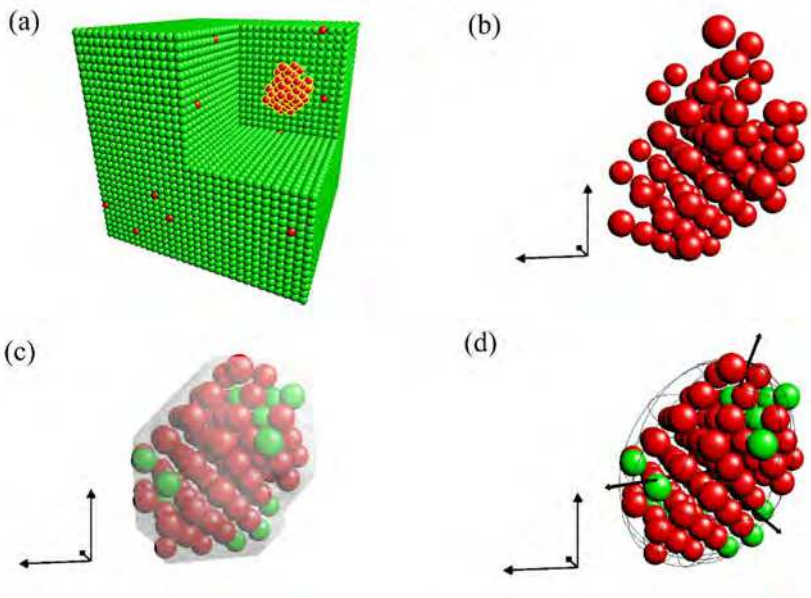

Figure 5.16 Illustration of extracting the shape information of the largest cluster in the simulation. (a) A

nano-sized cluster with around 100 Cu atoms is highlighted in a snapshot of simulation. The red spheres represent the Cu atoms and the green ones represent the Fe atoms. (b) The cluster is identified as a network of Cu atoms connected with each other with the nearest neighbor bonds. The gizmo on the left indicates the *x*-*y*-*z* coordinate of the simulation box. (c) The atoms are found within the best-fitted ellipsoid based on the network of Cu atoms. (d) The best-fitted ellipsoid is displayed with the arrow lines indicating the three radii of the ellipsoid.

In order to quantify the geometry factor of small and irregular clusters, a best-fitted ellipsoid approximation is introduced to characterize the shape of the small clusters during nucleation. By definition, the largest cluster is firstly characterized as the network formed by Cu atoms connected with the nearest neighbor bond. Then the Cu network is used as "skeleton" to find the best-fitted ellipsoid to quantitatively describe the shape information of the cluster, which is also illustrated in Figure 5.16(c) and (d).

The best-fitted ellipsoid is calculated from the inertia tensor[75] of the Cu "skeleton", which is defined as

$$\mathcal{T} = \sum_{i=1}^{n} \begin{pmatrix} \Delta y_i^{\,2} + \Delta z_i^{\,2} & -\Delta x_i \Delta y_i & -\Delta x_i \Delta z_i \\ -\Delta x_i \Delta y_i & \Delta x_i^{\,2} + \Delta z_i^{\,2} & -\Delta y_i \Delta z_i \\ -\Delta x_i \Delta z_i & -\Delta y_i \Delta z_i & \Delta x_i^{\,2} + \Delta y_i^{\,2} \end{pmatrix} \tag{5-13}$$

where (x_i, y_i, z_i) is the position of the i-th atom in an n-sized cluster and $(\Delta x_i, \Delta y_i, \Delta z_i)$ is the displacement of this atom to the geometrical center of the cluster, i.e. $\begin{cases} \Delta x_i = x_i - \bar{x} \\ \Delta y_i = y_i - \bar{y} \\ \Delta z_i = z_i - \bar{z} \end{cases}$, with $\bar{x} = 1/n \sum_{i=1}^{n} x_i$, $\bar{y} = 1/n \sum_{i=1}^{n} y_i$ and $\bar{z} = 1/n \sum_{i=1}^{n} z_i$.

Diagonalizing $\mathcal{T}$, one can obtain

$$Q^{-1}\mathcal{T}Q = \begin{pmatrix} I_1 & 0 & 0 \\ 0 & I_2 & 0 \\ 0 & 0 & I_3 \end{pmatrix} \tag{5-14}$$

where I_1, I_2 and I_3 are the principal inertia of moments (eigen values) on the principle axes (eigen vectors) $\boldsymbol{q}_1$, $\boldsymbol{q}_2$ and $\boldsymbol{q}_3$, with $Q = (\boldsymbol{q}_1, \boldsymbol{q}_2, \boldsymbol{q}_3)$ and $I_1 > I_2 > I_3$.

According to the relation between principal inertia of moments and corresponding radii in an ellipsoid with equal mass density, the radius of a best-fitted ellipsoid for a given cluster is determined by solving the following equations:

$$\begin{cases} I_1 = 1/5m(r_1^2 + r_2^2) \\ I_2 = 1/5m(r_1^2 + r_3^2) \\ I_3 = 1/5m(r_2^2 + r_3^2) \end{cases} \quad (5\text{-}15)$$

where r_1, r_2 and r_3 ($r_1 \geq r_2 \geq r_3$) denote the radii of the ellipsoid and m is the mass density of the cluster. Here, m is set to be 1, so that the volume of the ellipsoid found by equation (5-15) is conserved to $mV_{\text{ellip}} = 4/3\,\pi r_1 r_2 r_3 m = n$. The directions of radii $\boldsymbol{r}_1$, $\boldsymbol{r}_2$ and $\boldsymbol{r}_3$ are lying on the corresponding vectors $\boldsymbol{q}_1$, $\boldsymbol{q}_2$ and $\boldsymbol{q}_3$ (see Figure 5.17).

To demonstrate the anisotropy of cluster shape, an anisotropy factor is defined as $\xi = r_1/r_3$. For a sphere-like cluster, the anisotropy factor approximately equals to 1. With the shape of clusters getting more irregular, the degree of anisotropy, ξ, is also increasing. For some extreme cases, such as plate-like clusters, where all the Cu atoms are placed on one plane (see Figure 5.18), the anisotropy factor $\xi = \infty$.

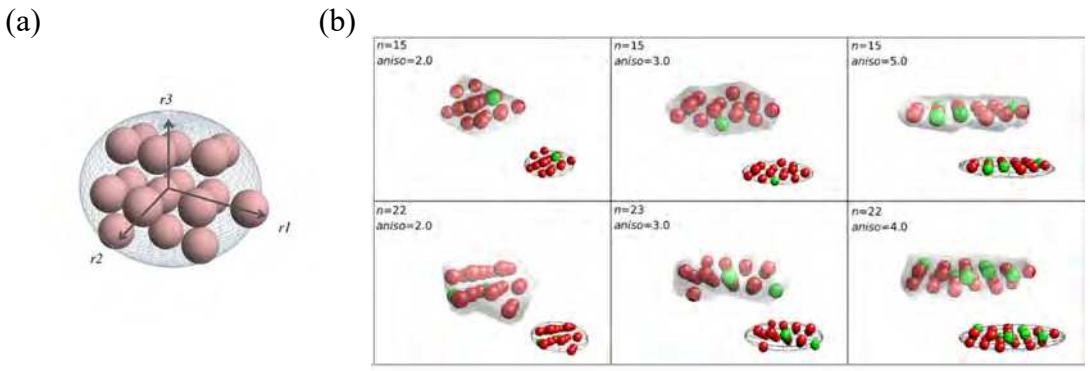

Figure 5.17 (a) Illustration of the best-fitted ellipsoid for a 17-atom cluster; (b) Snapshots of clusters with size $n < 30$ obtained from Umbrella Sampling.

In this work, the shape analysis is carried out to compute the radii of clusters in different size ranges with n=5~100 from configurations collected in Umbrella Sampling in Fe-1%Cu alloy at 500 and 600°C. To gain better statistics, 50000 configurations of clusters for each size are collected and used to calculate the averaged value of the radii. Since the biased potential in Umbrella Sampling only constrains the number of atoms

in a cluster, the geometrical arrangement of Cu atoms is not affected by the biased potential.

The snapshots of clusters observed during Umbrella Sampling are plotted with their corresponding best-fitted ellipsoids in Figure 5.19 to Figure 5.23, with cluster sizes from n=5~100 and anisotropy factors from ξ=1.0~11.0. From these snapshots, clusters with ξ=1.0~1.5 are observed in a sphere-like shape, and clusters with ξ=1.5~5.0 are more like ellipsoids, while clusters with ξ>5.0 are revealed in a needle-like shape. Small clusters with less than 50 atoms are observed to exhibit a more irregular shape. In the ultra-fine clusters, with n<15, some clusters appear in a plate-like form with ξ=∞, as illustrated in Figure 5.18. The chance to form such plate-like clusters is not high, but once observed, the majoraty of them are found to place the Cu atoms on the [1 1 0] plane.

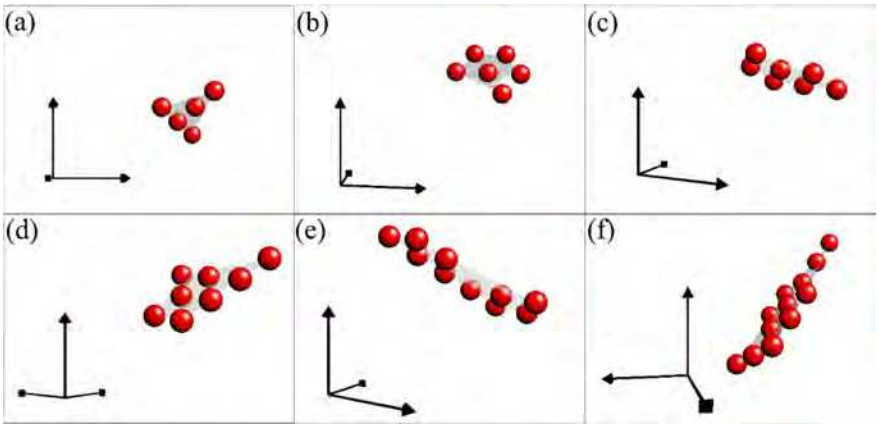

Figure 5.18 The plate-like early-stage clusters on [1 1 0] plane with (a) 5 atoms, (b) 6 atoms, (c) 7 atoms, (d) 8 atoms, (e) 10 atoms and (f) 12 atoms.

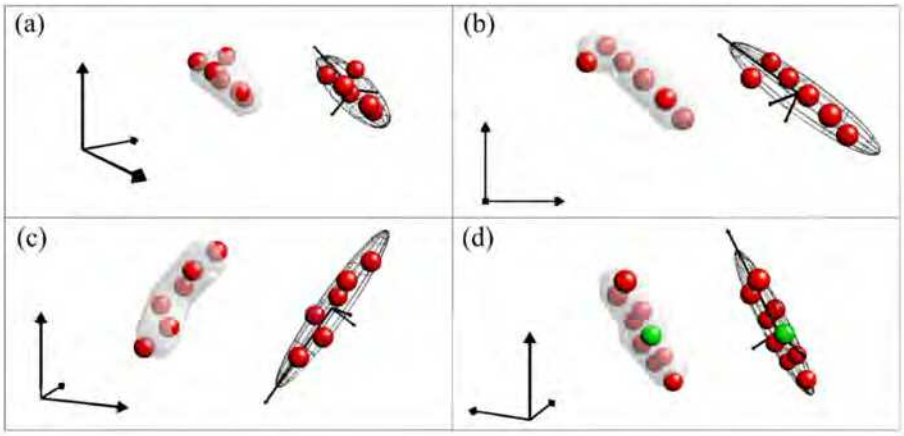

Figure 5.19 Small clusters (number of atoms<10) with anisotropy factor (a) ξ=3.0, (b) ξ=6.0, (c) ξ=8.1

and (d) ξ=8.2.

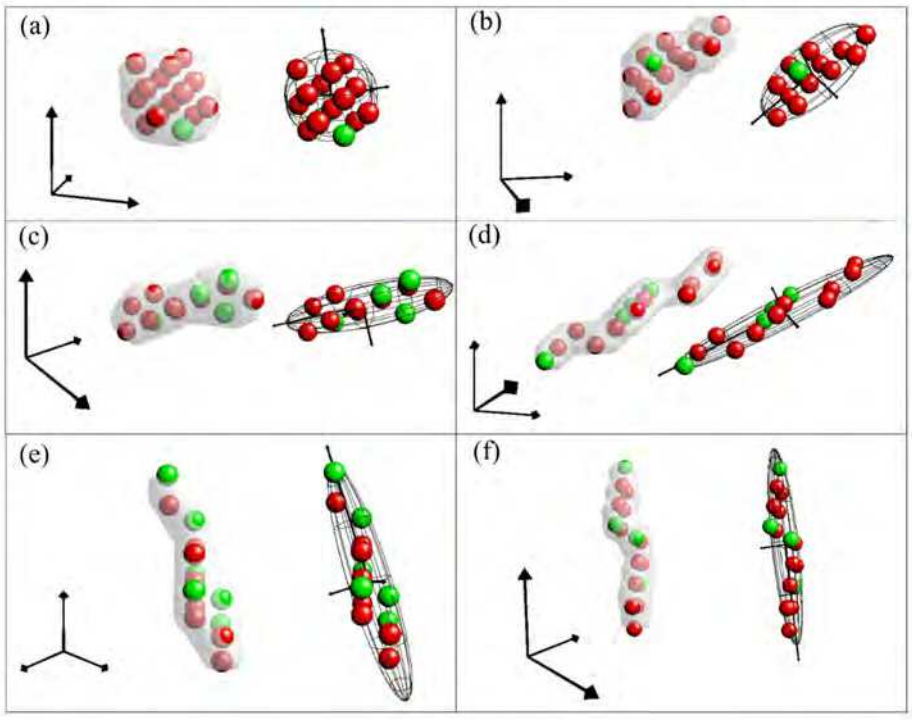

Figure 5.20 Small clusters with number of atoms around 15 with anisotropy factor (a) ξ=1.0, (b) ξ=2.5, (c) ξ=4.0, (d) ξ=11.5, (e) ξ=6.0 and (f) ξ=8.5.

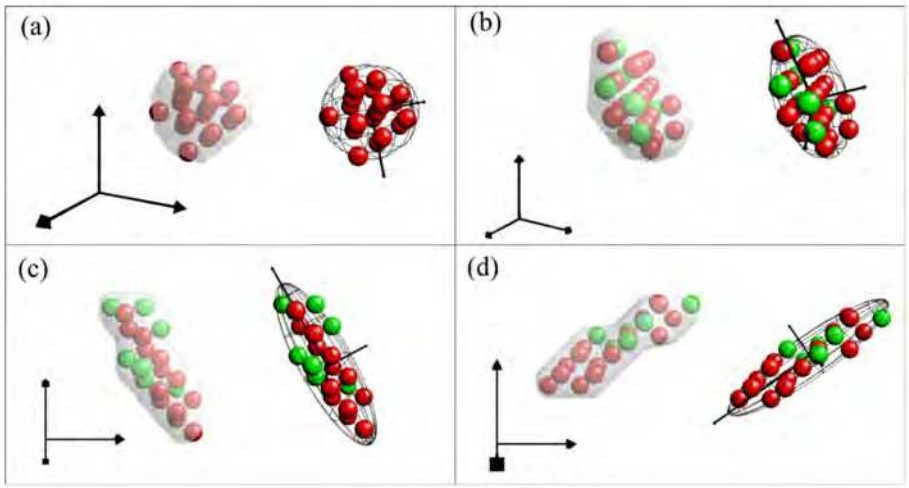

Figure 5.21 Small clusters with number of atoms around 20 with anisotropy factor (a) ξ=1.0, (b) ξ=2.5, (c) ξ=3.5 and (d) ξ=5.0.

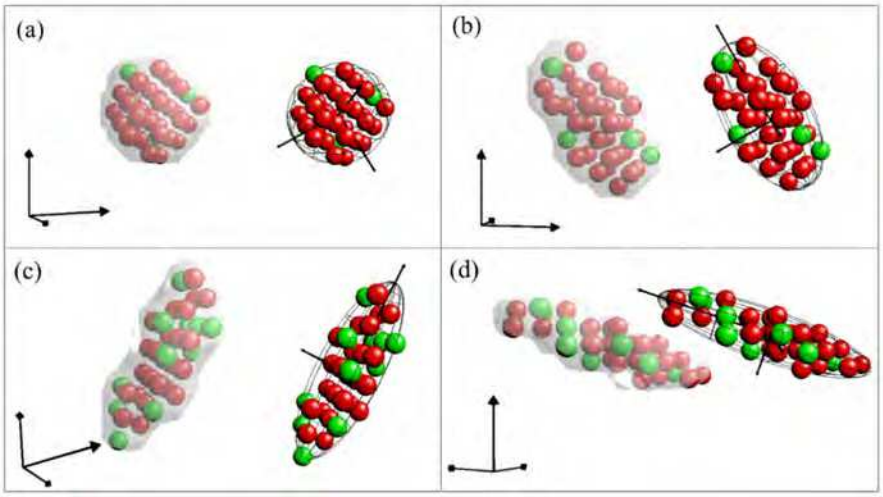

Figure 5.22 Clusters with number of atoms around 35 with anisotropy factor (a) ξ=1.0, (b) ξ=2.0, (c) ξ=3.0 and (d) ξ=4.5.

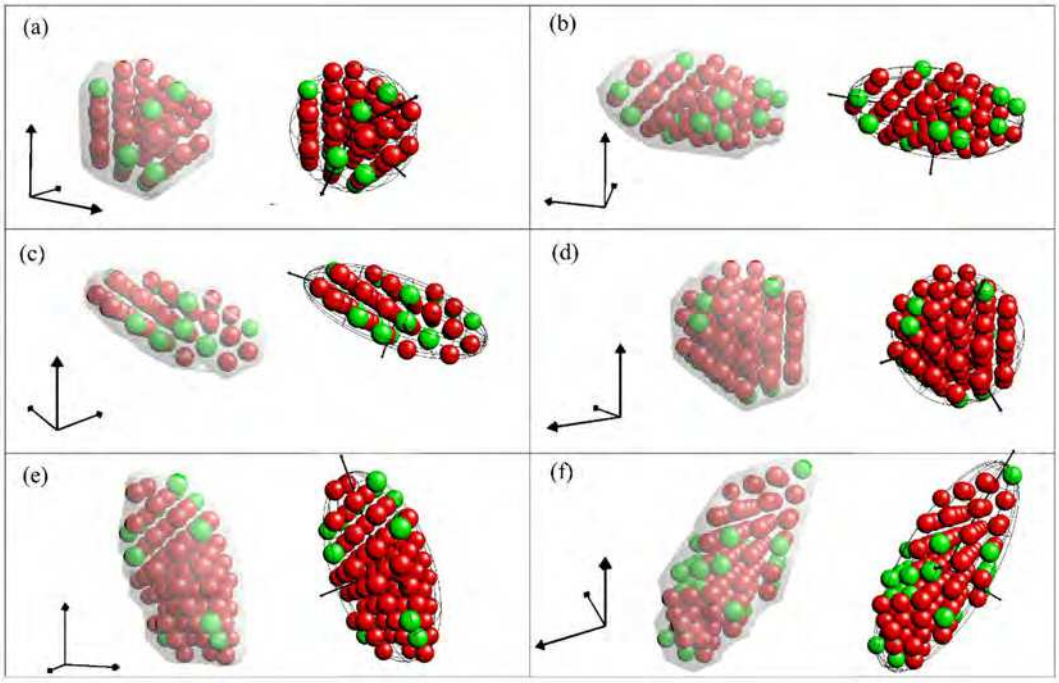

Figure 5.23 Stable clusters with number of atoms around 60 with anisotropy factor (a) ξ=1.0, (b) ξ=2.0 and (c) ξ=3.0; stable clusters with number of atoms around 100 with anisotropy factor (d) ξ=1.0, (e) ξ=2.0 and (f) ξ=2.5.

The anisotropy factor averaging over configurations with the largest cluster size as n is plotted in Figure 5.24(a). For small clusters within 20 atoms, the longest radius r_1 is about 2~4 times longer than the shortest radius r_3, and this anisotropic tendency is getting weaker for larger clusters. When critical clusters have sizes over 100 atoms, the ratio r_1/r_3 is gradually converging to 1. The temperature seems to have almost no

influence on the anisotropy factor of clusters during nucleation, e.g. the ratio r_1/r_3 of clusters observed at 600°C is only slightly higher than that at 500°C for clusters of the same size.

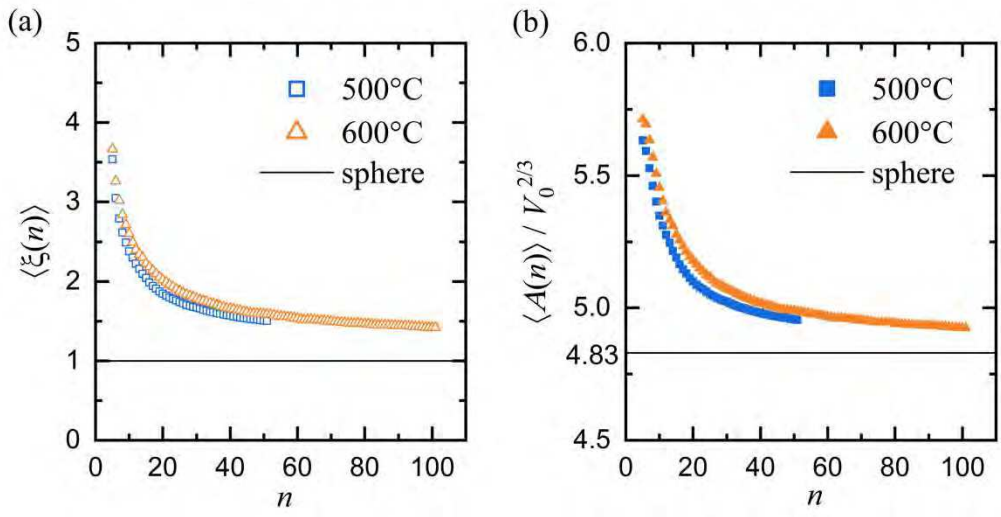

Figure 5.24 (a) The average anisotropy factor, i.e. ratio between the longest radius, r_1, and the shortest one, r_3, from the fitted ellipsoid of clusters of size n. (b) The geometry factor is calculated from the shape of Cu clusters during nucleation as a function of the cluster size. The straight lines indicate the values of (a) anisotropy factor and (b) geometry factor of a perfect sphere.

For each cluster, the precipitate/matrix interfacial area can be approximately calculated as the fitting ellipsoid surface area as

$$S = 4\pi \sqrt[1.6]{\frac{(r_1 \cdot r_2)^{1.6} + (r_2 \cdot r_3)^{1.6} + (r_3 \cdot r_1)^{1.6}}{3}} \qquad (5\text{-}16).$$

Therefore, the geometry factor for an n-atom cluster can be calculated by

$$A = \frac{S}{n^{2/3}} \qquad (5\text{-}17).$$

The average geometry factor of clusters of size n is displayed in Figure 5.24(b). The line in Figure 5.24(b) indicates the value of geometry factor in a perfect sphere, i.e. $A_{\text{sphere}} = (36\pi V_0^2)^{1/3}$, where V_0 is the unit volume of an atom in the bcc lattice. Compared with the spherical cluster, Cu clusters have higher geometry factors during nucleation. For clusters of critical size at 500°C, i.e. n^*=15, A is averagely 12% higher than that of

a sphere. When the critical cluster size increases to around n^*=38 at 600°C, the average geometry factor is still slightly higher, about 6%, than that of a sphere.

To gain a further understanding of the irregularity of clusters shape, the probability distribution of the anisotropy factor of n-size clusters, $\rho(n,\xi)$, is calculated as

$$\rho(n,\xi) = \rho(n)\rho(\xi \mid n) \tag{5-18}$$

where $\rho(n)$ is the un-biased probability distribution of n, as evaluated in Umbrella Sampling. $\rho(\xi \mid n)$ is the normalized probability distribution of ξ in all n-sized clusters observed in US, as $\int d\xi \rho(\xi \mid n) = 1$. Since the biased potential used in US only constrains the size of clusters, the geometry features of clusters are not influenced in the sampling. Therefore, equation (5-18) can give a reasonable estimation of $\rho(n,\xi)$ without performing the complex multi-dimension Umbrella Samplings. Considering that the free energy $F(n,\xi)$ is proportional to -ln$\rho(n,\xi)$, i.e. $F(n,\xi) \propto$ -ln$\rho(n,\xi)$, the contours of -ln$\rho(n,\xi)$ evaluated from the results of Umbrella Sampling for Fe-1%Cu alloy at 500 °C and 600 °C are plotted in Figure 5.25(a) and Figure 5.25(b), respectively.

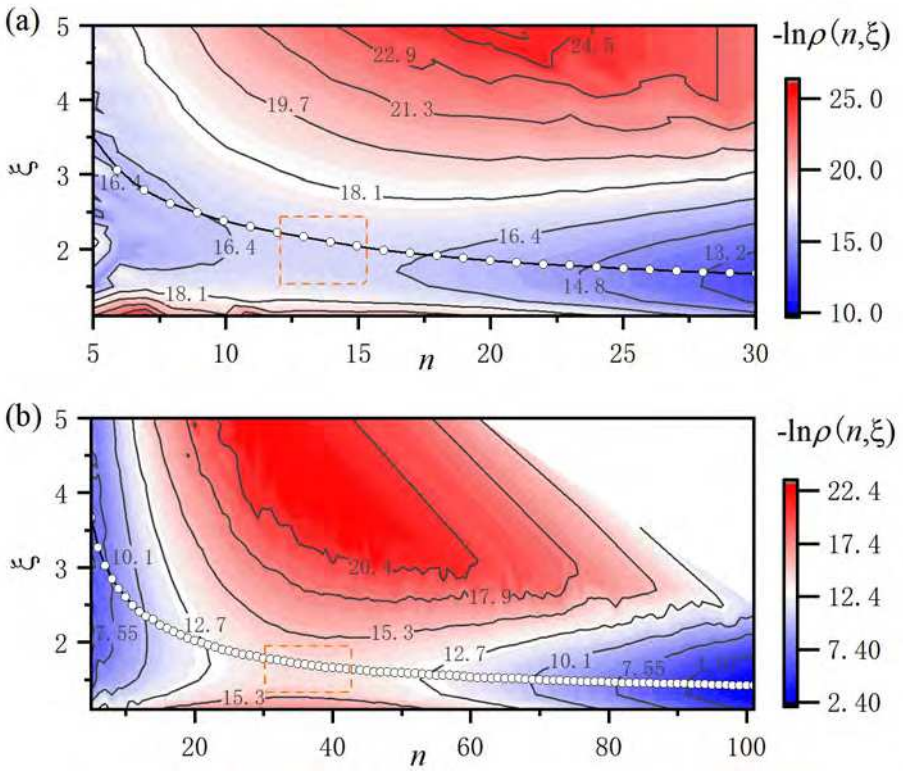

Figure 5.25 The contours for the equilibrated distribution of anisotropy factor of n-sized cluster at (a) 500 °C and (b) 600 °C. The dot line in each picture marks the average anisotropy factor <$\xi(n)$>. The

dashed-line rectangle indicates the saddle point area of the probability distribution.

In the contours, the distribution of ξ significantly diverges in small clusters with n<15, indicating that small clusters possess geometrical features in a random and chaotic manner. One can observe small clusters in high and low anisotropy factor almost with similar probability, and their shape does not resemble any macroscopic geometries, such as spheres, cubes or cylinders. As clusters become larger, the distribution starts to converge towards a lower spread of anisotropy factors. In both cases, most of the critical-size clusters, i.e. n^*=15 at 500°C and n^*=38 at 600°C, have anisotropy factors in the range of ξ=1.5~2.5, which is circled out by the dashed rectangles in Figure 5.25(a) and (b) for both cases. For super-critical clusters, n>30 at 500°C and n>60 at 600°C, the value of ξ is around 1.5.

Additionally, the distribution probability of the direction of the shortest axis r_3 at a given cluster size n, $\rho(n,$ norm($\boldsymbol{r}_3$)), is calculated in a similar fashion as $\rho(n,\mathrm{norm}(\mathbf{r}_3)) = \rho(n)\rho(\mathrm{norm}(\mathbf{r}_3)\,|\,n)$. The function norm($\boldsymbol{r}_3$) gives the unit vector of $\boldsymbol{r}_3$, which is orthogonal to the plane with the densest mass inertia. As illustrated in Figure 5.26(a), the unit/normalized vectors form a sphere with radius r=1 in space, while, through the symmetric operations in a bcc lattice, all unit vectors in space are equivalently moved in the red area with three corners representing the unit vector of directions <100>, <110> and <111>.

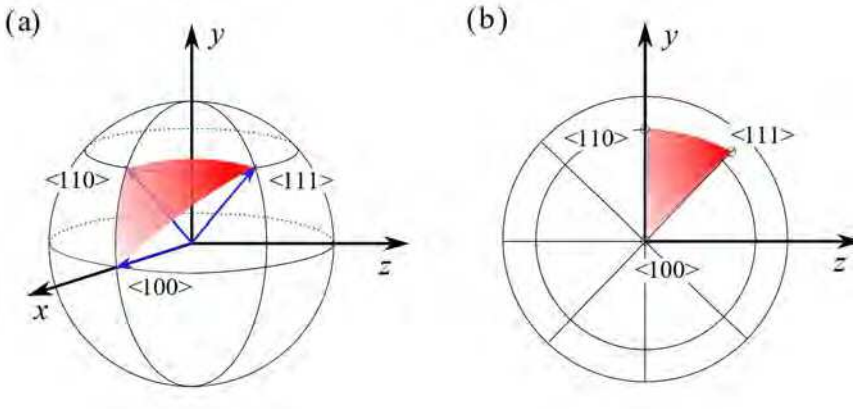

Figure 5.26 (a) The sphere formed by the unit vectors in 3D space. Considering the symmetrical operations in the bcc lattice, one only needs the vectors falling in the red area to uniquely define the vector space. (b) Projection of the vector sphere into the y-z plane.

In this work, $\rho(n, \text{norm}(\boldsymbol{r}_3))$ with n= 5, 10, 15, 35 and 50 are calculated from the clusters observed in Umbrella Sampling for Fe-1%Cu alloy at 600°C. In Figure 5.27, $\rho(n, \text{norm}(\boldsymbol{r}_3))$ is plotted as contours projected from the unit vector sphere onto the *y*-*z* plane in the form illustrated in Figure 5.26(b). The contours are rescaled as fractions to the largest value of $\rho(n, \text{norm}(\boldsymbol{r}_3))$ in each n, with the highest fraction, i.e. 1, being marked by blue and the lowest fraction by white. Accordingly, the contour with more blue area indicates that the direction of $\boldsymbol{r}_3$ is evenly distributed in vector space, i.e. there is no orientation preference for the plane with the densest mass inertia in clusters. In Figure 5.27(a), the distribution of the norm vector of $\boldsymbol{r}_3$ strongly peaks on direction <110> for clusters in size n=5. With clusters getting larger, the distribution of $\boldsymbol{r}_3$ direction starts smearing in vector space. In clusters with n=35 and 50, as illustrated in Figure 5.27(d) and (e), norm($\boldsymbol{r}_3$) is almost evenly distributed in the vector space. This observation reveals an interesting fact that, in the beginning of Cu cluster formation, the ultra-fine nuclei may have a preference to arrange the Cu atoms on the [1 1 0] plane of the bcc lattice, while the preference soon vanishes as clusters grow into larger size. The ultra-fine nuclei, with limited patterns to form the networks of Cu atoms, are prone to be affected by the crystallographic properties of the bcc lattice, which result in the preferred [1 1 0] plane for Cu nuclei in the beginning of clusters formation.

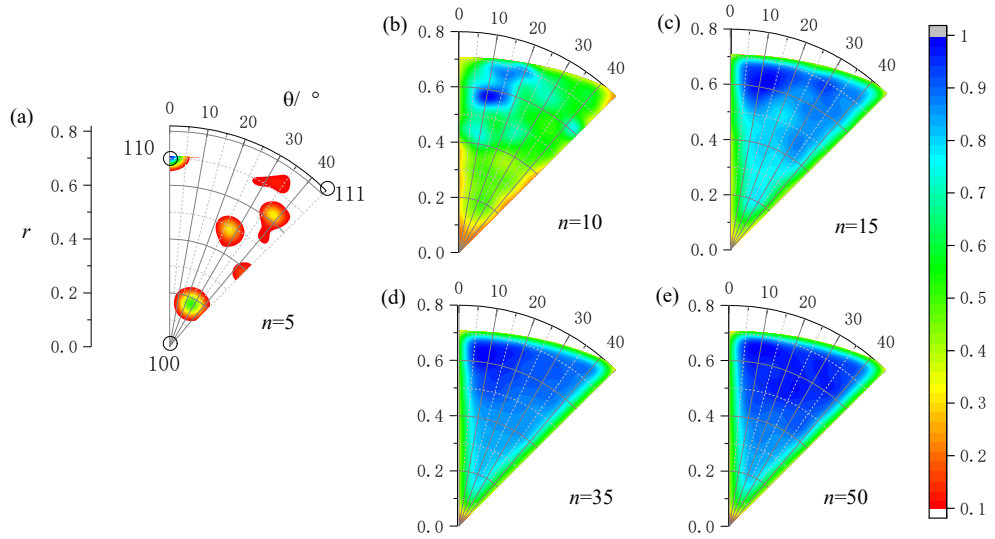

Figure 5.27 The probability distribution of directions of $\boldsymbol{r}_3$, $\rho(n, \text{norm}(\boldsymbol{r}_3))$, with sizes n=5, 10, 15, 35 and 50 measured in the Umbrella Sampling of Fe-1%Cu alloy at 600°C. Here, the contours of $\rho(n, \text{norm}(\boldsymbol{r}_3))$

is rescaled as the fraction to the largest value of $\rho(n, \text{norm}(\boldsymbol{r}_3))$.

5.6 Analysis of α-Fe/Cu interfacial energy

The α-Fe/Cu interfacial energy can be obtained by fitting the nucleation free energy computed from Umbrella Sampling (US) to the Classical Nucleation Theory (CNT) framework expressed by equation (5-9), where the fitted parameters are listed in Table 5-4. Figure 5.28 displays the fitted equation (5-9) (solid curve) and the free energy obtained by US (red dots) in Fe-1%Cu alloy at 500°C and 600°C. At 500°C, the volume energy, ΔG_{nucl}, is evaluated to be -11.24 kJ·mol^{-1} and the excess energy coefficient, $A\gamma$, is 1.34 J· m^{-2}, while, at 600°C, ΔG_{nucl} is -8.20 kJ·mol^{-1} and $A\gamma$ is 1.35 $J{\cdot}m^{-2}$. The unit of $A\gamma$ is transformed from J·mol$^{-2/3}$ to J·m^{-2} considering that, on average, 1 mol of bcc-Fe has a volume of 6.97×10^{-6} m^3 with a lattice constant of α-Fe as 2.85Å [76].

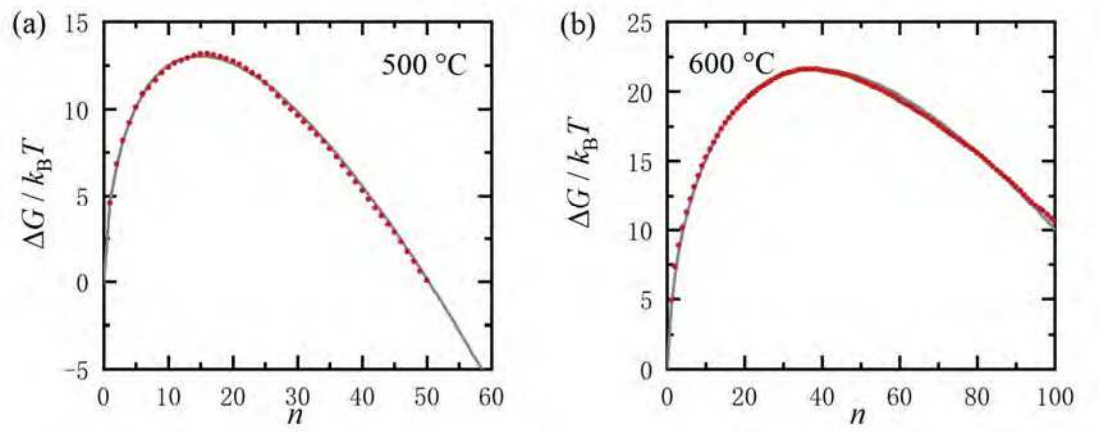

Figure 5.28 Nucleation free energy in Fe_1%Cu at (a) 500°C and (b) 600°C as evaluated by Umbrella Sampling (red dots). The solid curve is a fitting from equation (5-9).

It is emphasized that the surface energy term in equation (5-9), $A\gamma n^{2/3}$, does not include the change of supersaturation, i.e. the non-negligible reduction of Cu-content in the matrix during precipitation at constant temperature. Accordingly, when the Cu content in the matrix starts to decrease as the number of atoms in the cluster, *n,* exceeds

100 atoms, the fitting parameters (ΔG_{nucl} and $A\gamma$) are no longer consistent with n=0~100. To focus on the interfacial energy during nucleation, fitting of equation (5-9) is valid only within n=0~100 with the Cu-content of the matrix remaining around 0.9% at both 500 and 600 °C.

Based on the free energy and geometry factors from Umbrella Sampling, the Cu-precipitate/α-Fe interfacial energy γ as a function of cluster size n is calculated for nucleation processes in Fe-1%Cu at 500 and 600 °C. The results are plotted in Figure 5.29.

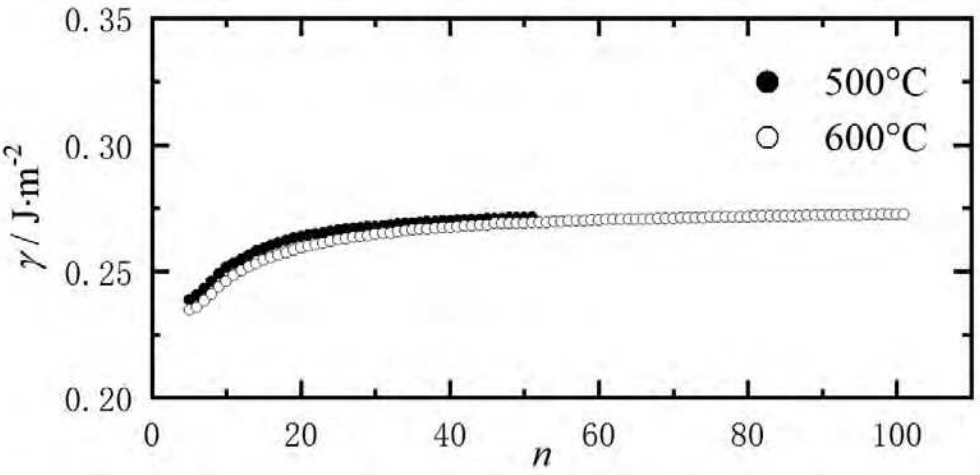

Figure 5.29 Cu-precipitate/α-Fe interfacial energy evaluated by US and VC-SCG ensemble in Cu precipitation at (a) 500°C and (b) 600°C.

At 500 and 600 °C, the effective interface energy γ has rather similar values at the same size n (see open circles on Figure 5.29), which gradually increase from 0.24eV to 0.28eV as the cluster size increases from n=10 to 100 atoms. These values are significantly lower than the values obtained from experimental determination of interfacial energies (about 0.56eV) for spherical Cu-precipitates in an Fe-1.5%Cu alloy in coarsening experiments at 500°C [69]. Despite the limitations in computational modelling, the discrepancy of predictions from US and experiment is reasonable considering that γ is measured for two different stages in precipitation, i.e., in the nucleation stage (present analysis) and during late-stage coarsening (experiments). In the coarsening stage, the interfaces between Cu-precipitates and Fe-matrix become

incoherent, which is an additional factor for differences between interfacial energies calculated in the nucleation stage, where interfaces are presumably coherent, and precipitates in the coarsening stage.

For comparison, a different method, the VC-SGC (Variance-Constrained Semi-Grand-Canonical) ensemble method [29][30], is employed to evaluate the interfacial energy for spherical Cu-precipitates in dilute Fe-Cu alloys. The predictions of Cu-precipitate/α-Fe interfacial energy by the VC-SGC ensemble are plotted in Figure 5.30 with open squares (500°C) and triangles (600°C) for clusters with 50 to 350 atoms.

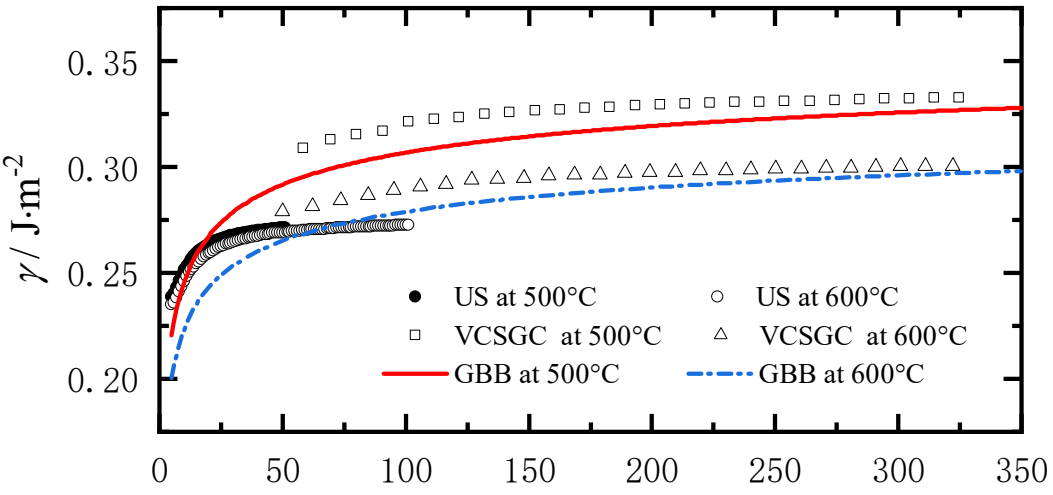

Figure 5.30 The geometry-corrected interface energy evaluated in this work is compared with the interface energy of equilibrated Cu clusters by the VC-SGC method and the overall predictions from the size-dependent GBB method [12].

In the VC-SGC ensemble, γ is calculated to range between 0.25~0.34 $J{\cdot}m^{-2}$ at 500 °C, and, on average, higher than this at 600 °C with 0.24~0.31 $J{\cdot}m^{-2}$. At both temperatures, γ gradually increases with cluster size with approximately $\gamma \propto n^{1/3}$, which is consistent with the Tolman-length effect [12,77][78] to interfacial energy on microscopic scale. As the cluster grows over 300 atoms, γ converges to the interfacial energy of a planar Cu-precipitate/α-Fe interface, which is 0.38 $J{\cdot}m^{-2}$ at 500 °C and 0.34 $J{\cdot}m^{-2}$ at 600 °C evaluated in the VC-SGS ensemble.

The interfacial energy, γ, is also compared with the size dependent GBB model, where γ is computed from the planer interfacial energy γ_{plan} as

$$\gamma(r) = \alpha(r)\gamma_{plan} \qquad (5\text{-}19).$$

In the GBB model, the clusters are assumed to be spherical and r in (5-19) denotes the radius of the sphere. $\alpha(r)$ is the correction factor depending on r as

$$\alpha(r) = 1 - 0.5455\frac{r_1}{r} + \left(0.0892 + 0.0542\ln\frac{r}{r_1}\right)\frac{r_1^2}{r^2} \qquad (5\text{-}20)$$

where r_1 is the nearest neighbor distance in bcc-Fe. In Figure 5.30, γ is plotted as a function of n, which is coupled with r as $V_0 n = 4/3\pi r^3$.

The Cu/α-Fe interfacial energy has similar values in nucleation evaluated by Umbrella Sampling at both 500 and 600°C, whereas in the VC-SCG ensemble, γ is on average lower at 600°C compared to its value at 500°C. Even though the clusters observed in US are much smaller, the trend of γ is not consistent with predictions from the VC-SCG ensemble on the overlapping region (n=50~100). This inconsistency is caused by a different Cu concentration in α-Fe during simulations in US and the VC-SCG ensemble. In the VC-SCG ensemble, Cu concentration in α-Fe is a little higher than the solubility limit of Cu at the respective temperature, around 0.16~0.33% at 500°C and 0.44~0.78% at 600°C, hence, the concentration gradient on Cu/α-Fe interface is higher at lower temperature, resulting an averagely higher interfacial energy. However, in Umbrella Sampling, even the simulations are performed at different temperatures, Cu concentration in α-Fe is almost constantly keeping around 0.8~0.9%. Considering that the geometry properties are not affected by temperature, it is reasonable for γ to have the similar values in Umbrella Samplings at different temperatures. The result indicates that the Cu/α-Fe interfacial free energy is not only dependent on the shape and size of precipitate (curvature change of interface), but also strongly related to the precipitate/matrix concentration discrepancy at the interface (concentration gradient). In the equilibrated co-existing Cu precipitate/α-Fe state (VC-SGC ensemble), the temperature indirectly influences the interfacial energy by altering the concentration gradient at the Cu/α-Fe interface. However, in the nucleation

transition (US method), temperature has little effect on the Cu/α-Fe interfacial energy, since the concentration of α-Fe parent phase is not evidently changing in the steady-state condition. But the temperature determines the degree of supersaturation, and, hence, it has a strong influence on the driving force in the nucleation free energy.

Another interesting observation is a contradicting trend of geometry factor and interfacial energy with cluster size during nucleation. The anisotropy in the shape of nuclei indicates that, even in homogeneous nucleation, small clusters exhibit a certain degree of anisotropy during growth due to the heterogeneity of crystallographic lattice on a microscopic level. However, this does not mean that the classical continuous models are incorrect for nucleation processes with small critical nuclei. The nucleation free energy curves in Fe-Cu system obey the form of classical nucleation theory very well, because the system evolution follows the path where the excess free energy is a minimum on the coordinate of cluster size, n. Therefore, even though the geometry factor and interface energy, γ, vary with size, n, the excess free energy coefficient, $A\gamma$, remains at an approximately constant value during the nucleation process before depletion happens. The excess free energy coefficient is also found to be almost constant, similar to the product of compressibility and surface tension in ideal gases during condensation [79].

6 Discussion

6.1 Role of statistical sampling methods

Conventional atomic-scale simulations, such as Monte Carlo methods [32][50], are widely used in studies of nucleation kinetics in diffusion-driven solid-solid phase transitions. In literature, various Monte Carlo algorithms have been proposed and successfully implemented in software to investigate the diffusion kinetics [80], cluster mobility [81] and vacancy-cluster interactions [82] in the Fe-Cu system. However, additional statistical sampling is necessary to provide an accurate quantitative analysis of the nucleation process with brute-force Monte Carlo simulations.

Considering the computational effort, Monte Carlo simulations are usually carried out in small-size samples with the order of a few tens of nanometers and only for short times. This, however, makes it likely to cause insufficient statistics in the simulation and lead to an inaccurate estimation of the number density of clusters, especially in weakly supersaturated cases [83]. For example, in chapter 5.3.2, the nucleation rate in Fe-1%Cu at 500°C is evaluated from the brute-force MC simulation using a comparably large simulation box with 100×100×100 bcc unit cells. Even though it is a moderately supersaturated case, the results show significant discrepancies between the repeated simulations. Compared with the brute-force MC simulation, the trajectory-based sampling methods, such as FFS and TIS, are much more efficient. The average computation cost of brute-force MC simulation to obtain a successful nucleation trajectory is logarithmically increasing with the free energy barrier of the nucleation transition, whereas the average time cost of FFS and TIS is linearly growing with the height of the energy barrier. Consequently, it is impractical to use brute-force simulations to study the nucleation transitions in weakly supersaturated cases.

In the evaluation of the nucleation free energy, Umbrella Sampling has also been implemented in the MatCalc software [31] and utilized for the purpose of providing sufficient statistics in quantitative analysis. From a statistical point of view, the nucleation free energy is corresponding to the equilibrated size distribution of clusters

in a certain supersaturated condition. This distribution will not be established in reality, since, during nucleation, there is always a net forward transition from small clusters to large stable ones until the phase separation is finally completed. When focusing on one cluster, the size distribution is equivalent to the probability of finding the cluster in a given size n on its own nucleation trajectory, which is proportional to the total time the cluster spends on size n during nucleation. However, due to the presence of a nucleation barrier, the chance to observe a cluster around its critical size n^* is extremely rare compared to it in other size, which results in large statistical errors in estimation of probability around n^*. In order to solve this problem, Umbrella Sampling uses a biased potential to enhance the samplings of size distribution around a given size range, so that one can obtain enough statistics of size distributions even around the critical size n^*. Then, the free energy profile is derived from the biased local size distribution through the Weighted Histogram Analysis Methods [26,38]. Additionally, both FFS and Umbrella Sampling procedures gain a large amount of transition trajectories and configurations of clusters in critical size, which enable further investigation of transition mechanism and clusters evolution with statistical foundation.

6.2 The early-stage clusters in Fe-Cu alloys

The Fe-Cu binary system is a well-studied model system in precipitation-hardening ferritic alloys, where Cu precipitates play an important role in materials strengthening. It is commonly acknowledged that, in thermally-aged dilute Fe-Cu alloys, copper precipitates undergo a BCC-9R-FCC transition during the precipitation process [84][85][86]. The chemical composition of these bcc precipitates, however, is still unclear. In recent Atom Probe (3DAP) investigations [64][65][66], the bcc Cu-rich precipitates are assumed to contain about 50% Fe atoms, while the results from small-angle neutron scattering (SANS) [74] indicate a significantly higher Cu content of more than 70%. Schober et al. [66] attribute this discrepancy to the assumption of non-magnetic Cu precipitates in SANS experiments and the insensitivity to very small

clusters of only sub-nanometer radius in 3DAP techniques. Unfortunately, no direct explanation for why the bcc precipitates contain such high Fe content is provided.

In this work, through analyzing the nucleation trajectories from FFS, the Cu cluster in critical size are found to contain more than 20% Fe for cases of high supersaturation. In disagreement to the experimental observation, the enrichment of Cu in critical clusters is observed only prior to their growth in size. The clusters become pure Cu as the critical nuclei grow into the super-critical clusters, while, according to 3DAP observations, super-critical Cu cluster with radius 1 nm ~ 1.5 nm (number of atoms 400 ~ 1000) still contain significant amount of Fe, around 40%-60%. So far, there is no convincing explanation for the high Fe content in bcc Cu clusters with radius over 1 *nm*. The nano-sized scale investigations from first principles calculations [87], Monte Carlo [80–82], Molecular Dynamics simulations [88] and Phase Field modeling [83] all predict pure bcc Cu clusters in the *super-critical* stage. In the work of Stechauner and Kozeschnik [89], the Inner Particle Diffusion Factor (IPDF) is used to explain the high amount of Fe in super-critical clusters. If IPDF is small, i.e. the diffusivities of elements inside bcc Cu clusters are assumed to be sluggish, the increase of Cu content in clusters is simultaneously happening with the clusters' growth. Therefore, one can observe a large amount of Fe in super-critical clusters in the simulation. However, the diffusivity inside the clusters is not assessable, i.e. IPDF is unable to obtained, since bcc Cu is thermodynamic unstable structure.

With respect to atomistic simulations, it is emphasized that the key simulation ingredient, i.e., the Fe-Cu interactions in metastable bcc Cu, are still lacking or, at least, uncertain, which can give another possible explanation for the high Fe amount in super-critical clusters Since bcc Cu is a mechanically unstable structure, the atomic interactions of Fe-Cu, Fe-Va and Cu-Va in bcc Cu is very difficult to obtain. In the first principles calculations, the bcc-Cu supercell directly transforms to fcc lattice with structural relaxation at 0 K. So far, the author has not found any literature addressing the atomic interactions in bcc Cu. However, the super-critical bcc Cu clusters with radius 1 nm ~ 1.5 nm, observed by 3DAP, contain more than 400 atoms, where the Fe atoms in clusters actually stay in a local bcc Cu environment. It is possible that the

super-critical bcc Cu clusters are subject to a strong strain field to transform from bcc structure to fcc. Before this structural transformation begins, certain amount of Fe in clusters could compensate that strain energy and stabilize the coherent bcc clusters. When clusters grow larger and start to transform into fcc structure, Fe in the clusters then begins to diffuse into the matrix to form the pure Cu fcc precipitates. Yet, this needs to be confirmed by further investigations.

The critical sizes of Cu clusters observed from energy profiles ranges from n^*=12~40 in dilute Fe-Cu alloys at 450~650°C. In contrast to the general understanding of clusters shape in homogeneous nucleation, the shape of Cu clusters with n<50 show an evident geometrical anisotropy. The degree of cluster anisotropy is strongly dependent on the cluster size, where smaller clusters have a higher degree of shape anisotropy on average. In homogeneous nucleation, the coherent nuclei are intuitively considered to be isotropic in shape, i.e. spherical. This assumption is reasonable, when the nucleus is large enough to form a distinguishable bulk, which is approximately to be seemed as consecutive. However, for ultra-fine nuclei, e.g. Cu clusters with n<60, there are no clear bulk and surface regions to be recognized, since a nucleus is actually tens of atoms placed next to each other on the bcc lattice. The crystal structure of the lattice itself influences the arrangement of atoms in an ultra-fine cluster. For example, the bcc Cu clusters with n=5~15 have a preference to align along the <1 1 0> plane. The influence from lattice pattern will degenerate as the clusters grow. This preference vanishes in clusters with n>25. The shape anisotropy of near-critical clusters in Fe-Cu alloys increases the contact area between nuclei and parent phase, which can lead to a higher atomic attachment rate and weaker nucleation driving force compared with the predictions from their corresponding CNT-type expressions.

6.3 Controversial definition for interphase surface

The interfacial energy plays a very important role in the simulation of the early stage of phase transitions in supersaturated solid solutions. This energy term controls the nucleation and growth of the second-phase precipitates and strongly influences the

coarsening kinetics as well as physical properties of the precipitates [67–69][90]. The evaluation of interfacial energy is difficult. The planar interfacial energy of two co-existing phases can be theoretically computed from the Cahn-Hilliard theory [70][71], provided that the interfacial energy gradient is known or calculated by the Generalized Nearest-Neighbor Broken-Bond (GBB) model [11][12] with energy parameters derived from the EAM (Embedded Atom Method) potential or thermodynamic databases. Alternatively, first principles methods [91] and statistical approaches with atomic simulation [29][30] also provide ways to compute coherent interfacial energies in various alloy systems. The curved interface, which is characteristic for nucleation transitions, is more complicated. A practical way is to derive the curved interfacial energy from the energy of a planar interface and apply an appropriate curvature correction. In continuum models, this correction is mainly based on the Tolman length equation [10]. For the broken bond models, the curvature correction is deduced from the reduced number of effective broken bonds across the curved interface [12]. Despite the dispute on the Tolman length equation, these approaches are still questionable in the application to the nanoscale small nuclei in nucleation transitions.

All models for the curved interfacial energy rely on a reasonable definition of the clusters where the bulk of new and old phases are distinguishably separated by the interface between them. Usually, a nucleus is treated as a sphere of bulk surrounded by the EDS (Equi-molar Defined Surface) [92] to preserve the total mass of the system. However, this description of nucleus is hardly satisfied by the critical-size clusters observed in the nucleation processes in Fe-Cu alloys. The critical-size clusters with less than 50 Cu atoms are actually groups of atoms connected with each other with nearest neighbor bonds. They show strong irregularity in the geometrical arrangement of atoms and almost every atom in the clusters is somehow in contact with the bcc-Fe phase. There is no “bulk” to be recognized in these early-stage Cu nuclei, which could be explaining the high amount of Fe discovered in Cu clusters during nucleation. In my opinion, the “interface” between a nucleus and its parent phase is formed before the “bulk” emerging as the result of density fluctuations in the nucleation process. However, it is a rather complex endeavor to characterize the interface. In this work, the clusters

observed in simulations are simply defined as ellipsoids with similar geometrical features, which are in contact with the parent phase by a sharp interface. The best-fitted ellipsoid is not the only way to describe the early-stage clusters. It is of utmost importance to emphasize that the geometrical factor, as well as the interfacial free energy, will change with a different characterization of clusters and definition of interface.

6.4 Pros and cons of RPP method

In this work, a Reweighted Partial Path Method (RPP) is developed and introduced to evaluate the free energy profile of diffusive processes using trajectory information from a single TIS or FFS calculation. The main steps in the RPP method are summarized as follows: (i) after the rate calculation for the transition A→B is finished, the unbiased path probability $\mathcal{P}_{\Lambda}(\mathbf{x}^{\tau})$ of every trajectory is calculated, e.g. using eq. (16) for FFS and the reweighted path ensemble method [43] for TIS; (ii) the partial paths are generated by breaking up the trajectories into path segments according to the effective crossing points on every interface; (iii) the decaying probability U_i, the one-interface crossing probability $p_i^{\ominus}$ and the density of partial path $P_i^{\ominus}(\lambda)$ ($L_i^{\ominus}(\lambda)$) are calculated from partial paths on interface i. (iv) the equilibrium distribution of the order parameter, i.e. $\left\langle \delta\left(\lambda(\mathbf{x}_t)-\lambda\right)\right\rangle$, is evaluated based on the quantities computed in the previous steps according to eq. (15). In Appendix C, some simpler examples to illustrate the RPP procedures in detail are also provided.

In principle, RPP is a related form of the *loop-boundary* method [42], which is proposed in PPTIS (Partial Path Transition Interface Sampling) [93,94] to derive the equilibrium state distribution from partial path ensembles. In the *loop-boundary* method, the equilibrium histogram of λ with $\lambda\in(\lambda_{i\text{-}1}, \lambda_i)$ is evaluated from the partial paths on interfaces i and i-1. PPTIS measures partial paths by performing the shooting algorithm on every interface, while RPP generates partial path from TIS trajectories and reweights

them based on the memory loss assumption. Therefore, similar to PPTIS, the validation of the memory loss assumption is also necessary for the RPP method. In this work, the validation is performed by comparing the first crossing probability of each interface measured in TIS with the one reconstructed from the one-interface crossing probability $p_i^{\ominus}$ in RPP. Since $p_i^{\ominus}$ contains the re-crossing information of interface *i* from all the other interfaces, the consistency in the results from this comparison indicates that the loss of memory is actually an effect in the behavior of trajectories, and vice versa. Except the validation of memory loss assumption proposed in this paper, there are other ways to detect the memory effect in a system, see Refs. [41] and [95]. The MFPT-FFS method proposed by Thapar et al. [96] is also built on a memory loss assumption to evaluate the free energy profile, but employing a different approach—using the Mean First Passage Time (MFPT) estimated from FFS trajectories to solve the stationary Fokker-Plank equation. When using the MFPT-FFS method, the system must be Markovian (memoryless), while RPP allows the system to have a short-range non-Markovian (memory) effect within adjacent interfaces. For a Markovian system, TIS/FFS-RPP and MFPT-FFS will give the same result in free energy evaluation.

The RPP method is very suitable for the study of rare events, such as nucleation processes, where the kinetics in the forward transition is of particular interest but the equilibrium calculation involving the reverse transition or Umbrella Sampling is time-consuming. However, one must be aware that RPP only uses "half" of the information in trajectory space, and the sampling weight of phase points is decreasing with interfaces getting farther away from the initial state. To make sure that RPP is accurate in the whole transition region, in the beginning, the TIS algorithm should collect enough trajectories on every interface, which will re-cross the interfaces behind the present one. In some cases, when the final state is much more energetically favorable than the initial state and when it is difficult to sample the re-crossing trajectories on interfaces close to the B region, then the RPP prediction for the energy profile may be incorrect for the area close to the B region. Still, the estimation of energy profile is reliable for the barrier

height looking from the side of the initial state. This is also a reason why application of the RPP method to processes with only one important transition are recommended.

Other issues regarding the order parameter and interface setting are similar to TIS [20] and PPTIS [41]. The order parameter should be a "proper" one, since the TIS algorithm is more sensitive to the choice of order parameter compared to TPS. As to the interface setting, the memory loss effect between interfaces is weakened as the interfaces get closer to each other according to Ref. [41]. Therefore, it is advised to avoid a dense setting of interfaces in the transition region for the TIS calculation.

The purpose of the RPP method is to provide a means for a quick estimation of the free energy profile. If one wishes to obtain a thorough understanding of the system for the density of states, average committer and other thermodynamic observables, one should employ a more sophisticated approach, such as the reweighted path ensemble [43], generalized replica exchange method (gREM) and its extensions [97][98].

In summary, RPP is an efficient method to evaluate the free energy profile on a given order parameter in TIS/FFS simulations. The advantage of RPP is that it only needs the trajectories from one calculation of TIS/FFS and does not require any additional samplings, i.e. no abundant extra computational cost. Therefore, the combined TIS/FFS-RPP method can simultaneously calculate the reaction rate constant and free energy profile in a transition. Still, there are limitations. The RPP method can only be used in the Markovian system or a system with short-range memory (non-Markovian) effect, so a check for long-range memory effect is necessary. The RPP method is also sensitive to the choice of order parameter. Normally, the order parameter should be a "proper" one. If the TIS/FFS uses a poor order parameter, the RPP method will give incorrect predictions of the free energy profile.

7 Summary

This thesis presents a comprehensive methodology to study the equilibrium and kinetic properties of early-stage precipitation in Fe-Cu system by implementing statistical sampling techniques to Monte Carlo simulations. The nucleation free energy as a function of cluster size is first evaluated by Umbrella Sampling for two concentrations at different temperatures. With Forward Flux Sampling, a large number of nucleation trajectories are generated and used to analyze the nucleation kinetics of Cu clusters. These simulation results are compared to predictions from Classical Nucleation Theory and good agreement is observed. The chemical composition of Cu nuclei is also investigated, showing that the first formed Cu clusters in dilute Fe-Cu alloys aged at low temperatures can contain a substantial amount of Fe atoms. During aging, the clusters first enrich in Cu content from inside the precipitate, and only afterwards growth of the particles commences. In contrast, when aged at a higher temperature, the clusters formed are almost pure Cu particles from the beginning and remain so throughout the subsequent precipitate growth stages. Analysis of the clusters shape shows that the clusters become increasingly non-spherical with decreasing cluster size and increasing supersaturation.

Additionally, a novel approach, the Reweighted Partial Path (RPP) method, is proposed and implemented to efficiently evaluate the energy profile in diffusive processes in a single computation of Transition Interface Sampling or Forward Flux Sampling. The RPP method assumes a loss of memory in the trajectories, which allows a reweighting strategy to calculate the average weights of partial paths on each transition interface. This method is successfully implemented in the calculation of nucleation free energy of Cu precipitates in Fe-Cu solid solution. The RPP-evaluated free energy profile shows a good agreement with Umbrella Sampling results. The accuracy and robustness of the RPP method are also discussed in this thesis. It is emphasized that the RPP method might fail in cases where the history of the trajectories

has a significant influence on the properties of the current state. Therefore, a validation of the memory-loss assumption must be performed in the assessment of RPP results.

References

[1] Volmer M., Weber A., Keimbildung in übersättigten Gebilden, Z. Für Phys. Chem. 119U (1926) 277. doi:10.1515/zpch-1926-11927.

[2] R. Becker, W. Döring, Kinetische Behandlung der Keimbildung in übersättigten Dämpfen, Ann. Phys. 416 (n.d.) 719–752. doi:10.1002/andp.19354160806.

[3] J. Frenkel, Statistical Theory of Condensation Phenomena, J. Chem. Phys. 7 (1939) 200–201. doi:10.1063/1.1750413.

[4] Ya.B. ZELDOVICH, On the Theory of New Phase Formation : Cavitation, Acta Physicochem USSR. 18 (1943) 1.

[5] J.E. McDonald, Homogeneous Nucleation of Vapor Condensation. I. Thermodynamic Aspects, Am. J. Phys. 30 (1962) 870–877. doi:10.1119/1.1941841.

[6] J.E. McDonald, Homogeneous Nucleation of Vapor Condensation. II. Kinetic Aspects, Am. J. Phys. 31 (1963) 31–41. doi:10.1119/1.1969234.

[7] J. Feder, K.C. Russell, J. Lothe, G.M. Pound, Homogeneous nucleation and growth of droplets in vapours, Adv. Phys. 15 (1966) 111–178. doi:10.1080/00018736600101264.

[8] K.C. Russell, Nucleation in solids: The induction and steady state effects, Adv. Colloid Interface Sci. 13 (1980) 205–318. doi:http://dx.doi.org/10.1016/0001-8686(80)80003-0.

[9] H.L. Lukas, S.G. Fries, B. Sundman, others, Computational thermodynamics: the Calphad method, Cambridge university press Cambridge, 2007.

[10] R.C. Tolman, The Effect of Droplet Size on Surface Tension, J. Chem. Phys. 17 (1949) 333–337. doi:10.1063/1.1747247.

[11] B. Sonderegger, E. Kozeschnik, Generalized Nearest-Neighbor Broken-Bond Analysis of Randomly Oriented Coherent Interfaces in Multicomponent Fcc and Bcc Structures, Metall. Mater. Trans. A. 40 (2009) 499–510. doi:10.1007/s11661-008-9752-6.

[12] B. Sonderegger, E. Kozeschnik, Size dependence of the interfacial energy in the generalized nearest-neighbor broken-bond approach, Scr. Mater. 60 (2009) 635–638. doi:https://doi.org/10.1016/j.scriptamat.2008.12.025.

[13] J. Svoboda, F.D. Fischer, P. Fratzl, E. Kozeschnik, Modelling of kinetics in multi-component multi-phase systems with spherical precipitates: I: Theory, Mater. Sci. Eng. A. 385 (2004) 166–174. doi:https://doi.org/10.1016/j.msea.2004.06.018.

[14] D. Landau, K. Binder, A Guide to Monte Carlo Simulations in Statistical Physics, Cambridge University Press, New York, NY, USA, 2005.

[15] C. Dellago, P.G. Bolhuis, F.S. Csajka, D. Chandler, Transition path sampling and the calculation of rate constants, J. Chem. Phys. 108 (1998) 1964–1977. doi:10.1063/1.475562.

[16] P. G. Bolhuis, C. Dellago, D. Chandler, Sampling ensembles of deterministic transition pathways, Faraday Discuss. 110 (1998) 421–436. doi:10.1039/A801266K.

[17] C. Dellago, P.G. Bolhuis, D. Chandler, On the calculation of reaction rate constants in the transition path ensemble, J. Chem. Phys. 110 (1999) 6617–6625. doi:10.1063/1.478569.

[18] P.G. Bolhuis, D. Chandler, C. Dellago, P.L. Geissler, Throwing ropes over rough mountain passes, in the dark, Annu Rev Phys Chem. 53 (2002) 291–318.

[19] C. Dellago, P.G. Bolhuis, P.L. Geissler, Transition Path Sampling, in: Adv. Chem. Phys., John Wiley & Sons, Inc., 2003: pp. 1–78. doi:10.1002/0471231509.ch1.

[20] T.S. van Erp, D. Moroni, P.G. Bolhuis, A novel path sampling method for the calculation of rate constants, J. Chem. Phys. 118 (2003) 7762–7774. doi:http://dx.doi.org/10.1063/1.1562614.

[21] R.J. Allen, P.B. Warren, P.R. ten Wolde, Sampling Rare Switching Events in Biochemical Networks, Phys Rev Lett. 94 (2005) 018104. doi:10.1103/PhysRevLett.94.018104.

[22] R.J. Allen, D. Frenkel, P.R. ten Wolde, Simulating rare events in equilibrium or nonequilibrium stochastic systems, J. Chem. Phys. 124 (2006). doi:http://dx.doi.org/10.1063/1.2140273.

[23] C.H. BENNETT, Molecular Dynamics and Transition State Theory: The Simulation of Infrequent Events, in: Algorithms Chem. Comput., AMERICAN CHEMICAL SOCIETY, 1977: pp. 63–97. doi:10.1021/bk-1977-0046.ch004.

[24] D. Chandler, Statistical mechanics of isomerization dynamics in liquids and the transition state approximation, J. Chem. Phys. 68 (1978) 2959–2970. doi:10.1063/1.436049.

[25] T.S. van Erp, D. Moroni, P.G. Bolhuis, A novel path sampling method for the calculation of rate constants, J. Chem. Phys. 118 (2003) 7762–7774. doi:http://dx.doi.org/10.1063/1.1562614.

[26] S. Kumar, J.M. Rosenberg, D. Bouzida, R.H. Swendsen, P.A. Kollman, Multidimensional free-energy calculations using the weighted histogram analysis method, J. Comput. Chem. 16 (1995) 1339–1350. doi:10.1002/jcc.540161104.

[27] F. Zhu, G. Hummer, Convergence and error estimation in free energy calculations using the weighted histogram analysis method, J. Comput. Chem. 33 (2012) 453–65.

[28] A.M. Ferrenberg, R.H. Swendsen, Optimized Monte Carlo data analysis, Phys Rev Lett. 63 (1989) 1195–1198. doi:10.1103/PhysRevLett.63.1195.

[29] B. Sadigh, P. Erhart, A. Stukowski, A. Caro, E. Martinez, L. Zepeda-Ruiz, Scalable parallel Monte Carlo algorithm for atomistic simulations of precipitation in alloys, Phys Rev B. 85 (2012) 184203. doi:10.1103/PhysRevB.85.184203.

[30] B. Sadigh, P. Erhart, Calculation of excess free energies of precipitates via direct thermodynamic integration across phase boundaries, Phys Rev B. 86 (2012) 134204. doi:10.1103/PhysRevB.86.134204.

[31] information on http://matcalc.at, n.d. http://matcalc.at.

[32] P. Warczok, D. Reith, M. Schober, H. Leitner, R. Podloucky, E. Kozeschnik, Investigation of Cu precipitation in bcc-Fe – Comparison of numerical analysis with experiment, IJMR. 102 (2011) 709–716.

[33] M. Glicksman, Diffusion in Solid: Field Theory, Solid-State Principles, and Applications, Wiley-Interscience, 2000.

[34] J. Fridberg, L. Torndahl, M. Hillert, Diffusion in Iron, JERNKONTORETS Ann. 153 (1969) 263.

[35] B. Jönsson, Assessment of the Mobilities of Cr, Fe and Ni in bcc Cr-Fe-Ni Alloys, ISIJ Int. 35 (1995) 1415–1421. doi:10.2355/isijinternational.35.1415.

[36] D. Reith, M. Stöhr, R. Podloucky, T.C. Kerscher, S. Müller, First-principles modeling of temperature- and concentration-dependent solubility in the phase-separating alloy FexCu1-x, Phys Rev B. 86 (2012) 020201. doi:10.1103/PhysRevB.86.020201.

[37] R. McGraw, Dynamics of Barrier Crossing in Classical Nucleation Theory†, J. Phys. Chem. B - J PHYS CHEM B. 105 (2001).

[38] S. Kumar, J.M. Rosenberg, D. Bouzida, R.H. Swendsen, P.A. Kollman, The weighted histogram analysis method for free-energy calculations on biomolecules. I. The method, J. Comput. Chem. 13 (1992) 1011–1021.

[39] C. Leitold, C. Dellago, Nucleation and structural growth of cluster crystals, J. Chem. Phys. 145 (2016) 074504. doi:10.1063/1.4960958.

[40] D. Kashchiev, Chapter 13 - Stationary nucleation, 1 (2000) 184–223. doi:http://dx.doi.org/10.1016/B978-075064682-6/50014-7.

[41] D. Moroni, P.G. Bolhuis, T.S. van Erp, Rate constants for diffusive processes by partial path sampling, J. Chem. Phys. 120 (2004) 4055–4065. doi:10.1063/1.1644537.

[42] D. Moroni, T.S. van Erp, P.G. Bolhuis, Simultaneous computation of free energies and kinetics of rare events, Phys Rev E. 71 (2005) 056709. doi:10.1103/PhysRevE.71.056709.

[43] J. Rogal, W. Lechner, J. Juraszek, B. Ensing, P.G. Bolhuis, The reweighted path ensemble, J. Chem. Phys. 133 (2010). doi:10.1063/1.3491817.

[44] G.M. White, Steady-State Random Walks with Application to Homogeneous Nucleation, J. Chem. Phys. 50 (1969) 4672. doi:10.1063/1.1670954.

[45] E. Povoden-Karadeniz, Thermodynamic database mc_fe.tdb, Version 2.050, Vienna University of Technology, 2015.

[46] K. Yuge, A. Seko, I. Tanaka, S.R. Nishitani, First-principles study of the effect of lattice vibrations on Cu nucleation free energy in Fe-Cu alloys, Phys Rev B. 72 (2005) 174201. doi:10.1103/PhysRevB.72.174201.

[47] C. Valeriani, R.J. Allen, M.J. Morelli, D. Frenkel, P. Rein Ten Wolde, Computing stationary distributions in equilibrium and nonequilibrium systems with forward flux sampling, J. Chem. Phys. 127 (2007) 1–11. doi:10.1063/1.2767625.

[48] M. Perez, F. Perrard, V. Massardier, X. Kleber, A. Deschamps, H. de Monestrol, P. Pareige, G. Covarel, Low Temperature Solubility of Copper in Iron : Experimental Study Using Thermoelectric Power, Small Angle X-ray Scattering and Tomographic Atom Probe, Philos. Mag. 85 (2005) 2197–2210.

[49] K.F. Kelton, A.L. Greer, C.V. Thompson, Transient nucleation in condensed systems, J. Chem. Phys. 79 (1983) 6261–6276. doi:10.1063/1.445731.

[50] F. Soisson, G. Martin, Monte Carlo simulations of the decomposition of metastable solid solutions: Transient and steady-state nucleation kinetics, Phys. Rev. B. 62 (2000) 203–214. doi:10.1103/PhysRevB.62.203.

[51] G. Stechauner, E. Kozeschnik, Thermo-kinetic modeling of Cu precipitation in α-Fe, Acta Mater. 100 (2015) 135–146. doi:10.1016/j.actamat.2015.08.042.

[52] R. Kampmann, R. Wagner, Kinetics of precipitation in metastable binary alloys - theory and application to Cu-1.9 at % Ti and Ni-14 at % Al, in: Decompos. Alloys Early Stages, Pergamon, 1984: pp. 91–103. http://www.sciencedirect.com/science/article/pii/B9780080316512500185.

[53] R. Wagner, R. Kampmann, P. Voorhees, Homogeneous Second-Phase Precipitation, in: Phase Transform. Mater., Wiley-VCH Verlag GmbH & Co. KGaA, 2005: pp. 309–407. http://dx.doi.org/10.1002/352760264X.ch5.

[54] H. Guo, M. Enomoto, C.J. Shang, Simulation of bcc-Cu precipitation in ternary Fe-Cu-M alloys, Comput. Mater. Sci. 141 (2018) 101–113. doi:https://doi.org/10.1016/j.commatsci.2017.09.023.

[55] R. Becker, W. Döring, Kinetische Behandlung der Keimbildung in übersättigten Dämpfen,

Ann. Phys. 416 (n.d.) 719–752. doi:10.1002/andp.19354160806.
[56] C. Vogler, F. Bruckner, B. Bergmair, T. Huber, D. Suess, C. Dellago, Simulating rare switching events of magnetic nanostructures with forward flux sampling, Phys Rev B. 88 (2013) 134409. doi:10.1103/PhysRevB.88.134409.
[57] E. Clouet, Modeling of Nucleation Processes, ASM Handb. 22A (2009) 203–219. http://arxiv.org/abs/1001.4131.
[58] E. Kozeschnik, C. Bataille, K. Janssens, Modeling solid-state precipitation, Momentum Press, 2013.
[59] S. Jungblut, C. Dellago, Pathways to self-organization: Crystallization via nucleation and growth, Eur. Phys. J. E. 39 (2016) 77. doi:10.1140/epje/i2016-16077-6.
[60] T. Nagano, M. Enomoto, Simulation of the growth of copper critical nucleus in dilute bcc Fe–Cu alloys, Scr. Mater. 55 (2006) 223–226. doi:http://dx.doi.org/10.1016/j.scriptamat.2006.04.015.
[61] E. Kozeschnik, Thermodynamic prediction of the equilibrium chemical composition of critical nuclei: Bcc Cu precipitation in α-Fe, Scr. Mater. 59 (2008) 1018–1021. doi:http://dx.doi.org/10.1016/j.scriptamat.2008.07.008.
[62] S. Primig, G. Stechauner, E. Kozeschnik, Early Stages of Cu Precipitation in 15–5 PH Maraging Steel Revisited − Part I: Experimental Analysis, Steel Res. Int. 88 (2017) 1600084–n/a. doi:10.1002/srin.201600084.
[63] G. Stechauner, S. Primig, E. Kozeschnik, Early Stages of Cu Precipitation in 15-5 PH Maraging Steel Revisited – Part II: Thermokinetic Simulation, Steel Res. Int. 88 (2017) 1600085–n/a. doi:10.1002/srin.201600085.
[64] D. Isheim, D.N. Seidman, Nanoscale studies of segregation at coherent heterophase interfaces in alpha-Fe based systems, Surf Interface Anal. 36 (2004) 569–574.
[65] D. Isheim, M.S. Galiano, M.E. Fine, D.N. Seidman, Interfacial segregation at Cu-rich precipitates in a high-strength low-carbon steel studied on a sub-nanometer scale, Acta Mater. 54 (2006) 841–849.
[66] M. Schober, E. Eidenberger, H. Leitner, P. Staron, D. Reith, R. Podloucky, A critical consideration of magnetism and composition of (bcc) Cu precipitates in (bcc) Fe, Appl Phys A. 99 (2010) 697–704.
[67] I.M. Lifshitz, V.V. Slyozov, The kinetics of precipitation from supersaturated solid solutions, J. Phys. Chem. Solids. 19 (1961) 35–50. doi:https://doi.org/10.1016/0022-3697(61)90054-3.
[68] W. Carl, Theorie der Alterung von Niederschlägen durch Umlösen (Ostwald-Reifung), Z. Für Elektrochem. Berichte Bunsenges. Für Phys. Chem. 65 (n.d.) 581–591. doi:10.1002/bbpc.19610650704.
[69] R. Monzen, K. Takada, K. Matsuda, Coarsening kinetics of Cu particles in an Fe-1.5 % Cu alloy, Z. Für Met. 94 (2003) 1241–1246. doi:10.3139/146.031241.
[70] J.W. Cahn, J.E. Hilliard, Free Energy of a Nonuniform System. I. Interfacial Free Energy, J. Chem. Phys. 28 (1958) 258–267. doi:10.1063/1.1744102.
[71] J.W. Cahn, J.E. Hilliard, Free Energy of a Nonuniform System. III. Nucleation in a Two-Component Incompressible Fluid, J. Chem. Phys. 31 (1959) 688–699. doi:10.1063/1.1730447.
[72] G.R. Speich, R.A. Oriani, The rate of coarsening of copper precipitate in an alpha-iron matrix, Met. Trans. 233 (1965) 623–631.
[73] E. Kozeschnik, J. Svoboda, F.D. Fischer, Shape factors in modeling of precipitation, Mater.

Sci. Eng. A. 441 (2006) 68–72. doi:https://doi.org/10.1016/j.msea.2006.08.088.
[74] M.K. Miller, B.D. Wirth, G.R. Odette, Precipitation in neutron-irradiated Fe-Cu and Fe-Cu-Mn model alloys: a comparison of APT and SANS data, Mater Sci Eng A. 353 (2003) 133–139.
[75] J. Law, I.T. Jolliffe, Principal Component Analysis., The Statistician. 36 (1987) 432. doi:10.2307/2348864.
[76] C. Kittel, Introduction to Solid State Physics, 6th Edition, Wliey, New York, 1987.
[77] R.C. Tolman, The Effect of Droplet Size on Surface Tension, J. Chem. Phys. 17 (1949) 333–337. doi:10.1063/1.1747247.
[78] A. Tröster, K. Binder, Positive Tolman Length in a Lattice Gas with Three-Body Interactions, Phys Rev Lett. 107 (2011) 265701. doi:10.1103/PhysRevLett.107.265701.
[79] P.A. Egelstaff, B. Widom, Liquid Surface Tension near the Triple Point, J. Chem. Phys. 53 (1970) 2667–2669. doi:10.1063/1.1674388.
[80] F. Soisson, A. Barbu, G. Martin, Monte carlo simulations of copper precipitation in dilute iron-cooper alloys during thermal aging and under electron irradiation, Acta Mater. 44 (1996) 3789–3800.
[81] P. Warczok, J. Ženíšek, E. Kozeschnik, Atomistic and continuums modeling of cluster migration and coagulation in precipitation reactions, Comput. Mater. Sci. 60 (2012) 59–65. doi:10.1016/j.commatsci.2012.02.033.
[82] F. Soisson, C.C. Fu, Cu-precipitation kinetics in alpha-Fe from atomistic simulations: Vacancy-tranping effects and Cu-cluster mobility, Phys Rev B. 76 (2007) 214102.
[83] D. Molnar, R. Mukherjee, A. Choudhury, A. Mora, P. Binkele, M. Selzer, B. Nestler, S. Schmauder, Multiscale simulations on the coarsening of Cu-rich precipitates in α-Fe using kinetic Monte Carlo, molecular dynamics and phase-field simulations, Acta Mater. 60 (2012) 6961–6971. doi:https://doi.org/10.1016/j.actamat.2012.08.051.
[84] E. Hornbogen, R.C. Glenn, A metallographic study of precipitation of copper from alpha iron, Tran Met. Soc AIME. 218 (1960) 1067–1070.
[85] P.J. Othen, M.L. Jenkins, G. Smith, W.J. Phytian, Transmission electron-microscope investigations of the structure of copper precipitates in thermally-aged Fe-Cu and Fe-Cu-Ni, Philos Mag Lett. 64 (1991) 383–391.
[86] P.J. Othen, M.L. Jenkins, G. Smith, High-resolution electron-microscopy studies of the structure of Cu precipitates in alpha-Fe, Philos. Mag. Lett. 70 (1994) 1–24.
[87] O.I. Gorbatov, I.K. Razumov, Yu.N. Gornostyrev, V.I. Razumovskiy, P.A. Korzhavyi, A.V. Ruban, Role of magnetism in Cu precipitation in α-Fe, Phys Rev B. 88 (2013) 174113. doi:10.1103/PhysRevB.88.174113.
[88] P. Erhart, B. Sadigh, Low-Temperature Criticality of Martensitic Transformations of Cu Nanoprecipitates in $\ensuremath\alpha$-Fe, Phys Rev Lett. 111 (2013) 025701. doi:10.1103/PhysRevLett.111.025701.
[89] G. Stechauner, E. Kozeschnik, Thermo-kinetic modeling of Cu precipitation in α-Fe, Acta Mater. 100 (2015) 135–146. doi:10.1016/j.actamat.2015.08.042.
[90] A.J. Ardell, Gradient energy, interfacial energy and interface width, Scr. Mater. 66 (2012) 423–426. doi:https://doi.org/10.1016/j.scriptamat.2011.11.043.
[91] M. Asta, J.J. Hoyt, Thermodynamic properties of coherent interfaces in f.c.c.-based Ag–Al alloys: a first-principles study, Acta Mater. 48 (2000) 1089–1096.

doi:https://doi.org/10.1016/S1359-6454(99)00412-7.
[92] J.W. Gibbs, On the Equilibrium of Heterogeneous Substances ..., The Academy, 1874. https://books.google.at/books?id=4375xQEACAAJ.
[93] D. Moroni, P.G. Bolhuis, T.S. van Erp, Rate constants for diffusive processes by partial path sampling, J. Chem. Phys. 120 (2004) 4055–4065. doi:10.1063/1.1644537.
[94] D. Moroni, T.S. van Erp, P.G. Bolhuis, Simultaneous computation of free energies and kinetics of rare events, Phys Rev E. 71 (2005) 056709. doi:10.1103/PhysRevE.71.056709.
[95] S.V. Krivov, Method to describe stochastic dynamics using an optimal coordinate, Phys Rev E. 88 (2013) 062131. doi:10.1103/PhysRevE.88.062131.
[96] V. Thapar, F.A. Escobedo, Simultaneous estimation of free energies and rates using forward flux sampling and mean first passage times, J. Chem. Phys. 143 (2015) 244113. doi:10.1063/1.4938248.
[97] Q. Lu, J. Kim, J.D. Farrell, D.J. Wales, J.E. Straub, Investigating the solid-liquid phase transition of water nanofilms using the generalized replica exchange method, J. Chem. Phys. 141 (2014) 18C525. doi:10.1063/1.4896513.
[98] P. Tian, S.Æ. Jónsson, J. Ferkinghoff-Borg, S.V. Krivov, K. Lindorff-Larsen, A. Irbäck, W. Boomsma, Robust Estimation of Diffusion-Optimized Ensembles for Enhanced Sampling, J. Chem. Theory Comput. 10 (2014) 543–553. doi:10.1021/ct400844x.
[99] N. Goga, A.J. Rzepiela, A.H. de Vries, S.J. Marrink, H.J.C. Berendsen, Efficient Algorithms for Langevin and DPD Dynamics, J. Chem. Theory Comput. 8 (2012) 3637–3649. doi:10.1021/ct3000876.
[100] H. Jung, K. Okazaki, G. Hummer, Transition path sampling of rare events by shooting from the top, J. Chem. Phys. 147 (2017) 152716. doi:10.1063/1.4997378.

Appendix

Appendix A:

The decaying probability that a trajectory, which crossed interface i from A, will return to A before continuing to cross B is defined as $U_i = P(\begin{smallmatrix}0\\M\end{smallmatrix}\big|\begin{smallmatrix}i\\0\end{smallmatrix}) = 1 - P(\begin{smallmatrix}M\\0\end{smallmatrix}\big|\begin{smallmatrix}i\\0\end{smallmatrix})$. According to the memory loss assumption, the following relations hold approximately for any positive integer q>0 [41],

$$\begin{aligned} P(\begin{smallmatrix}l\\m\end{smallmatrix}\big|\begin{smallmatrix}i\\i\pm q\end{smallmatrix}) &\approx P(\begin{smallmatrix}l\\m\end{smallmatrix}\big|\begin{smallmatrix}i\\i\pm 1\end{smallmatrix}) \\ P(\begin{smallmatrix}i+q\\i-1\end{smallmatrix}\big|\begin{smallmatrix}i\\i+1\end{smallmatrix}) &\approx P(\begin{smallmatrix}i+q\\i-1\end{smallmatrix}\big|\begin{smallmatrix}i\\i-1\end{smallmatrix})(\,p_i^{\pm}/p_i^{\pm}) \\ P(\begin{smallmatrix}i-q\\i+1\end{smallmatrix}\big|\begin{smallmatrix}i\\i-1\end{smallmatrix}) &\approx P(\begin{smallmatrix}i-q\\i+1\end{smallmatrix}\big|\begin{smallmatrix}i\\i+1\end{smallmatrix})(\,p_i^{=}/p_i^{\mp}) \end{aligned} \tag{A1}$$

Using the approximation in equation (A1), the following relation in decaying probability is derived as

$$\begin{aligned} \frac{U_{i+1}-U_i}{U_i-U_{i-1}} &= \frac{P(\begin{smallmatrix}0\\M\end{smallmatrix}\big|\begin{smallmatrix}i+1\\0\end{smallmatrix}) - P(\begin{smallmatrix}0\\M\end{smallmatrix}\big|\begin{smallmatrix}i\\0\end{smallmatrix})}{P(\begin{smallmatrix}0\\M\end{smallmatrix}\big|\begin{smallmatrix}i\\0\end{smallmatrix}) - P(\begin{smallmatrix}0\\M\end{smallmatrix}\big|\begin{smallmatrix}i-1\\0\end{smallmatrix})} = \frac{P(\begin{smallmatrix}M\\0\end{smallmatrix}\big|\begin{smallmatrix}i+1\\0\end{smallmatrix})\left(P(\begin{smallmatrix}i+1\\0\end{smallmatrix}\big|\begin{smallmatrix}i\\0\end{smallmatrix})-1\right)}{P(\begin{smallmatrix}M\\0\end{smallmatrix}\big|\begin{smallmatrix}i\\0\end{smallmatrix})\left(P(\begin{smallmatrix}i\\0\end{smallmatrix}\big|\begin{smallmatrix}i-1\\0\end{smallmatrix})-1\right)} \\ &= \frac{P(\begin{smallmatrix}0\\i+1\end{smallmatrix}\big|\begin{smallmatrix}i\\0\end{smallmatrix})}{P(\begin{smallmatrix}i+1\\0\end{smallmatrix}\big|\begin{smallmatrix}i\\0\end{smallmatrix})P(\begin{smallmatrix}0\\i\end{smallmatrix}\big|\begin{smallmatrix}i-1\\0\end{smallmatrix})} \approx \frac{P(\begin{smallmatrix}0\\i+1\end{smallmatrix}\big|\begin{smallmatrix}i\\i-1\end{smallmatrix})}{P(\begin{smallmatrix}i+1\\0\end{smallmatrix}\big|\begin{smallmatrix}i\\0\end{smallmatrix})P(\begin{smallmatrix}0\\i\end{smallmatrix}\big|\begin{smallmatrix}i-1\\i-2\end{smallmatrix})} \\ &\approx \frac{P(\begin{smallmatrix}0\\i+1\end{smallmatrix}\big|\begin{smallmatrix}i\\i+1\end{smallmatrix})(p_i^{=}/p_i^{\mp})}{P(\begin{smallmatrix}i+1\\0\end{smallmatrix}\big|\begin{smallmatrix}i\\0\end{smallmatrix})P(\begin{smallmatrix}0\\i\end{smallmatrix}\big|\begin{smallmatrix}i-1\\i\end{smallmatrix})(p_{i-1}^{=}/p_{i-1}^{\mp})} = \frac{\mathrm{P}_i^{+}\mathrm{P}_{i+1}^{-}(p_i^{=}/p_i^{\mp})}{\mathrm{P}_i^{-}\mathrm{P}_{i+1}^{+}(p_{i-1}^{=}/p_{i-1}^{\mp})} \end{aligned} \tag{A2}$$

Since $\frac{\mathrm{P}_i^{+}}{\mathrm{P}_i^{-}} = \frac{p_1^{\pm}p_2^{\pm}\cdots p_{i-1}^{\pm}}{p_1^{\mp}p_2^{\mp}\cdots p_{i-1}^{\mp}}$ [41], equation (A2) is rewritten as $\frac{U_{i+1}-U_i}{U_i-U_{i-1}} = \frac{p_{i-1}^{\mp}p_i^{=}}{p_{i-1}^{=}p_i^{\pm}}$. This relation can be expanded from U_{i+1} to U_1 as

$$U_{i+1}-U_i = \frac{p_{i-1}^{\mp}p_i^{=}}{p_{i-1}^{=}p_i^{\pm}}\left(U_i-U_{i-1}\right) = \ldots = \frac{p_1^{\mp}p_2^{\mp}\cdots p_{i-1}^{\mp}p_i^{=}}{p_1^{=}p_2^{\pm}\cdots p_i^{\pm}}\left(U_2-U_1\right) \tag{A3}$$

Summing up equation (A3) from 1 to i, we have

$$U_i - U_2 = \left(U_2-U_1\right)\sum_{m=2}^{i-1}\frac{p_1^{\mp}p_2^{\mp}\cdots p_{i-1}^{\mp}p_i^{=}}{p_1^{=}p_2^{\pm}\cdots p_i^{\pm}} \tag{A4}$$

Since $U_M = P(\begin{smallmatrix}0\\M\end{smallmatrix}\big|\begin{smallmatrix}M\\0\end{smallmatrix}) = 0$, U_2 is solved by equation (A4) as

$$U_2 = U_1\left[1+\sum_{m=2}^{M-1}\frac{p_1^{\mp}p_2^{\mp}\cdots p_{i-1}^{\mp}p_i^{=}}{p_1^{=}p_2^{\pm}\cdots p_i^{\pm}}\right]^{-1}\sum_{m=2}^{M-1}\frac{p_1^{\mp}p_2^{\mp}\cdots p_{i-1}^{\mp}p_i^{=}}{p_1^{=}p_2^{\pm}\cdots p_i^{\pm}} \tag{A5}$$

Through combination of equations (A4) and (A5), we derive an expression for the decaying probability for a given *i* as

$$U_i = U_1\left[1+\sum_{m=2}^{M-1}\frac{p_1^{\mp}p_2^{\mp}\cdots p_{i-1}^{\mp}p_i^{=}}{p_1^{=}p_2^{\pm}\cdots p_i^{\pm}}\right]^{-1}\sum_{m=i}^{M-1}\frac{p_1^{\mp}p_2^{\mp}\cdots p_{i-1}^{\mp}p_i^{=}}{p_1^{=}p_2^{\pm}\cdots p_i^{\pm}} \tag{A6}$$

According to the definition, the decaying probability at interface *i* can be rewritten as

$$U_i = P\binom{0}{M}\Big|\binom{i}{0} = 1-P\binom{M}{0}\Big|\binom{i}{0} = 1-\frac{1-U_1}{P_i^{+}} \tag{A7}$$

Since $\frac{U_2-U_1}{U_1-1} = \frac{P\binom{0}{M}\Big|\binom{2}{0}-P\binom{0}{M}\Big|\binom{1}{0}}{P\binom{0}{M}\Big|\binom{1}{0}-1} = \frac{P\binom{M}{0}\Big|\binom{2}{0}P\binom{0}{2}\Big|\binom{1}{0}}{P\binom{M}{0}\Big|\binom{1}{0}} = \frac{p_1^{=}}{p_1^{\pm}}$, equation (A3) is rewritten as

$$U_{i+1}-U_i = \frac{p_1^{\mp}p_2^{\mp}\cdots p_{i-1}^{\mp}p_i^{=}}{p_1^{\pm}p_2^{\pm}\cdots p_i^{\pm}}(U_1-1) \tag{A8}$$

Combining equations (A7) and (A8), we can derive the expression for P_i^{+} as

$$\mathrm{P}_i^{+} = \frac{1-U_1}{1-U_i} = \left(\sum_{m=1}^{i-1}\frac{p_1^{\mp}p_2^{\mp}\cdots p_{m-1}^{\mp}p_m^{=}}{p_1^{\pm}p_2^{\pm}\cdots p_m^{\pm}}\right)^{-1} \tag{A9}$$

Since $\frac{\mathrm{P}_i^{+}}{\mathrm{P}_i^{-}} = \frac{p_1^{\pm}p_2^{\pm}\cdots p_{i-1}^{\pm}}{p_1^{\mp}p_2^{\mp}\cdots p_{i-1}^{\mp}}$ [41], P_i^{-} is also derived from equation (A9)

$$\mathrm{P}_i^{-} = \left(\sum_{m=1}^{i-1}\frac{p_1^{\mp}p_2^{\mp}\cdots p_{m-1}^{\mp}p_m^{=}}{p_1^{\pm}p_2^{\pm}\cdots p_m^{\pm}}\right)^{-1}\prod_{j=1}^{i-1}\frac{p_j^{\mp}}{p_j^{\pm}} \tag{A10}$$

Appendix B:

Since the equilibrium distribution is preserved in trajectory space, there should be no net probability flux passing through the phase points on a given interface *i*. In this case, the average effective crossing on *i* from i+1 equals to the effective crossing from *i*-1, i.e. $\left\langle \psi_{i,i-1} \right\rangle = \left\langle \psi_{i,i+1} \right\rangle$. Combining with eq. (10), one can get $J = \left\langle \Psi_i^{\pm} \right\rangle - \left\langle \Psi_i^{\mp} \right\rangle = 0$. Therefore, the continuity relation by equation (4-14) at equilibrium is reduced to $\left\langle \Psi_i^{\mp} \right\rangle - \frac{p_i^{\pm}}{p_{i-1}^{\mp}} \left\langle \Psi_{i-1}^{\mp} \right\rangle = 0$. Hence,

$$\left\langle \Psi_i^{\mp} \right\rangle = \frac{p_1^{\pm} p_2^{\pm} \cdots p_i^{\pm}}{p_1^{\mp} p_2^{\mp} \cdots p_{i-1}^{\mp}} \left\langle \Psi_0^{\mp} \right\rangle \tag{B1}$$

In the unbiased path ensemble $\{\mathbf{x}^{\tau}\}_{\mathrm{A}}$, there are no trajectories coming from region B, hence $J_{\mathrm{A}} \neq 0$ and $\left\langle \Psi_{M-1}^{\mp} \right\rangle_{\mathrm{A}} = 0$. Based on continuity relation, one can write down the following equations in $\{\mathbf{x}^{\tau}\}_{\mathrm{A}}$ for every interface from 1 to *M*-1:

$$\begin{cases} \dfrac{1}{p_1^{=}} \left\langle \Psi_1^{\mp} \right\rangle_{\mathrm{A}} + J_{\mathrm{A}} = \dfrac{p_1^{\pm}}{p_1^{=}} \left\langle \Psi_0^{\mp} \right\rangle_{\mathrm{A}} \\ \quad \vdots \\ \dfrac{1}{p_i^{=}} \left\langle \Psi_i^{\mp} \right\rangle_{\mathrm{A}} - \dfrac{p_i^{\pm}}{p_i^{=} p_{i-1}^{\mp}} \left\langle \Psi_{i-1}^{\mp} \right\rangle_{\mathrm{A}} + J_{\mathrm{A}} = 0 \\ \quad \vdots \\ -\dfrac{p_{M-1}^{\pm}}{p_{M-1}^{=} p_{M-2}^{\mp}} \left\langle \Psi_{M-2}^{\mp} \right\rangle_{\mathrm{A}} + J_{\mathrm{A}} = 0 \end{cases} \tag{B2}$$

In equation (B2), we have *M*-1 unknowns, including $\left\{ \left\langle \Psi_i^{\mp} \right\rangle_{\mathrm{A}} \right\}_{i=1\ldots M-2}$ and J_{A}, in *M*-1 equations. According to Cramer rule in linear algebra, the solution of equation (B2) is

$$\begin{cases} \left\langle \Psi_i^{\mp} \right\rangle_{\mathrm{A}} = \left\langle \Psi_0^{\mp} \right\rangle_{\mathrm{A}} \dfrac{p_1^{\pm} p_2^{\pm} \cdots p_i^{\pm}}{p_1^{\mp} p_2^{\mp} \cdots p_{i-1}^{\mp}} \cdot \left[1 + \sum_{m=2}^{M-1} \dfrac{p_1^{\mp} p_2^{\mp} \cdots p_{m-1}^{\mp} p_m^{=}}{p_1^{=} p_2^{\pm} \cdots p_m^{\pm}} \right]^{-1} \sum_{m=i+1}^{M-1} \dfrac{p_1^{\mp} p_2^{\mp} \cdots p_{m-1}^{\mp} p_m^{=}}{p_1^{=} p_2^{\pm} \cdots p_m^{\pm}} \\ J_{\mathrm{A}} = \left\langle \Psi_0^{\mp} \right\rangle_{\mathrm{A}} \dfrac{p_1^{\pm}}{p_1^{=}} \left[1 + \sum_{m=2}^{M-1} \dfrac{p_1^{\mp} p_2^{\mp} \cdots p_{m-1}^{\mp} p_m^{=}}{p_1^{=} p_2^{\pm} \cdots p_m^{\pm}} \right]^{-1} \end{cases} \tag{B3}$$

Since $\left\langle \Psi_0^{\mp} \right\rangle_{\mathrm{A}} = \left\langle \psi_{0,1} \right\rangle_{\mathrm{A}}$ and $\left\langle \Psi_0^{\pm} \right\rangle = \left\langle \psi_{1,0} \right\rangle$, hence $U_1 = P(\begin{smallmatrix} 0 \\ M \end{smallmatrix} \Big| \begin{smallmatrix} 1 \\ 0 \end{smallmatrix}) = \dfrac{\left\langle \psi_{1,0} h_{0.M}^{f} \right\rangle}{\left\langle \psi_{1,0} \right\rangle} = \dfrac{\left\langle h_{\mathcal{A}} \psi_{0,1} \right\rangle}{\left\langle \psi_{1,0} \right\rangle} = \dfrac{\left\langle h_{\mathcal{A}} \right\rangle \left\langle \Psi_0^{\mp} \right\rangle_{\mathcal{A}}}{\left\langle \Psi_0^{\pm} \right\rangle}$. Since $\dfrac{\left\langle \Psi_0^{\mp} \right\rangle_{\mathrm{A}}}{\left\langle \Psi_0^{\pm} \right\rangle} = \dfrac{U_1}{\left\langle h_{\mathcal{A}} \right\rangle}$ and $\left\langle \Psi_0^{\mp} \right\rangle = \left\langle \Psi_0^{\pm} \right\rangle$, combining with eq.(B1), (A6) and (4-12), the effective crossing of interface i in $\{\mathbf{x}^{\tau}\}_{\mathrm{A}}$ is connected with its equilibrium average by

$$\begin{cases} \left\langle \Psi_i^{\mp} \right\rangle_{\mathrm{A}} = \dfrac{U_{i+1}}{\left\langle h_{\mathcal{A}} \right\rangle} \cdot \left\langle \Psi_i^{\mp} \right\rangle \\ \left\langle \Psi_i^{+}_{+} \right\rangle_{\mathrm{A}} = \dfrac{U_{i+1}}{\left\langle h_{\mathcal{A}} \right\rangle} \cdot \left\langle \Psi_i^{+}_{+} \right\rangle \end{cases} \quad \text{and} \quad \begin{cases} \left\langle \Psi_i^{\pm} \right\rangle_{\mathrm{A}} = \dfrac{U_{i+1}}{\left\langle h_{\mathcal{A}} \right\rangle} \cdot \left\langle \Psi_i^{\pm} \right\rangle + J_{\mathrm{A}} \\ \left\langle \Psi_i^{=} \right\rangle_{\mathrm{A}} = \dfrac{U_{i+1}}{\left\langle h_{\mathcal{A}} \right\rangle} \cdot \left\langle \Psi_i^{=} \right\rangle + \dfrac{p_i^{=}}{p_i^{\pm}} J_{\mathrm{A}} \end{cases}$$

$$J_{\mathrm{A}} = \left\langle \Psi_0^{\mp} \right\rangle_{\mathrm{A}} \cdot \frac{1 - U_1}{U_1} = \left\langle \Psi_0^{\pm} \right\rangle_{\mathrm{A}} P(\begin{smallmatrix} M \\ 0 \end{smallmatrix} \Big| \begin{smallmatrix} 1 \\ 0 \end{smallmatrix}) \qquad \text{(B4)}$$

Appendix C:

In this appendix, FFS-RPP method is applied in 3 examples: a single particle moving in a one-dimensional double-well potential with overdamped Langevin dynamics (Example 1) and Langevin dynamics with inertia (Example 2), and the single particle moving in a two-dimensional double-well potential with overdamped Langevin dynamics (Example 3).

Example 1:

In this example, we apply the FFS-RPP method in one particle moving with Langevin dynamics in a one-dimensional double-well potential,

$$\begin{aligned} v(t) &= \dot{x}(t) \\ m\dot{v}(t) + \gamma v(t) &= f(x) + \eta(t) \end{aligned} \qquad \text{(C1)}$$

where $x(t)$ is the position of particle at time t, γ is a constant friction, $f(x)$ is the force at x, and m is the mass of particle, which is set to 1 for convenience. $\eta(t)$ is the Gaussian noise satisfying $\langle\eta(t)\rangle=0$ and $\langle\eta(t)\ \eta(0)\rangle=2k_BT\gamma\delta(t)$, where $\delta(t)$ is the delta function, k_B is the Boltzmann constant and T is the temperature. We consider a potential

$$V(x) = 5k_BT(x^4 - 2x^2 + 1) \qquad \text{(C2)},$$

hence $f(x) = -\partial V(x)/\partial x$. Clearly, the two stable points in this system are located at $(\pm1, 0)$, and the saddle point is at $(0, 0)$ with a barrier height of $5k_BT$.

As the initial example, we consider an overdamped Langevin dynamics and the numerical integration of equation (C1) uses the following scheme

$$x(t+\Delta t) = x(t)\Delta t + \frac{Df(x)}{k_BT}\Delta t + \sqrt{2D\Delta t}\,\boldsymbol{g} \qquad \text{(C3)}$$

where Δt is the time increasement, D is the diffusion coefficient defined as $D=k_BT/\gamma$, and $\boldsymbol{g}$ is a random number generated from the normal distribution $\mathcal{N}(0,1)$. In simulations, $k_BT=0.1$, and $\gamma=10^4$. x is discretized with a unit of $x_0=0.01$, and trajectories are stored every $t_0=4$, with time increasement $\Delta t=0.05\ t_0$. The stable states A and B are defined around $(-1, 0)$ and $(1, 0)$, respectively. To study the transition A→B, the order parameter is chosen as $\lambda=x$, and FFS simulation is carried out with 12 interfaces

$\{\lambda_i\}_{i=0...11}$ and 1000 configurations on the boundary of A state. For convenience, λ_0 is set to be overlapped with λ_1, as $\lambda_0=\lambda_1=-0.8$, and $\lambda_{11}=0.8$. The details of FFS calculation is listed in Table C1.

Table C1 Interfaces and number of trajectories on each interface in FFS in Example 1. M_i trajectories are firing off from interface i and, among them, N_i trajectories reach i+1 before returning to i. $P(^{i+1}_{0}|^{i}_{0})$ is the crossing probability, which is calculated as $P(^{i+1}_{0}|^{i}_{0}) = N_i / M_i$.

i	λ_i	M_i	N_i	$M_i - N_i$	$P(^{i+1}_{0}\|^{i}_{0})$
1	-0.8	15183	1000	14183	6.59E-02
2	-0.7	8000	2808	5192	3.51E-01
3	-0.6	8000	1499	6501	1.87E-01
4	-0.4	8000	2118	5882	2.65E-01
5	-0.2	8000	3247	4753	4.06E-01
6	0	8000	5117	2883	6.40E-01
7	0.2	8000	6770	1230	8.46E-01
8	0.4	8000	7697	303	9.62E-01
9	0.6	8000	7953	47	9.94E-01
10	0.7	8000	7977	23	9.97E-01

After the FFS calculation for the transition A→B is finished, we use the RPP method to evaluate the equilibrium distribution of λ, $\left\langle \delta\left(\lambda(\mathbf{x}_t)-\lambda\right)\right\rangle$, from the trajectories obtained in FFS. The RPP procedures are as follows:

1. Calculation of $\mathcal{P}_{\mathrm{A}}(\mathbf{x}^{\tau})$, $\left\langle \Psi_i^{\Theta}\right\rangle_{\mathrm{A}}$ and p_i^{Θ}

The first thing to do is to do calculate $\mathcal{P}_{\mathrm{A}}(\mathbf{x}^{\tau})$—— the unbiased path probability of every trajectory in the ensemble with all paths starting from stable A state and ending in either A or B states. This probability can be easily calculated as (Equation (16) in the manuscript)

$$\mathcal{P}_{\mathrm{A}}(\mathbf{x}^{\tau}) = \begin{cases} P(_0^i|_0^1)/N_i & \text{if } \max\left(\lambda(\mathbf{x}^{\tau})\right) \in (\lambda_i, \lambda_{i+1}) \\ P(_0^M|_0^1) & \text{if } \max\left(\lambda(\mathbf{x}^{\tau})\right) \geq \lambda_M \end{cases} \quad \text{(C4)}$$

Then we locate the points when trajectories effectively crossing every interface and find out the crossing type Θ, i.e. Θ in $\pm$, $=$, $\overset{+}{+}$ and . The average of effective crossings on interface i, $\left\langle \Psi_i^{\Theta} \right\rangle_{\mathrm{A}}$, can be calculated as $\left\langle \Psi_i^{\Theta} \right\rangle_{\mathrm{A}} = \sum \mathcal{P}_{\mathrm{A}}(\mathbf{x}^{\tau}) n_i^{\Theta}(\mathbf{x}^{\tau})$, where $n_i^{\Theta}(\mathbf{x}^{\tau})$ describes how many times the trajectory $\mathbf{x}^{\tau}$ effectively crosses interface i with crossing type Θ. The average effective crossing, $\left\langle \Psi_i^{\Theta} \right\rangle_{\mathrm{A}}$, in Example 1 is listed in Table C2.

Table C2 the effective crossing on interfaces i, $\left\langle \Psi_i^{\Theta} \right\rangle_{\mathrm{A}}$, with Θ in $\pm$, $=$, $\overset{+}{+}$ and $\mp$.

i	$\left\langle \Psi_i^{\pm} \right\rangle_{\mathrm{A}}$	$\left\langle \Psi_i^{=} \right\rangle_{\mathrm{A}}$	$\left\langle \Psi_i^{\overset{+}{+}} \right\rangle_{\mathrm{A}}$	$\left\langle \Psi_i^{\mp} \right\rangle_{\mathrm{A}}$
1	6.59E-02	9.34E-01	0	6.56E-02
2	2.31E-02	4.27E-02	9.69E-03	2.29E-02
3	4.58E-03	2.82E-02	5.90E-04	4.34E-03
4	1.19E-03	3.98E-03	2.51E-04	9.48E-04
5	4.89E-04	9.50E-04	1.13E-04	2.49E-04
6	3.16E-04	2.86E-04	6.35E-05	7.61E-05
7	2.64E-04	1.16E-04	4.84E-05	2.34E-05
8	2.52E-04	6.04E-05	3.85E-05	1.14E-05
9	2.54E-04	3.59E-05	8.95E-05	1.39E-05
10	2.40E-04	1.03E-04	0	0

Under the assumption of memory loss, the partial crossing probability p_i^{Θ} at i can be calculated from $\left\langle \Psi_i^{\Theta} \right\rangle_{\mathrm{A}}$ as (Equation (9) in the manuscript) as

$$p_i^{\pm} = \frac{\left\langle \Psi_i^{\pm} \right\rangle_A}{\left\langle \Psi_i^{\pm} \right\rangle_A + \left\langle \Psi_i^{=} \right\rangle_A} \qquad p_i^{\mp} = \frac{\left\langle \Psi_i^{\mp} \right\rangle_A}{\left\langle \Psi_i^{\mp} \right\rangle_A + \left\langle \Psi_i^{\pm} \right\rangle_A} \tag{C5}$$

with $p_i^{=} = 1 - p_i^{\pm}$ and $p_i^{\pm} = 1 - p_i^{\mp}$. The values of p_i^{Θ} is displayed in Fig. C1(a). When the memory loss assumption is valid, the crossing probability P_i^{+} in FFS, defined as

$$\mathrm{P}_i^{+} = P\left(\begin{matrix} i \\ 0 \end{matrix} \middle| \begin{matrix} 1 \\ 0 \end{matrix}\right) = \prod_{j=1}^{i-1} P\left(\begin{matrix} i+1 \\ 0 \end{matrix} \middle| \begin{matrix} i \\ 0 \end{matrix}\right) \tag{C6}$$

should be the same as the ones calculated from partial crossing probability in RPP as

$$\mathrm{P}_i^{+} = \left(\sum_{m=1}^{i-1} \frac{p_1^{\mp} p_2^{\mp} \cdots p_{m-1}^{\mp} p_m^{=}}{p_1^{\pm} p_2^{\pm} \cdots p_m^{\pm}} \right)^{-1} \tag{C7}.$$

In Fig. C1(b), P_i^{+} with i=1…11 by equation (C6) (FFS) and equation (C7) (RPP) are compared, and the excellent agreement indicate that there is no memory effect between interfaces.

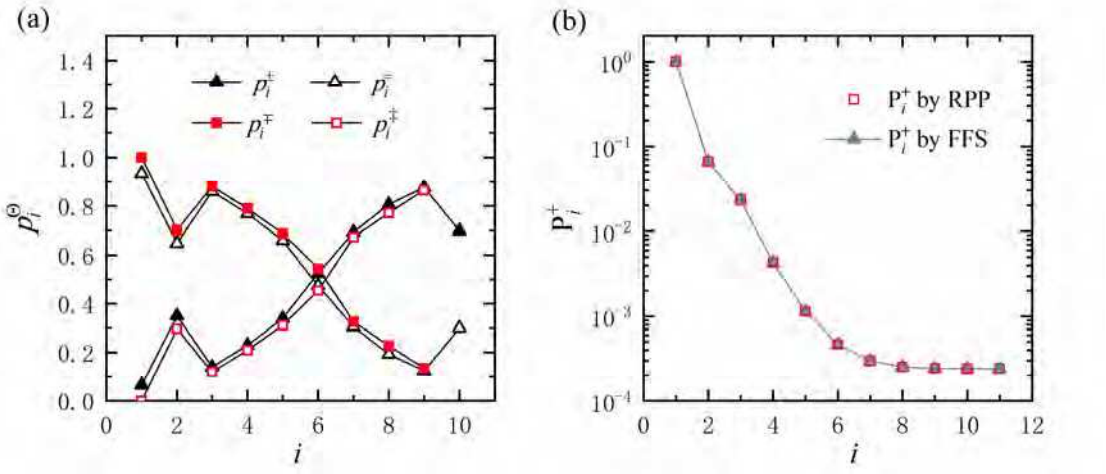

Fig. C1 (a) the partial crossing probability on each interface. (b) the crossing probability $\mathrm{P}_i^{+} = P\left(\begin{matrix} i \\ 0 \end{matrix} \middle| \begin{matrix} 1 \\ 0 \end{matrix}\right)$ evaluated from partial crossing probabilities in RPP (equation (C7)), compared the ones from FFS (equation (C6)).

2. Calculation of $P_i^{\Theta}(\lambda)$ and $L_i^{\Theta}(\lambda)$

Then,we need to compute the average density of λ in the partial paths, $P_i^{\Theta}(\lambda)$, and the average density of λ in the loop segment of partial path, $L_i^{\Theta}(\lambda)$, on every

interface. When a trajectory effectively crossed interface i at phase point $\mathbf{x}_t$, the histogram of λ in the partial path is calculated as $\rho_i^{\Theta}(\lambda)=\int_{t-\Delta t_{\Theta}^{b}}^{t+\Delta t_{\Theta}^{f}} dt'\ \delta\left(\lambda(\mathbf{x}_{t'})-\lambda\right)$, where Δt_{Θ}^{f} and Δt_{Θ}^{b} are the times when the trajectory first crosses interface i+1 (i−1) forward and backward from $\mathbf{x}_t$, respectively. For Θ in $\pm,\mp,=$ and $\begin{matrix}+\\+\end{matrix}$, $\left(\Delta t_{\Theta}^{f},\Delta t_{\Theta}^{b}\right)$ is taken as $\left(\Delta t_{i+1}^{f},\Delta t_{i-1}^{b}\right),\left(\Delta t_{i-1}^{f},\Delta t_{i+1}^{b}\right),\left(\Delta t_{i-1}^{f},\Delta t_{i-1}^{b}\right)$ and $\left(\Delta t_{i+1}^{f},\Delta t_{i+1}^{b}\right)$, respectively. In step 1, we have located the effective crossing points on i for every trajectory. At each effective crossing point, $\mathbf{x}_t$, one can obtain a histogram of λ, $\rho_i^{\Theta}(\lambda)$. Accordingly, the average density of λ in the partial path Θ having crossed i is calculated as $P_i^{\Theta}(\lambda)=\left\langle \rho_i^{\Theta}(\lambda)\right\rangle_{\Psi_i^{\Theta}}$. For illustration, $P_i^{\Theta}(\lambda)$ on interface i=6 is plotted in Fig. C2(a).

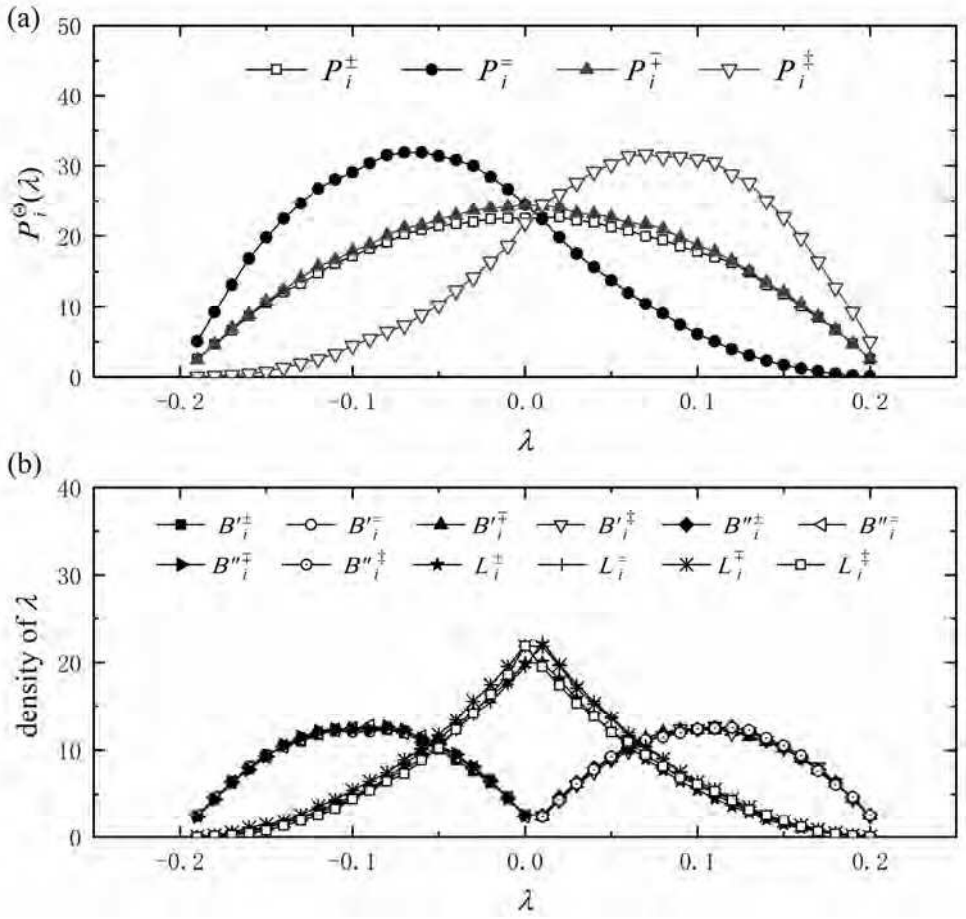

Fig. C2 (a) the average density of λ in the partial path on interface i=6; (b) the average density of λ in the segments of partial path on interface i=6, where $B_i^{'\Theta}$ and $B_i^{''\Theta}$ are the density of λ on the boundary

segments before and after the crossing point $\mathbf{x}_t$, respectively, and L_i^{Θ} is the density of λ on the loop segment, with Θ in $\pm$, $=$, $\overset{+}{+}$ and $\mp$.

The density of λ on the loop segment of partial paths is calculated in a similar way as $L_i^{\Theta}(\lambda)=\left\langle l_i^{\Theta}(\lambda)\right\rangle_{\Psi_i^{\Theta}}$, with $l_i^{\Theta}(\lambda)=\int_{t-\Delta t_{\Theta}^{b}}^{t+\Delta t_{\Theta}^{f}} dt'\,\delta\left(\lambda(\mathbf{x}_{t'})-\lambda\right)l_i(\mathbf{x}_{t'})$. When $\mathbf{x}_t$ is on the loop segment of partial path, $l_i(\mathbf{x}_t)=1$, otherwise, $l_i(\mathbf{x}_t)=0$. $L_i^{\Theta}(\lambda)$ on i=6 is plotted on Fig. C2(b) along with the average density of λ on the boundary segment before crossing point $\mathbf{x}_t$, $B_i^{'\Theta}$, and the average density of λ on the boundary segment after crossing point $\mathbf{x}_t$, $B_i^{''\Theta}$. Clearly, $P_i^{\Theta}(\lambda)=B_i^{'\Theta}(\lambda)+B_i^{''\Theta}(\lambda)+L_i^{\Theta}(\lambda)$.

3. Calculation of $\left\langle\delta\left(\lambda(\mathbf{x}_t)-\lambda\right)\right\rangle$

The final step is to use Equation (15) in the manuscript to calculate the equilibrium distribution of λ as

$$\left\langle\delta\left(\lambda(\mathbf{x}_t)-\lambda\right)\right\rangle=\frac{\left\langle\delta\left(\lambda(\mathbf{x}_t)-\lambda\right)\right\rangle_{\mathrm{A}}-J_{\mathrm{A}}C_i(\lambda)}{U_i} \qquad \text{(C8)}$$

where $C_i(\lambda)=P_{i-1}^{\pm}(\lambda)+\frac{p_{i-1}^{=}}{p_{i-1}^{\pm}}P_{i-1}^{=}(\lambda)+p_i^{\pm}L_i^{\pm}(\lambda)+p_i^{=}L_i^{=}(\lambda)-p_i^{=}L_i^{\mp}(\lambda)-\frac{p_i^{+}p_i^{=}}{p_i^{\mp}}L_i^{\pm}(\lambda)$.

$C_i(\lambda)$ is calculated based on the $P_i^{\Theta}(\lambda)$, $L_i^{\Theta}(\lambda)$ and p_i^{Θ} we have obtained in previous steps. Decaying probability U_i is defined as $U_i=P\left(\begin{smallmatrix}0\\M\end{smallmatrix}\middle|\begin{smallmatrix}i\\0\end{smallmatrix}\right)=1-\prod_{j=i}^{M-1}P\left(\begin{smallmatrix}j+1\\0\end{smallmatrix}\middle|\begin{smallmatrix}j\\0\end{smallmatrix}\right)$, and $J_{\mathrm{A}}=\left\langle\Psi_0^{\pm}\right\rangle_{\mathrm{A}}P\left(\begin{smallmatrix}M\\0\end{smallmatrix}\middle|\begin{smallmatrix}1\\0\end{smallmatrix}\right)$. Since the interface i=0 and i=1 are overlapped, $\left\langle\Psi_0^{\pm}\right\rangle_{\mathrm{A}}$=1, and $J_{\mathrm{A}}=P\left(\begin{smallmatrix}M\\0\end{smallmatrix}\middle|\begin{smallmatrix}1\\0\end{smallmatrix}\right)=\prod_{i=1}^{M-1}P\left(\begin{smallmatrix}i+1\\0\end{smallmatrix}\middle|\begin{smallmatrix}i\\0\end{smallmatrix}\right)$. Therefore, using the crossing probabilities listed in Table C1, U_i and J_{A} can be easily obtained. $\left\langle\delta\left(\lambda(\mathbf{x}_t)-\lambda\right)\right\rangle_{\mathrm{A}}$ is the stationary distribution of λ in transition A→B, which is calculated as $\left\langle\delta\left(\lambda(\mathbf{x}_t)-\lambda\right)\right\rangle_{\mathrm{A}}=\int_0^{\tau}\boldsymbol{\mathcal{P}}_{\mathrm{A}}(\mathbf{x}^{\tau})\delta\left(\lambda(\mathbf{x}_{t'})-\lambda\right)dt'$. In Fig. C3(a), $\left\langle\delta\left(\lambda(\mathbf{x}_t)-\lambda\right)\right\rangle_{\mathrm{A}}$ and $J_{\mathrm{A}}C_i(\lambda)$ are plotted as a function of λ.

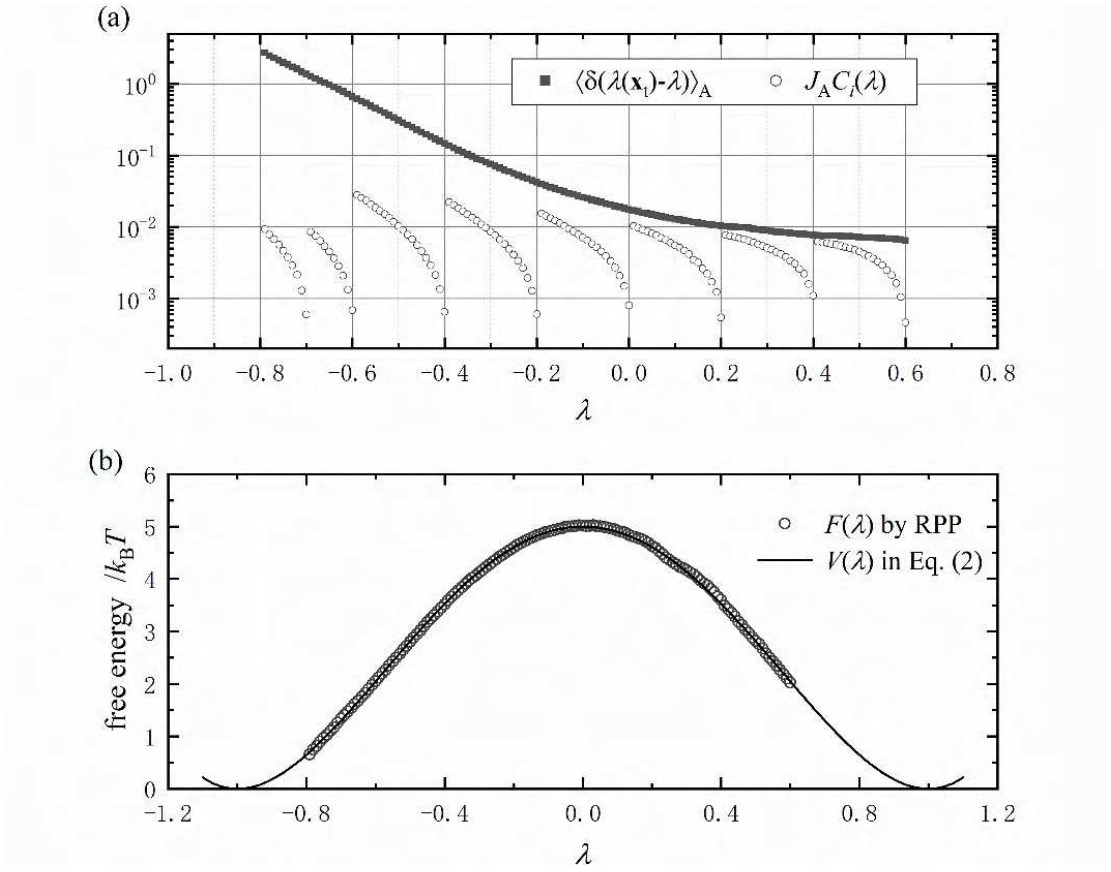

Fig. C3 (a) $\left\langle \delta\left(\lambda(\mathbf{x}_t)-\lambda\right)\right\rangle_A$, as the steady stationary distribution of λ transition from A→B, is plotted with the values of $J_A C_i(\lambda)$. (b) the free energy $F(\lambda)$ is evaluated by RPP method from FFS trajectories and compared with $V(\lambda)$ from equation (C2).

Using equation (C8), now one can obtain $\left\langle \delta\left(\lambda(\mathbf{x}_t)-\lambda\right)\right\rangle$, and accordingly the free energy on λ as $F(\lambda)=-k_B T \ln\left\langle \delta\left(\lambda(\mathbf{x}_t)-\lambda\right)\right\rangle + c$, where c is a constant. The free energy $F(\lambda)$ evaluated by RPP method reveals excellent agreement with $V(\lambda)$ by equation (C2) in Fig. C3(b).

Example 2

In this example, we still consider the one particle moving in the one-dimensional double-well potential, i.e. $V(x)$ in equation (C2), using Langevin dynamics with inertia. The numerical iteration for inertia dynamics follows a leap-frog impulsive Langevin integrator [99] as:

$$
\begin{aligned}
v'\left(t+\frac{\Delta t}{2}\right) &= v\left(t-\frac{\Delta t}{2}\right)+\frac{f(x)}{m}\Delta t,\\
\Delta v &= -\alpha v'\left(t+\frac{\Delta t}{2}\right)+\sqrt{\frac{k_{\mathrm{B}}T}{m}\alpha(2-\alpha)}\boldsymbol{g},\\
x(t+\Delta t) &= x(t)+\left(v'\left(t+\frac{\Delta t}{2}\right)+\frac{\Delta v}{2}\right)\Delta t,\\
v\left(t+\frac{\Delta t}{2}\right) &= v'\left(t+\frac{\Delta t}{2}\right)+\Delta v
\end{aligned}
\qquad \text{(C9)}
$$

where $\alpha = 1-e^{-\gamma\Delta t}$, $f(x) = -\partial V(x)/\partial x$, and $\boldsymbol{g}$ is a random number generated from normal distribution $\mathcal{N}(0,1)$. In this example, we consider two cases with γ=10, and γ=2. The rest parameters in equation (C9) are the same in the two cases as $k_{\mathrm{B}}T$=0.1, x_0=0.01, t_0=0.01, and Δt=t_0/20.

Like example 1, the two stable states A and B are set to be around x = −1.0 and x = 1.0, and the order parameter for transition A→B is set as λ= x in FFS. We also set 12 interfaces $\{\lambda_i\}_{i=0\ldots11}$ from −0.8 to 0.8, with λ_0 =−0.8, λ_{11}=0.8, and λ_0=λ_1 for simplicity, and 1000 configurations on λ_0 to start FFS. The details of FFS calculations are listed in Table C2 for the case with γ=10, and in Table C3 for the case with γ=2.

Table C2 Interfaces, number of trajectories and the crossing probability on each interface in FFS for γ=10 in Example 2.

i	λ_i	M_i	N_i	$M_i - N_i$	$P(^{i+1\,|\,i}_{0\,|\,0})$
1	-0.8	5000	1565	3435	3.13E-01
2	-0.7	5000	2065	2935	4.13E-01
3	-0.6	5000	1024	3976	2.05E-01
4	-0.4	5000	1422	3578	2.84E-01
5	-0.2	5000	2259	2741	4.52E-01
6	0	5000	3443	1557	6.89E-01
7	0.2	5000	4436	564	8.87E-01
8	0.4	5000	4847	153	9.69E-01
9	0.6	5000	4981	19	9.96E-01

10	0.7	5000	4990	10	9.98E-01

Table C3 Interfaces, number of trajectories and the crossing probability on each interface in FFS for γ=2 in Example 2.

i	λ_i	M_i	N_i	$M_i - N_i$	$P(^{i+1}_{0}\|^{i}_{0})$
1	-0.8	5000	2523	2477	5.05E-01
2	-0.7	5000	2376	2624	4.75E-01
3	-0.6	5000	1121	3879	2.24E-01
4	-0.4	5000	1576	3424	3.15E-01
5	-0.2	5000	2659	2341	5.32E-01
6	0	5000	4129	871	8.26E-01
7	0.2	5000	4859	141	9.72E-01
8	0.4	5000	4983	17	9.97E-01
9	0.6	5000	4996	4	9.99E-01
10	0.7	10252	10251	1	1.00E+00

Following the RPP procedure in example 1, the free energy as a function of λ, $F(\lambda)$, is evaluated in both cases. To compare the effect from inertia, the correlation function, $\frac{\langle v(t)v(0)\rangle}{\langle v(0)v(0)\rangle}$, is calculated and displayed in Fig. C4(b) and Fig. C6(b). When γ=10, the correlation of velocity decays to neglectable as t>30t_0 (see Fig. C4(b)), while the average length of partial path segments (see Fig. C4(a)) is around 50t_0 to 150t_0, suggesting that there is no strong correlation of velocity between partial paths in adjacent interfaces. In the case with γ=2, the average length of partial path segments (see Fig. C6(a)) is around 10t_0 to 80t_0, but the velocity is strongly correlated within t=100t_0 (see Fig. C6(b)), indicating that the correlation of partial path between interfaces is non-negligible in this case. However, since the dynamics in both cases is still Markovian, the condition for using RPP method is satisfied. The values of P_i^+ by FFS and RPP agree very well with each other in both cases (see Fig. C5 for γ=10 and Fig.

C7 for γ=2), as well as the free energy $F(\lambda)$ by RPP and $V(\lambda)$. In γ=2, $F(\lambda)$ is not continuous in the side near state B, because of the bad statistics from the short partial path on interfaces near state B. Despite of that, $F(\lambda)$ is in overall agreeable with $V(\lambda)$ and reveals the correct barrier of $V(\lambda)$ looking from state A.

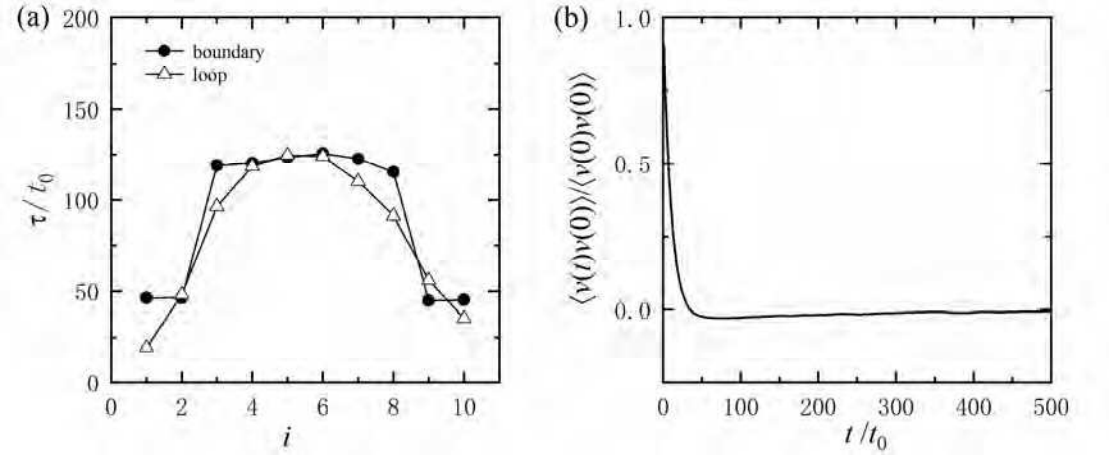

Fig. C4 In example 2 with γ=10, (a) the average path length of partial path segments. For interface i, boundary refers to the boundary segment in region [λ_i, λ_{i+1}], and loop refers to the loop segment on interface i. (b) the correlation function of velocity.

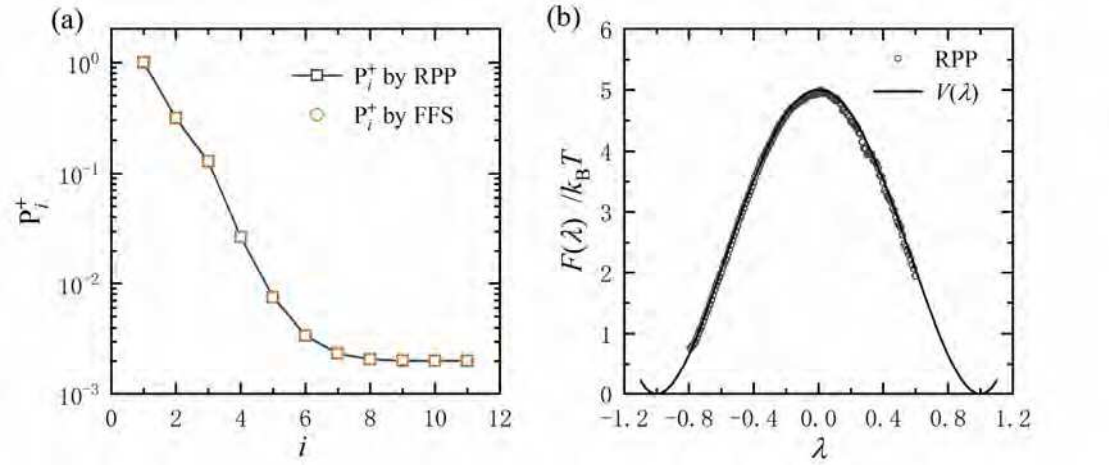

Fig. C5 In Example 2 with γ=10, (a) the crossing probability evaluated from RPP method compared with the one from FFS. (b) the free energy evaluated from RPP compared with $V(\lambda)$ in equation (C2).

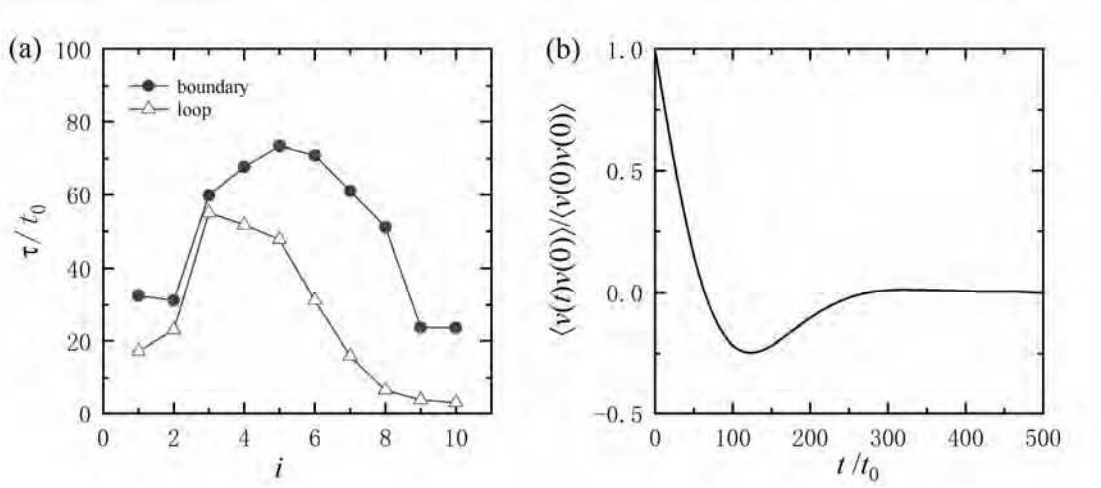

Fig. C6 In Example 2 with γ=2, (a) the average path length of partial path segments. For interface i, boundary refers to the boundary segment in region $[\lambda_i, \lambda_{i+1}]$, and loop refers to the loop segment on interface i. (b) the correlation function of velocity.

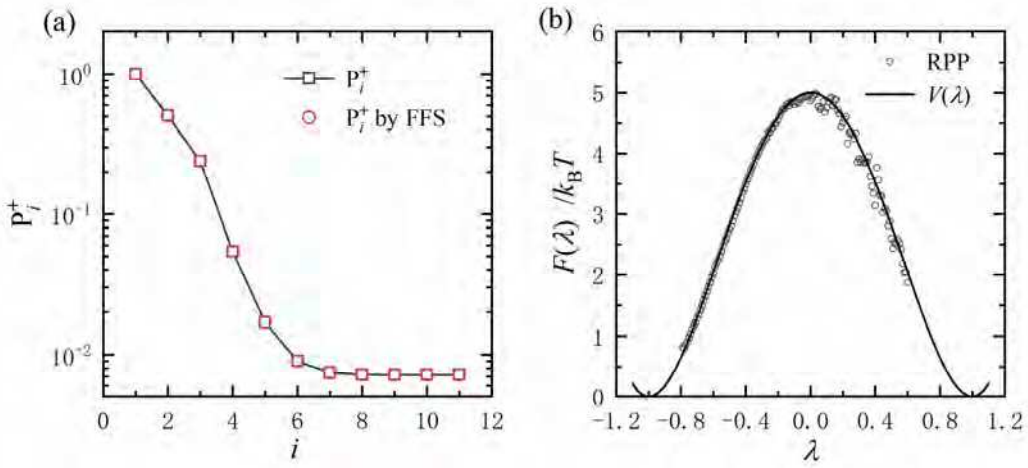

Fig. C7 In Example 2 with γ=2, (a) the crossing probability evaluated from RPP method compared with the one from FFS. (b) the free energy evaluated from RPP compared with $V(\lambda)$ in equation (C2).

Example 3

In this example, the one-particle system is in a two-dimensional potential [100]as

$$V(x,y) = 4k_BT\left(\left(x^2-1\right)^2+\left(x-y\right)^2\right) \qquad \text{(C10)}$$

where the two stable points are at (−1, −1) and (1, 1), and the saddle point is at (0, 0) with an energy barrier of $4k_BT$ as plotted on Fig.C8.

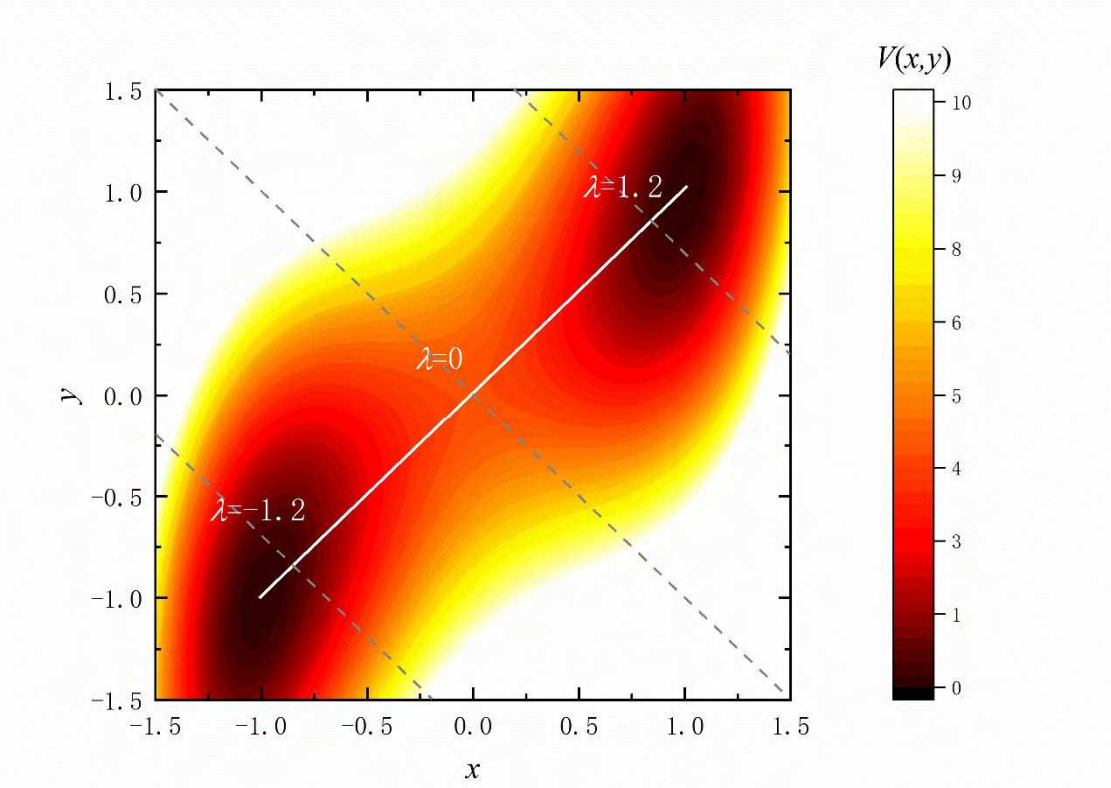

Fig. C8 the contour of the two-dimensional potential $V(x,y)$ in equation (C10). The white solid line marked the direction of order parameter, $\lambda=(x+y)/\sqrt{2}$, and the grey dashed lines are the interfaces defined by $\lambda=-1.2$, 0 and 1.2 in the phase space.

In this example, we use the overdamped Langevin dynamics to simulation the moving of the particle under $V(x, y)$, where the particle's position is denoted as $\boldsymbol{r}=(x, y)$. The trajectories are advanced as

$$\begin{aligned} x(t+\Delta t) &= x(t)+\frac{Df_x(x,y)}{k_{\mathrm{B}}T}\Delta t+\sqrt{2D\Delta t}\,\boldsymbol{g}_x \\ y(t+\Delta t) &= y(t)+\frac{Df_y(x,y)}{k_{\mathrm{B}}T}\Delta t+\sqrt{2D\Delta t}\,\boldsymbol{g}_y \end{aligned} \qquad \text{(C11)}$$

where $\boldsymbol{g}_x$ and $\boldsymbol{g}_y$ are two uncorrelated Gaussian random number generated from the s distribution $\mathcal{N}(0,1)$. f_x and f_y are the forces defined as $f_x(x,y)=-\partial V(x,y)/\partial x$ and $f_y(x,y)=-\partial V(x,y)/\partial y$, respectively. D is the diffusion coefficient defined as $D=k_{\mathrm{B}}T/\gamma$. In simulations, $k_{\mathrm{B}}T=0.1$, and $\gamma=10^4$. x and y are discretized with a unit of 0.01,

and trajectories are stored every t_0=4, with time increasement Δt =0.05t_0. The stable states A and B are defined around the point (−1, −1) and (1, 1), respectively. To study the transition A→B in FFS, the order parameter is chosen as $\lambda=(x+y)/\sqrt{2}$, and 16 interfaces $\{\lambda_i\}_{i=0\ldots15}$ are set along λ from −1.2 to 1.2. λ_0 is set to be overlapped with λ_1 as $\lambda_0=\lambda_1=-1.2$, and $\lambda_{15}=1.2$. FFS starts with 1000 configurations on λ_0. The details of FFS in example 3 are listed in Table C4.

Table C4. Interfaces, number of trajectories and the crossing probability on each interface in FFS for Example 3.

i	λ_i	M_i	N_i	$M_i - N_i$	$P(^{i+1}_{0}\|^{i}_{0})$
1	-1.2	10970	1000	9970	9.12E-02
2	-1.1	8000	3575	4425	4.47E-01
3	-1	8000	2880	5120	3.60E-01
4	-0.8	8000	3551	4449	4.44E-01
5	-0.6	8000	3689	4311	4.61E-01
6	-0.4	8000	3944	4056	4.93E-01
7	-0.2	8000	4406	3594	5.51E-01
8	0	8000	5382	2618	6.73E-01
9	0.2	8000	6482	1518	8.10E-01
10	0.4	8000	7305	695	9.13E-01
11	0.6	8000	7727	273	9.66E-01
12	0.8	8000	7853	147	9.82E-01
13	1	8000	7968	32	9.96E-01
14	1.1	8000	7952	48	9.94E-01

Following the RPP procedure in example 1, the free energy $F(\lambda)$ as a function of $\lambda=(x+y)/\sqrt{2}$ is evaluated for $\lambda\in[-1.2, 1.1]$. In Fig. C9(b), $F(\lambda)$ by RPP is compared with the free energy calculated from Umbrella Sampling (US). The choice of order

parameter $\lambda=(x+y)/\sqrt{2}$ is a straightforward but non-optimized one, but the free energy by RPP is overall consistent with the results from US with a slightly higher barrier. The crossing probability P_i^+ calculated in RPP is the same as the ones evaluated from FFS (see Fig. C9(a)). The criterion of comparing P_i^+ form RPP and FFS is not able to tell whether the order parameter is a good or poor one.

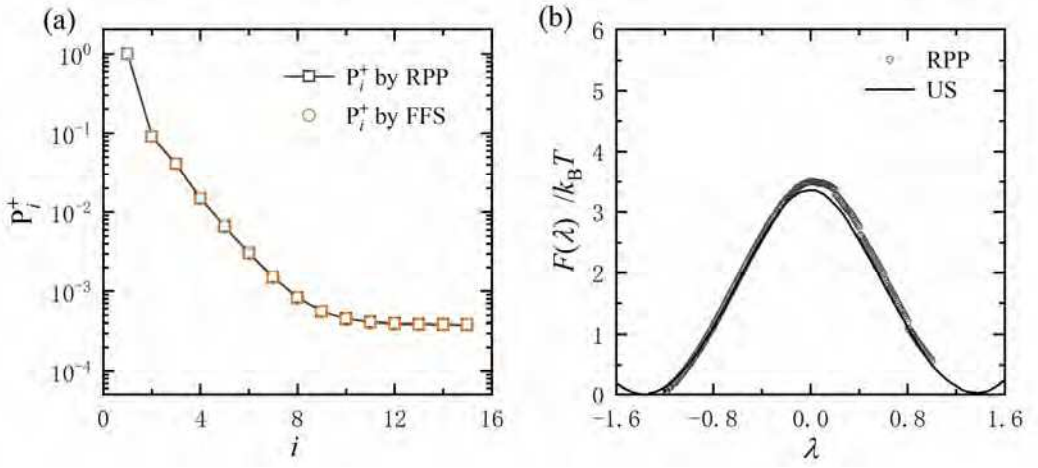

Fig.C9 In Example 3, (a) the crossing probability evaluated from RPP method compared with the one from FFS. (b) the free energy evaluated from RPP compared with the free energy evaluated withUmbrella Sampling (US).

Appedix D: Pubilications

Journal articles

[1] L.Qin, C.Dellago, and E. Kozeschnik, "An efficient method to reconstruct free energy profiles for diffusive processes in transition interface sampling and forward flux sampling simulations," **The Journal of Chemical Physics**, vol. 150, no. 9, p. 094 114, 2019. DOI: 10.1063/1.5080933.

[2] L. Qin, A. Redermeier, C. Dellago, E. Kozeschnik, and C. Karner, "Rigid-lattice monte carlo study of nucleation kinetics in dilute bcc fe-cu alloys using statistical sampling techniques," **Acta Materialia**, vol. 159, pp. 429–438, 2018. DOI: 10.1016/j.actamat.2018.08.035

[3] L. Qin and E. Kozeschnik, "Morphlogical analysis of Cu nanoparticles during nucleation in tempered Fe-Cu alloys", in preparation.

Conference Proceedings

[4] L. Qin, A. Redermeier, E. Kozeschnik, C. Karner, and C. Dellago, "A statistical methodology to reconstruct nucleation pathways in the fe-cu system," in THERMEC 2016, ser. Materials Science Forum, vol. 879, Trans Tech Publications Ltd, Feb. 2017, pp. 1529–1534. DOI: 10.4028/www.scientific.net/MSF.879.1529.

Rigid-lattice Monte Carlo study of nucleation kinetics in dilute bcc Fe-Cu alloys using statistical sampling techniques

Lin Qin[1, a *], Alice Redermeier[1, b], Christoph Dellago[2, e], Ernst Kozeschnik[1, c], Carina Karner[2,d]

[1] TU Wien, Institute of Materials Science and Technology, Vienna, Austria

[2] University of Vienna, Faculty of Physics, Vienna, Austria

[a]lin.qin@tuwien.ac.at, [b]alice.redermeier@tuwien.ac.at, [c]ernst.kozeschnik@tuwien.ac.at, [d]carina.karner@univie.ac.at, [e]christoph.dellago@univie.ac.at

Keywords: Nucleation Kinetics, Rare Event Sampling, Monte Carlo simulation

Abstract

The chemical composition and nucleation kinetics of Cu precipitates in thermally aged bcc Fe-Cu alloys is investigated with statistical sampling techniques combined with Monte Carlo simulation. The analysis of nucleation dynamics is performed by a rigid-lattice Monte Carlo algorithm based on the vacancy-exchange mechanism. At elevated aging temperatures from 450 to 650°C, the critical cluster size and the corresponding nucleation barrier are evaluated using an Umbrella Sampling technique. The nucleation rate of Cu precipitates is calculated on basis of nucleation trajectories harvested by Forward Flux Sampling (FFS). The fastest nucleation in dilute bcc Fe-Cu alloys is predicted to occur at 550 ~ 600°C, which is in good agreement with experimental findings. The critical Cu clusters at 450 to 650°C are found to contain 10 ~ 40 atoms with an increasing nucleation energy barrier from 10 to 23 $k_B T$. For small clusters with less than 30 atoms, a significant shape anisotropy is observed during nucleation. Special emphasis is placed on the Cu concentration profiles of critical nuclei, where we observe that the first formed Cu clusters contain a substantial amount of iron at lower annealing temperatures. However, the Cu content of the clusters increases rapidly to almost unity during aging. Growth of the clusters follows mostly after the nucleus has substantially enriched in Cu content.

1. Introduction

The Fe-Cu binary system is a well-studied model system in precipitation-hardening ferritic alloys, where Cu precipitates play an important role in materials strengthening. It is commonly acknowledged that, in thermally-aged binary Fe-1-30%Cu alloys, copper precipitates undergo a BCC-9R-FCC transition during the precipitation process [1][2][3]. The chemical composition of these bcc precipitates, however, is still unclear. In recent Atom Probe (3DAP) investigations [4][5][6], the bcc Cu-rich precipitates are assumed to contain about 50% Fe atoms, while the results from small-angle neutron

scattering (SANS) [7] indicate a significantly higher Cu content of more than 70%. Schober et al. [6] attribute this discrepancy to the assumption of non-magnetic Cu precipitates in SANS experiments and the insensitivity to very small clusters of only sub-nanometer radius in 3DAP techniques. Unfortunately, no direct explanation for why the bcc precipitates contain such high Fe content is provided.

The properties of the bcc precipitates are directly linked to the nucleation behavior that occurs in the early stages of Cu precipitation, which is hard to detect with present experimental measuring techniques [8] since this process involves ultra-fine nuclei and transient barrier crossing motions [9]. In theoretical descriptions of precipitation, such as the Kampman and Wagner (KWN model [10]) and Cahn-Hilliard based approaches [11][12][13], the nucleation kinetics is described by the growth of critical clusters with pre-defined particle size, chemical composition and number of density from Classical Nucleation Theory (CNT) [14][15][16][17]. However, the nucleation rate predicted by CNT is very sensitive to the choice of input parameter values, e.g., precipitate/matrix interfacial energy and atomistic attachment frequencies. These quantities are not straightforwardly obtained from experimental data or theoretic calculations.

An alternative way to study nucleation kinetics is provided by the Monte Carlo method [18][19][20][21][22][23], which allows for a detailed tracking of the formation trajectories of Cu particles during the whole precipitation process. In the literature, various Monte Carlo algorithms have been proposed and successfully implemented in software to investigate the diffusion kinetics [18], cluster mobility [23] and vacancy-cluster interactions [20] in the Fe-Cu system. However, the microscopic properties of critical or pre-critical clusters are not specifically addressed in these studies. One issue with this technique is that, considering the computational effort, Monte Carlo simulations are usually carried out in small-size samples with the order of a few tens of nanometers and only for short times, which are likely to cause insufficient statistics in the simulation and lead to an inaccurate estimation of the number density of clusters, especially in weakly supersaturated cases [22].

To address this issue, we study the nucleation kinetics of coherent Cu particles in dilute Fe-Cu alloys by applying enhanced statistical sampling techniques to Monte Carlo simulations. An Umbrella Sampling strategy [24][25] is employed to evaluate the equilibrium distribution of early-stage clusters and to reconstruct the nucleation free energy for single cluster as a function of its size [26]. The nucleation kinetics is investigated with a Forward Flux Sampling (FFS) technique [27] by harvesting trajectories of cluster formation and calculating the nucleation rates of Cu precipitates in the primary stage. Additional nucleation quantities, such as the atomic attachment frequency and the Zeldovich factor, are also evaluated and compared with predictions of CNT. Finally, the configurations with the largest clusters in critical size are collected from nucleation trajectories to perform the analysis of size, shape and concentration profiles as the major properties of critical clusters.

2. Methodology

2.1. Rigid-lattice Monte Carlo Simulation

The nucleation dynamics simulation for Cu precipitation in dilute bcc Fe alloys is performed with the Rigid Lattice Monte Carlo (LMC) scheme implemented in the software MatCalc [28]. A bcc lattice of 30×30×30 unit cells is used with periodic boundary condition. Atomic diffusivity is described by the vacancy exchange mechanism and real time is coupled to a Monte Carlo step (MCS) by defining the average time increment corresponding one vacancy jump [21] as $\Delta t = \frac{a^2 x_{\mathrm{Va,MC}}}{6D_{\mathrm{A}}} \cdot k$, where a is the nearest neighbor distance in bcc-Fe (2.468 Å), D_{A} is the macroscopic diffusion coefficient of the jumping atom A in bcc-Fe, $x_{\mathrm{Va,MC}}$ is the vacancy site fraction in the simulation box and k is a correction for the diffusion correlation effect in the vacancy exchange mechanism (0.727 for bcc lattice [29]).

The LMC steps are governed by an atomic interaction energy formulated in the Local Chemical Environment (LCE) framework expressed in reference to a particular center atom [21]. The energy of the system is calculated as the sum of all pair-wise bond energies extending from each atom up to the second nearest neighbors,

$$E = \frac{1}{2} \sum \sum_{i=1}^{2} n_{\mathrm{AB}}^{(i)} \varepsilon_{\mathrm{AB}}^{(i)} \tag{1}$$

where $n_{\mathrm{AB}}^{(i)}$ and $\varepsilon_{\mathrm{AB}}^{(i)}$ are the number of AB bonds and the corresponding bond energy in the i-th nearest neighbor shell. $\varepsilon_{\mathrm{AB}}^{(i)} = \chi_{\mathrm{A}} \varepsilon_{\mathrm{AB}}^{\mathrm{A}(i)} + \chi_{\mathrm{A}} \varepsilon_{\mathrm{AB}}^{\mathrm{B}(i)}$, where χ_{A} and χ_{B} are the atomic fractions of A and B in the local environment and $\varepsilon_{\mathrm{AB}}^{\mathrm{A}(i)}$ ($\varepsilon_{\mathrm{AB}}^{\mathrm{B}(i)}$) is the AB bond energy in a pure A and B environment, respectively. The summation includes all the possible combinations of bonds for A and B, representing the atomic species Cu and Fe, as well as Va, representing the substitutional vacancy. The LCE potential is a very flexible and robust energy model, whose parameters can be calibrated with various methodologies, such as experimental measurements, first principle calculations, or thermodynamic assessment. The details of this potential can be found in Ref. [21].

In the LMC framework, the acceptance probability for a vacancy exchange with a nearest neighbor atom is given by

$$P = \exp\left(-\frac{\Delta E}{k_{\mathrm{B}} T}\right) \tag{2}$$

where ΔE represents the total energy difference between the initial state and the state after the exchange event. If $\Delta E < 0$, $P = 1$.

Table 1 lists interaction energy of Fe-Cu on the first neighbor shell, $\varepsilon_{\mathrm{CuFe}}^{\mathrm{Cu}(1)}$ and $\varepsilon_{\mathrm{CuFe}}^{\mathrm{Fe}(1)}$, at different temperatures from 450 ~ 700°C. For other neighbor shells, $\varepsilon_{\mathrm{CuFe}}^{(i)} = (r_i / r_1)^{-6} \varepsilon_{\mathrm{CuFe}}^{(1)}$, where r_1 and r_i are the first and i-th nearest neighbor distances,

respectively. Using this setting of LCE potential, the solubility limits of Cu in bcc-Fe ($x_{Cu}^{bcc\_Fe}$) and Fe in bcc-Cu ($x_{Fe}^{bcc\_Cu}$) are calculated from the slab-diffusion LMC simulations[30], and the values are validated by thermodynamic assessment based on the Calphad approach [28,31,32] (see Table 1). Since we use the tracer diffusion coefficient (e.g. D_{Cu}, is 1.5 $m^2 \cdot s^{-1}$ [33], and D_{Fe} is 7.4 $m^2 \cdot s^{-1}$ [34] in bcc_Fe at 500°C) to couple the MC step with real time, there is no need to additionally define interactions for atom and vacancy, i.e. $\varepsilon_{CuVa}^{(i)}$ and $\varepsilon_{FeVa}^{(i)}$ are set to zero. The vacancy-vacancy interaction is also neglected, because only one vacancy is placed in the simulation sample.

Table 1. Values of $\varepsilon_{CuFe}^{Fe(1)}$ and $\varepsilon_{CuFe}^{Cu(1)}$ used in this work and the corresponding solubility limits of Cu in bcc-Fe ($x_{Cu}^{bcc\_Fe}$) and Fe in bcc-Cu ($x_{Fe}^{bcc\_Cu}$) reproduced by the LCE potential in the slab-diffusion LMC simulations [30]. Values of solubility limits from thermodynamic (TD) assessment [28,31,32] are listed for comparison.

T /°C	$\varepsilon_{CuFe}^{Cu(1)}$ /meV	$\varepsilon_{CuFe}^{Fe(1)}$ /meV	LMC		TD-assessment	
			$x_{Cu}^{bcc\_Fe}$ at.%	$x_{Fe}^{bcc\_Cu}$ at.%	$x_{Cu}^{bcc\_Fe}$ at.%	$x_{Fe}^{bcc\_Cu}$ at.%
450	48.8	45.2	0.039	0.033	0.042	0.032
500	47.5	44.8	0.080	0.062	0.077	0.063
550	46.3	44.5	0.126	0.115	0.131	0.116
600	45.1	44.0	0.210	0.198	0.212	0.199
650	44.1	43.6	0.333	0.322	0.329	0.320
700	43.1	43.0	0.494	0.497	0.494	0.490

2.2 Microscopic cluster description and order parameter

A cluster formed during simulation is recognized as a group of solute atoms connected with each other within the nearest neighbor distance. The size of a cluster is defined as the total number of solute atoms on this network. Clearly, the smallest cluster is a dimer (two Cu atoms next to each other within the nearest neighbor distance), and a Cu atom without any other Cu atom in its nearest neighbor shell is regarded as a solute atom in the matrix. This cluster detection recognizes all the clusters formed during nucleation including both, unstable pre-critical as well as stable post-critical ones, to provide a sound evaluation of the cluster size distribution.

In the present work, the order parameter describing the nucleation process is taken as the size of the largest cluster/precipitate in the simulation box. In classical theories, since nucleation is assumed to happen independently among clusters, the dynamic description of a single-cluster nucleation is used to represent the nucleation process of

the whole system on an average basis [9]. Therefore, the cluster size in CNT only refers to individual precipitates, which are not necessarily the "largest" ones. However, in our Monte Carlo simulation, we observe several of precipitates with different sizes simultaneously forming and dissolving in the matrix. Using the size of the largest clusters as order parameter represents a simple but efficient way to characterize the nucleation stage in atomic simulations.

2.3 Umbrella Sampling

From statistic point of view, the nucleation free energy is corresponding to the equilibrated size distribution of clusters in a certain supersaturated condition. This distribution will not be established in reality, since, during nucleation, there is always a net forward transition from small clusters to large stable ones until the phase separation completed. When focusing on one cluster, the equilibrium size distribution is equivalent to the probability of finding the cluster in a given size n on its own nucleation trajectory, which is proportional to the total time the cluster spends on size n during nucleation. However, due to the presence of nucleation barrier, the chance to observe a cluster around critical size n^* is extremely rare compared to it in other size, which results in large statistical errors in estimation of equilibrium probability around n^*. To solve the problem, we implement the Umbrella Sampling technique [24][25] in the evaluation of nucleation free energy in this work.

Umbrella Sampling [24][25] is a commonly used strategy to obtain the free energy profile along a chosen physical coordinate by performing a series of simulations under a biased potential to constrain the system inside local regions in configuration space. In our Umbrella Sampling simulations we choose the size of largest cluster n as this coordinate, or order parameter, and a set of windows is defined for the sampling with the bias energy given by $U_i = \frac{\kappa}{2}\left(n - n_i\right)^2$, where n_i is the restrained value of the i-th window and κ is a spring constant. According to probability theory, the number density observed in the i-th window sampling, $\rho_i(n)$, fulfills the following equation,

$$\rho_i(n) = f_i c_i(n) \rho(n) \tag{3}$$

where $\rho(n)$ is the unbiased equilibrium probability of a particle of size n, which is connected to the free energy by $F(n) = -k_B T \ln \rho(n)$. The factor $c_i(n)$ is related to the bias potential by $c_i(n) = \exp\left[-U_i(n)/k_B T\right]$, and f_i is a normalized factor defined as $f_i = 1 \Big/ \sum_{i=1}^{n} c_i(n)\rho(n)$.

Based on the maximum likelihood theory, the equilibrium probability of n can be written as

$$\rho(n) = \frac{M(n)}{\sum_i N_i f_i c_i(n)} \tag{4}$$

where $M(n)$ is the accumulated number of n-sized particles combining all the window samplings, and N_i is the total number of samples in the i-th window sampling. Equations (3) and (4) are known as the coupled nonlinear WHAM (Weighted Histogram Analysis Method) [24][35] equations, which can be solved iteratively for f_i and $\rho(n)$ until self-consistency is achieved.

It is stressed that $\rho(n)$, solved by WHAM, denotes the equilibrium probability of finding the system with size of the largest cluster equaling to n, which is clearly different from the equilibrium probability, $f(n)$, defined on a single cluster model in classical theories. Nevertheless, $\rho(n)$ and $f(n)$ will overlap for large n, when only one cluster of that size is observed in the Umbrella Sampling simulations [26]. Accordingly, the CNT-type/single-cluster free energy, $\Delta G(n)$, can be calculated as

$$\Delta G(n)/k_B T = \begin{cases} -\ln f(n) & n \le n_{\text{patch}} \\ -\ln \rho(n) + C & n > n_{\text{patch}} \end{cases} \tag{5}$$

where n_{patch} is the point where the two free energy curves are patched up and C is an adjustable coefficient to make the free energy continuous at the patching point. For small values of n, $n \le n_{\text{patch}}$, the probability $f(n)$ approximately equals to the stationary size distribution established when nucleation takes place [36], which is calculated by directly in a conventional, or brute-force, MC simulation without bias potential.

2.3. Forward Flux Sampling (FFS)

The Forward Flux Sampling (FFS) technique, as originally proposed by Allen et al. [27] to calculate the rate constant for rare reactions in complex biochemical switches, is utilized to study the nucleation rate of Cu precipitates.

In the FFS method one considers a typically high-dimensional phase space. Each point in this space represents a microscopic state of the system specified by the multi-dimensional coordinate $\boldsymbol{X}$. Regions A and B are two stable (metastable) states defined in terms of an order parameter $\lambda(\boldsymbol{X})$, such that the system is in state A if $\lambda(\boldsymbol{X}) < \lambda_0$, and in state B if $\lambda(\boldsymbol{X}) > \lambda_m$. A series of non-overlapping interfaces $\{\lambda_i\}_{i=1\ldots m-1}$ is defined between states A and B as illustrated in Fig.1. In FFS one first performs brute-force simulations starting in state A. Every time a trajectory forward-crosses λ_0, the respective system configuration is stored, and the simulation is restarted until N_0 configurations are collected. The average number of crossings through interface λ_0 out of state A per unit time is denoted as initial flux $\Phi_{A,0} = N_0 / \Delta t_{tot}$, where Δt_{tot} is the total time the system remains in state A during the simulation.

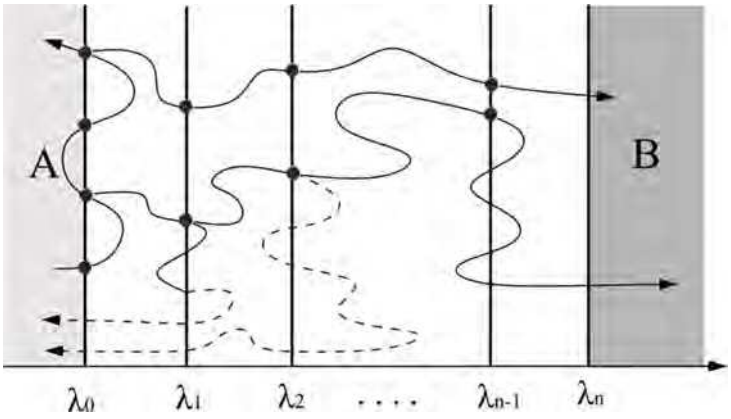

Fig. 1 Schematic of a phase region between stable states A and B, which is sectioned into a series of non-overlapping interfaces $\{\lambda_i\}_{i=1\ldots n-1}$.

In the next step, the collected configurations on λ_0 serve as starting points of trajectories which are followed until the trajectory either crosses λ_1 or returns back to state A. A total of M_0 trajectories are "fired" from λ_0 to generate a set of configurations on λ_1, which are used to start new trajectories and repeat the process for the next interface. From each interface λ_i, M_i trajectories are fired and harvested that either reach the next interface λ_{i+1} or return to state A. The probability that a trajectory, which has crossed λ_i coming from state A, continues to cross λ_{i+1} before returning to state A is defined as the crossing probability $P(\lambda_{i+1}\,|\,\lambda_i) = N_i^s / M_i$. Here, N_i^s is the number of trajectories that successfully cross λ_{i+1} from λ_i. The whole procedure is terminated when at least one trajectory reaches state B, and the transition rate constant k_{AB} can be obtained from [13]

$$k_{AB} = \Phi_{A,0} \prod_{i=0}^{m-1} P(\lambda_{i+1}\,|\,\lambda_i) \tag{6}$$

For a single nucleation event, the random (initial) state without large clusters is treated as reactant (state A) and the post-critical state, where sufficiently large and stable clusters have formed, is treated as product (state B). Generally, when using the largest cluster size n as order parameter, $\lambda(\boldsymbol{X})=n$, the nucleation trajectory is a time-dependent function of cluster size as $n(t)$. The forward crossing of a given interface λ_i at time t is defined as $n(t) > \lambda_i$, while the backward crossing is defined as $n(t) \leq \lambda_i$. The interfaces $\{\lambda_i\}_{i=0\ldots m}$ are a group of increasing values acting as milestones to determine the time to store the configurations in which the largest cluster first-time reaches or exceeds a given size λ_i. The reaction rate coefficient for a nucleation event expressed by eq. (6) can be considered as the frequency of forming one stable large cluster from the random solution, which is treated as a product of the frequency the largest cluster in the system attempting to grows over the a small size of λ_0, i.e. the initial flux $\Phi_{A,0}$, and the conditional probability of a cluster in size λ_0 grows to a large post-critical cluster

($n>\lambda_m$) before dissolving, i.e. the crossing probability $P(\lambda_m \mid \lambda_0) = \prod_{i=0}^{m-1} P(\lambda_{i+1} \mid \lambda_i)$.

Therefore, $1/k_{AB}$ is equivalent to the average time that the system needs to form one stable post-critical precipitate from the random state. Accordingly, denoting the volume of the MC simulation box by V, the nucleation rate is calculated as [37]

$$J = k_{AB} / V \tag{7}$$

3. Results and Discussion

3.1 Nucleation free energy

In the present Umbrella Sampling, a set of windows is defined with restrained values of $\{n_i\} = \{2, 4, 6, \ldots, 60\}$ and a spring constant of 0.23 $k_B T$ for all the samplings. The size of the largest cluster is tracked for every MC step, and after 5000 MC sweeps for equilibration, the value of n is recorded every iteration for 20000 MC sweeps in each window.

The free energy $F(n)$ for cluster formation in a Fe-1%Cu alloy at 600°C (solid curve in Fig. 2) is calculated by $F(n) = -k_B T \ln \rho(n)$, with $\rho(n)$ obtained using eqs. (3) and (4) applied to the umbrella sampling results. One can clearly observe a wide and comparably flat free energy barrier with the critical size, corresponding to the top of the barrier at around n=38. The local minimum at n=5 comes from the fact that the free energy $F(n)$ is a function of the *largest cluster* size, and due to the thermal fluctuations in random state, $F(n)$ sharply increases as n approaches 0. The position of the local minimum depends on the degree of supersaturation and the size of MC simulation box [26]. The brute-force simulation is performed to evaluate the equilibrium number density, $f(n)$, for small clusters. $-\ln f(n)$ is depicted by the dashed curve in Fig. 2. According to eq. (5), the CNT-type/single-cluster free energy $\Delta G(n)$ is reconstructed by merging the two curves at the patching point n=10 with the same gradient (illustrated by dotted line in Fig.2). To avoid ambiguity, the term *nucleation free energy* refers to $\Delta G(n)$ in this work.

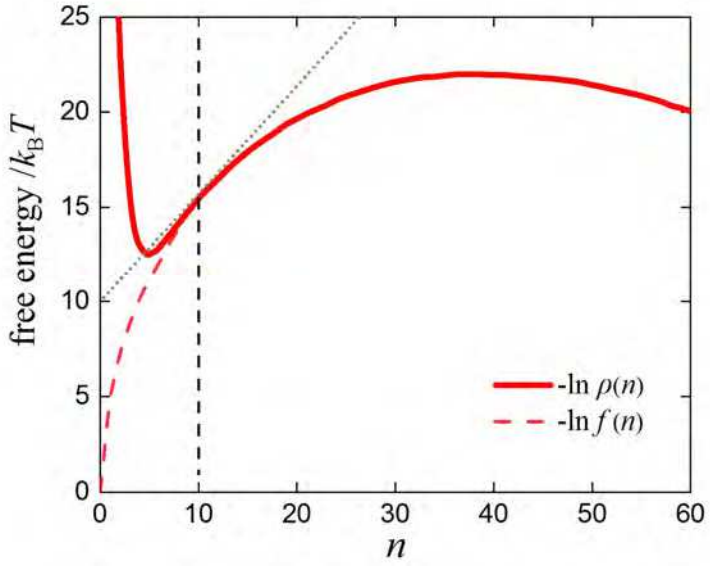

Fig. 2 Free energy of cluster formation in a Fe-1%Cu alloy at 600°C obtained from Umbrella Sampling (solid curve) and from brute-force simulation (dashed curve). The single-cluster free energy ΔG is obtained by patching up the two curves at the point n=10 (indicated by the dashed line) in this case. The dotted line represents the gradient of the free energy at the patching point.

The nucleation free energy is systematically calculated for Fe_1%Cu and Fe_1.5%Cu alloys in the temperature range from 450 to 650 °C. For Fe_1%Cu (Fig. 3a), the critical cluster size n^* increases from around 10 to 38 when the temperature rises from 450 to 600 °C, with the free energy barrier height gradually climbing from 12 to 22 k_BT. In the case of Fe_1.5%Cu (in Fig. 3b), aging in a higher temperature range from 500 to 650 °C, the critical cluster size increases from 10 to 30 atoms with the barrier height rising from 10 to 18 k_BT. A similar prediction follows from first-principles calculation [38], where the critical cluster size is calculated to be 12 with an activation barrier of 0.63 eV (9.5 k_BT) for nucleation in Fe_1.4%Cu alloy at 500°C. In both alloys, the free energy barrier becomes lower, but sharper, when the annealing temperature decreases. The free energy curves are also found to be well fitted in the classical form as $\Delta G(n) = an + bn^{2/3} + c$, where a is the volume contribution, b is the interfacial energy term and c is a normalization constant. Assuming that the clusters are spheres, the precipitate/matrix interfacial energy is evaluated to be approximately 0.28~0.30 $J{\cdot}m^{-2}$, is roughly estimated for dilute Fe-Cu alloys, in consistency with 0.27~0.34 $J{\cdot}m^{-2}$ obtained for the generalized nearest neighbor broken bond (GNNBB) model [39] with size correction for small clusters [40].

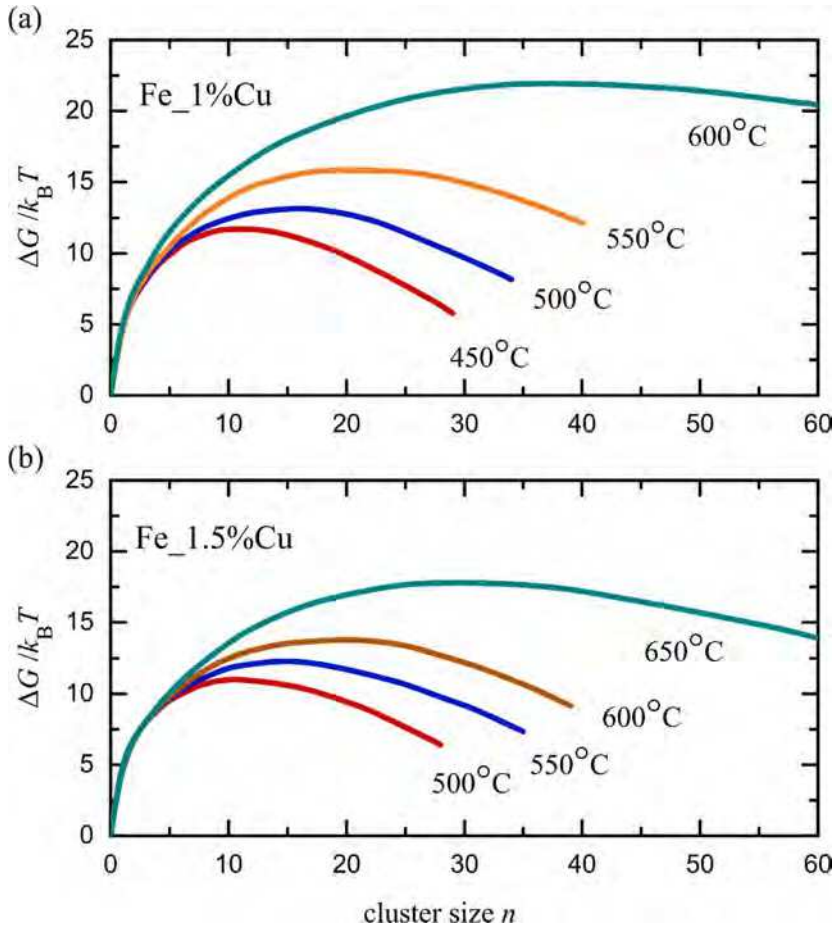

Fig. 3 Nucleation free energies of Fe-1%Cu (a) and Fe-1.5%Cu (b) alloys between 450°C and 650 °C obtained with the Umbrella Sampling technique.

3.2 FFS trajectories and nucleation rates

The nucleation trajectories in Fe_1%Cu and Fe_1.5%Cu alloys at 450 to 650°C are generated using MC dynamics and harvested by Forward Flux Sampling [27]. Nucleation rates calculated from eqs. (6) and (7) are plotted in Fig. 4 as solid lines. The nucleation rates of Cu precipitates between 450°C to 650°C are in the range of 10^{17}~ 10^{20} $m^{-3}s^{-1}$ in the Fe-1%Cu alloy and 10^{20}~ 10^{22} $m^{-3}s^{-1}$ in the Fe-1.5%Cu alloy. For both alloys, nucleation rates do not significantly increase at higher supersaturation and decreasing temperature, but rather decline by one order of magnitude due to the increasingly sluggish diffusion of substitutional elements. The maximum nucleation rates are observed at around 550°C in Fe-1%Cu and around 600°C in Fe-1.5%Cu, in good agreement with the isothermal time-temperature-precipitation (TTP) diagram reported by Perez et.al [41], where the fastest nucleation is observed at 600 ~ 650°C in Fe_1.2%Cu. It is worth noting that the nucleation rate obtained from FFS corresponds to the steady state nucleation rate defined in CNT, thus, transient nucleation effects, which are manifested in the incubation time [42], are not taken into account in this work.

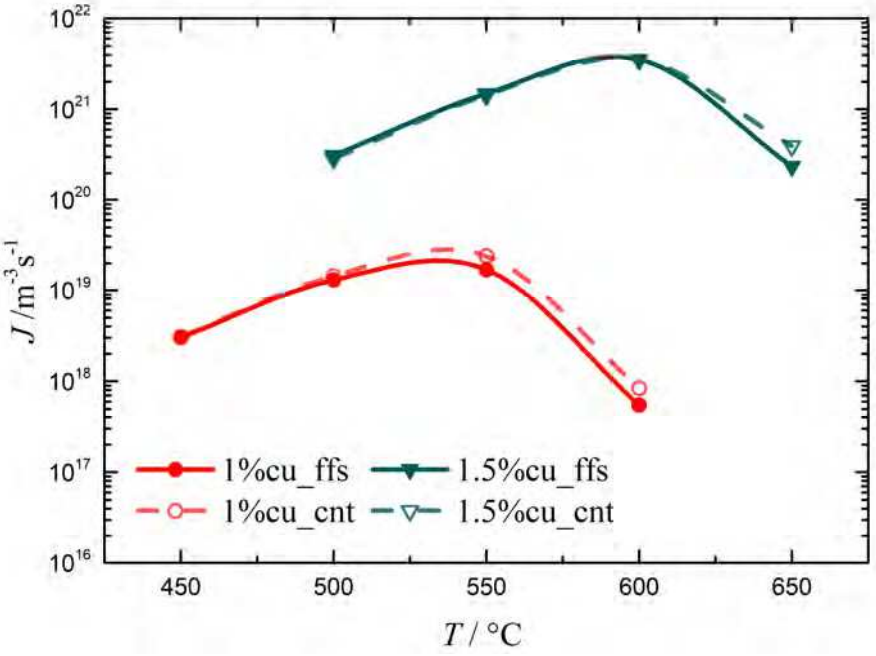

Fig. 4 Nucleation rates obtained by FFS (full markers) and CNT (open markers) for Fe-1%Cu and Fe-1.5%Cu at temperatures between 450°C and 650°C. The trend lines are the Bézier curves generated from each group of data points.

Unfortunately, there is not much quantitative information on nucleation rates available for the present Fe-Cu system, neither from atomistic simulations nor from experimental work. On one hand, experimental measurements for nucleation rates require accurate detection of the Cu particles (radius smaller than 0.5nm) formed in the earliest stages of precipitation, which is almost impossible with present experimental techniques. On the other hand, the steady-state nucleation stage is inherently difficult to be observed in conventional atomistic simulations, especially under high-supersaturated conditions. In the work carried out by Soisson and Martin [19], with an estimated critical cluster size derived from the steady-state cluster distribution, the nucleation rates for Fe-Cu alloys are only reported for rather high temperatures (1000K~1500K) calculated from brute-force Monte Carlo simulations.

In continuum precipitation models, the nucleation rate is a pre-determined parameter controlling the evolution of the number density of precipitates during the process until coarsening of clusters begins. In the work of Stechauner and Kozeschnik [17], simulations of Cu-precipitation in ferrite are carried out using the KWN model [10,43] (implemented in the software package MatCalc [28]), with the nucleation rates of Cu precipitates calculated in a CNT framework at every time interval during the simulation. In their work, the steady nucleation rates at the primary stage are found to be in the order of 10^{20}~ 10^{23} $m^{-3}s^{-1}$ in the Fe-1.4%Cu alloy [**]at 450 to 650°C, with the highest value, around 8×10^{22} $m^{-3}s^{-1}$, occurring between 600 ~ 650°C. Guo *et.al.* [13], using a

[**] the data was not published, but reproduced with the same MatCalc script from ref. [17]

similar model in the study of precipitation kinetics in an Fe-Cu-X ternary alloys, report values of 1.1×10^{21} $m^{-3}s^{-1}$ for the nucleation rate of Cu-rich particles at 800K [13].

3.3 Comparison with the brutal-force MC simulation

The evaluation of nucleation rate from the brutal-force MC simulations is based on the connection between time-dependent nucleation rate $J_{n,t}$ and number density of clusters as [42,44]

$$J_{n,t} = N_{n,t}k_n^+ - N_{n+1,t}k_{n+1}^- = \frac{\partial N_t(>n)}{\partial t} \quad (8)$$

At a given time t, $N_{n,t}$ denotes the number density of clusters containing n atoms, and $N_t(>n)$ denotes the number density of clusters with more than n atoms. $k_n^{+/-}$ is the transition frequency for clusters with n atoms to attach (+) / detach (-) a monomer, which is assumed to be a time-independent value during nucleation. $J_{n,t}$ is variant with time in the beginning of nucleation. After a short period (incubation time), the steady size distribution will be established, i.e. $\partial N_{n,t}/\partial t = 0$, such that $J_{n,t}$ becomes a constant value and $N_t(>n)$ starts to linearly increase in time with a rate of $J_{n,t}$. The constant $J_{n,t}$, known as the steady-state nucleation rate, is the nucleation rate evaluated in FFS by eq.(7). Here, we denote the steady-state nucleation rate as J_s.

To validate the FFS methods, we perform the brutal-force Monte Carlo simulations to analyze the steady-state nucleation rate of Cu clusters in Fe-1%Cu alloy at 500°C. The same LCE potential and diffusion coefficients are used as that in FFS calculation, but the size of MC sample is increased to 100×100×100 unit cells (28.5×28.5×28.5 nm^3) to ensure sufficient statistics to evaluate the time derivative of $N_t(>n)$. The system is first equilibrated at 1200°C and then quenched to 500°C. The measurement of $N_t(>n)$ begins right after the quenching. The thread value n in for the number density of clusters $N_t(>n)$ is set as the critical clusters size as n=15. In fact, the choice of thread value n does not affect the value of nucleation rate when steady-state condition is established [42]. The values of n in a range of 10~50 atoms give similar estimations for J_s in this case.

The brutal-force simulation is repeated for 100 times to gain an accurate estimation of $N_t(>15)$ in Fe-1%Cu alloy at 500°C. The averaged $N_t(>15)$ at each time t is displayed in Fig. 5(a) along with its Mean Square Root Deviation (MSRD) illustrated as error bars. According to Fig.5 (a), the linearly increasing region of $N_t(>15)$ is beginning in a short period of time after quenching. The averaged steady-state nucleation rate is around 1.68×10^{19} $m^{-3}\cdot s^{-1}$ with a deviation of $\pm0.30\times10^{19}$ $m^{-3}\cdot s^{-1}$ indicated by the dotted lines. Compared with the nucleation rate from FFS, 1.41×10^{19} $m^{-3}\cdot s^{-1}$, the evaluation from brutal-force method is slightly higher. This is because brutal-force simulations utilize a larger MC sample, which could have more concentration fluctuations in local area and result in a slightly higher J_s than the one evaluated in a smaller sample in FFS.

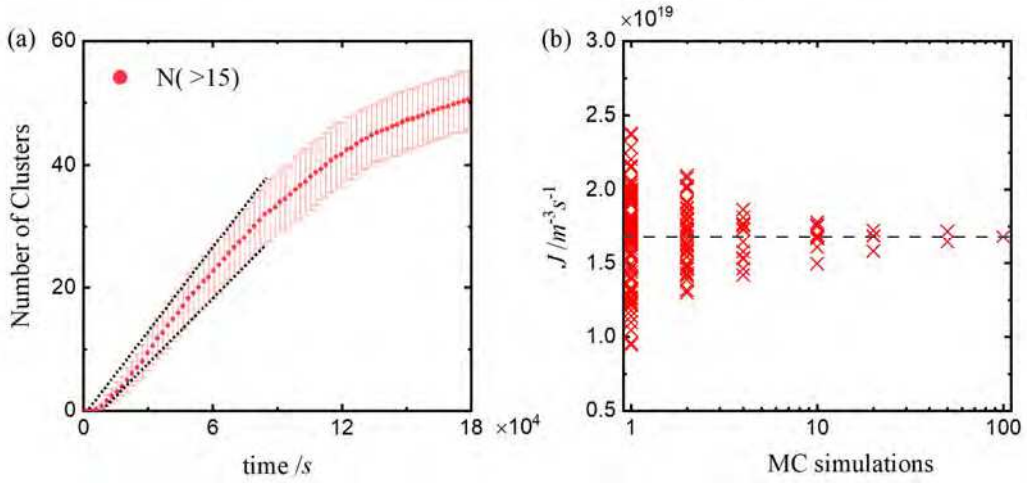

Fig. 5 (a) the number of clusters with size larger than 15, $N_t(>15)$,as a function of time evaluated by averaging over 100 brutal-force simulations in Fe-1%Cu alloy at 500°C. The error bars illustrate the root mean square error. The steady-state nucleation rate evaluated from the linearly increasing region is around 1.68×10^{19} $m^{-3}\cdot s^{-1}$ with a deviation of $\pm0.3\times10^{19}$ $m^{-3}\cdot s^{-1}$ indicated by the dotted lines. (b) The steady-state nucleation rate in Fe-1%Cu alloy at 500°C evaluated by $N_t(>15)$ averaging over 1 to 100 brutal-force simulations.

To test sensitivity of estimation J_s on the number of repeated simulations, we calculated J_s from $N_t(>15)$ in each individual brutal-force simulation as well as averaging over multiple simulations (see Fig. 5(b)). The steady-state nucleation rate evaluated by one simulation diverges from 0.9×10^{19} $m^{-3}\cdot s^{-1}$ to 2.4×10^{19} $m^{-3}\cdot s^{-1}$, and as averaging over more repeated simulations, the deviation of J becomes smaller and converges around 1.68×10^{19} $m^{-3}\cdot s^{-1}$ with 100 repeated simulation. According to Fig. 5(b), an averaged $N_t(>15)$ from over 20 repeated simulations in a MC sample of 100×100×100 unit bcc cell gives a reasonable estimation of nucleation rate in Fe-1%Cu alloy at 500°C. Generally, to reduce the stochastic error in evaluation of nucleation rate, brutal-force method needs to either enlarge the MC sampling size or increase the repeated times of simulations. Compared with the brutal-force method, FFS has much higher computation efficiency reaction rate coefficient especially in the cases with high transition barriers [45]. In this work, FFS harvest about 600 successful nucleation trajectories for calculation of J_s in Fe-1%Cu alloy at 500°C, and the total CPU time is about 50 hours on a single core. Supposing that one stable post-critical cluster formed in brutal-force simulation stands for one successful nucleation trajectory, we need to repeat the simulation for 20 times to harvest 600 trajectories, and the corresponding CPU time is about 80 hours on a single core. For a low supersaturated case, such as in Fe-1%Cu alloy at 600°C, FFS spends 680 hours on a single core to harvest 600 successful trajectories, while using brutal-force method, we are not able to observe nucleation in a feasible CPU time. Theoretically, the CPU time for brutal-force simulation exponentially increases with transition barrier[45], based on the CPU time for Fe-1%Cu alloy at 500°C, the brutal-force method is estimated to spend 650000 hours on a single core to harvest 600 successful nucleation trajectories.

3.4 Comparison with CNT

In Classical Nucleation Theory (CNT), the nucleation rate is expressed as [46][47]

$$J = NZ\upsilon^* \exp\left[-\frac{\Delta G(n^*)}{k_B T}\right] \tag{9}$$

where N is the number of potential nucleation sites, Z is the Zeldovich factor, υ^* is the atomic attachment rate, n is the number of atoms in the cluster and $\Delta G(n^*)$ is the free energy barrier at the critical cluster size n^*. The Zeldovich factor Z is related to the curvature of the free energy barrier at the critical size, $Z = \sqrt{-\frac{\Delta G''(n^*)}{2\pi k_B T}}$. Here, $\Delta G(n^*)$, n^* and Z can be directly evaluated from the free energy curve $\Delta G(n)$ as obtained in the previous sections. In classical theories, the nucleation free energy $\Delta G(n)$ is expressed as $\Delta G(n) = \Delta G_{\text{nucl}}\, n + \sigma n^{2/3}$, where ΔG_{nucl} is volume energy contribution, also known as the driving force. σ is interfacial energy term, given by the product of geometry factor A and the interfacial energy γ, i.e. $\sigma = A\gamma$. The nucleation free energy evaluated in US fits very well in this classical form, and the corresponding values of ΔG_{nucl} and σ obtained from the fitting are listed in Table 2.

Based on the regular solution model for binary system, the nucleation driving force in a supersaturated solid solution can be expressed as [46]

$$\Delta G_{\text{nucl}} = (1-y^{\text{e}})k_B T \ln\left(\frac{1-x^{\text{e}}}{1-x^0}\right) + y^{\text{e}} k_B T \ln\left(\frac{x^{\text{e}}}{x^0}\right) + \omega(x^0 - x^{\text{e}}) \tag{10}$$

where x^{e} and y^{e} is the equilibrated concentration of solute element in matrix phase and precipitation phase at temperature T, respectively. ω is the interaction parameter for a binary A-B system given by $\omega = z_{\text{L}}(\varepsilon_{\text{AA}} + \varepsilon_{\text{BB}} - 2\varepsilon_{\text{AB}})/2$, where ε_{ij} is the bond energy and z_{L} is the number of nearest neighbors. x^0 is the concentration of solute element in matrix during nucleation where a maximum value of ΔG_{nucl} is provided. In a dilute solution—the concentration of solute solution $x^{\text{s}} << 1$, $x^0 \approx x^{\text{s}}$. When $x^{\text{e}} << 1$, eq. (10) can be approximately rewritten as

$$\Delta G_{\text{nucl}} = -y^{\text{e}} k_B T \ln S \tag{11}$$

where S is the supersaturated degree given as $S = x^{\text{s}}/x^{\text{e}}$. Here, x^{s} is the initial Cu concentration in the alloy and x^{e} is the equilibrium Cu solubility at temperature T. Fig.6 displays the relation of driving force ΔG_{nucl} and supersaturated degree S for nucleation in Fe-1%Cu and Fe-1.5%Cu alloys in 450 to 650 °C. According to Table 1, the equilibrium bcc_Cu phase are almost pure Cu at temperature from 450 to 650 °C, i.e. $y^{\text{e}}=1$, therefore relation of ΔG_{nucl} and S suggested by eq.(11) is $\Delta G_{\text{nucl}} = -k_B T \ln S$ (illustrated by the solid line in Fig. 6). However, this tendency is not obeyed, and a non-linear relation is displayed between ΔG_{nucl} and $\ln S$. At high supersaturation, the nucleation driving force is much weaker than the one predicted by eq.(11). As $\ln S$

decreasing, the discrepancy is getting smaller, and ΔG_{nucl} starts approaching to the value of $-k_B T \ln S$. Eq. (11) is derived with the assumption that the clusters formed during nucleation inherit the properties of equilibrium precipitation phase. The trend line of ΔG_{nucl} in Fig.6 indicates that the Cu clusters formed during nucleation are all in metastable state and energetic unfavorable compared with the equilibrium precipitation phase.

Table 2. The driving force ΔG_{nucl} and interfacial energy term σ evaluated by fitting the nucleation free energy from US to classical form. S is the supersaturated degree.

	T / °C	ln$S$	$\Delta G_{nucl}/k_B T$ per Atom	$\sigma/k_B T$ per Atom$^{2/3}$
X_{Cu}=1.0%	450	3.23	-2.05	6.91
	500	2.52	-1.75	6.45
	550	2.07	-1.49	6.19
	600	1.56	-1.13	5.74
X_{Cu}=1.5%	500	2.93	-1.91	6.48
	550	2.48	-1.68	6.16
	600	1.96	-1.48	5.89
	650	1.51	-1.15	5.42

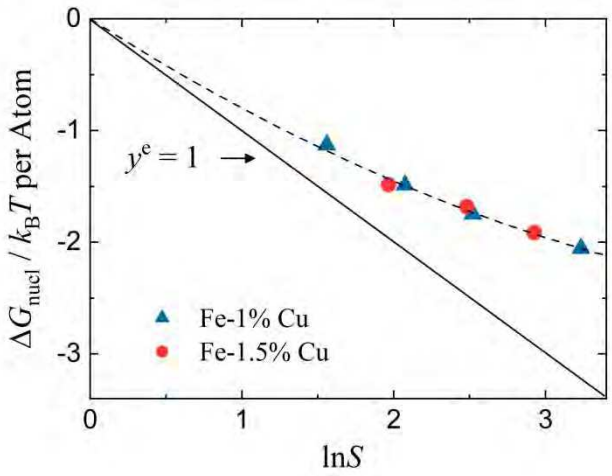

Fig. 6 The nucleation driving force ΔG_{nucl} as a function of ln$S$. The solid line illustrates the equation $\Delta G_{nucl} = -y^e k_B T \ln S$, with the Cu concentration in precipitates y^e=1. The dashed line marks the trend of ΔG_{nucl} considering that ΔG_{nucl} will vanish in the case without supersaturation.

The interfacial energy term σ does not show evident connection with the supersaturated degree (see Table 2), and at different temperatures, the value of σ slightly changes in a range between 4.9~5.2×10^{-4} $J{\cdot}mol^{-2/3}$. The geometry factor A is a unit transfer as $A=a/n^{2/3}$, where a is the matrix/precipitate interfacial area and n is the number of atoms in the precipitate. Supposing the precipitates are spheres and V_m is the effective volume of an atom, the geometry factor is calculated as $A=(4\pi)^{1/3}(3V_m)^{2/3}$. When using this spherical approximation, the interfacial energy γ is estimated in a range of 0.28~0.30 $J{\cdot}m^{-2}$ during Cu nucleation in dilute Fe-Cu alloys at 450~600°C. However, this is only a roughly estimation, since the shape of Cu clusters during nucleation is much complex than spheres, and the geometry factor needs to be carefully evaluated in this case.

The atomic attachment rate, υ^*, describing the frequency at which monomers are attaching to a critical cluster during nucleation [48], is evaluated from FFS trajectories by

$$\upsilon^* = \frac{P\left\{n(t+\Delta t) > n(t) \middle| n(t) = n^*\right\}}{\Delta t} \tag{12}$$

where $P\left\{n(t+\Delta t) > n(t) \middle| n(t) = n^*\right\}$ is the mean probability for a cluster at n^* to absorb one atom at the next time slice in each trajectory, and Δt is the average time interval that the system remains between adjacent slices. Since the attachment and detachment frequencies approximately have the same value on the top of energy barrier, the critical attachment rate can be also determined from the mean square displacement of cluster size[49] in a short time Δt, as $\upsilon^* = \frac{1}{2\Delta t}\left\langle \left(n(t+\Delta t)-n(t)\right)^2 \right\rangle_{n(t)=n^*}$.

In classical theories, a continuums-mechanical expression has been suggested by Svoboda et al. [16] for spherical precipitates in multi-component system as

$$\upsilon^* = \frac{4\pi(\rho^*)^2}{a^4\Omega}\left[\sum_{i=1}^{n}\frac{(c_{ki}-c_{0i})^2}{c_{0i}D_{0i}}\right]^{-1} \tag{13}$$

where ρ^* is the radius of the critical cluster, a is the nearest-neighbor atomic distance, Ω is the molar volume, c_{ki} are the concentrations of element i in the precipitate with index k, c_{0i} are the concentrations in the matrix, and D_{0i} is the tracer diffusivity of element i in the matrix.

In Fig. 7, the values of υ^* from FFS trajectories (Eq.(12)) are compared to the values obtained from CNT (Eq.(13)). Evidently, good agreement is achieved. In FFS, Cu nuclei are observed to change their size mainly by attachment or detachment of monomers in dilute alloys, while the contribution from small clusters (e.g. dimers or triplets) is rarely detected during nucleation. This phenomenon is in agreement with the classical description for atomic attachment expressed by eq. (13). However, small systematic deviations are observed particularly at lower temperatures. This effect can

probably be attributed to the non-spherical shape of very small critical clusters, which we observe in the analysis of the critical nucleus shape. Fig. 8 shows some snapshots of small clusters with less than 30 atoms observed in FFS. In order to characterize the geometry of nuclei, the clusters are fitted to ideal ellipsoids and an anisotropy factor ξ is defined as the ratio between the longest and shortest radius of the ellipsoid (ξ =1 for a sphere). In this work, the critical clusters in the size between 10 ~ 30 atoms are commonly observed in a non-spherical shape with average anisotropy factors ranging from 2.0 to 3.5.

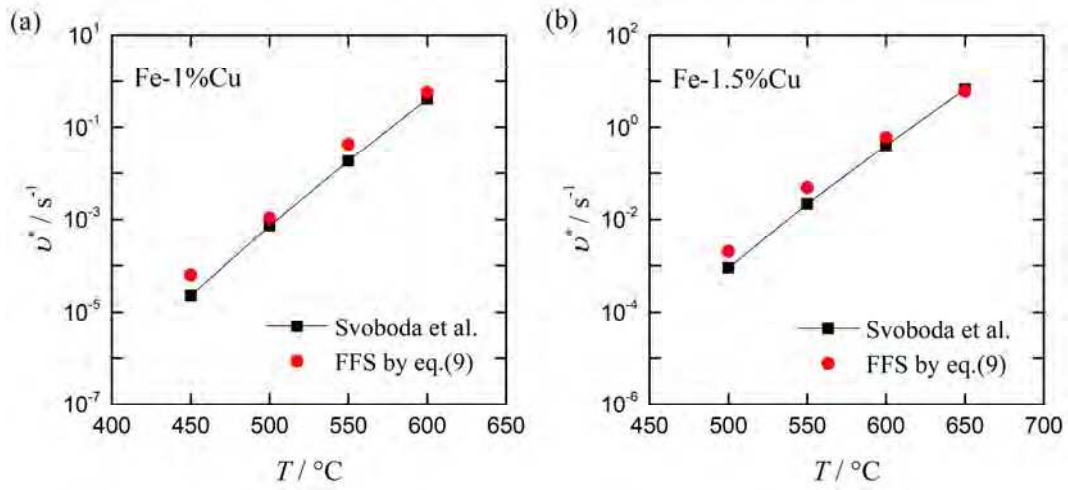

Fig. 7 Atomic attachment rate, υ^*, evaluated according to Svoboda et al. [16] compared with the prediction of Eq.(9).

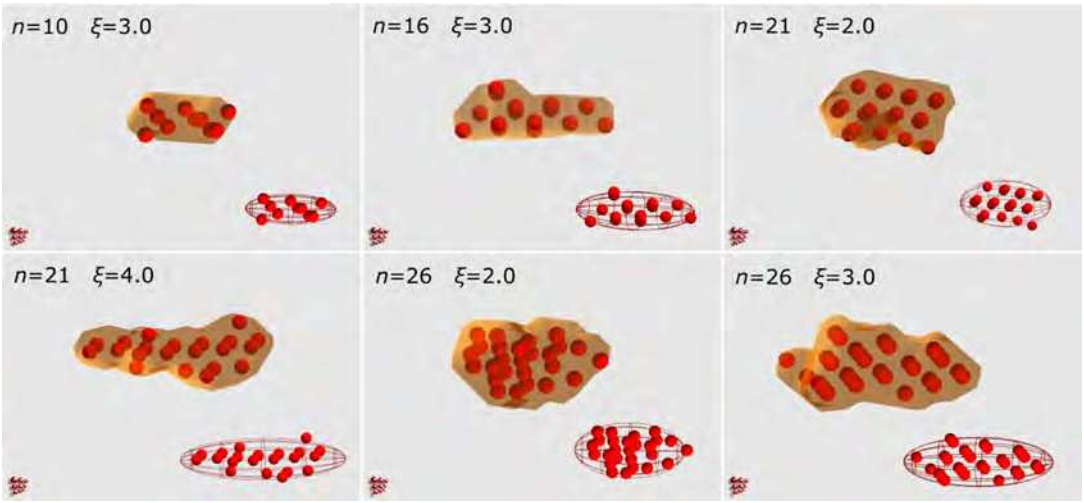

Fig. 8 Snapshots of small clusters with number of atoms n=10, 16, 21 and 26, and the best-fitted ellipsoid. Here, ξ denotes the anisotropy factor of the cluster, which is calculated as the ratio of the longest to the shortest radius of the ellipsoid.

Table 3 summarizes the values of CNT-type parameters as evaluated from the US free energy curve and the FFS nucleation trajectories. The CNT nucleation rate calculated using eq. (9) is plotted on Fig. 4 to compare with FFS predictions. It is not

surprising that the two methods give almost the same prediction on nucleation rates in this work, since the free energy used in eq. (9) is a direct reflection of the equilibrium properties of the atomic system, and the kinetics of cluster growth is also quite "classical" in dilute Fe-Cu alloys based on the above discussion.

Table 3. Number n^* of atoms in the critical cluster, Zeldovich factor Z, nucleation barrier $\Delta G(n^*)/k_BT$ and atomic attachment rate υ^* as evaluated from FFS trajectories for alloys with Cu contents of 1 at-% and 1.5 at-%. The nucleation rates J are calculated according to CNT (Eq. (9)).

	T / °C	n^*	Z	$\Delta G(n^*)/k_BT$	υ^* /s^{-1}	J /m^{-3}s^{-1}
X_{Cu}=1.0%	450	12	0.10	12.07	$6.32\cdot10^{-5}$	$3.06\cdot10^{18}$
	500	15	0.08	13.13	$1.07\cdot10^{-3}$	$1.44\cdot10^{19}$
	550	22	0.06	16.04	$4.24\cdot10^{-2}$	$2.40\cdot10^{19}$
	600	38	0.06	21.91	0.56	$8.39\cdot10^{17}$
X_{Cu}=1.5%	500	11	0.09	10.94	$2.01\cdot10^{-3}$	$2.87\cdot10^{20}$
	550	15	0.08	12.33	$4.81\cdot10^{-2}$	$1.42\cdot10^{21}$
	600	20	0.07	13.78	0.59	$3.49\cdot10^{21}$
	650	30	0.05	17.90	6.07	$3.95\cdot10^{20}$

3.4 Concentration profiles across precipitate/matrix interface

Finally, in this section, the concentration profiles across the precipitate/matrix interfaces are analyzed for clusters of critical size at different temperatures. In the evaluation, the center atom is defined as the one atom residing closest to the geometric center of the cluster, i.e. the center of fitted ellipsoid. The concentration profile is then calculated from the center up to the 20th neighbor shell as illustrated in Fig. 9(a). The Cu concentration in the i^{th} shell is determined as $c^{(i)} = n_{\mathrm{Cu}}^{(i)} / n_{\mathrm{tot}}^{(i)}$, where $n_{Cu}^{(i)}$ and $n_{tot}^{(i)}$ are the number of Cu atoms and total number of atoms in the i^{th} shell, respectively.

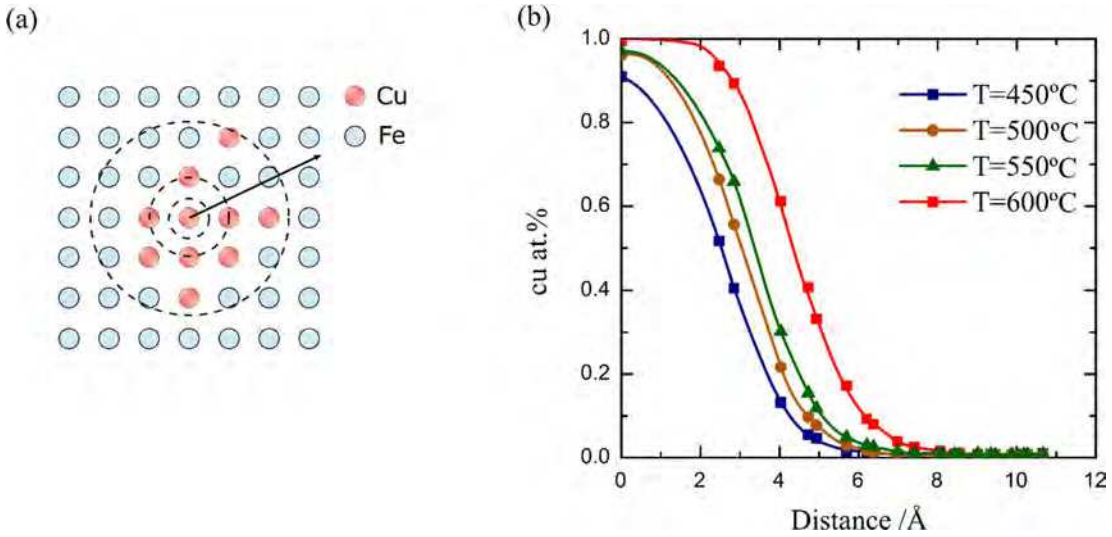

Fig. 9 (a) Illustration of the procedure for finding the geometric center of an irregular cluster and of the evaluation of the composition profile from the center atom to neighbor shells; (b) Concentration profile of critical clusters in Fe-1%Cu alloy at 450°C, 500°C, 550°C and 600 °C, where the corresponding critical sizes are 12, 15, 22 and 38 atoms, respectively.

The concentration profiles, averaged over 500 configurations of critical clusters with the same size, are shown in Fig. 9(b). In the Fe-1%Cu alloys, the critical nucleus at 500°C contains approximately 10% Fe in the center, with the Fe amount significantly increasing to approximately 50% in the first neighbor shell. At a temperature of 600°C, the Cu concentration increases to almost 100% in the center of the critical clusters. A similar observation of for the concentration profile of critical clusters is reported by Nagano and Enomoto [14] based on a study of cluster growth with the Cahn-Hilliard theory for dilute Fe-Cu alloys. According to their calculations, the Cu content at the center of critical clusters is around 85% at 400°C in Fe_1.5% alloy, and almost 100% when the temperature is increased to 550°C. The average concentration of Cu clusters was evaluated by Kozeschnik and Stechauner [17] based on the minimum $\Delta G(n^*)$ concept [15]. In their work, the critical clusters in Fe-1%Cu is estimated to contain 70% Cu at 500°C and gradually increase to almost 100% at 650°C.

In the present analysis, we do not further speculate on absolute numbers of the chemical composition of critical clusters because the actual value of this quantity is very sensitive to the choice of criterion defining the matrix/precipitate interface. Still, the concentration profiles of critical clusters indicate that the clusters formed first in dilute alloys are not always pure Cu clusters, and a substantial amount of Fe atoms can reside within Cu clusters at low temperature. At 600°C, the critical clusters maintain a high Cu content above 90% from the center up to the 2nd neighbor shell. At a temperature of 450°C, a large amount of Fe infiltrates into the core of the clusters and significantly reduces the Cu content around the center of the clusters. For small clusters with less than 20 atoms, no strict “core” region can be defined any more, since these small clusters are composed of only 2-3 layers of solute atoms, and almost every atom in the clusters is partially “exposed” to the matrix.

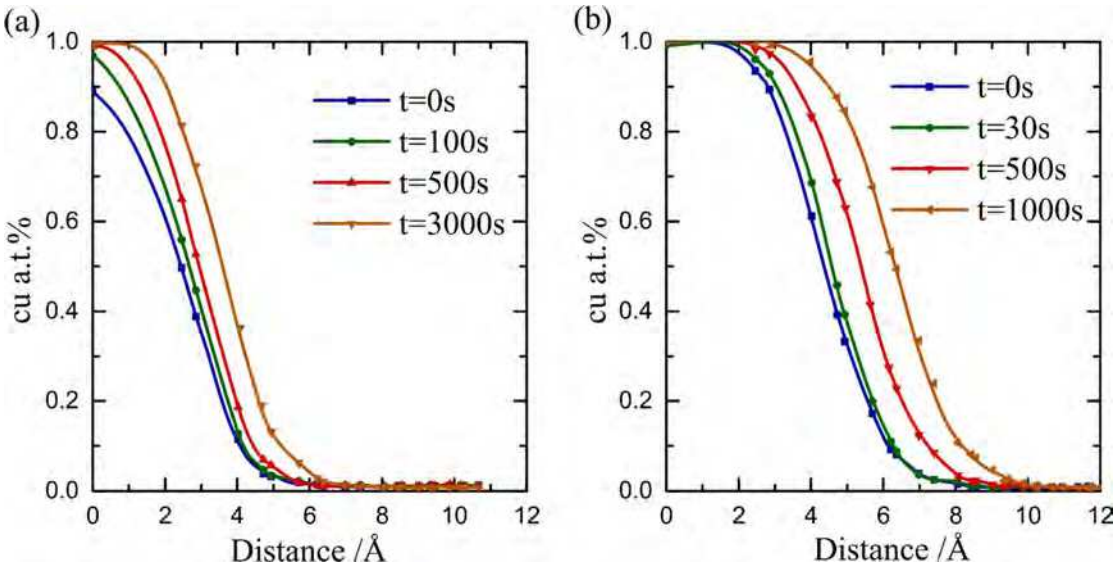

Fig. 10 Concentration profiles of clusters in a 1.5%Cu alloy at 500°C (a) and in a 1%Cu alloy at 600°C (b) when aging from the critical state for different times.

To analyze the concentration profiles of clusters during super-critical growth, for each temperature and chemical composition of the alloys, a group of configurations at "critical states", i.e. the states with the largest cluster of critical size, are taken from the nucleation trajectories in FFS and a brute-force simulation is performed for these configurations until the system forms a large stable cluster or decays back to the random state. Those simulations, which successfully form a stable supercritical cluster are stored and used to calculate the concentration profile of the largest clusters at different times. Figure 10 summarizes the evolution of concentration profiles in the clusters in a weakly supersaturated case (in Fe-1%Cu at 600°C) and strongly supersaturated case (in Fe-1.5%Cu at 500°C). At high temperature, the size of Cu clusters steadily increases without significant change in the chemical environment around it (Fig. 10 (b)). At low temperature, the clusters first tend to increase the Cu content to almost 100% until they finally start growing (Fig. 10(a)). This Cu-enrichment of clusters during nucleation at lower temperatures was recently confirmed by the Differential Scanning Calorimetry (DSC) experiment of 15-5 PH steel in continuous aging at 300 to 500°C [50][51]. However, according to Fig.10 (a), the enrichment of Cu content in clusters happens very fast. The clusters with over 20% Fe are mainly found to be in small size with radius less than 0.5 *nm*, and when growing over than 0.8*nm*, they are almost pure Cu clusters. This observation is inconsistent with the recent APT results [4][5][6], where 50%~70% Fe are found in large precipitate with radius 1~1.5 *nm*.

4. Conclusion

In the present work, we introduce a methodology to study the equilibrium and kinetic properties of early-stage precipitation in Fe-Cu system by implementing statistical sampling techniques to Monte Carlo simulations. The nucleation free energy as a function of cluster size is first evaluated by Umbrella Sampling for two concentrations at different temperatures. With Forward Flux Sampling, a large number of nucleation

trajectories are generated and used to analyze the form, which the nucleation kinetics of Cu clusters. These simulation results are compared to predictions from Classical Nucleation Theory and good agreement is observed. The chemical composition of Cu nuclei is also investigated, showing that the first formed Cu clusters in dilute Fe-Cu alloys aged at low temperatures can contain a substantial amount of Fe atoms. During aging, the clusters first enrich in Cu content from inside the precipitate, and only afterwards growth of the particles commences. In contrast, when aged at a higher temperature, the clusters formed are almost pure Cu particles from the beginning and remain so throughout the subsequent precipitate growth stages. Analysis of the shape of critical clusters shows that the clusters become increasingly non-spherical with decreasing cluster size and increasing supersaturation.

Acknowledgement

This work was supported by *the Austrian Science Fund (FWF): F4113 SFB ViCoM*. Part of the computation was performed on *the Vienna Scientific Cluster (VSC)*.

References

[1] E. Hornbogen, R.C. Glenn, A metallographic study of precipitation of copper from alpha iron, Tran Met. Soc AIME. 218 (1960) 1067–1070.

[2] P.J. Othen, M.L. Jenkins, G. Smith, W.J. Phytian, Transmission electron-microscope investigations of the structure of copper precipitates in thermally-aged Fe-Cu and Fe-Cu-Ni, Philos Mag Lett. 64 (1991) 383–391.

[3] P.J. Othen, M.L. Jenkins, G. Smith, High-resolution electron-microscopy studies of the structure of Cu precipitates in alpha-Fe, Philos. Mag. Lett. 70 (1994) 1–24.

[4] D. Isheim, D.N. Seidman, Nanoscale studies of segregation at coherent heterophase interfaces in alpha-Fe based systems, Surf Interface Anal. 36 (2004) 569–574.

[5] D. Isheim, M.S. Galiano, M.E. Fine, D.N. Seidman, Interfacial segregation at Cu-rich precipitates in a high-strength low-carbon steel studied on a sub-nanometer scale, Acta Mater. 54 (2006) 841–849.

[6] M. Schober, E. Eidenberger, H. Leitner, P. Staron, D. Reith, R. Podloucky, A critical consideration of magnetism and composition of (bcc) Cu precipitates in (bcc) Fe, Appl Phys A. 99 (2010) 697–704.

[7] M.K. Miller, B.D. Wirth, G.R. Odette, Precipitation in neutron-irradiated Fe-Cu and Fe-Cu-Mn model alloys: a comparison of APT and SANS data, Mater Sci Eng A. 353 (2003) 133–139.

[8] S. Lozano-Perez, G. Sha, J.M. Titchmarsh, M.L. Jenkins, S. Hirosawa, A. Cerezo, G.D.W. Smith, Comparison of the number densities of nanosized Cu-rich precipitates in ferritic alloys measured using EELS and EDX mapping, HREM and 3DAP, J. Mater. Sci. 41 (2006) 2559–2565. doi:10.1007/s10853-006-7768-0.

[9] R. McGraw, Dynamics of Barrier Crossing in Classical Nucleation Theory†, J. Phys. Chem. B - J PHYS CHEM B. 105 (2001).

[10] R. Kampmann, R. Wagner, Kinetics of precipitation in metastable binary alloys - theory and application to Cu-1.9 at % Ti and Ni-14 at % Al, in: Decompos. Alloys Early Stages, Pergamon,

1984: pp. 91–103. http://www.sciencedirect.com/science/article/pii/B9780080316512500185.

[11] J.W. Cahn, J.E. Hilliard, Free Energy of a Nonuniform System. I. Interfacial Free Energy, J. Chem. Phys. 28 (1958) 258–267. doi:10.1063/1.1744102.

[12] J.W. Cahn, J.E. Hilliard, Free Energy of a Nonuniform System. III. Nucleation in a Two-Component Incompressible Fluid, J. Chem. Phys. 31 (1959) 688–699. doi:10.1063/1.1730447.

[13] H. Guo, M. Enomoto, C.J. Shang, Simulation of bcc-Cu precipitation in ternary Fe-Cu-M alloys, Comput. Mater. Sci. 141 (2018) 101–113. doi:https://doi.org/10.1016/j.commatsci.2017.09.023.

[14] T. Nagano, M. Enomoto, Simulation of the growth of copper critical nucleus in dilute bcc Fe–Cu alloys, Scr. Mater. 55 (2006) 223–226. doi:http://dx.doi.org/10.1016/j.scriptamat.2006.04.015.

[15] E. Kozeschnik, Thermodynamic prediction of the equilibrium chemical composition of critical nuclei: Bcc Cu precipitation in α-Fe, Scr. Mater. 59 (2008) 1018–1021. doi:http://dx.doi.org/10.1016/j.scriptamat.2008.07.008.

[16] J. Svoboda, F.D. Fischer, P. Fratzl, E. Kozeschnik, Modelling of kinetics in multi-component multi-phase systems with spherical precipitates: I: Theory, Mater. Sci. Eng. A. 385 (2004) 166–174. doi:https://doi.org/10.1016/j.msea.2004.06.018.

[17] G. Stechauner, E. Kozeschnik, Thermo-kinetic modeling of Cu precipitation in α-Fe, Acta Mater. 100 (2015) 135–146. doi:10.1016/j.actamat.2015.08.042.

[18] F. Soisson, A. Barbu, G. Martin, Monte carlo simulations of copper precipitation in dilute iron-cooper alloys during thermal aging and under electron irradiation, Acta Mater. 44 (1996) 3789–3800.

[19] F. Soisson, G. Martin, Monte Carlo simulations of the decomposition of metastable solid solutions: Transient and steady-state nucleation kinetics, Phys. Rev. B. 62 (2000) 203–214. doi:10.1103/PhysRevB.62.203.

[20] F. Soisson, C.C. Fu, Cu-precipitation kinetics in alpha-Fe from atomistic simulations: Vacancy-tranping effects and Cu-cluster mobility, Phys Rev B. 76 (2007) 214102.

[21] P. Warczok, D. Reith, M. Schober, H. Leitner, R. Podloucky, E. Kozeschnik, Investigation of Cu precipitation in bcc-Fe – Comparison of numerical analysis with experiment, IJMR. 102 (2011) 709–716.

[22] D. Molnar, R. Mukherjee, A. Choudhury, A. Mora, P. Binkele, M. Selzer, B. Nestler, S. Schmauder, Multiscale simulations on the coarsening of Cu-rich precipitates in α-Fe using kinetic Monte Carlo, molecular dynamics and phase-field simulations, Acta Mater. 60 (2012) 6961–6971. doi:https://doi.org/10.1016/j.actamat.2012.08.051.

[23] P. Warczok, J. Ženíšek, E. Kozeschnik, Atomistic and continuums modeling of cluster migration and coagulation in precipitation reactions, Comput. Mater. Sci. 60 (2012) 59–65. doi:10.1016/j.commatsci.2012.02.033.

[24] S. Kumar, J.M. Rosenberg, D. Bouzida, R.H. Swendsen, P.A. Kollman, Multidimensional free-energy calculations using the weighted histogram analysis method, J. Comput. Chem. 16 (1995) 1339–1350. doi:10.1002/jcc.540161104.

[25] F. Zhu, G. Hummer, Convergence and error estimation in free energy calculations using the weighted histogram analysis method, J. Comput. Chem. 33 (2012) 453–65.

[26] C. Leitold, C. Dellago, Nucleation and structural growth of cluster crystals, J. Chem. Phys. 145 (2016) 074504. doi:10.1063/1.4960958.

[27] R.J. Allen, P.B. Warren, P.R. ten Wolde, Sampling Rare Switching Events in Biochemical Networks, Phys Rev Lett. 94 (2005) 018104. doi:10.1103/PhysRevLett.94.018104.

[28] information on http://matcalc.at, n.d. http://matcalc.at.
[29] M. Glicksman, Diffusion in Solid: Field Theory, Solid-State Principles, and Applications, Wiley-Interscience, 2000.
[30] D. Reith, M. Stöhr, R. Podloucky, T.C. Kerscher, S. Müller, First-principles modeling of temperature- and concentration-dependent solubility in the phase-separating alloy FexCu1-x, Phys Rev B. 86 (2012) 020201. doi:10.1103/PhysRevB.86.020201.
[31] E. Povoden-Karadeniz, Thermodynamic database mc_fe.tdb, Version 2.050, Vienna University of Technology, 2015.
[32] M.A. Turchanin, P.G. Agraval, I.V. Nikolaenko, Thermodynamics of alloys and phase equilibria in the copper-iron system, J. Phase Equilibria. 24 (2003) 307–319. doi:10.1361/105497103770330280.
[33] J. Fridberg, L. Torndahl, M. Hillert, Diffusion in Iron, JERNKONTORETS Ann. 153 (1969) 263.
[34] B. Jönsson, Assessment of the Mobilities of Cr, Fe and Ni in bcc Cr-Fe-Ni Alloys, ISIJ Int. 35 (1995) 1415–1421. doi:10.2355/isijinternational.35.1415.
[35] A.M. Ferrenberg, R.H. Swendsen, Optimized Monte Carlo data analysis, Phys Rev Lett. 63 (1989) 1195–1198. doi:10.1103/PhysRevLett.63.1195.
[36] D. Kashchiev, Chapter 13 - Stationary nucleation, 1 (2000) 184–223. doi:http://dx.doi.org/10.1016/B978-075064682-6/50014-7.
[37] T.S. van Erp, D. Moroni, P.G. Bolhuis, A novel path sampling method for the calculation of rate constants, J. Chem. Phys. 118 (2003) 7762–7774. doi:http://dx.doi.org/10.1063/1.1562614.
[38] K. Yuge, A. Seko, I. Tanaka, S.R. Nishitani, First-principles study of the effect of lattice vibrations on Cu nucleation free energy in Fe-Cu alloys, Phys Rev B. 72 (2005) 174201. doi:10.1103/PhysRevB.72.174201.
[39] B. Sonderegger, E. Kozeschnik, Generalized Nearest-Neighbor Broken-Bond Analysis of Randomly Oriented Coherent Interfaces in Multicomponent Fcc and Bcc Structures, Metall. Mater. Trans. A. 40 (2009) 499–510. doi:10.1007/s11661-008-9752-6.
[40] B. Sonderegger, E. Kozeschnik, Size dependence of the interfacial energy in the generalized nearest-neighbor broken-bond approach, Scr. Mater. 60 (2009) 635–638. doi:https://doi.org/10.1016/j.scriptamat.2008.12.025.
[41] M. Perez, F. Perrard, V. Massardier, X. Kleber, A. Deschamps, H. de Monestrol, P. Pareige, G. Covarel, Low Temperature Solubility of Copper in Iron : Experimental Study Using Thermoelectric Power, Small Angle X-ray Scattering and Tomographic Atom Probe, Philos. Mag. 85 (2005) 2197–2210.
[42] K.F. Kelton, A.L. Greer, C.V. Thompson, Transient nucleation in condensed systems, J. Chem. Phys. 79 (1983) 6261–6276. doi:10.1063/1.445731.
[43] R. Wagner, R. Kampmann, P. Voorhees, Homogeneous Second-Phase Precipitation, in: Phase Transform. Mater., Wiley-VCH Verlag GmbH & Co. KGaA, 2005: pp. 309–407. http://dx.doi.org/10.1002/352760264X.ch5.
[44] R. Becker, W. Döring, Kinetische Behandlung der Keimbildung in übersättigten Dämpfen, Ann. Phys. 416 (n.d.) 719–752. doi:10.1002/andp.19354160806.
[45] C. Vogler, F. Bruckner, B. Bergmair, T. Huber, D. Suess, C. Dellago, Simulating rare switching events of magnetic nanostructures with forward flux sampling, Phys Rev B. 88 (2013) 134409. doi:10.1103/PhysRevB.88.134409.
[46] E. Clouet, Modeling of Nucleation Processes, ASM Handb. 22A (2009) 203–219.

http://arxiv.org/abs/1001.4131.

[47] E. Kozeschnik, C. Bataille, K. Janssens, Modeling solid-state precipitation, Momentum Press, 2013.

[48] K.C. Russell, Nucleation in solids: The induction and steady state effects, Adv. Colloid Interface Sci. 13 (1980) 205–318. doi:http://dx.doi.org/10.1016/0001-8686(80)80003-0.

[49] S. Jungblut, C. Dellago, Pathways to self-organization: Crystallization via nucleation and growth, Eur. Phys. J. E. 39 (2016) 77. doi:10.1140/epje/i2016-16077-6.

[50] S. Primig, G. Stechauner, E. Kozeschnik, Early Stages of Cu Precipitation in 15–5 PH Maraging Steel Revisited − Part I: Experimental Analysis, Steel Res. Int. 88 (2017) 1600084–n/a. doi:10.1002/srin.201600084.

[51] G. Stechauner, S. Primig, E. Kozeschnik, Early Stages of Cu Precipitation in 15-5 PH Maraging Steel Revisited – Part II: Thermokinetic Simulation, Steel Res. Int. 88 (2017) 1600085–n/a. doi:10.1002/srin.201600085.

An efficient method to reconstruct free energy profiles for diffusive processes in transition interface sampling and forward flux sampling simulations

Lin Qin[1, a *], Christoph Dellago[2, b], Ernst Kozeschnik[1, c]

[1] TU Wien, Institute of Materials Science and Technology, Vienna, Austria

[2] University of Vienna, Faculty of Physics, Vienna, Austria

[a]lin.qin@tuwien.ac.at, [b]christoph.dellago@univie.ac.at, [c]ernst.kozeschnik@tuwien.ac.at

Keywords: Transition interface sampling, forward flux sampling, diffusive processes, free energy, Monte Carlo simulation

Abstract

We propose a Reweighted Partial Path (RPP) method to compute free energy profiles for diffusive processes in single Transition Interface Sampling (TIS) or Forward Flux Sampling (FFS) simulations. The method employs a partial path reweighting strategy, based on the memory loss assumption for diffusive systems, to derive the equilibrium distribution of states along a chosen order parameter from TIS or FFS trajectories. No additional calculations such as reverse TIS or Umbrella Sampling are required. The application of the RPP method is demonstrated by calculating the nucleation free energy of early-stage Cu precipitates in a dilute Fe-Cu alloy.

1.Introduction

Activated processes dominated by rare events, including chemical reactions, crystal nucleation and biochemical switching, play important roles in many areas of science and technology. In principle, molecular simulation techniques such as Monte Carlo and molecular dynamics simulations can be used to study the kinetics and mechanism of these processes. Due to the presence of high activation barriers, however, the waiting times for activated events can be many orders of magnitude longer than the time required for the transition event itself. This separation of time scale makes it impractical to study activate processes with sufficient statistics using conventional brute-force simulation on current computers.

Rare event problems can be tackled with trajectory-based sampling techniques that focus on the segments of the time evolution where the reaction of interest happens. For instance, in the transition path sampling (TPS) method [1][2][3][4][5] rare transition pathways are generated by carrying out a Monte Carlo simulation in trajectory space while maintaining reactivity at each instant of the simulation. Based on the TPS framework, van Erp *et al.* [6] introduced the Transition Interface Sampling (TIS) method for the efficient calculation of reaction rate constants, in which one considers

ensembles of trajectories crossing a series of interfaces between reactants and products. Following similar ideas, Allen *et al.* [7,8] proposed the Forward Flux Sampling (FFS) algorithm, which is also applicable to non-equilibrium systems where detailed balance is violated. In contrast to TIS, in FFS pathways are generated in a ratchet-like manner only in forward direction, which can slow down the sampling of trajectory space.

The main purpose of trajectory-based simulation methods is to reveal the transition mechanism and determine rate constant. To analyze equilibrium properties such as the reaction free energy, usually additional calculations are necessary. This can be done either employing a biased sampling technique such as Umbrella Sampling (US) [13] or performing an additional path simulation for the reverse transition [14,15]. Under certain circumstances, however, also free energies can be extracted directly from path sampling simulations. In particular, in the Partial-Path Transition Interface Sampling (PPTIS) method introduced by Moroni *et al.* [9,10] for diffusive processes, free energy profiles can be easily determined together with the rate constant without requiring additional calculations. The basic concept of PPTIS is very similar to other TIS methods, except that PPTIS utilizes a *memory-loss* assumption to extrapolate the long-range effective crossing flux from local partial path ensembles. The *memory-loss* assumption acts as a medium to connect the properties of long-range transition paths with the partial paths on every interface. Bearing this idea in mind, once a system obeys the *memory-loss* assumption, it is theoretically possible to use transition paths, sampled by a standard TIS algorithm (without sampling the reverse transition), to reconstruct the partial path ensembles and hence to evaluate free energy profiles. However, due to the unique sampling strategy of PPTIS, its free energy evaluation algorithm, called the *loop-boundary* method, cannot be directly implemented within other TIS approaches. In the present work, we propose a Reweighted Partial Path (RPP) method that addresses this problem and makes it possible to determine free energy profiles using the trajectory information from a single TIS calculation. Like PPTIS, the reweighting strategy of RPP assumes that the dynamics loses memory quickly enough such that crossings of subsequent interfaces are uncorrelated with each other. The RPP method can also be applied to calculate free energy profiles from trajectories sampled with FFS.

The remainder of this article is organized as follows. In section 2.1 we first introduce the memory loss assumption of PPTIS. Then, in section 2.2, we explain the theory behind the Reweighted Partial Path method. We prove that, under the memory loss assumption, the equilibrium histogram of the order parameter can be derived from trajectories sampled with TIS or FFS for a single transition. In section 3, we illustrate the RPP method in combination with FFS by determining the nucleation free energy of Cu clusters in dilute bcc Fe. In this example, the memory loss assumption is validated and the RPP prediction is in a good agreement with the free energy evaluated with Umbrella Sampling. Finally, a brief summary of the RPP method is given in section 4. We also discuss the difference between the PPTIS and the RPP method and review some technical details that are useful for implementing the RPP method.

2.Theory

2.1 Memory loss assumption in PPTIS

Consider a reversible transition between two stable phases, A and B, in a high dimensional system specified by the vector $\mathbf{x}$ in phase space. Regions A and B are defined in terms of an order parameter $\lambda(\mathbf{x})$, such that the system is in state A if $\lambda(\mathbf{x}) < \lambda_A$, and in state B if $\lambda(\mathbf{x}) > \lambda_B$. A trajectory or path, $\mathbf{x}^\tau = \{\mathbf{x}_0, \cdots, \mathbf{x}_t, \cdots, \mathbf{x}_\tau\}$, consists of a discrete sequence of phase points or snapshots $\mathbf{x}_t$ indexed by time t, where τ is the total duration or length of the path. The probability of observing a particular trajectory $\mathbf{x}^\tau$ is given by $\mathcal{P}(\mathbf{x}^\tau) = \rho(\mathbf{x}_0) \prod_{t=0}^{\tau-\Delta t} p(\mathbf{x}_t \to \mathbf{x}_{t+\Delta t})$, where $\rho(\mathbf{x}_0)$ is the equilibrium probability density of $\mathbf{x}_0$, for instance in the canonical ensemble, and $p(\mathbf{x}_t \to \mathbf{x}_{t+\Delta t})$ is the Markovian probability of transitioning from $\mathbf{x}_t$ to $\mathbf{x}_{t+\Delta t}$ in the time interval Δt. For an ergodic system, the equilibrium distribution is also preserved in trajectory space such that the equilibrium average of an observable $g(\mathbf{x})$ can be calculated as an average over trajectories,

$$\langle g(\mathbf{x}) \rangle = \int \mathcal{D}\mathbf{x}^\tau \mathcal{P}(\mathbf{x}^\tau) \int_0^\tau dt\, g(\mathbf{x}_t). \tag{1}$$

In the derivations that follow we will also make use of the weighted average for an observable $g(\mathbf{x})$ and a weight function $w(\mathbf{x})$, defined as $\langle g(\mathbf{x}) \rangle_w = \dfrac{\langle g(\mathbf{x}) w(\mathbf{x}) \rangle}{\langle w(\mathbf{x}) \rangle}$.

In TIS [6], the region between states A and B is partitioned by a series of M+1 non-overlapping interfaces defined by corresponding values $\{\lambda_i\}_{i=0\ldots M}$ of the order parameter. The interfaces are selected such that the first and the last interface coincide with the boundaries of region A and B, respectively, $\lambda_0 = \lambda_A$ and $\lambda_M = \lambda_B$. Trajectories are categorized into ensembles based on the interfaces they cross. To describe the crossing order of a trajectory through two interfaces i and j ($i \neq j$), the two-fold characteristic functions are introduced as:

$$\begin{aligned} \bar{h}^b_{i,j}(\mathbf{x}) &= \begin{cases} 1 & \text{if } t^b_i(\mathbf{x}) < t^b_j(\mathbf{x}) \\ 0 & \text{otherwise} \end{cases} \\ \bar{h}^f_{i,j}(\mathbf{x}) &= \begin{cases} 1 & \text{if } t^f_i(\mathbf{x}) < t^f_j(\mathbf{x}) \\ 0 & \text{otherwise} \end{cases} \end{aligned} \tag{2}$$

where $t^b_i(\mathbf{x})$ and $t^f_i(\mathbf{x})$ are the time durations tracing backward and forward, respectively, from phase point $\mathbf{x}$ until the trajectory crosses interface i for the first time. Hence, $\bar{h}^b_{i,j}(\mathbf{x}) = 1$ means that, before visiting $\mathbf{x}$, the trajectory first crossed j and then i without having revisited j. On the other hand, $\bar{h}^f_{i,j}(\mathbf{x}) = 1$ indicates that the trajectory presently visits $\mathbf{x}$ and will continue to reach i before j. Note that these characteristic

functions depend both on the phase space point **x** as well as on the particular trajectory going through **x**. When the system is ergodic, both interfaces i and j will be crossed in finite time, hence $\bar{h}^b_{i,j}(\mathbf{x})+\bar{h}^b_{j,i}(\mathbf{x})= \bar{h}^f_{i,j}(\mathbf{x})+\bar{h}^f_{j,i}(\mathbf{x})= 1$. Next, we use $h_{\mathcal{A}}(\mathbf{x}) = \bar{h}^b_{0,M}(\mathbf{x})$ and $h_{\mathcal{B}}(\mathbf{x}) = \bar{h}^b_{M,0}(\mathbf{x})$ to define the TIS overall states $\mathcal{A}$ and $\mathcal{B}$. According to this definition, a point **x** is assigned to overall state $\mathcal{A}$ if region A is reached before B when the trajectory through **x** is followed backwards in time. Hence, overall states $\mathcal{A}$ and $\mathcal{B}$ consist of points **x** located on trajectories coming from A and B, respectively.

Based on the characteristic function, the general crossing function is defined as

$$\psi_{i,j}(\mathbf{x}_t) = \bar{h}^{\mathrm{b}}_{j,i}(\mathbf{x}_t)\theta(\lambda_i - \lambda(\mathbf{x}_t))\theta(\lambda(\mathbf{x}_{t+\Delta t}) - \lambda_i) \tag{3}$$

where θ is the Heaviside step-function and Δt is the time step. For the phase point $\mathbf{x}_t$ visited by a trajectory at time t, $\psi_{i,j}(\mathbf{x}_t)$ will equal 1 only if the trajectory comes directly from j and immediately crosses i in the next time step of length Δt. For convenience, an effective crossing function is defined as

$$\begin{aligned}\Psi^{l,m}_{i,j}(\mathbf{x}_t) &= \bar{h}^{\mathrm{b}}_{j,i}(\mathbf{x}_t)\theta(\lambda_i - \lambda(\mathbf{x}_t))\theta(\lambda(\mathbf{x}_{t+\Delta t}) - \lambda_i)\bar{h}^f_{l,m}(\mathbf{x}_t) \\ &= \psi_{i,j}(\mathbf{x}_t)\bar{h}^f_{l,m}(\mathbf{x}_t)\end{aligned} \tag{4}$$

When $\Psi^{l,m}_{i,j}(\mathbf{x}_t)=1$, the trajectory, which crosses i at $\mathbf{x}_t$ directly from j, will visit l earlier than m, otherwise $\Psi^{m,l}_{i,j}(\mathbf{x}_t)=0$. Clearly, $\Psi^{m,l}_{i,j}(\mathbf{x}_t)+\Psi^{l,m}_{i,j}(\mathbf{x}_t) = \psi_{i,j}(\mathbf{x}_t)$.

For a system evolving diffusively with high-friction character, it is reasonable to assume that the memory of trajectories is lost over a certain time and, hence, some distance in phase space along the λ-axis. If the transition interfaces, $\{\lambda_i\}_{i=1\ldots M-1}$, between states A and B are properly set such that the memory of trajectories only persists between adjacent interfaces, the average of an observable $g(\mathbf{x}_t)$ when the trajectories cross interface i coming from a faraway interface approximately equals the average over the trajectories coming from the adjacent interface [9],

$$\left\langle g(\mathbf{x}_t)\right\rangle_{\psi_{i,i\pm q}} \approx \left\langle g(\mathbf{x}_t)\right\rangle_{\psi_{i,i\pm 1}} \tag{5}$$

where q is a given integer. As a matter of fact, the exact expression of memory loss defined in PPTIS[9] is $\left\langle g(\mathbf{x}_t)\right\rangle_{\phi_{i,i\pm q}} \approx \left\langle g(\mathbf{x}_t)\right\rangle_{\phi_{i,i\pm 1}}$, where $\phi_{i,j}(\mathbf{x}_t) = \lim_{\Delta t\to 0}\frac{1}{\Delta t}\psi_{i,j}(\mathbf{x}_t)$ equals the velocity of crossing interface i at time t in a trajectory coming directly from j before recrossing i. In practice, Δt is given as a small but fixed time step in simulation instead of carrying out the limit $\Delta t \to 0$, and hence the definition of memory loss in PPTIS is equivalent to that expressed by eq. (5).

Since the memory loss should be also obeyed for paths coming from the same stable state, eq. (5) can be extended as

$$\begin{cases} \left\langle g(\mathbf{x}_t)\right\rangle_{\psi_{i,\mathrm{A}}} \approx \left\langle g(\mathbf{x}_t)\right\rangle_{\psi_{i,i-1}|\mathrm{A}} \\ \left\langle g(\mathbf{x}_t)\right\rangle_{\psi_{i,\mathrm{B}}} \approx \left\langle g(\mathbf{x}_t)\right\rangle_{\psi_{i,i+1}|\mathrm{B}} \end{cases} \tag{6}$$

where $\left\langle g(\mathbf{x}_t)\right\rangle_{\psi_{i,i\pm q}|\mathrm{A(B)}} = \dfrac{\left\langle \hat{h}_{\mathcal{A}(\mathcal{B})}(\mathbf{x}) g(\mathbf{x}_t)\psi_{i,i\pm q}\right\rangle / \left\langle \hat{h}_{\mathcal{A}(\mathcal{B})}(\mathbf{x})\right\rangle}{\left\langle \hat{h}_{\mathcal{A}(\mathcal{B})}(\mathbf{x})\psi_{i,i\pm q}\right\rangle / \left\langle \hat{h}_{\mathcal{A}(\mathcal{B})}(\mathbf{x})\right\rangle} = \dfrac{\left\langle g(\mathbf{x}_t)\psi_{i,i\pm q}\right\rangle_{\mathrm{A(B)}}}{\left\langle \psi_{i,i\pm q}\right\rangle_{\mathrm{A(B)}}}$. Here, $\left\langle ...\right\rangle_{\mathrm{A(B)}}$ is an averaging over the paths coming from one of the stable regions A(B) and ending in either A or B. Since $\left\langle g(\mathbf{x}_t)\right\rangle_{\psi_{i,i\pm1}} = \omega_{\mathrm{A}}^{i,i\pm1}\left\langle g(\mathbf{x}_t)\right\rangle_{\psi_{i,i\pm1}|\mathrm{A}} + \omega_{\mathrm{B}}^{i,i\pm1}\left\langle g(\mathbf{x}_t)\right\rangle_{\psi_{i,i\pm1}|\mathrm{B}}$, where $\omega_{\mathrm{A(B)}}^{i,i\pm1} = \left\langle \hat{h}_{\mathcal{A}(\mathcal{B})}(\mathbf{x})\psi_{i,i\pm q}\right\rangle / \left\langle \psi_{i,i\pm q}\right\rangle$ and $\omega_{\mathrm{A}}^{i,i\pm1} + \omega_{\mathrm{B}}^{i,i\pm1} = 1$, combined with eqs. (5) and (6), one can easily get the relation

$$\left\langle g(\mathbf{x}_t)\right\rangle_{\psi_{i,i\pm1}} \approx \left\langle g(\mathbf{x}_t)\right\rangle_{\psi_{i,i\pm1}|\mathrm{A}} \approx \left\langle g(\mathbf{x}_t)\right\rangle_{\psi_{i,i\pm1}|\mathrm{B}} \tag{7}$$

Equation (7) indicates that average properties observed in trajectories, which crossed i from $i\pm1$ in paths coming from A, are approximately equal to the averages observed in paths coming from B.

The crossing probability $P(\begin{smallmatrix} m \\ l \end{smallmatrix}\big|\begin{smallmatrix} i \\ j \end{smallmatrix})$, which describes a path having crossed interface i from j and which will continue to reach interface m before l, is expressed using the crossing functions as

$$P(\begin{smallmatrix} m \\ l \end{smallmatrix}\big|\begin{smallmatrix} i \\ j \end{smallmatrix}) = \frac{\left\langle \Psi_{i,j}^{m,l}\right\rangle}{\left\langle \psi_{i,j}\right\rangle} = \frac{\left\langle \psi_{i,j}\bar{h}_{l,m}^{f}\right\rangle}{\left\langle \psi_{i,j}\right\rangle} = \left\langle \bar{h}_{m,l}^{f}\right\rangle_{\psi_{i,j}} \tag{8}.$$

In PPTIS [9], the one-interface crossing probabilities are defined as $p_i^{\pm} \equiv P(\begin{smallmatrix} i+1 \\ i-1 \end{smallmatrix}\big|\begin{smallmatrix} i \\ i-1 \end{smallmatrix})$, $p_i^{=} \equiv P(\begin{smallmatrix} i-1 \\ i+1 \end{smallmatrix}\big|\begin{smallmatrix} i \\ i-1 \end{smallmatrix})$, $p_i^{\mp} \equiv P(\begin{smallmatrix} i-1 \\ i+1 \end{smallmatrix}\big|\begin{smallmatrix} i \\ i+1 \end{smallmatrix})$ and $p_i^{+} \equiv P(\begin{smallmatrix} i+1 \\ i-1 \end{smallmatrix}\big|\begin{smallmatrix} i \\ i+1 \end{smallmatrix})$. According to the memory loss assumption, $\left\langle \bar{h}_{m,l}^{f}(\mathbf{x}_t)\right\rangle_{\psi_{i,i\pm1}} \approx \left\langle \bar{h}_{m,l}^{f}(\mathbf{x}_t)\right\rangle_{\psi_{i,i\pm1}|\mathrm{A}} \approx \left\langle \bar{h}_{m,l}^{f}(\mathbf{x}_t)\right\rangle_{\psi_{i,i\pm1}|\mathrm{B}}$. Hence, the one-interface crossing probability can be rewritten as

$$\begin{aligned} p_i^{\pm} &\equiv \frac{\left\langle \Psi_i^{\pm}\right\rangle}{\left\langle \psi_{i,i-1}\right\rangle} \approx \frac{\left\langle \Psi_i^{\pm}\right\rangle_{\mathrm{A(B)}}}{\left\langle \psi_{i,i-1}\right\rangle_{\mathrm{A(B)}}} \qquad p_i^{=} \equiv \frac{\left\langle \Psi_i^{=}\right\rangle}{\left\langle \psi_{i,i-1}\right\rangle} \approx \frac{\left\langle \Psi_i^{=}\right\rangle_{\mathrm{A(B)}}}{\left\langle \psi_{i,i-1}\right\rangle_{\mathrm{A(B)}}} \\ p_i^{\mp} &\equiv \frac{\left\langle \Psi_i^{\mp}\right\rangle}{\left\langle \psi_{i,i+1}\right\rangle} \approx \frac{\left\langle \Psi_i^{\mp}\right\rangle_{\mathrm{A(B)}}}{\left\langle \psi_{i,i+1}\right\rangle_{\mathrm{A(B)}}} \qquad p_i^{+} \equiv \frac{\left\langle \Psi_i^{+}\right\rangle}{\left\langle \psi_{i,i+1}\right\rangle} \approx \frac{\left\langle \Psi_i^{+}\right\rangle_{\mathrm{A(B)}}}{\left\langle \psi_{i,i+1}\right\rangle_{\mathrm{A(B)}}} \end{aligned} \tag{9}$$

where $\langle \Psi_i^{\Theta} \rangle$ with $\Theta = \pm, \mp, =, {}_{+}^{+}$ is a short notation for $\langle \Psi_i^{\pm} \rangle = \langle \Psi_{i,i-1}^{i+1,i-1} \rangle$, $\langle \Psi_i^{=} \rangle = \langle \Psi_{i,i-1}^{i-1,i+1} \rangle$, $\langle \Psi_i^{\pm} \rangle = \langle \Psi_{i,i+1}^{i+1,i-1} \rangle$ and $\langle \Psi_i^{\mp} \rangle = \langle \Psi_{i,i+1}^{i-1,i+1} \rangle$.

2.2 Reweighted Partial Path Method

2.2.1 Reweighted effective crossing

In unbiased ensembles, the transition paths originate from basin A or B, and end in A or B after visiting the transition region. Supposing a trajectory reaches interface i from i-1, it will continue to cross the adjacent interfaces (i+1 or i-1) until it leaves the transition region and reaches A or B. Considering the continuity of trajectories, the average crossing of i from i-1, $\langle \psi_{i,i-1} \rangle$ (see Fig.1(a)), equals the average effective crossing of i-1 from both i and i-2, e.g. $\langle \psi_{i,i-1} \rangle = \langle \Psi_{i-1}^{\pm} \rangle + \langle \Psi_{i-1}^{\pm} \rangle$. Similarly, the effective crossing of interface i-1 from i also obeys the continuity relation as illustrated in Fig.1(b) so that $\langle \psi_{i-1,i} \rangle = \langle \Psi_i^{\mp} \rangle + \langle \Psi_i^{=} \rangle$. Bearing in mind that $\langle \psi_{i-1,i} \rangle = \langle \Psi_{i-1}^{\mp} \rangle + \langle \Psi_{i-1}^{\pm} \rangle$ and $\langle \psi_{i,i-1} \rangle = \langle \Psi_i^{\pm} \rangle + \langle \Psi_i^{=} \rangle$, the continuity relation can be written as

$$\begin{cases} \langle \Psi_{i-1}^{\pm} \rangle - \langle \Psi_{i-1}^{\mp} \rangle = \langle \Psi_i^{\pm} \rangle - \langle \Psi_i^{\mp} \rangle \\ \langle \Psi_{i-1}^{\mp} \rangle + \langle \Psi_{i-1}^{+} \rangle = \langle \Psi_i^{\mp} \rangle + \langle \Psi_i^{=} \rangle \end{cases} \quad (10).$$

If we denote $J = \langle \Psi_{i-1}^{\pm} \rangle - \langle \Psi_{i-1}^{\mp} \rangle = \langle \Psi_i^{\pm} \rangle - \langle \Psi_i^{\mp} \rangle$, according to eq. (9), eq. (10) can be rewritten as

$$\frac{1}{p_i^{=}} \langle \Psi_i^{\mp} \rangle - \frac{p_i^{\pm}}{p_i^{=} p_{i-1}^{\mp}} \langle \Psi_{i-1}^{\mp} \rangle + J = 0 \quad (11)$$

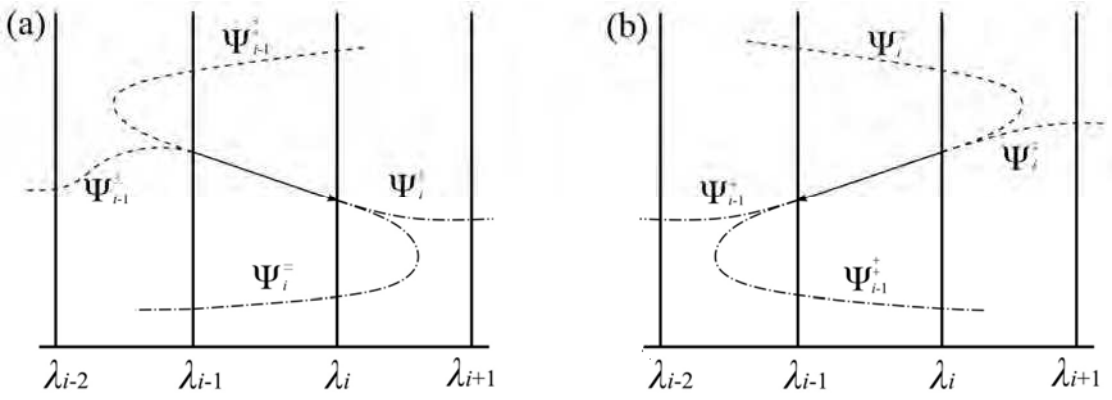

Fig. 1 Illustration of the continuity relation for (a) the effective crossing of interface i from i-1, and (b) the effective crossing of interface i-1 from i.

The continuity relation should also be obeyed by the trajectories exclusively coming from state A(B) and ending in either A or B, as $\frac{1}{p_i^{=}}\left\langle \Psi_i^{\mp} \right\rangle_{\mathrm{A(B)}} - \frac{p_i^{\pm}}{p_i^{=} p_{i-1}^{\mp}} \left\langle \Psi_{i-1}^{\mp} \right\rangle_{\mathrm{A(B)}} + J_{\mathrm{A(B)}} = 0$, with $J_{\mathrm{A(B)}} = \left\langle \Psi_i^{\pm} \right\rangle_{\mathrm{A(B)}} - \left\langle \Psi_i^{\mp} \right\rangle_{\mathrm{A(B)}}$. Now, let's only consider the trajectories coming from state A and ending in either A or B. According to the boundary conditions, $\left\langle \Psi_{M-1}^{\mp} \right\rangle_{\mathrm{A}} = 0$, the relation between the effective crossing $\left\langle \Psi_i^{\Theta} \right\rangle_{\mathrm{A}}$ and $\left\langle \Psi_i^{\Theta} \right\rangle$ is derived by solving eq. (11) for every interface (see Appendix B),

$$\begin{cases} \left\langle \Psi_i^{\mp} \right\rangle_{\mathrm{A}} = \dfrac{U_{i+1}}{\left\langle h_{\mathcal{A}} \right\rangle} \cdot \left\langle \Psi_i^{\mp} \right\rangle \\ \left\langle \Psi_i^{\pm} \right\rangle_{\mathrm{A}} = \dfrac{U_{i+1}}{\left\langle h_{\mathcal{A}} \right\rangle} \cdot \left\langle \Psi_i^{\pm} \right\rangle \end{cases} \quad \text{and} \quad \begin{cases} \left\langle \Psi_i^{\pm} \right\rangle_{\mathrm{A}} = \dfrac{U_{i+1}}{\left\langle h_{\mathcal{A}} \right\rangle} \cdot \left\langle \Psi_i^{\pm} \right\rangle + J_{\mathrm{A}} \\ \left\langle \Psi_i^{=} \right\rangle_{\mathrm{A}} = \dfrac{U_{i+1}}{\left\langle h_{\mathcal{A}} \right\rangle} \cdot \left\langle \Psi_i^{=} \right\rangle + \dfrac{p_i^{=}}{p_i^{\pm}} J_{\mathrm{A}} \end{cases} \tag{12}$$

where $U_i = P\left(\begin{matrix} 0 \\ M \end{matrix} \middle| \begin{matrix} i \\ 0 \end{matrix}\right) = 1 - P\left(\begin{matrix} M \\ 0 \end{matrix} \middle| \begin{matrix} i \\ 0 \end{matrix}\right)$ and $J_{\mathrm{A}} = \left\langle \Psi_0^{\pm} \right\rangle_{\mathrm{A}} \left(1 - U_1\right)$. U_i denotes the decaying probability from interface i in the transition from A to B, which corresponds to the probability that a trajectory, coming from A, returns to A before reaching B after it crossed interface i. Equation (12) indicates that, under the memory loss assumption, the average effective crossing of interface i from adjacent interfaces, $\left\langle \Psi_i^{\Theta} \right\rangle$, is connected with weighted average in the paths coming from A, $\left\langle \Psi_i^{\Theta} \right\rangle_{\mathrm{A}}$, by the decaying probability in transition A to B. Similar relations between $\left\langle \Psi_i^{\Theta} \right\rangle_{\mathrm{B}}$ and $\left\langle \Psi_i^{\Theta} \right\rangle$ can also be derived with boundary conditions $\left\langle \Psi_1^{\pm} \right\rangle_{\mathrm{B}} = 0$, by solving the equation (11) for every interface.

2.2.2 Equilibrium histogram of λ from reweighted partial paths

When a trajectory effectively crossed the interface i from i-1 or i+1, a partial path is recognized as the continuous path segment remaining between i-1 and i+1. For example, in Fig. 2(b) when the trajectory crosses i-1 at point b coming from i-2 and leaves the interface region by crossing i at point e, it is considered as an effective crossing of i-1 represented as $\Psi_{i-1}^{\pm}(b) = 1$. The path segment from $a \rightarrow e$ is recognized as a partial path on i-1 with the crossing type denoted by $\pm$. As illustrated in Fig. 2(a), there are four types of partial paths on interface i, denoted by $\Theta = \pm, \mp, =, \begin{matrix} + \\ + \end{matrix}$, with each one corresponding to an effective crossing of interface i. In unbiased ensembles, partial paths can be generated by breaking up the trajectories into path segments based on the

effective crossing of every interface. Accordingly, one partial path is coupled with one effective crossing, hence the unbiased number density of partial paths on interface i with type Θ is equal to the average effective crossing $\left\langle \Psi_i^{\Theta} \right\rangle$ in trajectory space. For the partial paths generated from trajectories exclusively coming from A (B), the number density of partial paths on i equals $\left\langle \Psi_i^{\Theta} \right\rangle_{\mathrm{A(B)}}$.

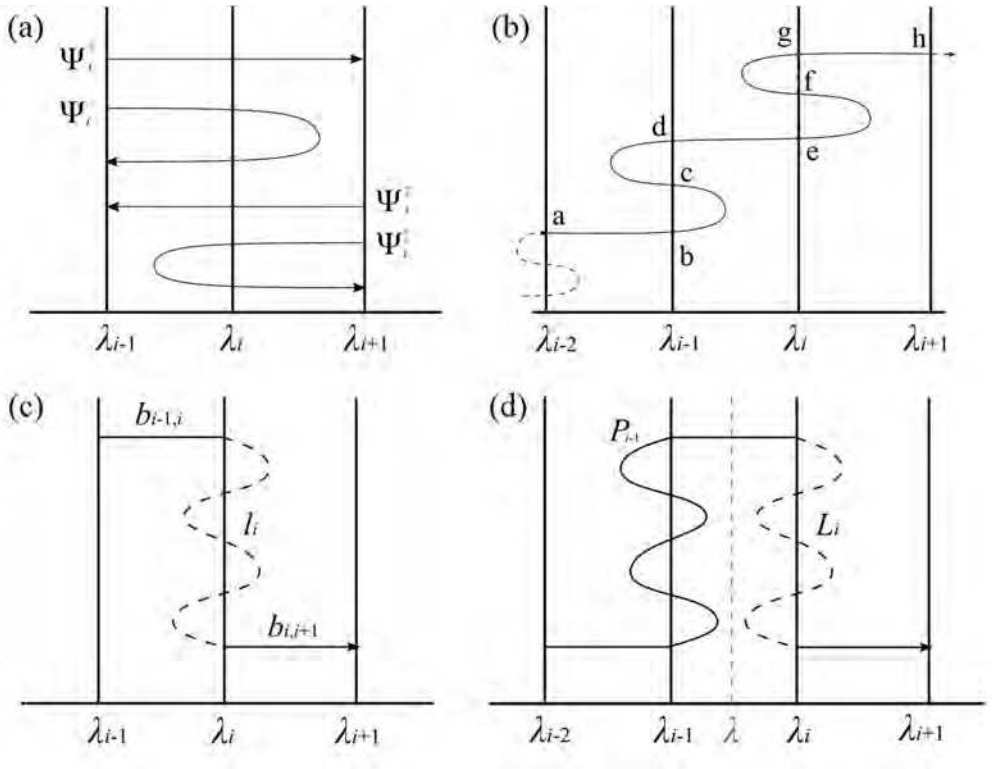

Fig. 2 (a) Four types of partial paths corresponding to four effective crossings at interface i; (b) A trajectory effectively crosses interface i-1 and then i at points b and e, respectively. According to the definition, the partial path generated on i-1 is the segment $a \rightarrow e$ and the partial path generated on i is $d \rightarrow h$; (c) A partial path on interface i is divided into three parts: two boundary segments (solid lines) and a loop segment (dashed line). (d) The boundary path segment between λ_{i-1} and λ_i is shared by partial paths on interface i-1 and i. To avoid double counting the histogram of λ, where $\lambda \in (\lambda_{i-1}, \lambda_i)$, the phase points falling on λ are treated as being visited by the partial paths on interface i-1 and the loop of partial paths on i. This is equivalent to using the loop of partial paths in i-1 and the partial paths on i to calculate the histogram of λ.

Similar to the *loop-boundary* method [10] in PPTIS, the partial paths on i are divided into three parts: two boundary segments and a loop part (illustrated in Fig. 2(c)). The loop part is defined as the segment between the first crossing point and the last crossing point of the middle interface marked by the dashed line in Fig. 2(c). The boundary parts are defined as the segments from the path boundary point to the last and first crossing point of interface i, marked by the solid lines in Fig. 2(c). When a trajectory consecutively crossed two adjacent interfaces, there is an overlapping part between the

partial paths generated by the trajectory on the two interfaces. For instance, the path segment $d\to e$ is shared by partial paths $a\to e$ and $d\to h$, when the trajectory crossed interface i-1 and i in a row. In the meantime, $d\to e$ is a boundary segment between interface i-1 and i for partial paths $a\to e$ and $d\to h$. Therefore, to avoid double counting, the histogram of phase points from a trajectory in a small bin $[\lambda-\delta\lambda, \lambda+\delta\lambda]$ with $\lambda\in(\lambda_{i-1}, \lambda_i)$ (see Fig. 2(d)) can be calculated by the histogram from partial paths on interface i-1 combined with the histogram of λ in the loop part of partial paths on interface i as

$$\left\langle \delta\left(\lambda(\mathbf{x}_t)-\lambda\right)\right\rangle = \sum_{\Theta=\pm,\mp,=,\substack{+\\+}} \left\langle \Psi_{i-1}^{\Theta}\right\rangle P_{i-1}^{\Theta}(\lambda)+\left\langle \Psi_{i}^{\Theta}\right\rangle L_{i}^{\Theta}(\lambda) \qquad (13)$$

where $P_{i-1}^{\Theta}(\lambda)$ is the average histogram of λ in the partial path of type Θ on interface i-1, and $L_i^{\Theta}(\lambda)$ is the average histogram of λ from the loop on the partial path of type Θ on interface i. This is equivalent to calculating the histogram of λ from the partial paths on i and the loop of partial paths on i-1, as $\left\langle \delta\left(\lambda(\mathbf{x}_t)-\lambda\right)\right\rangle = \sum_{\Theta=\pm,\mp,=,\substack{+\\+}} \left\langle \Psi_{i-1}^{\Theta}\right\rangle L_{i-1}^{\Theta}(\lambda)+\left\langle \Psi_{i}^{\Theta}\right\rangle P_{i}^{\Theta}(\lambda)$.

When a trajectory effectively crossed interface i at phase point $\mathbf{x}_t$, the histogram of λ in the partial path is calculated as $\rho_i^{\Theta}(\lambda)=\int_{t-\Delta t_{\Theta}^{b}}^{t+\Delta t_{\Theta}^{f}} dt'\ \delta\left(\lambda(\mathbf{x}_{t'})-\lambda\right)$, where Δt_{Θ}^{f} and Δt_{Θ}^{b} are the times when the trajectory first crosses interface i+1 (i-1) forward and backward from $\mathbf{x}_t$, respectively. For Θ in $\pm,\mp,=$ and $\substack{+\\+}$, $\left(\Delta t_{\Theta}^{f},\Delta t_{\Theta}^{b}\right)$ is taken as $\left(\Delta t_{i+1}^{f},\Delta t_{i-1}^{b}\right)$, $\left(\Delta t_{i-1}^{f},\Delta t_{i+1}^{b}\right)$, $\left(\Delta t_{i-1}^{f},\Delta t_{i-1}^{b}\right)$ and $\left(\Delta t_{i+1}^{f},\Delta t_{i+1}^{b}\right)$, respectively. Accordingly, the average density of λ in the partial path Θ having crossed i is defined as $P_i^{\Theta}(\lambda)=\left\langle \rho_i^{\Theta}(\lambda)\right\rangle_{\Psi_i^{\Theta}}$. Similarly, the density of λ in the loop part (illustrated as dashed line in Fig.2 (c)) of partial path having crossed i can be also calculated as $L_i^{\Theta}(\lambda)=\left\langle l_i^{\Theta}(\lambda)\right\rangle_{\Psi_i^{\Theta}}$, with $l_i^{\Theta}(\lambda)=\int_{t-\Delta t_{\Theta}^{b}}^{t+\Delta t_{\Theta}^{f}} dt'\ \delta\left(\lambda(\mathbf{x}_{t'})-\lambda\right) l_i(\mathbf{x}_{t'})$. Here, $l_i(\mathbf{x}_{t'})$ is a characteristic function [10], where $l_i(\mathbf{x}_{t'})=1$ if $\mathbf{x}_{t'}$ is on the loop of the partial path, otherwise $l_i(\mathbf{x}_{t'})=0$. According to the memory loss assumption, $\left\langle \rho_i^{\Theta}\right\rangle_{\Psi_i^{\Theta}} \approx \left\langle \rho_i^{\Theta}\right\rangle_{\Psi_i^{\Theta}|\mathrm{A(B)}}$ and $\left\langle l_i^{\Theta}\right\rangle_{\Psi_i^{\Theta}} \approx \left\langle l_i^{\Theta}\right\rangle_{\Psi_i^{\Theta}|\mathrm{A(B)}}$, therefore

$$\begin{aligned}\left\langle \delta\left(\lambda(\mathbf{x}_t)-\lambda\right)\right\rangle_{\mathrm{A}} &= \sum_{\Theta=\pm,\mp,=,\substack{+\\+}} \left\langle \Psi_{i-1}^{\Theta}\right\rangle_{\mathrm{A}} \left\langle \rho_i^{\Theta}\right\rangle_{\Psi_i^{\Theta}|\mathrm{A}} + \left\langle \Psi_{i}^{\Theta}\right\rangle_{\mathrm{A}} \left\langle l_i^{\Theta}\right\rangle_{\Psi_i^{\Theta}|\mathrm{A}} \\ &\approx \sum_{\Theta=\pm,\mp,=,\substack{+\\+}} \left\langle \Psi_{i-1}^{\Theta}\right\rangle_{\mathrm{A}} P_{i-1}^{\Theta}(\lambda)+\left\langle \Psi_{i}^{\Theta}\right\rangle_{\mathrm{A}} L_i^{\Theta}(\lambda)\end{aligned} \qquad (14).$$

Combining eqs. (12), (13) and (14), the equilibrium histogram of λ is written as

$$\left\langle \delta\left(\lambda(\mathbf{x}_t)-\lambda\right)\right\rangle = \frac{\left\langle \delta\left(\lambda(\mathbf{x}_t)-\lambda\right)\right\rangle_{\mathrm{A}} - C_i(\lambda)J_{\mathrm{A}}}{U_i}\cdot\left\langle h_{\mathcal{A}}\right\rangle \qquad (15)$$

where $C_i(\lambda) = P_{i-1}^{\pm}(\lambda) + \frac{p_{i-1}^{=}}{p_{i-1}^{\pm}}P_{i-1}^{=}(\lambda) + p_i^{\pm}L_i^{\pm}(\lambda) + p_i^{=}L_i^{=}(\lambda) - p_i^{=}L_i^{\mp}(\lambda) - \frac{p_i^{+}p_i^{=}}{p_i^{\mp}}L_i^{+}(\lambda)$.

In eq. (15), $\left\langle \delta\left(\lambda(\mathbf{x}_t)-\lambda\right)\right\rangle_{\mathrm{A}}$ is the unbiased histogram of λ in the ensemble with paths coming from A and ending either in A or B. This path ensemble can be obtained in a single TIS calculation for the transition A→B by assigning an unbiased path weight $\mathcal{P}_{\mathrm{A}}(\mathbf{x}^{\tau})$ to each TIS trajectory, $\mathbf{x}^{\tau}$, using a reweighting strategy, e.g. the reweighted path ensemble method [14]. The partial paths on each interface can be generated by breaking up TIS trajectories based on the type of effective crossing, and the average of effective crossings are determined as $\left\langle \Psi_i^{\Theta}\right\rangle_{\mathrm{A}} = \sum \mathcal{P}_{\mathrm{A}}(\mathbf{x}^{\tau})n_i^{\Theta}(\mathbf{x}^{\tau})$, where $n_i^{\Theta}(\mathbf{x}^{\tau})$ describes how many times the trajectory $\mathbf{x}^{\tau}$ effectively crosses interface i with type Θ. With the memory loss assumption, $p_i^{\Theta}, P_i^{\Theta}$ and L_i^{Θ} can also be evaluated in a single TIS calculation for transition A→B, and hence one can obtain the equilibrium histogram of λ, i.e. $\left\langle \delta\left(\lambda(\mathbf{x}_t)-\lambda\right)\right\rangle$, by eq.(15).

In PPTIS, the partial paths are sampled from every transition interface in an unbiased manner — the trajectories are shot from the phase points on interface i forward and backward until they hit the adjacent interface i-1 or i+1. The averaged histogram P_i^{Θ} and L_i^{Θ} can be directly measured from the partial path gathered on interface i. When calculating the equilibrium histogram of λ, $\left\langle \delta\left(\lambda(\mathbf{x}_t)-\lambda\right)\right\rangle$, using the *loop-boundary* method, the average weights of partial paths on adjacent interfaces, e.g. $\left\langle \Psi_{i-1}^{\Theta}\right\rangle$ and $\left\langle \Psi_i^{\Theta}\right\rangle$ in eq. (13), are reweighted according to the histogram of the commonly shared boundary path segment between interfaces. Therefore, in PPTIS, there is no need to derive the relation of $\left\langle \Psi_i^{\Theta}\right\rangle$ and $\left\langle \Psi_i^{\Theta}\right\rangle_{\mathrm{A(B)}}$ in the calculation of equilibrium histogram of λ. However, due to the unique sampling strategy in PPTIS, this *loop-boundary* method cannot be directly used in a general TIS calculation. For a TIS single transition, i.e. A→B or B→A, one can evaluate the average histogram P_i^{Θ} and L_i^{Θ} from partial paths generated by breaking up TIS trajectories, but the weights (or

the effective crossing) of partial paths on each interface are $\left\langle \Psi_i^{\Theta} \right\rangle_{\mathrm{A(B)}}$ instead of $\left\langle \Psi_i^{\Theta} \right\rangle$. To evaluate the equilibrium histogram of λ, in RPP method, we derive the relation of $\left\langle \Psi_i^{\Theta} \right\rangle$ and $\left\langle \Psi_i^{\Theta} \right\rangle_{\mathrm{A(B)}}$ (see eq.(12)) and implement the *loop-boundary* method in the general TIS calculation for a single transition (see eq. (15)).

To the transitions known to be diffusive, both PPTIS and TIS+RPP can be used to simultaneously evaluate the transition rate constant and energy profile. As to a transition, which is not certain to be diffusive, one can first do TIS to calculate the reaction rate constant, and then use RPP to reconstruct the energy profile and validate the memory loss assumption afterwards (see example in section 3.3). If the validation is failed, i.e. RPP result is not reliable, one can still do a reverse TIS or Umbrella Sampling simulation to re-evaluate the energy profile. Since RPP does not require additional sampling, the computational cost for the energy profile is negligible.

Now let us consider an extreme case where the phase space is projected on a discrete order parameter λ_i, each i representing a state. The transition consists of the system's consecutive jumps from one state to another adjacent state. If complete memory loss is assumed, i.e. the frequency of jumping from state i to $i\pm1$ only depends on state i, then $p_i^{\mp} = p_i^{=}$ and $p_i^{+} = p_i^{\pm}$. Still considering $\{\lambda_i\}$ as transition interfaces, there is only one phase point $\mathbf{x}_t$, as $\lambda(\mathbf{x}_t)=\lambda_i$, on each partial path on interface i, i.e. $P_i^{\Theta}(\lambda_i) = \delta(\lambda(\mathbf{x}_t),\lambda_i)$. This phase point can be categorized to either boundary segment or loop segment of the partial path, while in both cases $C_i(\lambda_i)$ equals to 0. Therefore, in the complete memory loss assumption, eq. (15) can be rewritten as $\left\langle \delta\left(\lambda(\mathbf{x}_t)-\lambda_i\right)\right\rangle = \left\langle \delta\left(\lambda(\mathbf{x}_t)-\lambda_i\right)\right\rangle_{\mathrm{A}} / U_i$.

A similar model for the complete memory loss assumption can be found in the work of White [16] and Kashchiev [17] for homogeneous nucleation through random attachment and detachment of monomers. Here, the same conclusion is reached, namely that the equilibrium number density of clusters of size i equals its stationary number density in a nucleation reaction divided by the decaying probability of clusters of size i dissolving to monomers instead of growing into a post-critical cluster.

3. Simulation Results

3.1 Model for Cu precipitate nucleation in a dilute Fe-Cu alloy

FFS is a variant of the TIS method, which inherits the basic theory from TIS but employs a ratchet-like manner to generate trajectories through transition interfaces. In principle, the trajectories in FFS are TIS trajectories, which originate from one of the basins (A or B), cross interface i, and return to A or B. The evaluation of the unbiased path weight $\mathcal{P}_{\mathrm{A(B)}}(\mathbf{x}^{\tau})$ is simple and straightforward [15] and our reweighting procedure can be easily applied to FFS-trajectories. As an example, we demonstrate

how to use the our RPP method to calculate the rate constant and free energy profile for homogeneous nucleation of copper clusters in a dilute Fe-Cu alloy from FFS-trajectories.

The nucleation simulation is carried out using a Metropolis Monte Carlo algorithm on a rigid bcc lattice of 54000 atoms of a Fe-1%Cu alloy at 600°C. A pairwise Local Chemical Environment (LCE) potential [18] is used to describe the system's energy as $E = \sum_{i=1}^{2} \sum_{\mathrm{X,Y}} n_{\mathrm{XY}}^{(i)} \varepsilon_{\mathrm{XY}}^{(i)}$, where $n_{\mathrm{XY}}^{(i)}$ and $\varepsilon_{\mathrm{XY}}^{(i)}$ are the number of XY bonds and the corresponding bond energy in the i-th nearest neighbor shell (X and Y denote the atomic species). $\varepsilon_{\mathrm{XY}}^{(i)} = \chi_{\mathrm{X}} \varepsilon_{\mathrm{XY}}^{\mathrm{X}(i)} + \chi_{\mathrm{Y}} \varepsilon_{\mathrm{XY}}^{\mathrm{Y}(i)}$, where χ_{X} and χ_{Y} are the atomic fractions of X and Y in the local environment and $\varepsilon_{\mathrm{XY}}^{\mathrm{X}(i)}$ ($\varepsilon_{\mathrm{XY}}^{\mathrm{Y}(i)}$) is the XY bond energy in a pure X and Y environment, respectively. The summation runs over all the possible combinations of bonds in X and Y, representing the atomic species Cu and Fe, as well as vacancy. Here, one vacancy is placed on a substitutional site to trigger the atomic diffusion by exchanging the vacancy with a nearest neighbor atom.

According to the Metropolis algorithm, the acceptance probability for the vacancy exchange is given by $P = \min\left[1, \exp\left(-\Delta E / k_{\mathrm{B}} T\right)\right]$, where ΔE represents the total energy difference between the initial state and the state after the exchange event. The Monte Carlo step (MCS) is coupled with real time by defining the average time increment from one vacancy jump [18] as $\Delta t = \frac{a^2 x_{\mathrm{Va,MC}}}{D_{\mathrm{X}}} \cdot k$, where a is the nearest neighbor distance in bcc-Fe (2.468 Å), D_{X} is the macroscopic diffusion coefficient of the jumping atom X in bcc-Fe, $x_{\mathrm{Va,MC}}$ is the vacancy site fraction in the simulation box and k is a correction for the diffusion correlation effect in the vacancy exchange mechanism (0.727 for bcc lattice [19]).

3.2 Computation of the rate constant with FFS

To study the kinetics of the nucleation, we use the Forward Flux Sampling (FFS) [7][8] method to generate nucleation trajectories and evaluate the reaction rate constant of this event. The order parameter, λ, is chosen as the size of the largest clusters, and the cluster size is defined as the number of atoms contained in the cluster. The system is in a metastable random state when the size of the largest cluster is smaller than 5 atoms, i.e. $\lambda_0 = 5$. And the stable post-critical cluster is considered to be formed when the largest cluster grows over 65 atoms, thus $\lambda_M = 65$. Between the phase boundaries, we define 13 interfaces in the transition region for FFS, therefore M=14. Except for $\lambda_2 = 7$, $\lambda_i = 5\times(i\text{-}1)$ for $i = 3, \ldots, 14$. For convenience, the boundary of the random state is set to overlap with the first interface as $\lambda_1 = \lambda_0 = 5$.

The sampling procedure follows the standard FFS strategy described in Ref. [8], but the trajectories are stored in a TIS manner including the information after firing off the

trajectory from a phase point on the interface as well as the history inherited by this phase point. The crossing probability of interface i is calculated as $P(^{i+1}_{0}|^{i}_{0}) = N_i / M_i$, where M_i is the total number of trajectories fired off from interface i, and N_i is the number of trajectories which have reached interface i+1 before returning to region A. The reaction rate constant k_{AB} is calculated as $k_{AB} = \Phi_A \prod_{i=1}^{M-1} P(^{i+1}_{0}|^{i}_{0})$, where Φ_A is the initial flux of the system leaving region A and entering the transition region from the first interface. In the FFS calculation for Cu nucleation, the probability $P(^{B}_{0}|^{1}_{0}) = \prod_{i=1}^{M-1} P(^{i+1}_{0}|^{i}_{0})$ is estimated to be 6.44×10^{-7}, and the initial flux Φ_A is calculated to be $0.53 s^{-1}$, yielding a rate constant for Cu nucleation of 3.42×10^{-7} s^{-1}.

3.3 Computation of the free energy profile with the RPP method

In the transition of A→B, FFS generates trajectories starting from the boundary of basin A in a ratchet-like manner through interfaces. When a trajectory first reaches interface i at phase point $\mathbf{x}_t$ before returning to A, $\mathbf{x}_t$ is stored as the starting points in the search of trajectories crossing the next interface i+1. It is noted that the trajectory, which successfully reaches the next interface instead of returning to region A, is not a complete path but will be continued by firing off trajectories at the next interface until finally region A or B is reached. Patching up the fired-off trajectories on every interface from FFS, one can obtain the ensemble with paths exclusively coming from A and ending in A or B, i.e. $\{\mathbf{x}^\tau\}_A$. The unbiased probability of a path $\mathbf{x}^\tau$ in $\{\mathbf{x}^\tau\}_A$ can be estimated as [8][15]

$$\mathcal{P}_A(\mathbf{x}^\tau) = \begin{cases} P(^{i}_{0}|^{1}_{0}) / N_i & \text{if } \max\left(\lambda(\mathbf{x}^\tau)\right) \in (\lambda_i, \lambda_{i+1}) \\ P(^{M}_{0}|^{1}_{0}) & \text{if } \max\left(\lambda(\mathbf{x}^\tau)\right) \geq \lambda_M \end{cases} \tag{16}$$

As to other TIS methods, Rogal *et al.* [14] proposed a reweighting strategy to calculate the path probability in unbiased ensembles, based on the weighting factors from a Weighted Histogram Analysis Method (WHAM) [13] in the procedure of patching up the crossing probabilities of trajectories in every interface ensemble.

After the weighting procedure, the average of effective crossings on each interface can be calculated as $\left\langle \Psi_i^\Theta \right\rangle_A = \sum \mathcal{P}_A(\mathbf{x}^\tau) n_i^\Theta(\mathbf{x}^\tau)$, where $n_i^\Theta(\mathbf{x}^\tau)$ describes how many times the trajectory $\mathbf{x}^\tau$ effectively crosses interface i with crossing type Θ. According to the memory loss assumption, the one-interface crossing probability is estimated by eq. (9) from the effective crossing in ensemble $\{\mathbf{x}^\tau\}_A$. The result is plotted in Fig. 3. In this work, λ_0 and λ_1 are set to be overlapping. Once a trajectory reached λ_1 from λ_2,

it will end in state A. In this case, $\langle \psi_{1,2} \rangle_{\mathrm{A}} = \langle \Psi_1 \rangle_{\mathrm{A}}$, therefore $p_1^{\mp} = 1$ and $p_1^{\pm} = 0$ according to eq. (9). In the meantime, since all the trajectories in $\{\mathbf{x}^{\tau}\}_{\mathrm{A}}$ will end when they reach state B, there is no effective crossing of M-1 from M, i.e. $\langle \psi_{M-1,M} \rangle_{\mathrm{A}} = 0$. Therefore, the value of one-interface crossing probabilities at M-1=13, $p_{13}^{\mp}$ and $p_{13}^{\pm}$, cannot be evaluated in the FFS calculation for the forward transition.

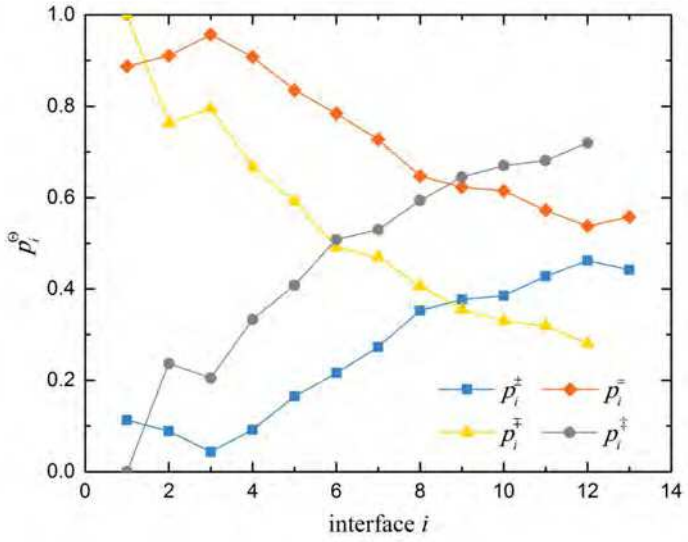

Fig. 3 One-interface crossing probabilities calculated from the reweighted FFS trajectories for every interface.

The one-interface crossing probability $p_i^{\ominus}$ is an average probability of the first-time crossing and re-crossing interface i from the adjacent interface. The implicit message of the memory loss assumption is that when the trajectories presently crossing i do not have the memory in the phase region beyond the adjacent interface, there is no difference between the first crossing and re-crossing probabilities. Based on the memory loss assumption, Moroni et al. [9] derived the connection between the crossing probabilities P_i^{+} (P_i^{-}), where $\mathrm{P}_i^{+} = P(\begin{smallmatrix} i \\ 0 \end{smallmatrix} \big| \begin{smallmatrix} 1 \\ 0 \end{smallmatrix})$ and $\mathrm{P}_i^{-} = P(\begin{smallmatrix} 0 \\ i \end{smallmatrix} \big| \begin{smallmatrix} i-1 \\ i \end{smallmatrix})$, and one-interface crossing probability $p_i^{\ominus}$ as

$$\mathrm{P}_i^{+} \approx \frac{p_{i-1}^{\pm}\mathrm{P}_{i-1}^{+}}{p_{i-1}^{\pm} + p_{i-1}^{=}\mathrm{P}_{i-1}^{-}}, \qquad \mathrm{P}_i^{-} \approx \frac{p_{i-1}\mathrm{P}_{i-1}^{-}}{p_{i-1}^{\pm} + p_{i-1}^{=}\mathrm{P}_{i-1}^{-}} \tag{17}.$$

Equation (17) is an implicit expression of P_i^{+} (P_i^{-}), which requires the information of $p_i^{\ominus}$ and P_{i-1}^{+} (P_{i-1}^{-}) for every interface and then iteratively solves for the value of

the crossing probability from $P_1^+(P_1^-)$ to $P_M^+(P_M^-)$. For convenience, eq. (17) can be rewritten in a separate form for P_i^+ and P_i^- simply as the function of one-interface crossing probability (see Appendix A) as

$$P_i^+ \approx \left(\sum_{m=1}^{i-1} \frac{p_1^{\mp} p_2^{\mp} \cdots p_{m-1}^{\mp} p_m^{=}}{p_1^{\pm} p_2^{\pm} \cdots p_m^{\pm}} \right)^{-1}, \quad P_i^- \approx \left(\sum_{m=1}^{i-1} \frac{p_1^{\mp} p_2^{\mp} \cdots p_{m-1}^{\mp} p_m^{=}}{p_1^{\pm} p_2^{\pm} \cdots p_m^{\pm}} \right)^{-1} \prod_{j=1}^{i-1} \frac{p_j^{\mp}}{p_j^{\pm}} \qquad (18).$$

Equations (17) and (18) are the expressions of crossing probability under the condition that the memory-loss assumption is valid in the system. Therefore, we can do a quick check for the memory loss assumption in the target system by comparing the result of crossing probability P_i^+ from the FFS calculation and eq. (17) or (18). Figure 4 plots the crossing probabilities, P_i^+ and P_i^-, evaluated from the one-interface crossing probability by eq. (18), compared with the crossing probability P_i^+ measured in the FFS calculation (red squares in Fig. 4). The good agreement indicates that the one-interface crossing probability is approximately the same in the first crossing and re-crossing of each interface, which is an evidence for long-range memory loss. If a large discrepancy were observed in the predictions for P_i^+ by FFS and eq. (18), the system would apparently not be memoryless and the RPP method would produce an incorrect equilibrium distribution of states on the chosen order parameter.

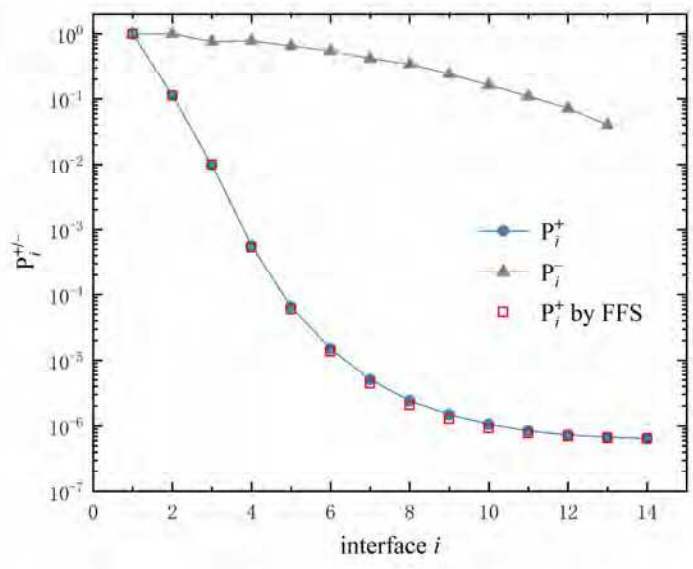

Fig. 4 Crossing probability calculated from one-interface crossing probabilities by eq. (18), compared with the crossing probability from the FFS algorithm.

The average distribution of λ in the partial path, $P_i^{\Theta}(\lambda)$, and the loop of the partial path, $L_i^{\Theta}(\lambda)$, is calculated at the same time with the effective crossing. Once the phase point $\mathbf{x}_t$ of an effective crossing is located on a trajectory, the histograms of λ, $\rho_i^{\Theta}(\mathbf{x}_t,\lambda)$ and $l_i^{\Theta}(\mathbf{x}_t,\lambda)$, can be determined by tracing along the trajectory from $\mathbf{x}_t$ forwardly and backwardly until the trajectory reaches the adjacent interface. The average density of λ in the partial path and the loop is calculated by $P_i^{\Theta}(\lambda)=\frac{\sum \mathcal{P}_{\mathrm{A}}(\mathbf{x}^{\tau})\rho_i^{\Theta}(\mathbf{x}_t,\lambda)}{\left\langle \Psi_i^{\Theta}\right\rangle_{\mathrm{A}}}$ and $L_i^{\Theta}(\lambda)=\frac{\sum \mathcal{P}_{\mathrm{A}}(\mathbf{x}^{\tau})l_i^{\Theta}(\mathbf{x}_t,\lambda)}{\left\langle \Psi_i^{\Theta}\right\rangle_{\mathrm{A}}}$. Since no trajectories cross $\lambda_{M\text{-}1}$ from λ_M in $\{\mathbf{x}^{\tau}\}_{\mathrm{A}}$, $P_{M-1}(\lambda)$ and $L_{M-1}(\lambda)$ are unknown for $\lambda\in[\lambda_{M\text{-}2}, \lambda_M]$. Therefore, according to eq. (15), the equilibrium distribution of the order parameter, $\left\langle \delta(\mathbf{x})-\lambda\right\rangle$, is only derived for $\lambda\in[\lambda_0, \lambda_{M\text{-}2}]$ in the RPP method. The free energy, $F(\lambda)$, is evaluated from the equilibrium distribution by $F(\lambda)=-k_BT\ln\left\langle \delta(\mathbf{x})-\lambda\right\rangle+c$, where c is a constant from normalization.

The free energy calculated by RPP from FFS trajectories is plotted on Fig. 5 by the red circles, compared with the results of standard Umbrella Sampling (US) [13] shown as blue solid line. In the transition phase region, $\lambda\in[8, 55]$, the RPP method gives a very close prediction of free energy compared with US. A broad and high activation barrier is provided by both methods with the highest point showing around λ = 35. Since the FFS algorithm only collects those trajectories visiting the transition region, the trajectories that linger in stable region are not included for the estimation of equilibrium distribution in RPP method. This is the reason for the discrepancy between the RRP and US results in the area close to region A. To correct the discrepancy, one can evaluate the distribution of λ from brute-force simulations around region A, and then patch up the free energy with the predictions from the RPP method.

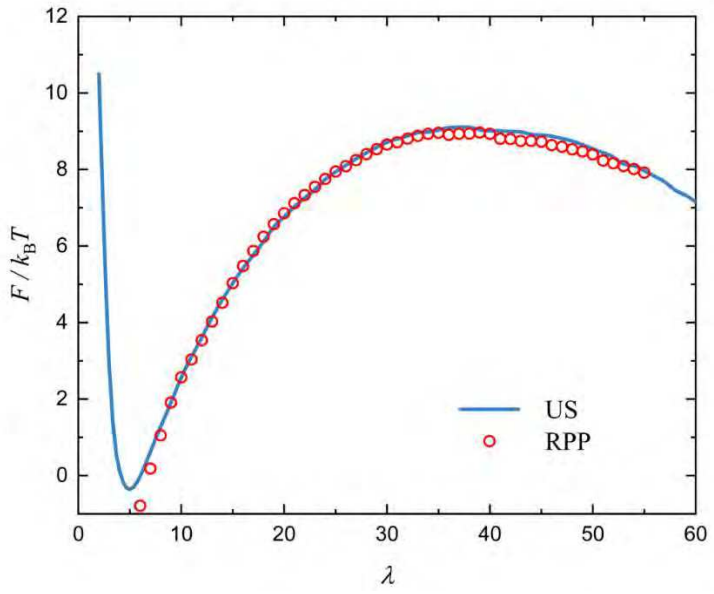

Fig. 5 Free energy of nucleation as a function of largest cluster size calculated by the Reweighted Partial Path method (red circles) compared with the one from Umbrella Sampling.

4. Discussion

In this work, we introduced a Reweighted Partial Path Method to evaluate the free energy profile of diffusive processes using trajectory information from a single TIS or FFS calculation. The main steps in the RPP method are summarized as follows: (i) after the rate calculation for the transition A→B is finished, the unbiased path probability $\mathcal{P}_{\mathrm{A}}(\mathbf{x}^{\tau})$ of every trajectory is calculated, e.g using eq. (16) for FFS and the reweighted path ensemble method [14] for TIS; (ii) the partial paths are generated by breaking up the trajectories into path segments according to the effective crossing points on every interface; (iii) the decaying probability U_i, the one-interface crossing probability p_i^{Θ} and the density of partial path $P_i^{\Theta}(\lambda)$ ($L_i^{\Theta}(\lambda)$) are calculated from partial paths on interface i. (iv) the equilibrium distribution of the order parameter, i.e. $\left\langle \delta\left(\lambda(\mathbf{x}_t)-\lambda\right)\right\rangle$, is evaluated based on the quantities computed in the previous steps according to eq. (15).

In principle, RPP is a related form of the *loop-boundary* method [10], which is proposed in PPTIS to derive the equilibrium state distribution from partial path ensembles. In the *loop-boundary* method, the equilibrium histogram of λ with $\lambda\in(\lambda_{i-1}, \lambda_i)$ is evaluated from the partial paths on interface i and i-1. PPTIS measures partial paths by performing the shooting algorithm on every interface, while RPP generates partial path from TIS trajectories and reweights them based on the memory loss assumption. Therefore, similar to PPTIS, the validation of the memory loss assumption is also necessary for the RPP method. In this work, the validation is performed by

comparing the first crossing probability of each interface, measured in TIS with the one reconstructed from the one-interface crossing probability $p_i^{\ominus}$ in RPP. Since $p_i^{\ominus}$ contains the re-crossing information of interface i from all the other interfaces, the consistency in the results from this comparison indicates that the loss of memory is actually an effect in the behavior of trajectories, and vice versa. There are other ways to check the memory loss assumption as outlined in Ref. [9].

The RPP method is very suitable for the study of rare events, such as nucleation processes, where the kinetics in the forward transition is of particular interest but the equilibrium calculation involving the reverse transition or Umbrella Sampling is time-consuming. However, one must be aware that RPP only uses "half" of the information in trajectory space, and the sampling weight of phase points is decreasing with interfaces getting farther away from the initial state. To make sure that RPP is accurate in the whole transition region, in the beginning, the TIS algorithm should collect enough trajectories on every interface, which will re-cross the interfaces behind the present one. In some cases, when the final state is much more energetically favorable than the initial state and when it is difficult to sample the re-crossing trajectories on interfaces close to the B region, then the RPP prediction for the energy profile may be incorrect for the area close to the B region. Still, the estimation of energy profile is reliable for the barrier height looking from the side of the initial state. This is also a reason why we recommend application of the RPP method to processes with only one important transition. Other issues regarding the order parameter and interface setting are similar to TIS [6] and PPTIS [9]. The order parameter should be a "proper" one, since the TIS algorithm is more sensitive to the choice of order parameter compared to TPS. As to the interface setting, the sign of memory loss between interfaces is weakened as the interfaces get closer to each other according to Ref. [9]. Therefore, it is advised to avoid a dense setting of interfaces in the transition region for the TIS calculation.

5. Conclusion

We proposed a Reweighted Partial Path method to efficiently evaluate the equilibrium state distribution for diffusive processes with a high-friction character in a single computation of Transition Interface Sampling or Forward Flux Sampling. Our method assumes a loss of memory in the trajectories, which allows a reweighting strategy to calculate the average weights of partial paths on each transition interface. The reweighted partial paths are directly used in the *loop-boundary* algorithm to compute the equilibrium distribution of λ in the transition region. This method is successfully implemented in the calculation of nucleation free energy of Cu precipitates in Fe-Cu solid solution. The RPP-evaluated free energy profile shows good agreement with Umbrella Sampling results. The accuracy and robustness of the RPP method are also discussed in this paper. It is emphasized that the RPP method might fail in cases where the history of the trajectories has a significant influence on the properties of the current state. Therefore, a validation of the memory-loss assumption must be performed in the assessment of RPP results.

Acknowledgement

This work was supported by *the Austrian Science Fund (FWF): F4113 SFB ViCoM.* Part of the computation was performed on *the Vienna Scientific Cluster (VSC).*

Appendix A:

The decaying probability that a trajectory, which crossed interface i from A, will return to A before continuing to cross B is defined as $U_i = P(\begin{smallmatrix}0\\M\end{smallmatrix}\big|\begin{smallmatrix}i\\0\end{smallmatrix}) = 1 - P(\begin{smallmatrix}M\\0\end{smallmatrix}\big|\begin{smallmatrix}i\\0\end{smallmatrix})$. According to the memory loss assumption, the following relations hold approximately for any positive integer q>0 [9],

$$\begin{aligned} &P(\begin{smallmatrix}l\\m\end{smallmatrix}\big|\begin{smallmatrix}i\\i\pm q\end{smallmatrix}) \approx P(\begin{smallmatrix}l\\m\end{smallmatrix}\big|\begin{smallmatrix}i\\i\pm 1\end{smallmatrix}) \\ &P(\begin{smallmatrix}i+q\\i-1\end{smallmatrix}\big|\begin{smallmatrix}i\\i+1\end{smallmatrix}) \approx P(\begin{smallmatrix}i+q\\i-1\end{smallmatrix}\big|\begin{smallmatrix}i\\i-1\end{smallmatrix})(\,p_i^{+}/p_i^{\pm}) \\ &P(\begin{smallmatrix}i-q\\i+1\end{smallmatrix}\big|\begin{smallmatrix}i\\i-1\end{smallmatrix}) \approx P(\begin{smallmatrix}i-q\\i+1\end{smallmatrix}\big|\begin{smallmatrix}i\\i+1\end{smallmatrix})(\,p_i^{=}/p_i^{\mp}) \end{aligned} \tag{19}$$

Using the approximation in eq. (19), the following relation in decaying probability is derived as

$$\begin{aligned} \frac{U_{i+1}-U_i}{U_i-U_{i-1}} &= \frac{P(\begin{smallmatrix}0\\M\end{smallmatrix}\big|\begin{smallmatrix}i+1\\0\end{smallmatrix}) - P(\begin{smallmatrix}0\\M\end{smallmatrix}\big|\begin{smallmatrix}i\\0\end{smallmatrix})}{P(\begin{smallmatrix}0\\M\end{smallmatrix}\big|\begin{smallmatrix}i\\0\end{smallmatrix}) - P(\begin{smallmatrix}0\\M\end{smallmatrix}\big|\begin{smallmatrix}i-1\\0\end{smallmatrix})} = \frac{P(\begin{smallmatrix}M\\0\end{smallmatrix}\big|\begin{smallmatrix}i+1\\0\end{smallmatrix})\left(P(\begin{smallmatrix}i+1\\0\end{smallmatrix}\big|\begin{smallmatrix}i\\0\end{smallmatrix})-1\right)}{P(\begin{smallmatrix}M\\0\end{smallmatrix}\big|\begin{smallmatrix}i\\0\end{smallmatrix})\left(P(\begin{smallmatrix}i\\0\end{smallmatrix}\big|\begin{smallmatrix}i-1\\0\end{smallmatrix})-1\right)} \\ &= \frac{P(\begin{smallmatrix}0\\i+1\end{smallmatrix}\big|\begin{smallmatrix}i\\0\end{smallmatrix})}{P(\begin{smallmatrix}i+1\\0\end{smallmatrix}\big|\begin{smallmatrix}i\\0\end{smallmatrix})P(\begin{smallmatrix}0\\i\end{smallmatrix}\big|\begin{smallmatrix}i-1\\0\end{smallmatrix})} \approx \frac{P(\begin{smallmatrix}0\\i+1\end{smallmatrix}\big|\begin{smallmatrix}i\\i-1\end{smallmatrix})}{P(\begin{smallmatrix}i+1\\0\end{smallmatrix}\big|\begin{smallmatrix}i\\0\end{smallmatrix})P(\begin{smallmatrix}0\\i\end{smallmatrix}\big|\begin{smallmatrix}i-1\\i-2\end{smallmatrix})} \\ &\approx \frac{P(\begin{smallmatrix}0\\i+1\end{smallmatrix}\big|\begin{smallmatrix}i\\i+1\end{smallmatrix})(p_i^{=}/p_i^{\mp})}{P(\begin{smallmatrix}i+1\\0\end{smallmatrix}\big|\begin{smallmatrix}i\\0\end{smallmatrix})P(\begin{smallmatrix}0\\i\end{smallmatrix}\big|\begin{smallmatrix}i-1\\i\end{smallmatrix})(p_{i-1}^{=}/p_{i-1}^{\mp})} = \frac{\mathrm{P}_i^{+}\mathrm{P}_{i+1}^{-}(p_i^{=}/p_i^{\mp})}{\mathrm{P}_i^{-}\mathrm{P}_{i+1}^{+}(p_{i-1}^{=}/p_{i-1}^{\mp})} \end{aligned} \tag{20}$$

Since $\frac{\mathrm{P}_i^{+}}{\mathrm{P}_i^{-}} = \frac{p_1^{\pm}p_2^{\pm}\cdots p_{i-1}^{\pm}}{p_1^{\mp}p_2^{\mp}\cdots p_{i-1}^{\mp}}$ [9], eq.(20) is rewritten as $\frac{U_{i+1}-U_i}{U_i-U_{i-1}} = \frac{p_{i-1}^{\mp}p_i^{=}}{p_{i-1}^{=}p_i^{\pm}}$. This relation can be expanded from U_{i+1} to U_1 as

$$U_{i+1}-U_i = \frac{p_{i-1}^{\mp}p_i^{=}}{p_{i-1}^{=}p_i^{\pm}}\left(U_i-U_{i-1}\right) = \ldots = \frac{p_1^{\mp}p_2^{\mp}\cdots p_{i-1}^{\mp}p_i^{=}}{p_1^{=}p_2^{\pm}\cdots p_i^{\pm}}\left(U_2-U_1\right) \tag{21}$$

Summing up eq. (21) from 1 to i, we have

$$U_i - U_2 = \left(U_2-U_1\right)\sum_{m=2}^{i-1}\frac{p_1^{\mp}p_2^{\mp}\cdots p_{i-1}^{\mp}p_i^{=}}{p_1^{=}p_2^{\pm}\cdots p_i^{\pm}} \tag{22}$$

Since $U_M = P(\begin{smallmatrix}0\\M\end{smallmatrix}\big|\begin{smallmatrix}M\\0\end{smallmatrix}) = 0$, U_2 is solved by eq. (22) as

$$U_2 = U_1\left[1+\sum_{m=2}^{M-1}\frac{p_1^{\mp}p_2^{\mp}\cdots p_{i-1}^{\mp}p_i^{=}}{p_1^{=}p_2^{\pm}\cdots p_i^{\pm}}\right]^{-1}\sum_{m=2}^{M-1}\frac{p_1^{\mp}p_2^{\mp}\cdots p_{i-1}^{\mp}p_i^{=}}{p_1^{=}p_2^{\pm}\cdots p_i^{\pm}} \tag{23}$$

Through combination of eqs. (22) and (23), we derive an expression for the decaying probability for a given i as

$$U_i = U_1\left[1+\sum_{m=2}^{M-1}\frac{p_1^{\mp}p_2^{\mp}\cdots p_{i-1}^{\mp}p_i^{=}}{p_1^{=}p_2^{\pm}\cdots p_i^{\pm}}\right]^{-1}\sum_{m=i}^{M-1}\frac{p_1^{\mp}p_2^{\mp}\cdots p_{i-1}^{\mp}p_i^{=}}{p_1^{=}p_2^{\pm}\cdots p_i^{\pm}} \tag{24}$$

According to the definition, the decaying probability at interface *i* can be rewritten as

$$U_i = P\left(\begin{matrix}0\\M\end{matrix}\middle|\begin{matrix}i\\0\end{matrix}\right) = 1-P\left(\begin{matrix}M\\0\end{matrix}\middle|\begin{matrix}i\\0\end{matrix}\right) = 1-\frac{1-U_1}{P_i^+} \tag{25}$$

Since $\frac{U_2-U_1}{U_1-1} = \frac{P\left(\begin{matrix}0\\M\end{matrix}\middle|\begin{matrix}2\\0\end{matrix}\right)-P\left(\begin{matrix}0\\M\end{matrix}\middle|\begin{matrix}1\\0\end{matrix}\right)}{P\left(\begin{matrix}0\\M\end{matrix}\middle|\begin{matrix}1\\0\end{matrix}\right)-1} = \frac{P\left(\begin{matrix}M\\0\end{matrix}\middle|\begin{matrix}2\\0\end{matrix}\right)P\left(\begin{matrix}0\\2\end{matrix}\middle|\begin{matrix}1\\0\end{matrix}\right)}{P\left(\begin{matrix}M\\0\end{matrix}\middle|\begin{matrix}1\\0\end{matrix}\right)} = \frac{p_1^{=}}{p_1^{\pm}}$, eq. (21) is rewritten as

$$U_{i+1}-U_i = \frac{p_1^{\mp}p_2^{\mp}\cdots p_{i-1}^{\mp}p_i^{=}}{p_1^{\pm}p_2^{\pm}\cdots p_i^{\pm}}(U_1-1) \tag{26}$$

Combining eq.(25) and (26), we can derive the expression for P_i^+ as

$$P_i^+ = \frac{1-U_1}{1-U_i} = \left(\sum_{m=1}^{i-1}\frac{p_1^{\mp}p_2^{\mp}\cdots p_{m-1}^{\mp}p_m^{=}}{p_1^{\pm}p_2^{\pm}\cdots p_m^{\pm}}\right)^{-1} \tag{27}$$

Since $\frac{\mathrm{P}_i^+}{\mathrm{P}_i^-} = \frac{p_1^{\pm}p_2^{\pm}\cdots p_{i-1}^{\pm}}{p_1^{\mp}p_2^{\mp}\cdots p_{i-1}^{\mp}}$ [9], P_i^- is also derived from eq.(27)

$$P_i^- = \left(\sum_{m=1}^{i-1}\frac{p_1^{\mp}p_2^{\mp}\cdots p_{m-1}^{\mp}p_m^{=}}{p_1^{\pm}p_2^{\pm}\cdots p_m^{\pm}}\right)^{-1}\prod_{j=1}^{i-1}\frac{p_j^{\mp}}{p_j^{\pm}} \tag{28}$$

Appendix B:

Since the equilibrium distribution is preserved in trajectory space, there should be no net probability flux passing through the phase points on a given interface *i*. In this case, the average effective crossing on *i* from i+1 equals to the effective crossing from *i*-1, i.e. $\left\langle\psi_{i,i-1}\right\rangle = \left\langle\psi_{i,i+1}\right\rangle$. Combining with eq. (10), one can get $J = \left\langle\Psi_i^{\pm}\right\rangle - \left\langle\Psi_i^{\mp}\right\rangle = 0$. Therefore, the continuity relation by eq. (11) at equilibrium is reduced to $\left\langle\Psi_i^{\mp}\right\rangle - \frac{p_i^{\pm}}{p_{i-1}^{\mp}}\left\langle\Psi_{i-1}^{\mp}\right\rangle = 0$. Hence,

$$\left\langle\Psi_i^{\mp}\right\rangle = \frac{p_1^{\pm}p_2^{\pm}\cdots p_i^{\pm}}{p_1^{\mp}p_2^{\mp}\cdots p_{i-1}^{\mp}}\left\langle\Psi_0^{\mp}\right\rangle \tag{29}$$

In the unbiased path ensemble $\{\mathbf{x}^{\tau}\}_{\mathrm{A}}$, there are no trajectories coming from region B, hence $J_{\mathrm{A}} \neq 0$ and $\left\langle \Psi_{M-1}^{\mp} \right\rangle_{\mathrm{A}} = 0$. Based on continuity relation, one can write down the following equations in $\{\mathbf{x}^{\tau}\}_{\mathrm{A}}$ for every interface from 1 to M-1:

$$\begin{cases} \dfrac{1}{p_1^{=}}\left\langle \Psi_1^{\mp} \right\rangle_{\mathrm{A}} + J_{\mathrm{A}} = \dfrac{p_1^{\pm}}{p_1^{=}}\left\langle \Psi_0^{\mp} \right\rangle_{\mathrm{A}} \\ \quad \vdots \\ \dfrac{1}{p_i^{=}}\left\langle \Psi_i^{\mp} \right\rangle_{\mathrm{A}} - \dfrac{p_i^{\pm}}{p_i^{=} p_{i-1}^{\mp}}\left\langle \Psi_{i-1}^{\mp} \right\rangle_{\mathrm{A}} + J_{\mathrm{A}} = 0 \\ \quad \vdots \\ -\dfrac{p_{M-1}^{\pm}}{p_{M-1}^{=} p_{M-2}^{\mp}}\left\langle \Psi_{M-2}^{\mp} \right\rangle_{\mathrm{A}} + J_{\mathrm{A}} = 0 \end{cases} \tag{30}$$

In eq. (30), we have M-1 unknowns, including $\left\{\left\langle \Psi_i \right\rangle_{\mathrm{A}}\right\}_{i=1\ldots M-2}$ and J_{A}, in M-1 equations. According to Cramer rule in linear algebra, the solution of eq. (30) is

$$\begin{cases} \left\langle \Psi_i^{\mp} \right\rangle_{\mathrm{A}} = \left\langle \Psi_0^{\mp} \right\rangle_{\mathrm{A}} \dfrac{p_1^{\pm} p_2^{\pm} \cdots p_i^{\pm}}{p_1^{\mp} p_2^{\mp} \cdots p_{i-1}^{\mp}} \cdot \left[1 + \sum_{m=2}^{M-1} \dfrac{p_1^{\mp} p_2^{\mp} \cdots p_{m-1}^{\mp} p_m^{=}}{p_1^{=} p_2^{\pm} \cdots p_m^{\pm}} \right]^{-1} \sum_{m=i+1}^{M-1} \dfrac{p_1^{\mp} p_2^{\mp} \cdots p_{m-1}^{\mp} p_m^{=}}{p_1^{=} p_2^{\pm} \cdots p_m^{\pm}} \\ J_{\mathrm{A}} = \left\langle \Psi_0^{\mp} \right\rangle_{\mathrm{A}} \dfrac{p_1^{\pm}}{p_1^{=}} \left[1 + \sum_{m=2}^{M-1} \dfrac{p_1^{\mp} p_2^{\mp} \cdots p_{m-1}^{\mp} p_m^{=}}{p_1^{=} p_2^{\pm} \cdots p_m^{\pm}} \right]^{-1} \end{cases} \tag{31}$$

Since $\left\langle \Psi_0^{\mp} \right\rangle_{\mathrm{A}} = \left\langle \psi_{0,1} \right\rangle_{\mathrm{A}}$ and $\left\langle \Psi_0^{\pm} \right\rangle = \left\langle \psi_{1,0} \right\rangle$, hence $U_1 = P\left(\begin{smallmatrix} 0 \\ M \end{smallmatrix} \middle| \begin{smallmatrix} 1 \\ 0 \end{smallmatrix}\right) = \dfrac{\left\langle \psi_{1,0} h_{0.M}^{f} \right\rangle}{\left\langle \psi_{1,0} \right\rangle} = \dfrac{\left\langle h_{\mathcal{A}} \psi_{0,1} \right\rangle}{\left\langle \psi_{1,0} \right\rangle} = \dfrac{\left\langle h_{\mathcal{A}} \right\rangle \left\langle \Psi_0^{\mp} \right\rangle_{\mathcal{A}}}{\left\langle \Psi_0^{\pm} \right\rangle}$. Since $\dfrac{\left\langle \Psi_0^{\mp} \right\rangle_{\mathrm{A}}}{\left\langle \Psi_0^{\pm} \right\rangle} = \dfrac{U_1}{\left\langle h_{\mathcal{A}} \right\rangle}$ and $\left\langle \Psi_0^{\mp} \right\rangle = \left\langle \Psi_0^{\pm} \right\rangle$, combining with eq.(29), (24) and (9), the effective crossing of interface i in $\{\mathbf{x}^{\tau}\}_{\mathrm{A}}$ is connected with its equilibrium average by

$$\begin{cases} \left\langle \Psi_i^{\mp} \right\rangle_{\mathrm{A}} = \dfrac{U_{i+1}}{\left\langle h_{\mathcal{A}} \right\rangle} \cdot \left\langle \Psi_i^{\mp} \right\rangle \\ \left\langle \Psi_i^{+} \right\rangle_{\mathrm{A}} = \dfrac{U_{i+1}}{\left\langle h_{\mathcal{A}} \right\rangle} \cdot \left\langle \Psi_i^{+} \right\rangle \end{cases} \quad \text{and} \quad \begin{cases} \left\langle \Psi_i^{\pm} \right\rangle_{\mathrm{A}} = \dfrac{U_{i+1}}{\left\langle h_{\mathcal{A}} \right\rangle} \cdot \left\langle \Psi_i^{\pm} \right\rangle + J_{\mathrm{A}} \\ \left\langle \Psi_i^{=} \right\rangle_{\mathrm{A}} = \dfrac{U_{i+1}}{\left\langle h_{\mathcal{A}} \right\rangle} \cdot \left\langle \Psi_i^{=} \right\rangle + \dfrac{p_i^{=}}{p_i^{\pm}} J_{\mathrm{A}} \end{cases}$$

$$J_{\mathrm{A}} = \left\langle \Psi_0^{\mp} \right\rangle_{\mathrm{A}} \cdot \frac{1 - U_1}{U_1} = \left\langle \Psi_0^{\pm} \right\rangle_{\mathrm{A}} P\left(\begin{smallmatrix} M \\ 0 \end{smallmatrix} \middle| \begin{smallmatrix} 1 \\ 0 \end{smallmatrix}\right) \tag{32}$$

References

[1] Dellago, C., Bolhuis, P. G., Csajka, F. S., and Chandler, D., 1998, "Transition Path Sampling and the Calculation of Rate Constants," J. Chem. Phys., **108**(5), pp. 1964–1977.

[2] G. Bolhuis, P., Dellago, C., and Chandler, D., 1998, "Sampling Ensembles of Deterministic Transition Pathways," Faraday Discuss, **110**(0), pp. 421–436.

[3] Dellago, C., Bolhuis, P. G., and Chandler, D., 1999, "On the Calculation of Reaction Rate Constants in the Transition Path Ensemble," J. Chem. Phys., **110**(14), pp. 6617–6625.

[4] Bolhuis, P. G., Chandler, D., Dellago, C., and Geissler, P. L., 2002, "Throwing Ropes over Rough Mountain Passes, in the Dark," Annu Rev Phys Chem, **53**, pp. 291–318.

[5] Dellago, C., Bolhuis, P. G., and Geissler, P. L., 2003, "Transition Path Sampling," *Advances in Chemical Physics*, John Wiley & Sons, Inc., pp. 1–78.

[6] van Erp, T. S., Moroni, D., and Bolhuis, P. G., 2003, "A Novel Path Sampling Method for the Calculation of Rate Constants," J. Chem. Phys., **118**(17), pp. 7762–7774.

[7] Allen, R. J., Warren, P. B., and ten Wolde, P. R., 2005, "Sampling Rare Switching Events in Biochemical Networks," Phys Rev Lett, **94**(1), p. 018104.

[8] Allen, R. J., Frenkel, D., and ten Wolde, P. R., 2006, "Simulating Rare Events in Equilibrium or Nonequilibrium Stochastic Systems," J. Chem. Phys., **124**.

[9] Moroni, D., Bolhuis, P. G., and Erp, T. S. van, 2004, "Rate Constants for Diffusive Processes by Partial Path Sampling," J. Chem. Phys., **120**(9), pp. 4055–4065.

[10] Moroni, D., van Erp, T. S., and Bolhuis, P. G., 2005, "Simultaneous Computation of Free Energies and Kinetics of Rare Events," Phys Rev E, **71**(5), p. 056709.

[11] Christoffersen, R. E., 1977, *Algorithms for Chemical Computations*, AMERICAN CHEMICAL SOCIETY, WASHINGTON, D. C.

[12] Chandler, D., 1978, "Statistical Mechanics of Isomerization Dynamics in Liquids and the Transition State Approximation," J. Chem. Phys., **68**(6), pp. 2959–2970.

[13] Zhu, F., and Hummer, G., 2012, "Convergence and Error Estimation in Free Energy Calculations Using the Weighted Histogram Analysis Method," J. Comput. Chem., **33**, pp. 453–65.

[14] Rogal, J., Lechner, W., Juraszek, J., Ensing, B., and Bolhuis, P. G., 2010, "The Reweighted Path Ensemble," J. Chem. Phys., **133**(17).

[15] Valeriani, C., Allen, R. J., Morelli, M. J., Frenkel, D., and Rein Ten Wolde, P., 2007, "Computing Stationary Distributions in Equilibrium and Nonequilibrium Systems with Forward Flux Sampling," J. Chem. Phys., **127**(11), pp. 1–11.

[16] White, G. M., 1969, "Steady-State Random Walks with Application to Homogeneous Nucleation," J. Chem. Phys., **50**(11), p. 4672.

[17] Kashchiev, D., 2000, "Chapter 13 - Stationary Nucleation," **1**, pp. 184–223.

[18] Warczok, P., Reith, D., Schober, M., Leitner, H., Podloucky, R., and Kozeschnik, E., 2011, "Investigation of Cu Precipitation in Bcc-Fe – Comparison of Numerical Analysis with Experiment," IJMR, **102**, pp. 709–716.

[19] Glicksman, M., 2000, *Diffusion in Solid: Field Theory, Solid-State Principles, and Applications*, Wiley-Interscience.

A statistical methodology to reconstruct nucleation pathways in the Fe-Cu system

Lin Qin[1, a *], Alice Redermeier[1, b], Ernst Kozeschnik[1, c], Carina Karner[2, d], Christoph Dellago[2, e]

[1] TU Wien, Institute of Materials Science and Technology, Vienna, Austria

[2] University of Vienna, Faculty of Physics, Vienna, Austria

[a]lin.qin@tuwien.ac.at, [b]alice.redermeier@tuwien.ac.at, [c]ernst.kozeschnik@tuwien.ac.at, [d]carina.karner@univie.ac.at, [e]christoph.dellago@univie.ac.at

Keywords: Nucleation Kinetics, Rare Event Sampling, Monte Carlo simulation

Abstract

In precipitation strengthened ferritic alloys, the Fe-Cu binary system is a well-studied model system. Still, many unsettled questions remain about the early stages of bcc Cu precipitation, most of which refer to the shape and composition of the critical and post-critical nuclei. Since the critical nucleation states are hard to investigate by experimental methods, we propose a computational strategy to reconstruct precipitation pathways and identify the nucleation states making use of Monte Carlo simulations combined with Rare Event Sampling methods. The precipitation process is reproduced by Monte Carlo simulations with an energy description based on the Local Chemical Environment approach, applying efficient pair potentials, which are dependent on the chemical environment, and the Forward Flux Sampling technique. This method provides profound insight into the shape and composition of the early-stage precipitates and also the critical cluster size and shape in dependency of the temperature and supersaturation.

Introduction

The Fe-Cu binary system is a well-studied model system in precipitation strengthened ferritic alloys, where Cu precipitates play an important role in materials strengthening. High resolution electron microscopy studies have confirmed that, in thermally-aged binary Fe-1-30%Cu alloys, copper precipitates undergo a BCC-9R-FCC transition during precipitation process [1][2]. But the composition of bcc cooper precipitates in the early precipitation stages is still a mystery. In recent Atom Probe (3DAP) investigations [3][4][5], the bcc Cu-rich precipitates are assumed to contain about 50% Fe atoms, while the results from small-angle neutron scattering (SANS) [6] infer a significantly higher cooper content of more than 70%. Schober et al. [5] attribute this discrepancy to the assumption of non-magnetic Cu precipitates in SANS

experiments and the insensitivity to very small clusters of only sub-nanometer radius in 3DAP techniques. Unfortunately, no direct explanation for why the bcc precipitates contain such high Fe content is provided. Kozeschnik [7] studies this problem within the framework of classical nucleation theory (CNT). He points out that certain amount of Fe in critical precipitates can lower the nucleation barrier, and the composition corresponding to the minimum nucleation barrier is the "real" critical composition.

Atomistic-scale approaches, such as Density Functional Theory (DFT) and Monte Carlo simulations, provide an alternative way to investigate the early-stage precipitation in Fe-Cu system. Although questions about binding energies, diffusion mechanism and cluster mobility are thoroughly discussed in former works [8][9][10], direct investigations of the critical states and nucleation rates are rarely addressed. In the present work, we propose a computational strategy to reconstruct precipitation pathways and identify critical nucleation states making use of Monte Carlo simulations combined with Rare Event Sampling methods.

Methodology

1. Forward Flux Sampling

Forward Flux Sampling (FFS) is a typical rare event sampling method proposed by Allen et al. [11] to calculate the rate constant for nucleation events in, originally, complex biochemical switches. This method does not require prior knowledge of the phase-space density and can be implemented in any other stochastic dynamic scheme. According to the FFS formalism, the nucleation rate is expressed as [12]

$$J_s = k/V \tag{1}$$

Where k is the transition rate constant for a nucleation event and V is the volume of the system.

The order parameters used in forward flux sampling do not necessarily to be the reaction coordinate but must be adequate to distinguish different stages of the system in nucleation events. In this work, we choose the size of the biggest precipitate formed in the system, x, as order parameters representing the particular stage in the nucleation process. In this way, the transition rate constant in FFS can be written as

$$k = \Phi_0 P\left(x_n \mid x_0\right) \tag{2}$$

where x_0 and x_n are two interfaces used to characterize the initial (supersaturated) state and the final (post-critical) state, respectively. $P\left(x_n \mid x_0\right)$ is the probability of a nucleation event to reach the final state on the condition that the nucleation path starts from the supersaturated state ($x<x_0$) and crosses the first interface x_0. Φ_0 is the initial flux through the first interface x_0, which equals to the inverse of average time for a system to initiate nucleation (incubation time is not included in the flux).

Normally, x_0 is set to a small *non-zero* value, considering the fluctuation of cluster size in the supersaturated state, whereas x_0 needs to be sufficiently large to represent a cluster size when the growth stage begins.

To improve the sampling efficiency, a series of non-overlapped interfaces $\{x_i\}$ are introduced between x_0 and x_n. The crossing probability, $P(x_{i+1} \mid x_i)$, is defined as the probability that the system of cluster size x_i grows into cluster size x_{i+1}, before shrinking back to the supersaturated state. In this way, $P(x_n \mid x_0)$ can be expressed as a product of crossing probabilities of the sequence of interfaces between $[x_0, x_n]$ with

$$P(x_n \mid x_0) = \prod_{i=0}^{n-1} P(x_{i+1} \mid x_i) \tag{3}$$

The detailed procedure for sampling the crossing probability is described in Allen's previous work [11][13].

2. Growth Probability

In nucleation events, a given x-sized cluster can grow and reach a sufficiently large supercritical size with a certain probability. If the cluster size is a well-defined order parameter for a nucleation process, we can analogously describe the probability that the system in cluster size x grows into the supercritical state before decaying to the supersaturated state by the Growth Probability $\mathcal{P}(x)$. Accordingly, the growth probability can be expressed as the crossing probability in FFS

$$\mathcal{P}(x) = P(x_n \mid x) \tag{4}$$

where $x \in [x_i, x_{i+1}]$ and x_n is a sufficiently large cluster size.

If x is considered as an additional interface (sub-interface) between $[x_i, x_{i+1}]$, the crossing probability $P(x_{i+1} \mid x_i)$ can be written as $P(x_{i+1} \mid x_i) = P(x_{i+1} \mid x) \cdot P(x \mid x_i)$, where $P(x \mid x_i)$ is the sub-crossing probability of x in the path ensemble of interface x_i [14]. Therefore,

$$\begin{aligned} \mathcal{P}(x) = P(x_n \mid x_{i+1}) \cdot P(x_{i+1} \mid x) &= \frac{P(x_n \mid x_0)}{P(x \mid x_i) \cdot P(x_i \mid x_0)} \\ &= \frac{\prod_{j=0}^{n-1} P(x_{j+1} \mid x_j)}{P(x \mid x_i) \cdot \prod_{j=0}^{i-1} P(x_{j+1} \mid x_j)} \end{aligned} \tag{5}$$

A general expression for the growth probability of an x-sized cluster to subsequently growing into a supercritical precipitate before shrinking to supersaturated state is derived by ter Horst et al. [15] as

$$\mathcal{P}(x) = \frac{1}{2}\left\{1 + \operatorname{erf}\left[\beta(x - x^*)\right]\right\} \tag{6}$$

with the error function $\mathrm{erf}(x) = 2/\sqrt{\pi}\int_0^x e^{-x^2}dx$, x^* is the critical nucleation size, and $\beta = \sqrt{\frac{-\Delta G''(x^*)}{2k_BT}} = \sqrt{\pi}Z$, where Z is the Zeldovich factor. By fitting the growth probability from FFS to equation 6, the critical size of the nucleus and the Zeldovich factor can be estimated. A similar way of estimating this factor can also be found in the *mean first passage time* method [16], which is not applied in the present work.

Simulation details

The forward flux sampling procedure for obtaining nucleation rates is performed with the fixed lattice Monte Carlo method implemented in the software MatCalc [17]. A bcc simulation box of 50×50×50 unit cells is used with periodic boundary conditions for all simulations. Atomic diffusivity is described by the vacancy exchange mechanism and the real time is coupled to Monte Carlo Step (MCS) by defining the time increment from one vacancy jump as $\Delta t = \frac{a^2 x_{\mathrm{Va,MC}}}{D_A}\cdot k$, where a is the nearest neighbor distance in bcc-Fe (2.485 angstrom), D_A is the diffusion coefficient of the jumping atom A in bcc-Fe, $x_{\mathrm{Va,MC}}$ is the vacancy site fraction in the simulation box (1/250000) and k is a correction for diffusion correlation effect in the vacancy exchange mechanism. The MC simulations apply the Metropolis algorithm and are governed by an atomic interaction energy depending on the Local Chemical Environment of the center atom [10].

The order parameter to characterize the nucleation stages is the size of largest precipitate in simulation box. Identification of clusters is based on the local concentration of Cu within the nearest neighboring shell — a site with local Cu concentration greater than 5/9 will be considered as belonging to a cluster. Under this strict condition for cluster detection, only the core of clusters will be measured and the fluctuation of cluster size in the supersaturated state is small. Therefore, we set the first interface x_0 in the range of cluster size of 3~5, and the last interface x_n in the range of cluster sizes of 30~50, for sampling under different predefined nucleation conditions, i.e. supersaturation. Internal interfaces are set by linear intervals of 5, to avoid unnecessary size fluctuations in MC simulations. In fact, the interface setting will not influence the sampling result for nucleation rate as long as the two important boundary interfaces are properly defined [14]. In each interface sampling, FFS harvest at least 300 paths connecting to the next interface and the total number of paths harvested is more than 500. The initial flux is sampled by collecting 300 trajectories that positively cross x_0 before reaching the final state.

Results

1. Nucleation rates

For comparison, the nucleation rates for Cu-precipitation are evaluated by FFS and a classical nucleation theory continuum model (MatCalc) [18] for an Fe-1%Cu alloy

aged at 400°C, 450°C, 500°C and 550°C and an Fe-1.5%Cu alloy aged at 450°C, 500°C, 550°C and 600°C (Fig. 1). It is worth noting that the nucleation rate obtained from FFS is the steady nucleation rate, since the sampling starts from the boundary condition of supersaturated state and, thus, the incubation time is not taken into account. In classical nucleation theory, the steady nucleation rate is calculated by $J = NZv^* \exp\left[-\Delta G\left(x^*\right)/RT\right]$, where N is the number of potential nucleation sites, Z is the Zeldovich factor, v^* is the atomic attachment rate, R is the gas constant and $\Delta G(x^*)$ is the energy barrier at critical size x^*.

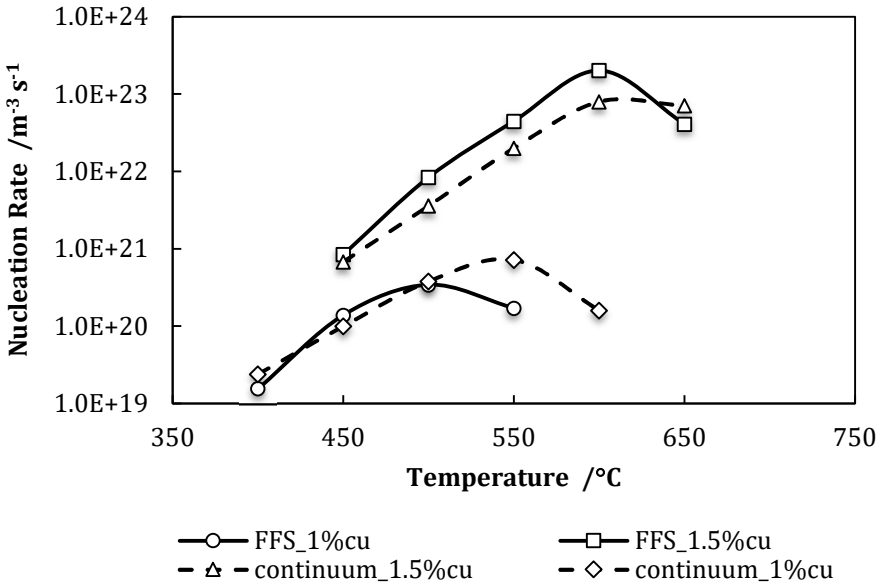

Fig. 1 Comparison of nucleation rates obtained by FFS and the continuum model for Fe-1%Cu and Fe-1.5%Cu at temperatures between 400 and 650°C.

As a consequence of calibrating the pair-interaction energies on the same energy data as in the continuums simulation, see ref. [10], even though based on different methodologies, FFS and continuum model give very similar predictions of the nucleation rates. At low temperatures (< 450°C,) and high superstation, the crossing probability $P\left(x_n \mid x_0\right)$ is very high (around 10^{-2}) due to a low nucleation barrier, but the low diffusivity of the system limits the flux through first interface and restricts nucleation events happening per unit time. However, when temperature goes over 600°C, the initial flux Φ_0 increases significantly, but this contribution to the nucleation rate is offset as the crossing probability drops to around 10^{-5} in the mean time. The maximum nucleation rate emerges around 500°C for Fe-1%Cu and 600°C for Fe-1.5%Cu.

2. Zeldovich factor and critical size

In classic nucleation theory, the Zeldovich factor is defined as the curvature of the energy barrier at the critical point, $Z = \sqrt{-\frac{\Delta G''(n^*)}{2\pi k_B T}}$, while in the growth probability, Z describes the increasing trend of the growth probability with cluster size according to equation 6. In the Fe-1%Cu alloy (Fig.2), a rapid increase of the growth probability at 400°C corresponds to a Z factor of 0.28, and a slow increase at 550°C indicates a Z factor of 0.07. Generally, smaller values in Z correspond to a broader and smoother nucleation barrier, which indicate frequent recurrent behavior and longer time for precipitates to grow into a supercritical size. In a nucleation process, once a precipitate grows over the critical size but not sufficiently large, it still has a certain probability to shrink back into a pre-critical state. This recurrent behavior is more frequently observed in sampling nucleation pathways at higher temperature.

The evaluation of the Zeldovich factor and the critical size for Fe-1%Cu and Fe-1.5%Cu alloys are summarized in Fig.3. The two parameters are also evaluated by the continuum model based on a mean-field model and spherical precipitate shape [7]. The critical size observed in the continuum model is larger than that from FFS because the majority of critical precipitates observed in sampling are approximately ellipsoidal with a higher surface-to-volume ratio compared to a perfect sphere. The average chemical composition of the critical precipitates is about 0.9 in Cu, which is not surprising, since we use a very strict condition for Cu precipitate detection and only cores of precipitates (Cu >0.8) will be considered. A similar algorithm with cluster erosion process in APT is also used to analyze the critical state of Fe-1%Cu at 500°C, where critical precipitates reveal an average composition of Cu in the range of 0.5~0.7 with very irregular shapes.

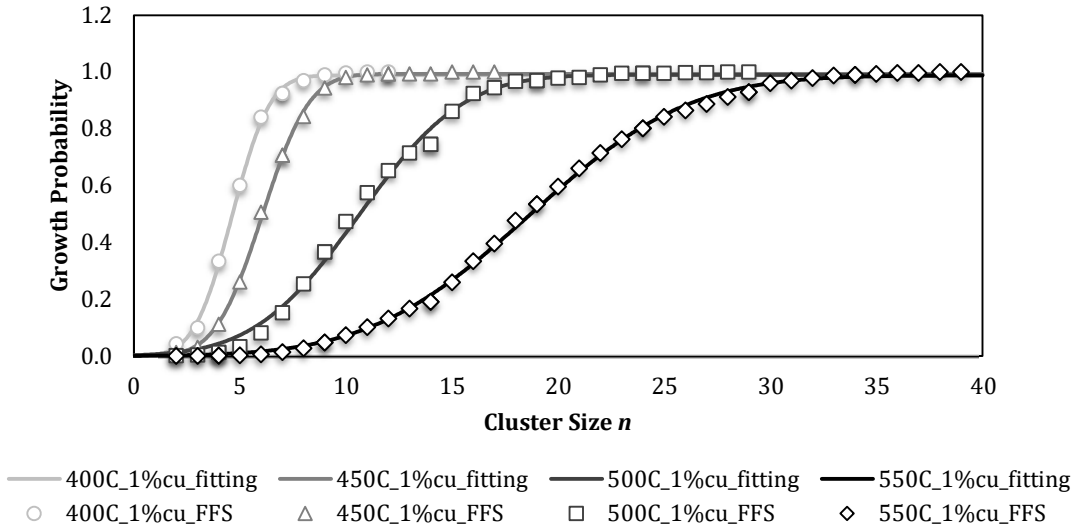

Fig. 2 Growth Probability of precipitates in Fe-1%Cu alloy at different temperatures, where dots are calculated probabilities from FFS and lines are fitting curves to the error function.

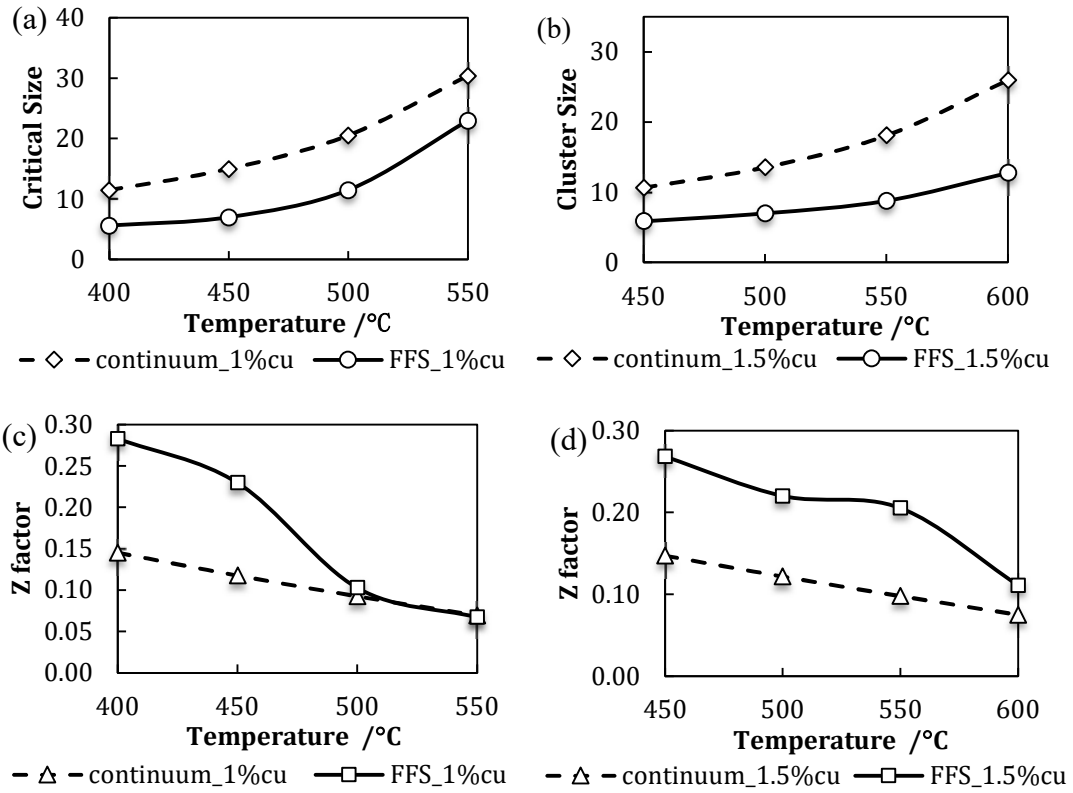

Fig. 3 Critical size of precipitates in Fe-1%Cu (a) and Fe-1.5%Cu (b) alloys aging at different temperatures obtained with FFS (solid line) and classical nucleation theory (dashed line).

Summary

In this work, we proposed a computational strategy combining Forward Flux Sampling and Monte Carlo simulation to investigate nucleation in the Fe-Cu system. This method successfully predicts nucleation rates of bcc early-stage cooper precipitates in Fe-1%Cu and Fe-1.5%Cu alloys and identifies the respective critical state on each nucleation pathway. Other kinetic measures of relevant quantities, such as Zeldovich factor and critical size, are also investigated in this work.

This work was supported by *the Austrian Science Fund (FWF): F4113 SFB ViCoM*, and part of the computation was done on *the Vienna Scientific Cluster (VSC)*.

References

[1] E. Hornbogen and R. C. Glenn, A metallographic study of precipitation of copper from alpha iron, Tran. Met. Soc. AIME 218 (1960) 1067–1070.

[2] P. J. Othen, M. L. Jenkins, G. Smith, and W. J. Phytian, Transmission electron-microscope investigations of the structure of copper precipitates in thermally-aged Fe-Cu and Fe-Cu-Ni, Philps. Mag. Lett. 64 (1991) 383–391.

[3] D. Isheim and D. N. Seidman, Nanoscale studies of segregation at coherent heterophase interfaces in alpha-Fe based systems, Surf. Interface Anal 36 (2004) 569–574.

[4] D. Isheim, M. S. Galiano, M. E. Fine, and D. N. Seidman, Interfacial segregation at Cu-rich precipitates in a high-strength low-carbon steel studied on a sub-nanometer scale, Acta Mater. 54 (2006) 841–849.
[5] M. Schober, E. Eidenberger, H. Leitner, P. Staron, D. Reith, and R. Podloucky, A critical consideration of magnetism and composition of (bcc) Cu precipitates in (bcc) Fe, Appl. Phys. A 99 (2010) 697–704.
[6] M. K. Miller, B. D. Wirth, and G. R. Odette, Precipitation in neutron-irradiated Fe-Cu and Fe-Cu-Mn model alloys: a comparison of APT and SANS data, Mater. Sci. Eng. A 353 (2003) 133–139.
[7] E. Kozeschnik, Thermodynamic prediction of the equilibrium chemical composition of critical nuclei: Bcc Cu precipitation in α-Fe, Scr. Mater. 59 9 (2008) 1018 – 1021.
[8] F. Soisson, A. Barbu, and G. Martin, Monte carlo simulations of copper precipitation in dilute iron-cooper alloys during thermal aging and under electron irradiation, Acta Mater. 44 (1996) 3789–3800.
[9] F. Soisson and C. C. Fu, Cu-precipitation kinetics in alpha-Fe from atomistic simulations: Vacancy-tranping effects and Cu-cluster mobility, Phys. Rev. B 76 (2007) 214102.
[10] P. Warczok, D. Reith, M. Schober, H. Leitner, R. Podloucky, and E. Kozeschnik, Investigation of Cu precipitation in bcc-Fe – Comparison of numerical analysis with experiment, IJMR 102 (2011) 709–716.
[11] R. J. Allen, P. B. Warren, and P. R. ten Wolde, Sampling Rare Switching Events in Biochemical Networks, Phys. Rev. Lett. 94 1 (2005) 018104.
[12] S. Jungblut and C. Dellago, Caveats of mean first-passage time methods applied to the crystallization transition: Effects of non-Markovianity, J. Chem. Phys. 142 (2015) 064103.
[13] R. J. Allen, D. Frenkel, and P. R. ten Wolde, Simulating rare events in equilibrium or nonequilibrium stochastic systems, J. Chem. Phys. 124 (2006) .
[14] T. S. van Erp, D. Moroni, and P. G. Bolhuis, A novel path sampling method for the calculation of rate constants, J. Chem. Phys. 118 17 (2003) 7762–7774.
[15] J. H. ter Horst and D. Kashchiev, Determination of the nucleus size from the growth probability of clusters, J. Chem. Phys. 119 (2003) 2241–2246.
[16] J. Wedekind, R. Strey, and D. Reguera, New method to analyze simulations of activated processes, J. Chem. Phys. 126 (2007) 134103.
[17] information on http://matcalc.at
[18] G. Stechauner and E. Kozeschnik, Thermo-kinetic modeling of Cu precipitation in α-Fe, Acta Mater. 100 (2015) 135–146.